Proceedings of

2nd ISEED

The 2nd International Symposium on Expertise of Engineering Design

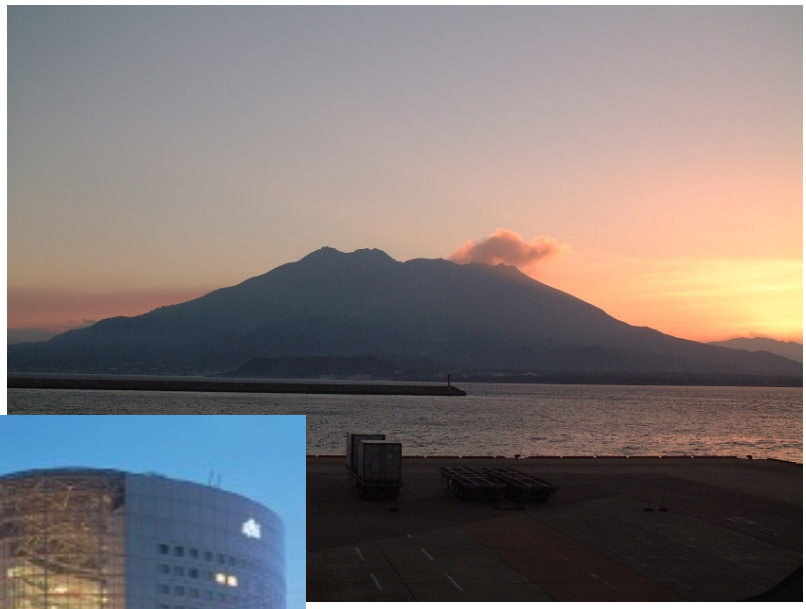

10 to 11 May, 2017
Hotel Kyocera, Kirishima, Kagoshima, Japan

EDITORS IN CHIEF
Takashi Tsutsumi

Proceedings of

The 2nd International Symposium on Expertise of Engineering Design

Published by

National Institute of Technology,
Kagoshima College, Japan
1460-1 Shinkoh, Hayato-cho,
Kirishima city, Kagoshima, Japan

ISSN 2433-6041

CONTENTS

ORGANIZING COMMITTEES

Chairman

Prof. Dr. Takashi Tsutsumi
(National Institute of Technology, Kagoshima College, Japan)

Co-Chairman

Prof. Dr. Masahito Yamauchi
(National Institute of Technology, Kagoshima College, Japan)

Secretary

Assoc. Prof. Dr. Mariko Sakamoto
(National Institute of Technology, Kagoshima College, Japan)

Technical Committee

Dr. Anis Ur Rehman
(National Institute of Technology, Kagoshima College, Japan)
Dr. Rini Asnida Abdullah
(Universiti Teknologi Malaysia, Malaysia)
Dr. Shazwin Mat Taib
(Universiti Teknologi Malaysia, Malaysia)

OPPORTUNITIES FOR INTERNATIONAL COLLABORATION IN ENGINEERING RESEARCH

Kathryn A. Mumford[1]*, Christoph Schmucker[1], Junchao Ma[1], Geoffrey W. Stevens[1]

[1] *Department of Chemical and Biomolecular Engineering, University of Melbourne, Melbourne, Australia, 3010.*

*Corresponding Author: *mumfordk@unimelb.edu.au*

Abstract: National and International food and water security requires the dedicated management of agricultural soils and appropriate treatment of contaminated land and water. These are, by their nature, global issues and as such are a leading area for International Collaboration. The Department of Chemical and Biomolecular Engineering, at the University of Melbourne has developed significant and long lasting international collaborations over the past 20 years to address these important issues. Here we present and discuss the variety of mechanisms used to manage, finance and enhance these collaborations, along with a snapshot of the excellent rsearch outcomes obtained to date.

Keywords: *International Collaboration, Australia, China, Japan, Water Treatment, Fertiliser efficiency*

1.0 Introduction

National and International food and water security requires the dedicated management of agricultural soils and appropriate treatment of contaminated land and water. These are, by their nature, global issues and as such are a leading area for International Collaboration. The Department of Chemical and Biomolecular Engineering, at the University of Melbourne has developed significant and long lasting international collaborations over the past 20 years to address these important issues. Here we present and discuss the variety of mechanisms used to manage, finance and enhance these collaborations, along with a snapshot of the excellent rsearch outcomes obtained to date.

1.1 Enhancing Performance of Agricultural Soils

In 2016, the Department of Chemical and Biomolecular Engineering joined an Australia-China Joint Research Centre entitled “Healthy Soils for Sustainable Food Production”. This joint research centre is funded through the Australian and Chinese Governments. It involves a number of collaborators from Australia and China including from research institutes, Universities and Industrial Partners. Key members are: Chinese Academy of Agricultural Sciences, Chinese Academy of Sciences, Nanjing Agricultural University, The University of New England, The University of Western Australia, Commonwealth Scientific and Industrial Research Organisation (CSIRO), Incitec Pivot Limited and Xinyangfeng Fertiliser Co. Ltd.

Chemical Engineering is supporting this collaboration through the development of a range of new fertiliser products to increase the efficiency of input use. These products are controlled release fertilisers which aim to reduce nutrient losses to air, ground water and run off, whilst remaining fully biodegradable and cost effective.

These fertilisers are being developed via the solvent vapour treatment of liquid marbles, that have been stabilised with various functional monomers. Liquid marbles may be formed via the deposition of salt solutions of nutrients onto an inclined bed of dried polymer powder. As the aqueous drop rolls on the

powder bed, the liquid becomes encapsulated by the polymer, rendering it both hydrophobic and nonwetting. Upon exposure to solvent vapour, the polymer plasticises and a 'polymer capsule' is formed, which may be subsequently dehydrated (Figure 1).

The polymer is fully biodegradable, and upon degradation releases bioavailable carbon. Examples of the types of materials used include; poly - [2-(diethylamino) ethyl methacrylate]- (PDEA-)(Bruining, Blaauwgeers et al. 2000; Fujii, Suzaki et al. 2011); glycerol monomethacrylate (Thompson, Armes et al. 2010) and poly (n- isopropylacrylamide) (Yusa, Morihara et al. 2014; Das, Ghosh et al. 2015).

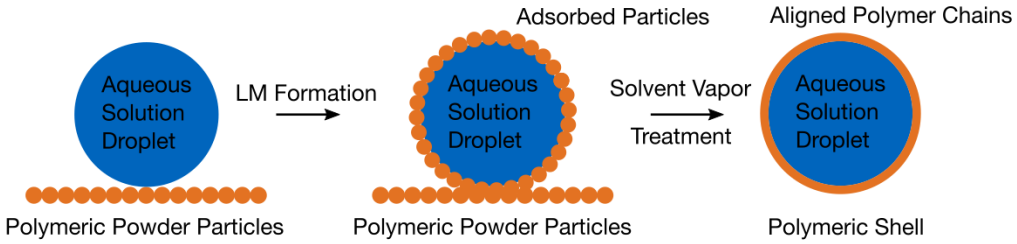

Figure 1: Formation of Liquid Marble

This type of material has many advantages over currently available products, primarily due to the almost limitless tunability of the surface chemistry of the film formed and the ease of manufacture. Specifically, for fertiliser products, these benefits include:

- Control over water permeation rates into the capsule via manipulation of the pore size of the polymer film coating. The pore size of the polymer coating is determined by the polymer selection and solvent treatment time, with longer treatment times resulting in reduced porosity (Ueno, Hamasaki et al. 2014). This design capability is significant as water permeation and subsequent nutrient dissolution and migration through the film is the major nutrient transport pathway.

- External stimulus triggers film disintegration. The functional groups on the polymer coating may be selected to enable targeted release of nutrients in response to specific external stimulus. This design feature enables the potential matching of nutrient release to crop demand. Examples include: pH (Fujii, Kameyama et al. 2010), UV (Nakai, Fujii et al. 2013) and temperature (Yusa, Morihara et al. 2014) amongst others.

The combination of these design features provides an added capability for fertiliser product design for specific applications and requirements, thereby improving nitrogen efficiencies.

1.2 Materials and engineering designs to enhance Contaminated Site Remediation processes.

Japan

Research regarding the development of novel materials for the treatment of contaminanted soil and water, including both heavy metals and organics, is currently being conducted in collaboration with Kanazawa Institute of Technology and Miyazaki University. These colloborations are primarily supported via the exchange of Masters Level students and Research Fellows. Funding is typically through the Japanese Society for the Promotion of Science (JSPS) Postdoctoral Fellowships and Australian Research Council "Linkage International Awards".

Key areas of research interests include:

- The adsorption behavior of heavy metals onto chemically modified MCM-41.(Northcott, Miyakawa et al. 2010; Watanabe, Miyakawa et al. 2010).

- Chitosan coated silica for heavy metal and nutrient removal.(Arora, Eddy et al. 2010).
- Synthesis, characterization and performance of chlorosilane coated zeolites for the removal of soluble organics and nutrient addition to enhance biodegradation processes. (Northcott, Bacus et al. 2010)

Of these, the synthesis, characterization and performance of chlorosilane coated zeolites is of particular interest. Inherently, due to the net negative charge of the aluminosilicate lattice of zeolites, they prefer to exchange cations rather than absorb organic compounds. However, if the zeolite surface is coated with covalently bound chlorosilane materials, (Figure 2), it becomes hydrophobic and will sorb organics on to the surface whilst still exchanging cations within the mineral structure.

Due to the dual capture mechanism of the chlorosilane coated material, it may be used for a number of different purposes, including:

- treatment of waters contaminated with both organics and heavy metals, or
- to aid in the biodegradation of organic contaminates via the addition of nutrient cations from the internal zeolite structure to where to organic contaminants are captured.

Both of these applications are currently under investigation.

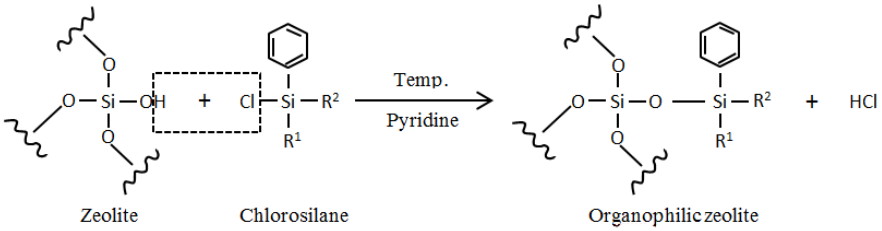

Figure 2: Chlorosilane coating of zeolite minerals

Pakistan

Research work conducted in collaboration with Pakistaini Universities have predominantly focused on the development of strategies for the utilization of Expanded Polystyrene (EPS) foam waste to manufacture useful materials. This is an important area as styrofoam waste has a number of negative characteristics, including; high chemical stability, large volumes and limited degradation potential resulting in it being recognized as an environmental threat and significant waste management problem. A key area of interest has been on the functionalization of polystyrene with nitrogen containing species, which have the potential to retain toxic heavy metals such as Ni(II) ions from aqueous solutions. These developments have been shown to have significant potential.

The links developed with Pakistan have predominantly been funded through Non-Government Organisations such as the Organisation for the Prohibitation of Chemical Weapons (OPCW), and have been facilitated by the exchange of Research Fellows.

Canada

Understanding the hydrocarbon degradation pathways by microbial communities is an important research area as it directly impacts on the design of reactive substrates i.e. what type of material will enhance biofilm growth and hence contaminant degradation. Work in this area is predominantly being conducted in collaboration with Queens University, Canada. Funding is primarily obtained from the Australian

Government via Australian Antarctic Division Science Grants and collaboation is enhance via Research Fellow visits between the institutions.

Recently work has focused on the examination of microbial communities that are actively degrading hydrocarbon contaminants on adsorbent materials using amplicon pyrosequencing. The reaction of these communities to petroleum hydrocarbons and ammonium supplementation was assessed. It was found that the increased presence of hydrocarbons reduced the microbial diversity of the biofilm communities, resulting in a shift to a population high in *Actinobacteria* and *Proteobacteria* (Freidman, Gras et al. 2016; Freidman, Gras et al. 2016).

2.0 Conclusions

Many opportunities exist for productive international collaboration in Engineering Research. Here, one research area was selected, that is, soil and water management for agriculture and contaminated site remediation. Active collaborations between Australia, Japan, China, Pakistan and Canada were demonstrated. Although these collaborations are managed, funded and supported via different mechanisms, outstanding research outcomes for all projects have been obtained with student and Research Fellow exchanges on-going.

References

Arora, M., N. Eddy, K. Mumford, Y. Baba, J. Perera and G. Stevens (2010). *Surface modification of natural zeolite by chitosan and its use for nitrate removal in cold regions.* Cold Regions Science and Technology 62(2-3 July 2010).

Bruining, M. J., H. G. Blaauwgeers, R. Kuijer, E. Pels, R. M. Nuijts and L. H. Koole (2000). *Biodegradable three-dimensional networks of poly(dimethylamino ethyl methacrylate). Synthesis, characterization, and in vitro studies of structural degardation and cytotoxicity.* Biomaterials 21(6): 595-604.

Das, D., P. Ghosh, A. Ghosh, C. Haldar, S. Dhara, A. B. Panda and S. Pal (2015). *Stimulus-responsive, biodegradable, biocompatible, covalently cross-linked hydrogel based on Dextrin and poly-(n-isopropulacrylamide).* ACS Applied Materials and Interfaces 7(26): 14338 - 14351.

Freidman, B. L., S. L. Gras, I. Snape, G. W. Stevens and K. A. Mumford (2016). *Application of controlled nutrient release to permeable reactive barriers.* Journal of Environmental Management 169: 145-154.

Freidman, B. L., S. L. Gras, I. Snape, G. W. Stevens and K. A. Mumford (2016). *The performance of ammonium exchanged zeolite for the biodegradation of petroleum hydrocarbons migrating in soil water.* Journal of Hazardous Materials 313: 272-282.

Fujii, S., S. Kameyama, S. P. Armes, D. Dupin, M. Suzaki and Y. Nakamura (2010). *pH-responsive liquid marbles stabilized with poly(2-vinylpyridine) particles.* Soft Matter 6(3): 635-640.

Fujii, S., M. Suzaki, S. P. Armes, D. Dupin, S. Hamasaki, K. Aono and Y. Nakamura (2011). *Liquid Marbles Prepared from pH-Responsive Sterically Stabilized Latex Particles.* Langmuir 27(13): 8067-8074.

Nakai, K., S. Fujii, Y. Nakamura and S. Yusa (2013). *Ultra-violet light responsive liquid marbles.* Chemistry Letters 42: 586-588.

Northcott, K., J. Bacus, N. Taya, Y. Komastu, J. Perera and G. Stevens (2010). *Synthesis and characterisation of hydrophobic zeolite for the treatment of hydrocarbon contaminated ground water.* Journal of Hazardous Materials 183(1-3): 434-440.

Northcott, K., K. Miyakawa, S. Oshima, Y. Komastu, J. Perera and G. Stevens (2010). *The adsorption of divalent metal cations on mesoporous silicate MCM-41.* Chemical Engineering Journal 157(1).

Thompson, K. L., S. P. Armes, D. W. York and J. A. Burdis (2010). *Synthesis of sterically-stabilized latexes using well-defined poly(glycerol monomethacrylate) macromonomers.* Maromolecules 43(2169-2177).

Ueno, K., S. Hamasaki, E. J. Wanless, Y. Nakamura and S. Fujii (2014). *Microcapsules fabricated from liquid marbles stabilized with Latex particles.* Langmuir 30: 3051-3059.

Watanabe, K. Miyakawa, Fujinaga, S. Oshima, Y. Komastu, K. Northcott, J. Perera and G. Stevens (2010). *Adsorption behaviour of copper ions on chemically modified MCM-41.* Journal of Ion Exchange 21(3).

Yusa, S., M. Morihara, K. Nakai, S. Fujii, Y. Nakamura, A. Maruyama and N. Shimada (2014). *Thermo-responsive liquid marbles.* Polymer Journal 46(3): 145-148.

A NEW WIND / WATER TURBINE WITH CIRCULAR CYLINDER PROPELLER DRIVEN BY LONGITUDINAL VORTEX

Tsutomu Takahashi[1]*

[1] *Department of Mechanical Engineering, Nagaoka University of Technology, 1603-1 Kamitomioka, Nagaoka, Niigata, 940-2188 Japan*

*Corresponding Author: *ttaka@nagaokaut.ac.jp*

Abstract: A new lift force generation mechanism on a circular cylinder has been developed. A circular cylinder is located in uniform flow and a strip-plate is set behind it in the cruciform arrangement with a suitable gap distance. When the circular cylinder moves parallel along the strip-plate, a longitudinal vortex forms in the backside of the cylinder near the strip-plate. The steady lift force is induced by the vortex. The mechanical configuration of this new driving system is very simple and it can apply to design a propeller consisted by the circular cylinder blades with change the strip-plate to a ring plate. Both the horizontal and vertical axis turbines driven by this mechanism were designed and tested. The most important form factor is the gap between the blades and the wake ring plate and it can easily control the lift force and the rotation speed by adjusting it. Some prototype turbines for the wind and water flow were built up and tested. In this presentation, the performance of this turbine, the effect of the shape factors and the application of this turbine will be demonstrated and discussed.

Keywords: *Wind turbine, propeller, circular cylinder blade, longitudinal vortex, steady lift force*

1.0 Introduction

The conventional blade of the propeller of the wind turbines is a thin twisted plate with a suitable incident angle to generate lift force and its cross-sectional shape is similar to the wing of the airplane to increase the power efficiency and to reduce the drag. The blades, in general, are weak for bending force and there is a difficulty of manufacturing. A spinning circular cylinder can generate steady lift force that is induced by Magnus effect. The Flettner type rotor employed this driving force was applied to a ship and wind turbines, but it was not practically used because of their complex mechanism of the spinning. On a circular cylinder located perpendicular to the uniform flow, the alternative lift force occurs by Karman vortices shedding. It can induce a vibration when the cylinder is supported elastically. It is called Karman vortex-induced vibration. It caused some serious accidents but it is not easy to utilize this vibration to generate the electricity because it causes in the very narrow velocity range of the flow. Our group

developed a new driving mechanism of the vortex-induced vibration, that is, the longitudinal vortex induced vibration. Kato et al. (2006) reported that a circular cylinder with a crisscross arranged strip-plate in the wake was strongly oscillated by shedding the longitudinal vortices. In both vortex-induced vibration, the time average of the lift force is zero and it cannot apply for the driving mechanism to the wind turbine.

Recently, Takahashi et al. (2016) found a new mechanism to generate steady lift force on a circular cylinder from the uniform flow. When a circular cylinder locates perpendicular to the uniform flow with a crisscross arranged strip-plate in the wake and it moves along the strip-plate with a constant velocity, a longitudinal vortex forms steadily behind the cylinder and a strong suction flow from the frontal area to the vortex is induced. The flow field around the circular cylinder moving along the strip-plate that was a result of CFD is shown in Fig.1. This mechanism can apply to the rotation motion by changing the strip-plate to the ring plate and the parallel motion of the circular cylinder to the rotation motion. The simplest design of the wind turbine applied this driving mechanism is shown in Fig.2. This wind turbine is consisted only by a circular cylinder, a rotation axis and a ring-shaped wake plate. The geometrical shape is very simple compared with the conventional propeller because the blade is a circular cylinder. In this study, the fundamental mechanism of this new turbine driving system is introduced by the experimental and the numerical results. The special feature of the simplest model, which is consisted by a single circular cylinder as a propeller blade, is examined. Finally, some example of the application is introduced, and their ability and possibility are discussed.

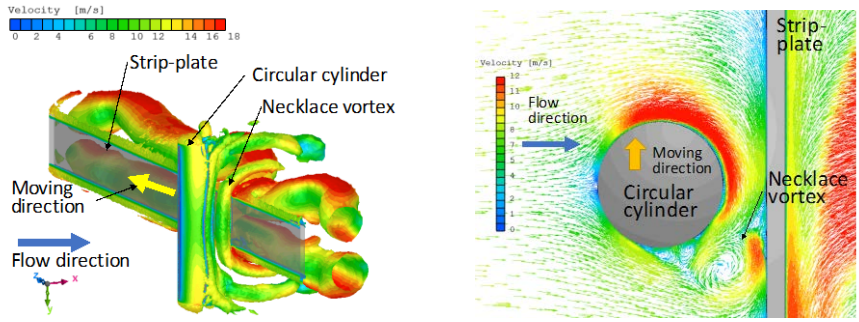

(a) (b)

Figure 1: CFD result of velocity field around moving circular cylinder along crisscross arranged strip-plate. (a)three-dimensional view of longitudinal vortex (necklace vortex) and (b)cross sectional view perpendicular to cylinder.

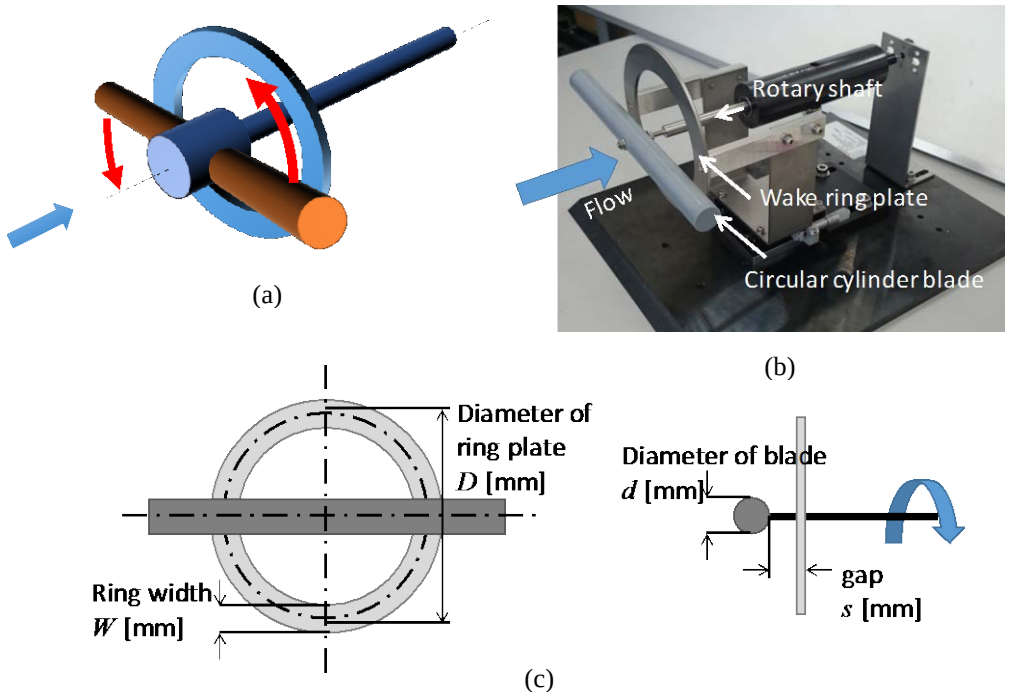

(a)

(b)

(c)

Figure 2: Single circular cylinder blade wind turbine driven by longitudinal vortex. (a)Schematic diagram, (b)photograph of trial test module and (c)important shape factors.

2.0 Mechanism of A New Turbine

2.1 Steady lit force generation on a circular cylinder

When a circular cylinder is placed perpendicular to the uniform flow and a strip-plate is set in the wake area of the cylinder with the crisscross arrangement, the necklace shaped or the trailing shaped longitudinal vortices shed periodically near the intersectional area and their shedding position is alternatively change from the up and down side of the cylinder. This vortex shedding induces the alternative lift force on the cylinder but the average value of the lift force is zero. When the cylinder moves parallel to the strip-plate with a constant velocity, a necklace shaped longitudinal vortex forms in the backside of the cylinder near the intersectional area, as shown in Fig.1(a). In this calculation, the diameter and the length of the circular cylinder are 20mm and 60mm, respectively. The width of the strip-plate is 30mm. The gap between the cylinder and the strip-plate is 7mm. The cross-sectional flow field perpendicular to the cylinder at the center plane of the strip-plate is shown in Fig.1(b). The longitudinal vortex makes a strong suction flow

from the frontal area to the gap and the negative pressure occurs on the front surface of the cylinder. It becomes the steady lift force acting on the cylinder.

2.2 Rotation motion induced by longitudinal vortex

In order to apply the lift force induced by the longitudinal vortex to the rotation motion, we designed a new turbine, which has a ring plate in place of the strip-plate. A rotation shaft is attached on the cylinder to change the parallel motion to the rotation. This is the simplest design of the turbines driven by the longitudinal vortex, which consists mainly only the three parts, a circular cylinder as a propeller, a ring plate and a rotation shaft. The schematic diagram of this simplest design is shown in Fig.2 and the test module used in the trial test is shown in Fig.2(b). The important form factors of this turbine is shown in Fig.2(c). When the circular cylinder is stopped, that is zero angular velocity, the longitudinal vortices shed unregularly and it causes fluctuating angular motion on the cylinder. Once the angular velocity exceeds a critical value, the cylinder starts to rotate one direction. The rotation direction, CW or CCW, is dependent on the initial direction. The cylinder is accelerated to a certain velocity and reaches on a stable rotation.

3.0 Feature of New Turbine and Possibility

3.1 Feature of wind turbine driven by longitudinal vortex

The simplest shape of the wind turbine driven by the longitudinal vortex, which has a single circular cylinder as a propeller, was designed as shown in Fig.2 and tested to understand the feature of this new turbine driven mechanism. The diameter d and length of the circular cylinder are 20mm and 220mm, respectively. The diameter D of the ring plate is 155mm. Figure 3(a) shows the relationship between the flow velocity and the rotation speed. The rotation speed increases linearly with increasing the flow velocity and the tip speed ratio λ ($=\omega D/2U$, ω is angular velocity) is about 0.28 even in the fastest condition, W/d=1.5. Here, W is the width of the ring plate. The rotation speed of this turbine is more than ten times slower the conventional propeller turbine and also than the Savonius type windmills. On the other hand, the torque is larger than the conventional propeller. The linearity of the rotation speed to the flow velocity keeps more than 30m/s that is the limit of our wind tunnel instrument. It is an important feature that is based on this turbine mechanism and is different from the theory of the conventional propeller. As seen in Fig.3(a), W is one of the important shape factors of this turbine mechanism. Another important factor is the gap between the cylinder and the ring, s, and the influence of s/d on the rotation speed is shown in Fig.3(b). There is an optimum value, s/d=0.35 in these experiments and the driving force suddenly disappears when the gap becomes smaller than it. It means that this turbine can control easily by changing the gap.

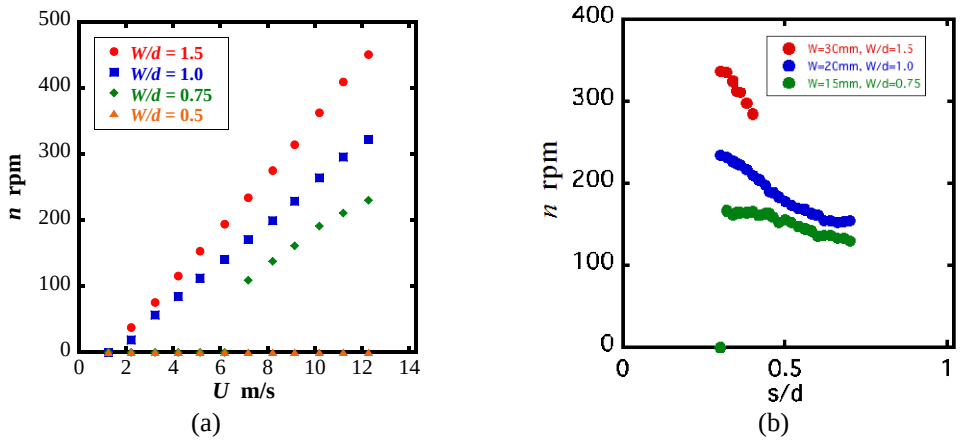

Figure 3: Influence of shape factors on rotation speed,
(a) effect of flow velocity and ring width, (b) effect of gap.

3.2 Application and possibility of new turbine

The multi-blade type turbines are also tested. The multi-blades system is effective of this driving mechanism because each blade gets the driving force with enough pitch of the blades and can attach on the rotation shaft through the slender stem to reduce the confliction of the blades near the center area. Figure 4 shows a test module of the twelves blade wind turbine. The short circular cylinder blade can be applied to increase the number of the blades since the active area of the driving force on the blade is limited near the intersectional part of the ring plate. The rotation speed is almost kept a constant independent of the number of the blades until the limited pitch of the blades.

This new driving mechanism can apply to the water turbine. Figure 5 shows photographs of the tested water turbine. The small air bubbles are used for the flow visualization. In this case, the six circular cylinders are used as a blade. Figure 6(a) is a photograph of the vertical axis type wind turbine using this longitudinal vortex driving mechanism. A concentric cylinder is used in place of the ring plate in this design. This turbine can rotate to CW and CCW direction as same as the horizontal axis type shown in Fig.2 but it can be driven independent of the wind direction. Figure 2(b) shows the relationship between the rotation speed and the flow velocity. The linearity of the rotation speed to the flow velocity is the same as the horizontal type but the efficiency is lower.

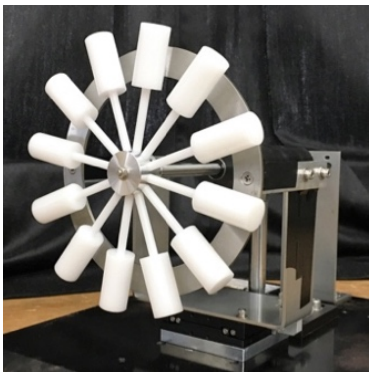

Figure 4: Photograph of twelve circular cylinder blades wind turbine driven by longitudinal vortex.

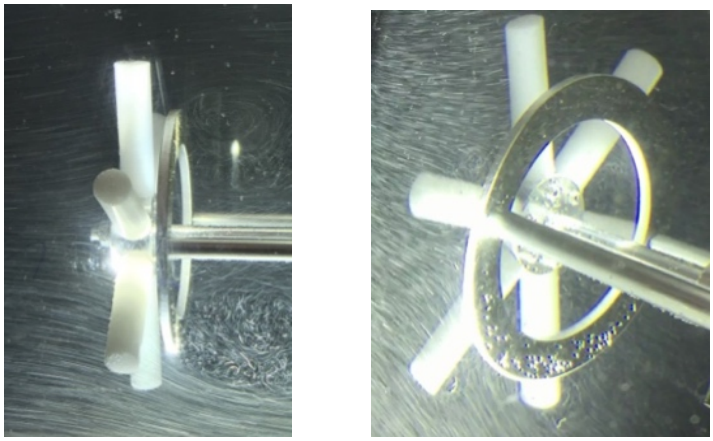

Figure 5: Photographs of six circular cylinder blades water turbine.

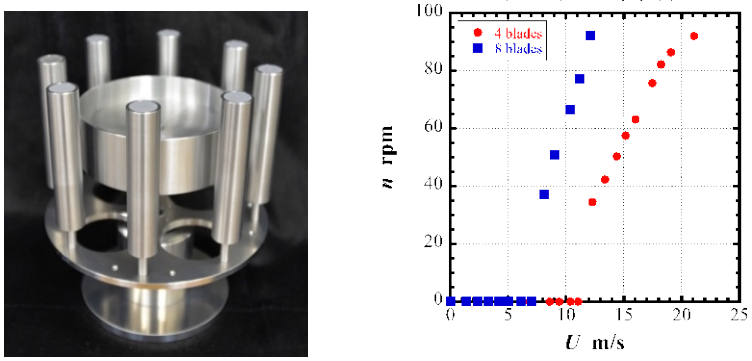

(a) (b)

Figure 5: Horizontal axis wind turbine, (a) photograph of eight blades turbine, (b) relationship between rotation speed and flow velocity.

4.0 Conclusions

The new turbine mechanism which uses circular cylinder blades and is driven by longitudinal vortex has been developed. It has a very simple structure and generates high torque at low rotation speed. By the simple shape, the possibility for the industrial application is very high. Further investigation and improvement are important.

References

Takahashi, T. et al., An innovative wind/water turbine with circular cylinder propeller driven by longitudinal vortex, Proceeding of 1st WWEC Conference, Tokyo, 2016.

KATO, N. et al., Influence of Cross-Sectional Configuration on the Longitudinal Vortex Excitation of the Upstream Cylinder in Cruciform Two-Cylinder System, Journal of Fluid Science and Technology, Vol.1, No.2, 2006, 126-137.

GEOMECHANICS: ITS EMERGENCE, APPLICATION AND FUTURE IN MALAYSIA

Rini Asnida Abdullah

[1] *Department of Geotechnics and Transportation, Universiti Teknologi Malaysia, 81310 Johor Bahru, Johor, Malaysia*

Corresponding Author: *asnida@utm.my*

Abstract: The word Geomechanics comes from the Greek prefix, where geo- meaning "earth"; and "mechanics", which involves the geologic study of the behavior of soil and rock. In civil engineering, constructions are associated not only soil, but also and rock materials. Many have assumed that rock is a strong material and it is commonly used as the foundation. Yet, Malaysia, as the tropical country with high weathering rate, rocks are weathered. Weathered rocks are problematic materials to the construction. With reagrds to this, the numeric value that favoured by the engineer does not always work. The failure occurred at Highland Tower, Bukit Antarabangsa and Bukit Lanjan, Malaysia were the eye opener to the application of the Geomechanics rather than the Geotechnical alone. In addition, case studies of underground tunnelling work in Malaysia,i.e. Stormwater Management And Road Tunnel (SMART) and the MRT tunnel construction will also be highlited with reference to the karstic limestone. Application of the Geomechnics in Malaysia is now has been more widely accepteed with many construction that relate with the weathered rock, fault and other geological featues. The future development of East Coast Rail Link (ECRL) and underground city will also promote the function of Geomechanics in Malaysia.

Keywords: *Geomechanics, tunelling, Bukit Lanjan, Bukit Antarabangsa*

SLOPE STABILIZATION BY TREE INDUCED SUCTION

N Ali[1], M F Ishak[2], A Kassim[1]

[1] *Faculty of Civil Engineering, Universiti Teknologi Malaysia*
[2] *Faculty of Civil Engineering and Earth Resources, University Malaysia Pahang*

Abstract

This paper explores the effect of active root zone related to slope stabilization. The matric suction produced by mature tree was determined during high and moderated intensity of rainfall event condition, which related to significant changes on stability of the slope. The increasing of soil moisture and pore water pressure can significantly reduce shear strength of soil which lead to slope failure. The field monitoring result showed that there was a substantially increase in soil suction near the vicinity of tree. The findings indicate that the influence of rain fall event can cause variation to soil suction that is related to factor of safety. Furthermore, water uptake from root activity created dry condition that substantially increased the factor of safety against slope failure has improved up to 45%.

Keywords: Tree water uptake, Slope stabilization, Unsaturated soil.

Introduction

The instability of soil slopes continues to affect large worldwide populations for each year, in particular at the areas of steep terrain that experience prolonged hot and dry periods followed by intense rainfall events. In conjunction to that, shallow slope instability has become a common problem to man-made and natural slopes. Hence, it is significantly important to find an economically and eco-friendly solution to rise how vegetation can be an element for sustainability of slope. Therefore, this research explore how vegetation might be selected as an approach to help maintaining and enhancing the soil strength by reducing moisture content and hence reduce the risk of slope failure.

Acacia mangium tree was first introduced in the state of Sabah in 1967 and then planted in peninsular Malaysia as the main species compensation plantation forest project. This plant species grow between 4m to 5m a year, medium-sized, growing up to 20 m high. Acacia mangium tree is a fast-transpiring tree species with high daily water consumption reaching an average up to 4.6 mm d^{-1}. A study on the water consumption of acacia mangium tree in the Malaysian state of Sabah, Borneo was reported by Cienciala (2000). Furthermore, acacia mangium tree is tolerance with a variety of tropical climate conditions (Adnan M., 2008). These include tropical dry to moist conditions and subtropical dry zones to wet forest zones. Therefore, this tree has been selected and suitable preserved for this research.

Prolonged antecedent rainfall would significantly alter the pore water pressure conditions prior to the main rainfall event, such that the initial pore water pressure distribution prior to the antecedent rainfall became all but irrelevant. The effects of rainfall on the stability of the slope seemed to relate by duration of the rainfall event, with the longer the rainfall period, the lower the slope factor of safety. Preserve of a mature tree can readily increase the factor of safety against slope failure due to tree water uptake in relation to soil slope (N. Ali & Rees, 2008).

Slope failure commonly occurs when the shear strength of the soil is reduced through a decrease in effective stress due to pore water pressure increment (Glendinning S. et al, 2009).

Vegetation may prevent collapse by reducing water pressure (increasing suction through water uptake) due to suction produced by vegetation will act to stabilise slopes by increasing effective stress and thus increasing soil shear strength. Simon and Collison (2001) claimed as a key finding that the hydrologic effect is as important as mechanical effect, which can bring beneficial by increasing FOS up to 71%. It should also be noted that if trees are cut down, failure can be the result when pore water pressures recover because strain softening has already occurred (due to previous seasonal cyclic loading effects). This is important in the management of vegetation and engineers must be wary of felling trees without understanding the hydrology condition. Importantly, preserve of a mature tree can readily increase the factor of safety against slope failure due to tree water uptake in relation to soil slope (Ali N. & Rees S.W., 2008)

The objectives of this study were to determine matric suction soil moisture on the slope with mature tropical tree (acacia mangium) preserved at the toe of the slope, which suction have been generated within this area. The equipment was installed at certain depth and distance to measure soil suction. Therefore, it is just considering the main factor of drying influenced by mature tree. During no rainfall event, the soil becomes dry and the analysis of the changes soil suction at various depth and distance from tree trunk were conducted. In associated with this, effect of tree induced suction was used to perform a stability analysis at active root tree. In this scope of this research, the mechanical aspect of tree root such as tensile strength and bonding between root and soil which can lead to increasing soil strength are assumed negligible in this study.

Theoretical Background

To assess mature tree effects on slope stability, hydrologic data (matric suction) were used in computer modelling. In these cases, it may be appropriate to perform slope stability analyses which include the shear strength contribution from the negative pore-water pressure. Matric suction (negative pore-water pressure) above the water table has the effect of increasing the apparent cohesion of a soil. A modified form of the Mohr-Coulomb equation can be used to link shear strength to soil suction. The use of theory of limit equilibrium of forces and moments was used to compute the FOS (Factor of Safety) against failure.

The limit equilibrium method of slices is widely used for its simplicity particularly when compared to the finite element method (Fredlund and Rahardjo, 1993, Renaud et al. 2003). The FOS is defined as that factor by which the shear strength of the soil must be reduced in order to bring the mass of soil into a state of limiting equilibrium along a selected slip surface. The equation *(1)* produced by Rees S.W. and Ali N. (2012) were used to calculate stability of a slope by performing divided the soil mass above the circular slip surface into vertical slices.

$$F = \frac{\sum c' lR + NR \tan \phi' + SRl \tan \phi^b}{\sum Wx} \qquad (1)$$

The equation was defined as, where c'= effective cohesion (kPa), l = length of the slice (m), N = total normal force on the base of the slice (kN), R = the radius for a circular slip surface (m), S= force produced by matric suction on the unsaturated part (kNm-1), φ' = effective angle of internal friction
(degrees), φ^b = an angle indicating the rate of increase

in shear strength relative to matric suction, W = weight of the slice (kN).

Materials and Methods

The study was carried out at slope with the existence of mature tropical tree Acacia mangium situated at latitude (+1°33’ 32.03”) and longitude (+103° 38’ 38.04”). The tree was located at the toe of slope at Faculty of Electrical Engineering Universiti Teknologi Malaysia as shown in Figure 1.

Figure 1 Acacia mangium tree located at the toe of slope

To develop soil moisture profile due to influence of acacia manggium tree, Jet-fill tensiometer (Figure 2) was use. Jet-fill tensiometer (Soilmoisture Equipment Corp. CA) is used since it can measure directly the soil suction that range between 0 kPa to 100 kPa. A tensiometer comprises of a tube with a porous ceramic tip on the bottom, a vacuum gauge near the top, and a sealing cap. As the soil dries and water moves out of the tensiometer, it create vacuum inside the tensiometer that is indicated on the gauge. When the vacuum created just equals the “soil suction”, water will stop flowing out of the tensiometer. The dial gauge reading is a direct measure of the force required in removing water from the soil. The tensiometers installed at the depth of 0.5m, 1.0m and 1.5m and the distance from tree for the insertion of tensiometer were measured according to 0.1h, 0.2h, 0.4h etc (where h is the height of the tree) making up a ‘station’ or ‘nest’. Six station were placed at the flat and slope area named as Flat 1, Flat 2 & Flat 3 and Slope 1, Slope 2 & Slope 3 (Figure 3). Each station consisted of three tensiometer installed which is consider as top, middle and bottom of the root zone.

Figure 2 Tensiometer

Figure 3 Tensiometer installed at slope

Results and Discussion

The suction distribution responded to several rainfall patterns in month of December was used to analysis and observation in certain interval of time. The isolation of data toward the effect of tree induce suction during the monitoring at slope can be denoted as pattern A (December 4) in Figure 4 influenced by heavy rainfall occurred, pattern B (December 10) in

Figure 5 with moderate rainfall occurred and pattern C (December 16) in Figure 6 after 6 days without rainfall.

Figure 4 shows pattern A of suction distribution through the soil profile after 54mm/day rainfall event on December, 4. The respond showed that suction at all depth dropped dramatically at lowest value was recorded. The lowest suction was encountered at distance of 4m from tree trunk at depth 0.5m, 1.0m and 1.5m were 2kpa, 4kpa and 12kpa respectively. The suction recorded at depth 0.5m, 1.0m and 1.5m without tree are much lower than at distance of 4m from tree trunk. However, for this high rainfall event the pore- water pressure at all depth did not achieve saturated condition (0kpa suction value).

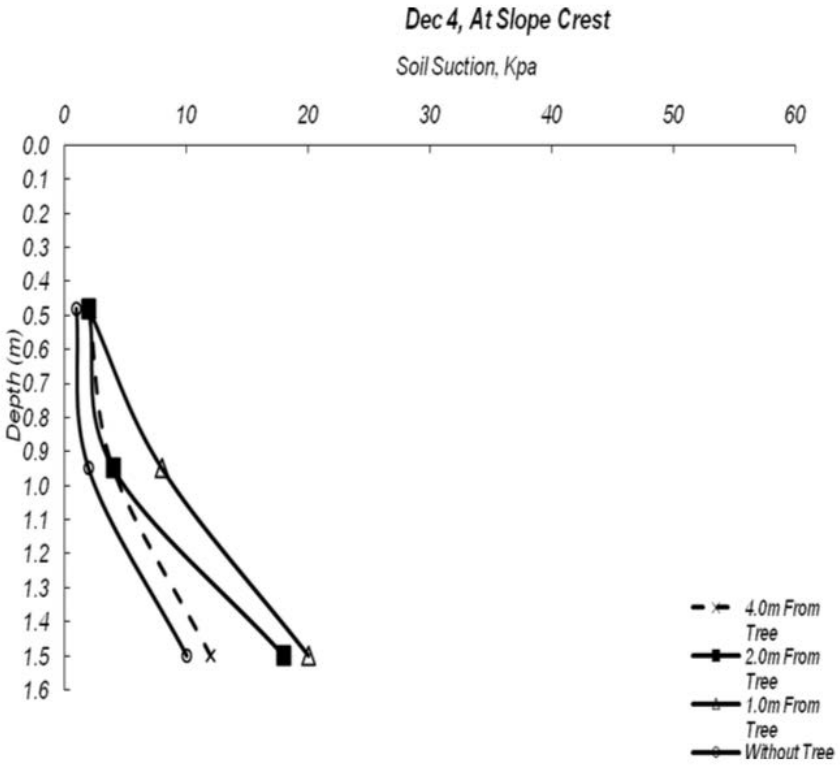

Figure 4 soil suction profile pattern A on 4 December

Figure 5 show soil suction profiles B on December 10, matric suction increased significantly due to effect of tree induce suction. It is indicated that, after 6 day without rainfall event the pattern of soil suction substantially increased at depth 0.5m until 1.0m. Although, the slope was subjected to receive moderated rainfall amount (14mm/day) but soil suction profile distribution was still high compare to December 4. This is due to tree water water uptake that contributed to induce suction through soil appreciable only at the shallow depth and near the trunk. Still, suction profile distribution without tree is much lower at all depth compared to at the distance of 4m from tree trunk.

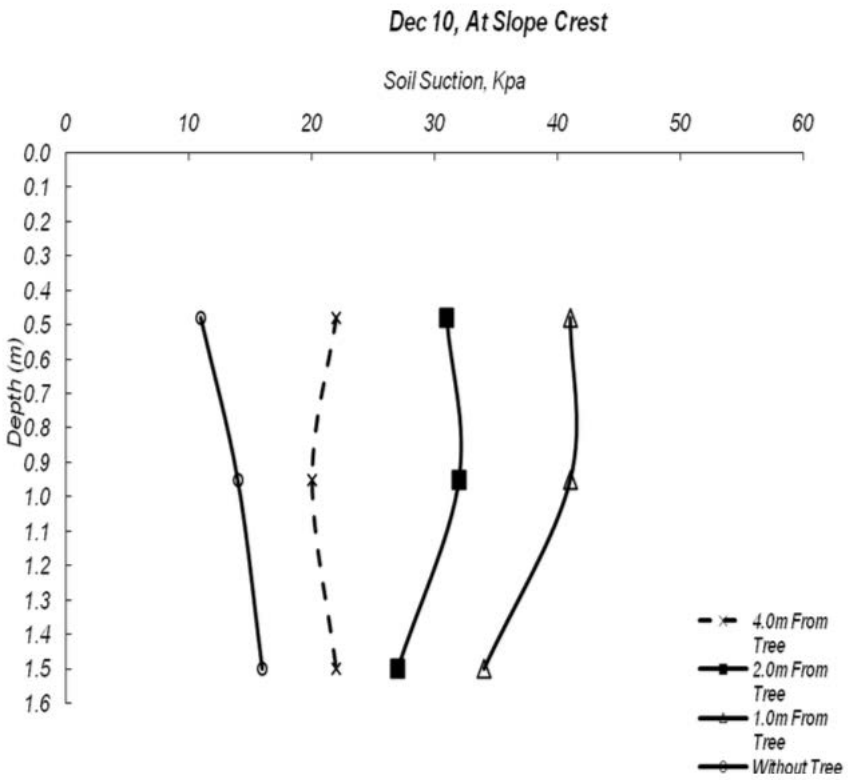

Figure 5 soil suction profile pattern B on 10 December

Soil suction profile pattern C (December 16) in Figure 6 shows substantial increment after 6 day without rainfall. The highest suction profile was encountered at depth 0.5m, 1.0m and 1.5m with 58kPa, 60kPa and 46kPa respectively at distance of 1m from tree trunk. The minimum effect of tree induce suction was encounter at distance of 4m from tree trunk, which recorded the lowest value were 28kPa, 31kPa and 34kPa at depth 0.5m, 1.0m and 1.5m. As mention before and still, suction profile distribution without tree was much lower at all depths compared to the distance of 4m from tree trunk.

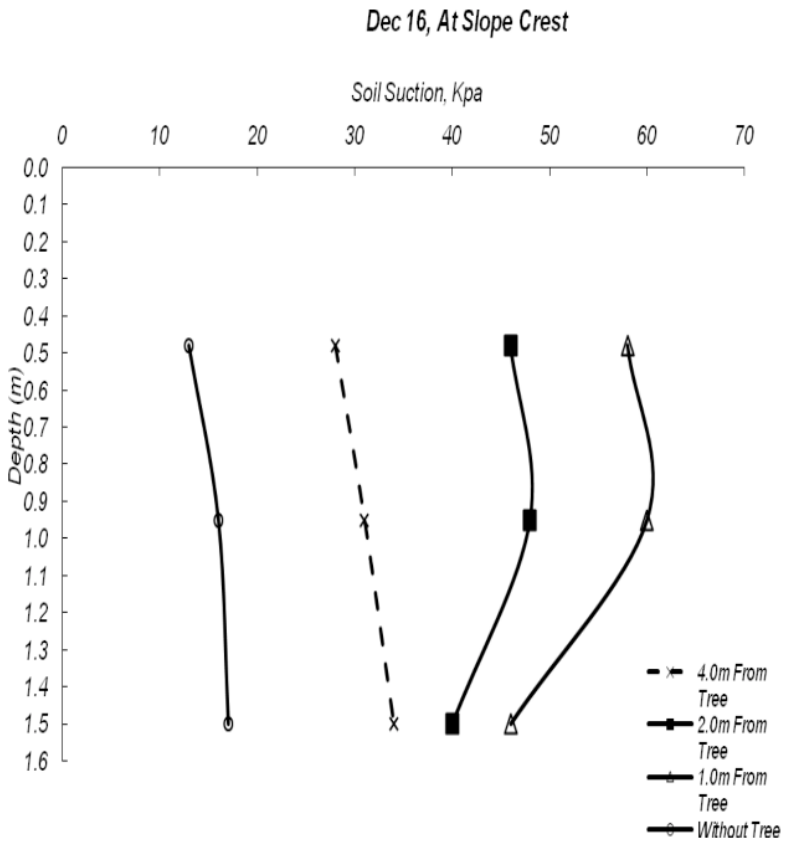

Figure 6 soil suction profile pattern C on 16 December

The lowest FOS for the critical slip failure was encounter using limit equlibrium method (LE) model (slope/w) in saturated condition was 1.70. This value was used as controled value to determine the percentage difference of FOS for other conditions. Table 1 shows the comparison of FOS after numerical stability analysis was performed at various conditions considered on December 4 and December 16 the percentage difference when compare to unsaturated slope with and without tree at toe of slope. In table 1, the lowest FOS on December 4 was encounter due to high intensity of rain fall event (54mm/day). However, FOS for unsaturated slope with tree at toe (1.88) was much higher than FOS without tree (1.73), which significanly different by 8.84%. On December 16, FOS as shown in table 1 substaintially increased due to the increasing matric suction was recorded. Still, FOS for unsaturated slope with tree at toe (3.08) was much higher than FOS without tree (2.12), with significanly different by 45.54%. From the results, it can be seen that changes in matric suction due to the effect of tree induce suction substantially increase the FOS by 8.84% from 1.73 to 1.88 on December 4 and increase the FOS by 45.54% from 2.12 to 3.08 on 16 December.

Table 1 Comparison of FOS on December 4 and 16

	Unsaturated Slope Without Tree	Unsaturated Slope With Tree at Toe	Percentage Different,(%) Unsaturated Slope With Tree at Toe
FOS on 4 December	**1.73**	**1.88**	**8.84**
FOS on 16 December	**2.12**	**3.08**	**45.54**

Other FOS comparison have been made on 4 and 16 December due to effect of tree water uptake is show in table 2. From the results for tree water uptake cases consideration it can be seen that changes in matric suction due to tree induce suction at active root zone after moderate and high intensity rainfall (which suction have been generated within this area) can substantially increase the FOS by 38.96% from 1.88 to 3.08.

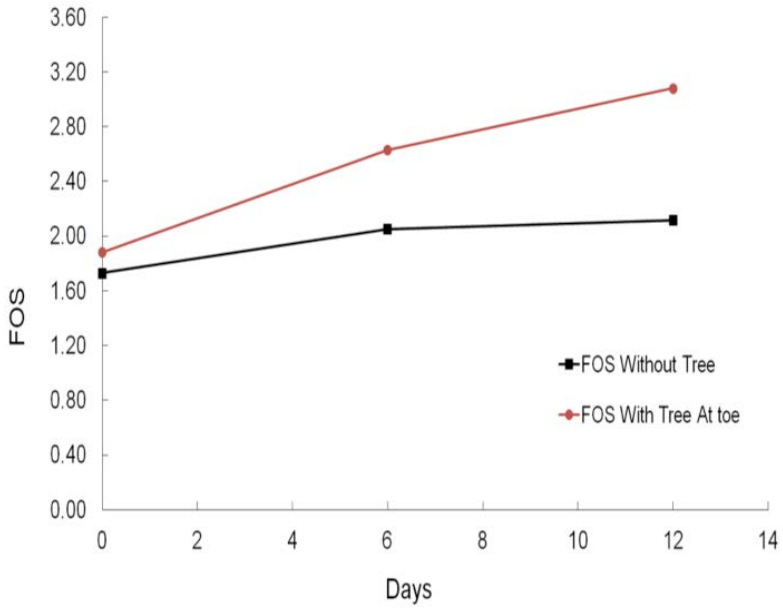

Figure 7 The Variation of FOS In Time Due To Tree Induce Suction

Figure 7 reveal the result and change in the FOS after analysis of monitored data. It shows that FOS can rise up with various times in 12 day of analysis period in the conditions of moderate and high intensity rainfall. This figure shows that FOS varies with time and increases with matric suction in soil with and without tree at toe of slope.

Conclusion

Based on the finding on field monitoring result it is expected that the established pattern of root water uptake is likely to happen when condition is high, moderately rainfall was occurring. A root tree zone could help to reinforce the soil by increasing matric suction related to increasing FOS. This study indicated that matric suction generated caused by the presence of mature tropical tree (acacia mangium) at toe of the slope can readily increase the FOS against slope failure up to 45.54%.

The FOS calculation presented here considered only hydrological effects which are related to soil matric suction generated by active root zone driven by transpiration. Mechanical effect that arised from the tensile strength of root and bonding between root and soil are assumed beyond the scope of this study. A part from provided a 'free' refreshment condition or acoustic screen, it can also help in strengthening the slope via active root zone to absorb water from soil. Consideration is needed for practical cases when cutting down and felling the trees without understanding the hydrological condition can increased the risk of landslide and erosion on slope.

The effect of acacia mangium tree can be acceptable as low cost solution to problem of erosion and slope instability that can increase the factor of safety of slope. From this study suggest more consideration is given to the hydrologic influence, which also can bring increment to soil shear strength. In fact, this research has also revealed that acacia mangium planted is beneficial in producing suction via root and in stabilizing the soil.

References

Adnan Mohamad (2008). Pokok-pokok untuk tanaman Bandar. Jabatan Landskap Negara, Kuala Lumpur.

Ali N., Rees S.W. (2008). Preliminary analysis of tree- induced suctions on slope stability. Proceedings Of The First European Conference On Unsaturated Soils, 2008, Durham, United Kingdom. CRC Press, Taylor & Francis Group, London, Uk. P 811 – 816.

Alva AK, Om Prakash · Ali Fares, Arthur G. Hornsby (1999). Distribution of rainfall and soil moisture content in the soil profile under citrus tree canopy and at the dripline. Irrig Sci (1999), Springer-Verlag 1999, 18: 109–115.

Biddle P. G. (1983). Pattern of soil drying and moisture deficit in the vicinity of trees on clay soils. Ge´Otechnique, 33, No. 2, 107 – 126.

Biddle, P.G. (1998). Tree root damage to buildings. Wil- lowmead Publishing Ltd, Wantage.

BSI. (1990). Methods of Test for Soils for Civil Engineering Purposes, (BS 1377: Part 1-9). British Standards Institution, London.

Cienciala, E., Kucera, J., Malmer A. (2000). Tree sap flow and stand transpiration of

two Acacia mangium plantations in sabah, Borneo. Journal of hydrology 236, 109-120.

Craig, R.F. (2004). Soil mechanics. 5th Ed., Chapman & Hall, London.

Fredlund, D.G. and Rahardjo, H. (1993). Soil Mechanic for unsaturated Soils. Canada: John Wiley & Sons, Inc, Printed Ltd.

Greenway DR (1987). Vegetation and slope stability. In: Anderson MG, Richards KS (eds) Slope stability. Wiley, Chichester, pp 187–230

Greenwood, J.R. (2006). SLIP4EX—A program for routine slope stability analysis to include the effects of vegetation, reinforcement and hydrological changes. Geotechnical and Geological Engineering, 24: 449–465.

Indraratna, B., Fatahi, B., Khabbaz, H., (2006). Numerical analysismof Matric Suction Effects of Tree Roots. Geotech. Eng., Proc. Inst. Civil Eng. 159, 77-90.

Marie Genet , Alexia Stokes, Thierry Fourcaud, Joanne E. Norris, (2009). The influence of plant diversity on slope stability in a moist evergreen deciduous forest. Journal Ecological Engineering 36 (2010) 265-275.

O. Normaniza, H.A. Faisal, S.S. Barakbah (2007). Engineering properties of leucaena leucocephala for preventing of slope failure. Journal Ecological Engineering 32 (2008) 215-221.

Renaud, J.P., Anderson, M.G., Wilkinson, P.L., Lloyd, D.M. & Wood, D.M. (2003). The importance of visualisation of results from slope stability. ICE Proc. Geotechnical Engineering, 156(1): 27–33.

Soilmoisture Equipment Corp. (1984). 2725 series Jet- Fill Tensiometers Manual.

Simon, A. & Collison, A.J. (2002). Quantifying the mechanical and hydrologic effects of Riparian vegetation on stream- bank stability. Earth Surface Processes and Landforms, 27: 527– 546.

Simon, A., Curini, A., Darby, S.E. & Langendoen, E.J. (2000). Bank and near-bank processes in an incised channel. Geomorphology, 35: 193– 217.

Stephanie Glendinning, Fleur Loveridge, Ruth Elizabeth Starr-Keddle, M. Fraser Bransby, Paul N. Hughes, (2009). Role of vegetation in sustainability of infrastructure slopes. Geotech. Eng., Proc. Inst. Civil Eng. 162, 101-110.

S.W. Rees, N. Ali, (2012). Tree Induced Soil Suction And Slope Stability. Geomechanics and Geoengineering: An International Journal. Taylor & Francis Group, London, Uk. Vol. 7, No. 2, 103-113.

THE MECHANICAL PROPERTIES OF MODIFIED CONCRETE WITH *EUCHEUMA COTTONI*

Izni Syahrizal B. Ibrahim[1], Norhafizan B Majid[2], Noor Nabilah Bt Sarbini[3], Zainul Akmar B. Zakaria[4,] Mohd Hanim B Osman[1]

1. Forensic Engineering Centre, Institute for Smart Infrastructure and Innovative Construction
2. Human Resources Division, Ministry of Higher Education, Putrajaya Malaysia
3. Faculty of Civil Engineering
4. Institute of Bioproduct Development, Faculty of Chemical and Energy Engineering

Universiti Teknologi Malaysia, 81310 UTM Johor Bahru, Johor, Malaysia

**Corresponding Author : hafizan_kkjs@yahoo.com.my*

Abstract : Seaweed, a rich source of vitamins, minerals and other vital material is used in the present study to improve the strength of concrete. Seaweed is known for its effectiveness in gelling and thickening properties of which may increase the bonding mechanism when mixed together in concrete. This is because seaweed will fill the porous parts in the concrete mixture and therefore will improve the performance throughout the service life of the structures. In construction, cracking in concrete is the main reason for the decreasing service life of the structure. Therefore, it is advisable to restrict the development of early age micro cracking from appearing before it further developed into larger crack. This research aim is to investigate the mechanical properties of concrete namely compressive strength, splitting tensile strength, flexural strength and water absorption when seaweed is added into the mixture. The seaweed species used in this study is from the *Eucheuma Cottoni* and in powdered form. The seaweed species is gradually added into the concrete mixture in stages of 0.1%, 0.25%, 0.5%, 1.0% and 5% from the weight of cement. The findings show that concrete with the powdered *Euchema Cottoni* increases the compressive, splitting tensile and flexural strengths for an optimum mix composition of 0.25%. This innovative material is an alternative to existing concrete mixture and will become green construction material for sustainable concrete

Keyword : Seaweed; *Eucheuma Cottoni* ; concrete; mechanical properties

1.0 Introduction

Seaweed, a rich source of vitamins, minerals and other vital material is used in this study to improve the strength of concrete. Seaweed is known to have effective gelling and thickening properties, and because of this when it is added into other cementitious materials may improve the bonding mechanism. Seaweed when is added together with cement, will improve the performance by filling the porous areas in the cement-based mixture. This study proposed the use of sustainable material in concrete in order to improve the quality and at the same time improved the performance in the long-term.

In construction, cracking in concrete is the main reason for the decreasing service life of a structure. Therefore, it is advisable to restrict the development of early age micro-cracking from appearing before developing into larger macro-crack. This prevention step must be taken to avoid higher cost required for repairing work. One of the methods that can be used to confine early development of micro-cracking is to increase the strength of concrete through the use of appropriate additives.

The east coast of Peninsular Malaysia and west coast of Sabah and Sarawak waters in border to the South China Sea is rich with marine algae resources. A total of 364 taxa of marine algae (seaweeds) were reported to come from the South China Sea area of Malaysia (Phang *et. al.* 2010). Seaweed (algae), which is a rich source of minerals, vitamins and other vital materials, has been used in this study to improve the properties of cement-based mortar. The natural polymer modified mortar is expected to perform as an excellent bonding mechanism to improve the strength and enhanced the durability of concrete. These are the key factors for concrete to achieve sustainability. Seaweed provides the advantage as emulsifier, suspensor, condenser and stabilizer (Retno Susilorini *et.al.,* 2014). Algal precipitate is a rich source of calcium, silica and carbonate material. The compressive strength of the test specimen of 10% and 20% cement replacement with algal precipitate was found to increase to that of the control specimens (Niveditha *et.al*., 2014). Seaweed was also used in the development of unfired brick. According to Dove (2014) who conducted a study on renewable materials in the United Kingdom, found that it can help to improve the whole life cycle impact of buildings. Previous study also found that seaweed has rheological properties that act as a gel and thickening agent. This properties may perform as epoxy resin to bind composite materials such as concrete (Barros *et.al.*, 2013). Furthermore, the characteristics of seaweed that are group into polysaccharide (containing *Kappa Carrageenan*) potentially act as a strong gel when added together in concrete. Polysaccharide is a bio-polymer extracted from plants. It is used as cement admixtures and provides several advantages as bonding properties to mortar. Polysaccharide gums in cement paste system have a significantly higher effect on the viscosity at low shear rate than at higher shear rate. (Ghio, Monteiro, & Demsetz, 1994)

Malaysia is also rich with seaweed species such as *Kappaphycus Alverazii*. Based on its variety of usage, seaweed industry can provide opportunity towards commercialization. At the same time, the industry can create jobs and improve the socio-economic of the farming community.

The study on seaweed in the concrete is still new and only few findings are available. Furthermore, the findings by other researcher are still at the fundamental stage (Suhendro, 2014). However, test results on its potential as binding agent is remarkable as reported by Dove (2014) and Barros (2013). Therefore, this study will provide conclusive findings on the potential of seaweed in concrete for its mechanical properties (compressive strength, tensile strength, flexural strength, water absorption and micro-structure). The test results from the experimental work will be used to determine the optimum dosage of seaweed in concrete.

2.0 Materials and Methodology

2.1 Materials and Mix Composition

The main materials used in this study are concrete and seaweed. The seaweed species used is of the *Eucheuma Cottoni* as shown in Figure 1, which contained cellulose of polysaccharide *Kappa Carrageenan*. *Kappa Carageenan* which is extracted from *Eucheuma Cottoni* is supplied by a manufacturer in powdered form from Tawau, Sabah. Figure 2 shows the powdered form of *Kappa Carrageenan*. In order to identify the characterization of *Kappa Carageenan* precipitates, Energy Dispersive X-Ray Analysis (EDX) and Scanning Electron Analysis (SEM) is first carried out on the seaweed in powdered formed as shown in Figure 2.

Figure 1 Seaweed species of the *Eucheuma Cottoni* in its natural surrounding

Figure 2 *Kappa Carrageenan* in powdered formed

In this study, the concrete strength is designed to achieve 35 MPa at 28 days, while the percentage of seaweed to be added in the mixture is 0% (control), 0.1%, 0.25%, 0.5%, 1% and 5% of the cement weight.

2.2 Specimens and Testing Method

The specimen used to determine the mechanical properties of seaweed added in concrete are as follows:

(a) Cubes of 150 mm width × 150 mm length × 150 mm height for the compressive strength

(b) Cylinders of 100 mm diameter × 200 mm height for the splitting tensile strength, and

(c) Prisms of 100 mm width × 100 mm height × 500 mm length for the flexural strength.

For each testing, three specimens are prepared to ensure the validity of the test results. The compressive strength test was carried out at 1, 7, 14 and 28 days, while the splitting tensile test was carried out at 7, 14 and 28 days. As for the flexural strength test, it was only carried out on the 28 days. The procedures for each test are shown in Figure 3. Curing of all test specimens are carried out until the test day as shown in Figure 3(b). Fresh concrete properties of all the mixes are measured using the slump test method in accordance with BS EN 12350-2: 2009. Meanwhile, in order to determine the hardened concrete properties, compressive strength, splitting tensile and flexural strength is carried out in accordance with BS EN 12390-3: 2009, ASTM C 496/C 496M–04 and BS EN 12390-5: 2009, respectively.

(a)

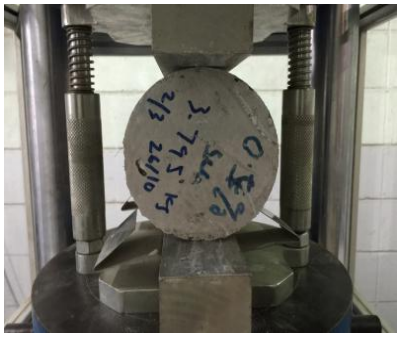

(b)

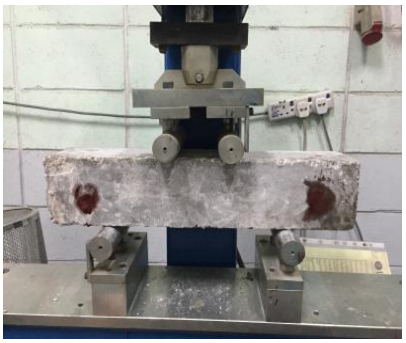

(c)

(d)

Figure 3 (a) Compressive strength test, (b) Splitting tensile test, (c) Flexural strength test, and (d) Curing of all test specimens

3.0 Result and Discussion

3.1 Characterization of *Kappa Carageenan* Precipitates

Energy Dispersive X-Ray Analysis (EDX) results shown in Figure 4 indicate the presence of Carbon, Oxygen, Sodium, Magnesium, Aluminium, Silicon, Pottasium, Calcium Ion and Copper in the seaweed powder precipitate with predominant peak at 2θ (Bragg's angle). Meanwhile, Scanning Electron Analysis (SEM) has revealed the shape and structure of precipitates as shown in Figure 5. At the magnification of 500×, the results from the SEM show that the width diameter of the *Kappa Carageenan* is 8.4 mm. The shape and structure of the precipitates shown in Figure 5 also found that it have similarity to polysaccharide gum and natural polymer.

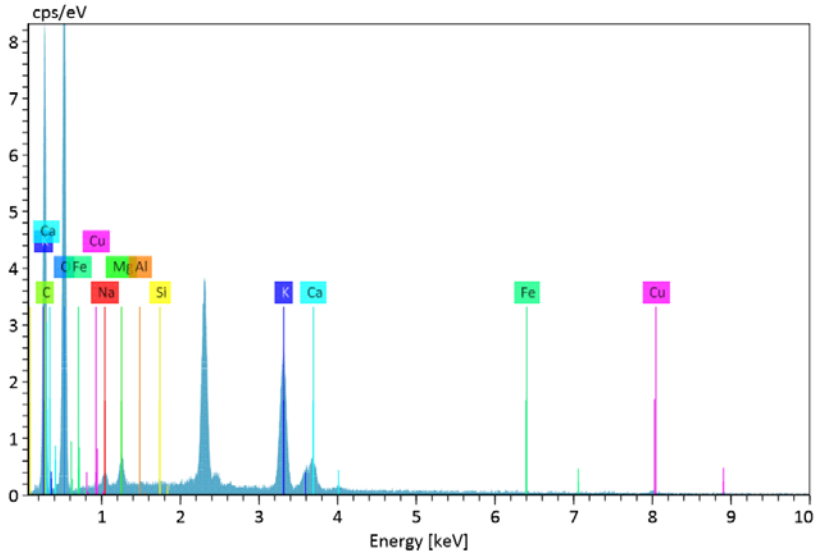

Figure 4 Energy Dispersive X-Ray Analysis (EDX) of *Kappa Carageenan*

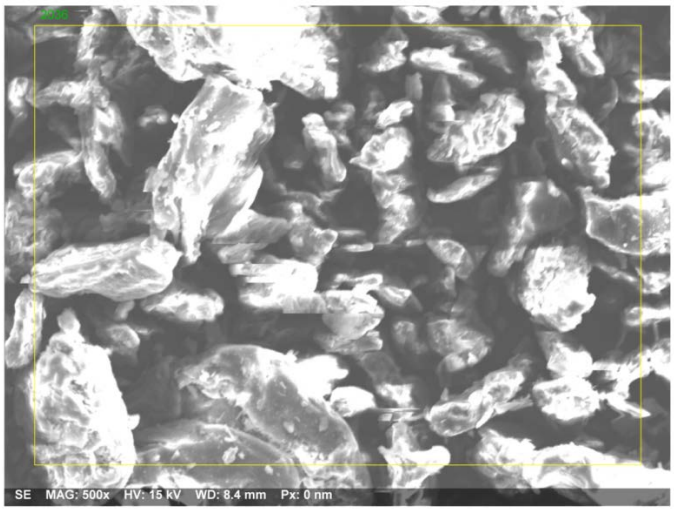

Figure 5 Scanning Electron Analysis (SEM) of *Kappa Carageenan*

3.2 Mechanical Properties of Modified Concrete with Seaweed

The compressive strength of the modified concrete with seaweed from 24 hours (1 day) and up to 28 days of curing for the 6 mix compositions including the control is observed in this study. The highest compressive strength after 24 hours (1 day) is achieved by the 0.1% mix (19.02 MPa) as shown in Figure 6, showing a 50% increase from the control strength. Meanwhile, the highest compressive strength at 7 days is found for the 0.1% mix at 39.7 MPa, while the lowest is the 5% mix at 12.1 MPa. The strength for the 0.1% mix shows that it is 41.3% higher than the targeted strength of 23.33 MPa (2/3 of the 28 days strength of 35 MPa). Furthermore, the strength development also shows that the 0.1% is even higher than the control mix at both 24 hours (1 day) and 7 days; an increase of 11.8% and 11.6%, respectively. This shows that the 0.1% mix has good early strength development as compared with the other mixtures. Meanwhile, at 14 and 28 days, the highest compressive strength is achieved for the 0.25% mix at 43.7 MPa and 47.1 MPa, respectively. At 28 days, the 0.25% mix shows a strength increase of about 16.7% from the control. Furthermore, the 0.25% mix has the highest compressive strength at 28 days as compared with the other mix. The compressive strength development of the 0.1% and 0.25% mixes gradually increases at 1, 7, 14 and 28 days. On the other hand, the 0.5%, 1% and 5% mixes showing a lower compressive strength development even though there is an increase pattern between 7, 14 and 28 days. The study also found that the lowest compressive strength is observed for the 5% mix, regardless of the day of testing from 24 hours (1 day) up to the 28 days of curing. The result of the experiment test suggested that high dosage of seaweed composition (1% and 5%) will not give great improvement on the bonding mechanism in order to increase the compressive strength. Referring to the relationship in Figure 6, the findings can be concluded that the specimen of modified concrete with seaweed is almost consistent when measured on its compressive strength.

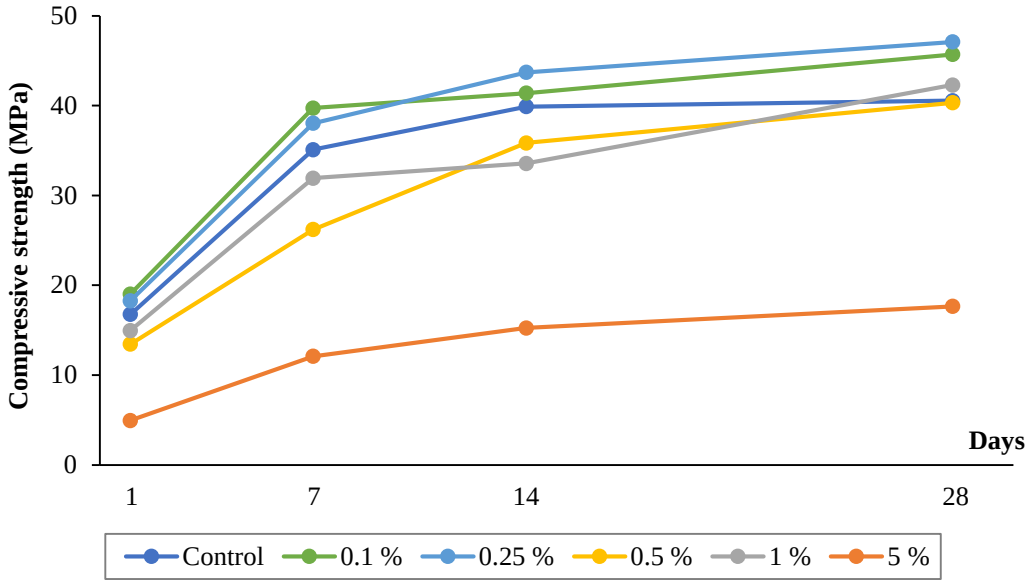

Figure 6 Compressive strength of modified concrete with seaweed at 1, 7, 14 and 28 days

Concrete is excellent in compressive strength but not good in tensile strength, therefore, the influence of seaweed powder is expected to improve for the splitting tensile strength. From the relationship in Figure 7, the 0.1%, 0.25%, 0.5% and 1% mixes of the splitting tensile strength at 7 days shows an increase as compared to that of the control. However, for the 5% mix, similar pattern is observed to that of the compressive strength showing the lowest splitting tensile test at all test day (7, 14 and 28 days). At 14 days, only the 0.25% and 0.1% mixes show an increase in the splitting tensile strength as compared with the control. The relationship in Figure 7 also shows a consistent strength increase at 7, 14, 28 days for the 0.25% mix, which is also higher than the control; therefore the 0.25% mix can be considered as the optimum percentage mix for the modified concrete with seaweed in terms of its splitting tensile strength. As the same finding from the compressive strength, high percentage dosage of seaweed in concrete (0.5 %, 1% and 5%) will not provide great improvement on its splitting tensile strength.

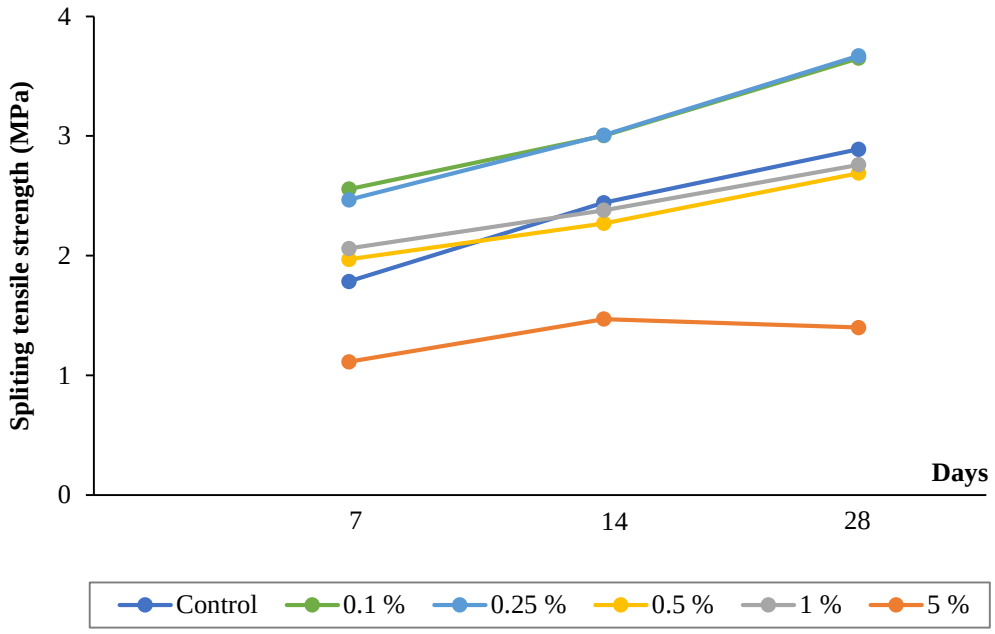

Figure 7 Splitting tensile strength of modified concrete with seaweed at 7, 14 and 28 days

The flexural strength on modified concrete with seaweed at 28 days for the 5 mix compositions and one control are shown in Figure 8. The highest flexural strength at 28 days is achieved for the 0.25% mix at 3.44 MPa. The result shows a 3.5% increase of its flexural strength from the control. Furthermore, the findings also found that adding too much seaweed can cause weakness to its bonding mechanism, which in time reduced the flexural strength. For example, a 5% mix of seaweed in concrete causes a decreased by more than 50% of its flexural strength as compared to that of the control.

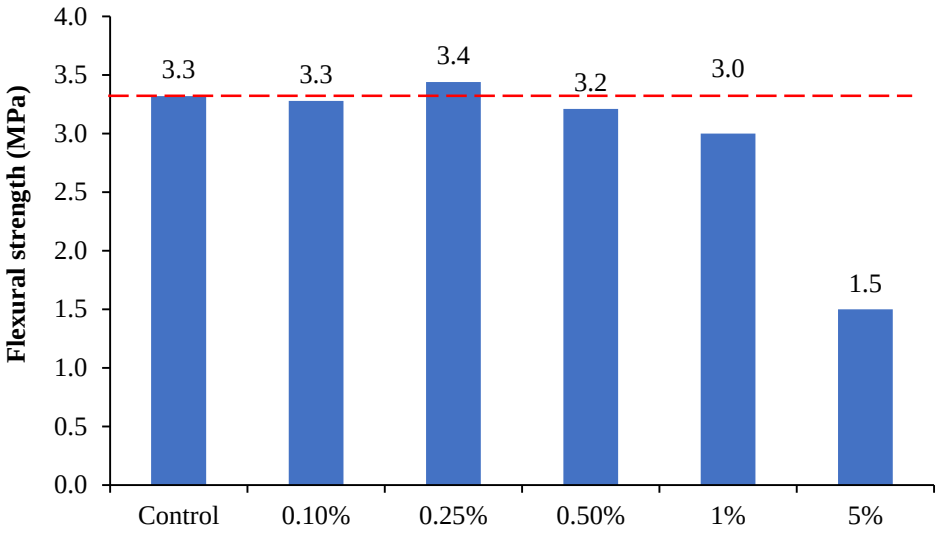

Figure 8 Flexural strength of modified concrete with seaweed at 28 days

One of the important properties of good quality concrete is low permeability. Generally, a concrete with low permeability resists ingress of water. Water enters pores in the cement paste an even in the aggregate. High water absorption will decrease the concrete strength. The results of water absorption test conducted on the specimens at 28 days are presented in Figure 9. Generally, water absorption rate for all mixes is low as compared with the control. The results show that the absorption rate is 6.7% for the control, while the other mixes with seaweed are in the range of 5.36% – 6.68%. This shows that the mix with seaweed in concrete does not cause high rate of water absorption.

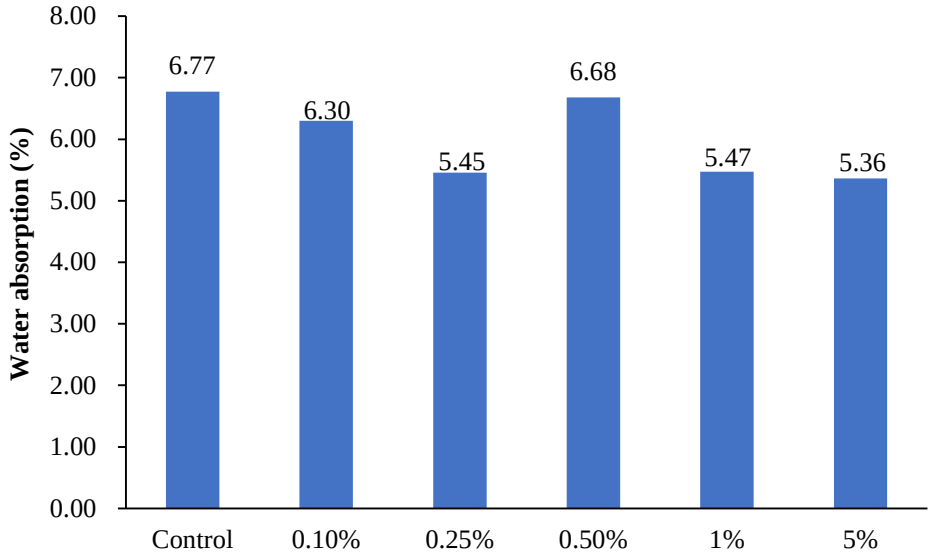

Figure 9 Water absorption test results of modified concrete with seaweed at 28 days

4.0 Conclusion

Experimental work had been carried out to study the mechanical properties of concrete with seaweed. The percentage of seaweed added in the concrete mixture is in the percentage of 0.1%, 0.25%, 0.5%, 1% and 5%. The findings from the test results show that concrete with *Euchema Cottoni* increases the compressive, splitting tensile and flexural strengths with optimum mix composition of 0.25% from the weight of cement. Concrete with seaweed is an alternative to existing concrete mixture in order to develop green construction material for sustainable concrete.

References

Barros FCN, da Silva DC, Sombra VG, Maciel JC, Feitosa JPA, Freitas ALP and de Paula RCM. (2013). Structural Characterization of Polysaccharide Obtained from Red Seaweed Gracilaria Caudata (J Agardh). Short Communication: Carbohydrate Polymers. 92: 598 – 603

Dove, C. (2014). The development of unfired earth bricks using seaweed biopolymers. In *WIT Transactions on the Built Environment* (Vol. 142, pp. 219–230). WITPress.

Ghio, V. A., Monteiro, P. J. M., & Demsetz, L. A. (1994). The rheology of fresh cement paste containing polysaccharide gums. *Cement and Concrete Research*, *24*(2), 243–249

Niveditha, C., Sarayu, K., A, R. M., V, R. K., & Iyer, N. R. (2014). Marine Algae for Cement Mortar Strengthening. *Journal of Civil Engineering Research 2014*, *4*, 23–25

Phang SM (2010). Seaweed Resources in Malaysia: Current Status and Future Prospects. ISSN: 1463-4988 (Print) 1539-4077 (Online). Kuala Lumpur.

Suhendro, B. (2014). Toward Green Concrete for Better Sustainable Environment. *Procedia Engineering*, *95*(Scescm), 305–320.

Susilorini, R. M. I. R., Hardjasaputra, H., Tudjono, S., Hapsari, G., Wahyu, S. R., Hadikusumo, G., & Sucipto, J. (2014). The Advantage of Natural Polymer Modified Mortar with Seaweed: Green Construction Material Innovation for Sustainable Concrete. *Procedia Engineering*, *95*(Scescm), 419–425.

Standard of Testing

ASTM C 496/C 496M – 04 – Standard Test Method for Splitting Tensile Strength of Cylindrical Concrete Specimens)

BS EN 12390-2: 2009 – Testing Fresh Concrete

BS EN 12390-3: 2009 – Testing hardened concrete. Compressive strength of test specimens

BS EN 12390-5: 2009 – Testing hardened concrete. Flexural strength of test specimens

BOUNDARY CONDITION FOR DIAMETRICAL COMPRESSION TEST USING DIFFERENT SHAPE OF LOADING DISTRIBUTION ON THE CENTER AND EDGE OF CONTACT AREA

Takashi Tsutsumi[1]* & Rini Asnida Abdullah[2]

[1] *Department of Civil Engineering, National Institute of Technology, Kagoshima College*
Kirishima, Kagoshima, 899-5193, Japan
[2] *Faculty of Civil Engineering, Universiti Teknologi Malaysia*
Skudai, 81310, Johor, Malaysia

*Corresponding Author: *tsutsumi@kagoshima-ct.ac.jp*

Abstract: To investigate the tensile strength for brittle materials, diametrical compression test has been used widely because of its convenience. Generally, the applied load on diametrical compression test is assumed as a pair of concentrated force to obtain the tensile strength. However, the contact areas arise between the loading platen and specimen in the fact. In addition, it is observed that these contact areas increase as the value of force increases during the test. Previous studies show that these contact areas affect the value of tensile stress arising on the loading radius. Therefore the applied load should be treated as distributed load on the contact area to obtain the tensile strength using diametrical compression test. In this study, the shape which consists with uniform loading at the center and cosine curve at both edges is proposed as distribution of load on the contact area. Under this distribution of load, calculations are carried out for not only isotropic but also circular specimens using theoretical solution. And some numerical results for deformation of specimen and distribution of tensile stress on the loading radius are shown in graphical representation and compared with some result shown in previous studies. Furthermore, this assumption by authors is verified with these results.

Keywords: *Diametrical Compression test, Boundary condition, Distribution of applied load, Deformation, Tensile stress on loading radius*

1.0 Introduction

Diametrical compression test (also termed as indirect tensile strength test) is a method for measuring tensile strength of a brittle material like rocks. The test is performed by

placing a disc-shaped sample (disc thickness twice its diameter) in between two rigid platens. Compressive load is applied via steel platen which is in contact with the sample. Since tensile strength of brittle material is much smaller than its compressive strength. Therefore, the brittle material fails under tensile manner, usually in the form of vertical diametrical fracture. The test induces a biaxial state of stress in which the stress at the center of the circular plane is compressive in *x*-direction (σ_x), and tensile in y-direction (σ_y). Theoretically, for an isotropic material, the tensile stress reaches a maximum at a constant magnitude of $P/(\pi a)$, where P represents the applied load and a represents the radius of the circular plane (Sokolnikoff, 1956).

Several attempts have been seen for modeling. Cauweleart et al. (1994) obtained a solution using the theoretical results for a semi-infinite plate under concentrated force. The theoretical solution for orthotropic specimen under concentrated force was shown by Claesson and Bohloli (1998), Exadaktylos (2001) and Exadaktylos and Kaklis (2001). The theoretical solution under uniform radial load distributed on whole contact area was shown and were compared with the result from some experiments by Chen et al. (1998) and Markides et al. (2010). Analytical models using finite element were used by Lemmon and Blackketter (1996) to evaluate the distribution of tensile stress for diametrical compression test. The contact area between the specimens and two loading platens was set at 2, 4 and 8% of the circumference of the specimen with uniform loading whose direction is same as loading applied to the platens. The results of this study are in agreement with the theoretical model, using orthotropic stress functions under the same conditions, as proposed by Tsutsumi & Hirashima (2000). The results show that the tensile stress generating near the loading platens is influenced by the contact area between the loading platens and the specimen. For isotropic materials (i.e., with material properties that are uniform along each axis), the maximum tensile stress generates at the center of disk when the contact area increases. For orthotropic materials, the maximum tensile stress also generates at the center of circular plane when the angle of the principal material direction to the loading direction is close to $\pi/4$. And the maximum value is almost constant regardless of the contact area. On the other hand, the maximum tensile stress generates near the loading platen decreases with increasing contact area, when the angle between the principal material direction and the loading direction is small. The latter shows that that contact area has a significant influence on tensile strength measurements.

In previous studies, the distribution of stresses applied on the loading platens was assumed to be uniform. In reality, the maximum applied stress seems to generate at the center of loading platens, and decreases as the distance from the center increases. Eventually, the applied load seems to disappear at the edges of the contact area. In order to satisfy this boundary condition on the contact area, the cosine curve was adopted as the distribution of loading applied on loading platens in a theoretical model for diametrical loading test by authors. The distribution of tensile stress on the loading radius under this loading is similar to that under uniform loading (Tsutsumi and Kukino, 2015). However, maximum value of displacement occurring at the center of the loading platens does not agree with the results from experiments (Kukino and Tsutsumi 2014).

In this study, the proposed theoretical stress distribution consists of a uniform load at the center and cosine curve at both ends of the contact area between the sample and the platens. Under these loading conditions, calculations are carried out using theoretical solution. The specimens used are isotropic or orthotropic, homogeneous, continuous and without any micro-cracks. The elastic solution using boundary condition proposed in this study is used to obtain the deformation of specimen's surface around the loading platen and the distributions of tensile stress on the loading radius for the isotropic or orthotropic circular plane.

2.0 Fundamental equations

In this paper, the problem of the application of opposing concentrated loads P to the diametrical axis of an orthotropic column specimen of radius a is treated as shown in Figure 1; Here, φ is the angle between the loading axis and the principal elastic axis, and E_1 and E_2 are the respective elastic moduli in the direction of the principal elastic axis.
By denoting the loading axis as x, and the perpendicular direction in the plane of the loading axis as y, the following equations representing the resultant forces on surface X_n and Y_n, going anticlockwise from the x-axis in the x and y directions, on the boundary circumference of a column-shaped specimen, which are related to stress components σ_x, σ_y and τ_{xy} are obtained:

$$\left.\begin{aligned} X_n &= \sigma_x \cos(n,x) + \tau_{xy} \cos(n,y), \\ Y_n &= \tau_{xy} \cos(n,x) + \sigma_y \cos(n,y). \end{aligned}\right\} \tag{1}$$

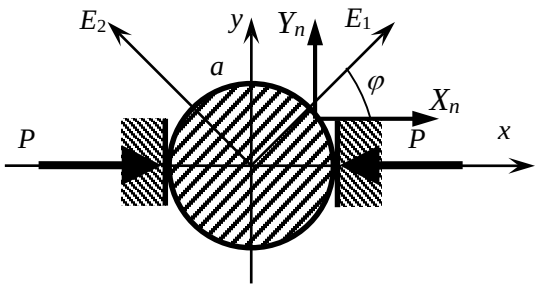

Figure 1: Orthotropic circular disk under diametrical compression

The stress components σ_x, σ_y and τ_{xy}, and the displacement components u_x and u_y are expressed by the following (Lekhnitskii, 1968).

$$\left.\begin{aligned}\sigma_x &= 2\,\mathrm{Re}\left[\mu_1^{\,2}\Phi_1'(z_1)+\mu_2^{\,2}\Phi_2'(z_2)\right],\\ \sigma_y &= 2\,\mathrm{Re}\left[\Phi_1'(z_1)+\Phi_2'(z_2)\right],\\ \tau_{xy} &= -2\,\mathrm{Re}\left[\mu_1\Phi_1'(z_1)+\mu_2\Phi_2'(z_2)\right].\end{aligned}\right\} \tag{2}$$

$$\left.\begin{aligned}u_x &= 2\,\mathrm{Re}\left[p_1\Phi_1(z_1)+p_2\Phi_2(z_2)\right],\\ u_y &= 2\,\mathrm{Re}\left[q_1\Phi_1(z_1)+q_2\Phi_2(z_2)\right].\end{aligned}\right\} \tag{3}$$

Here, Re denotes the real part of the complex functions in brackets. $'$ means the first derivative of $\Phi_k(z_k)$ with respect to z_k.

The integral calculi about resultant forces for the *x*-directions and *y*-directions on the surface are expanded as Fourier series with *M* terms, as follows:

$$\left.\begin{aligned}\int_0^s X_n\,ds &= \beta_0+\sum_{m=1}^{M}\left(\beta_m e^{im\theta}+\overline{\beta}_m e^{-im\theta}\right),\\ -\int_0^s Y_n\,ds &= \alpha_0+\sum_{m=1}^{M}\left(\alpha_m e^{im\theta}+\overline{\alpha}_m e^{-im\theta}\right).\end{aligned}\right\} \tag{4}$$

Here, the bar denotes the complex conjugate. α_m and β_m for the problem in this paper are determined in the next section.

The complex stress functions for an orthotropic circular plate with radius *a* are expanded as the series expressed below (Lekhnitskii, 1968):

$$\left.\begin{aligned}\Phi_1(z_1) &= A_0+A_1z_1+\sum_{m=2}^{M}A_mP_{1m}(z_1),\\ \Phi_2(z_2) &= B_0+B_1z_2+\sum_{m=2}^{M}B_mP_{2m}(z_2).\end{aligned}\right\} \tag{5}$$

Here $P_{km}(z_k)$ (k=1,2) is a power series of the *m*-th order and is expressed by the following equation.

$$P_{km}(z_k) = -\frac{1}{a^m(1-i\mu_k)^m} \times\left\{\left(z_k+\sqrt{z_k^{\,2}-a^2\left(1-\mu_k^{\,2}\right)}\right)^2+\left(z_k-\sqrt{z_k^{\,2}-a^2\left(1-\mu_k^{\,2}\right)}\right)^2\right\}\quad(k=1,2). \tag{6}$$

where, μ_k are the roots of the characteristic equation.

$$a_{11}\mu^4 - 2a_{16}\mu^3 + (2a_{12} + a_{66})\mu^2 - 2a_{26}\mu + a_{22} = 0. \tag{7}$$

a_{ij} (i, j=1, 2, 6) represents elastic compliances for plane stress condition. The complex variable z_k and power series $P_{km}(z_k)$ are represented on the cylindrical boundary as follows:

$$\left.\begin{aligned} z_k &= \frac{a}{2}\{(1-\mu_k)e^{i\theta} + (1+i\mu_k)e^{-i\theta}\}, \\ P_{km} &= -\left(e^{im\theta} + t_k{}^m e^{-im\theta}\right), \quad t_k = \frac{1+i\mu_k}{1-i\mu_k}. \qquad (k=1,2) \end{aligned}\right\} \tag{8}$$

By using the complex functions $\Phi_k(z_k)$, the integral calculi on resultant stresse are expressed as follows:

$$\left.\begin{aligned} \int_0^s X_n ds &= \mathrm{Re}[\mu_1\Phi_1(z_1) + \mu_2\Phi_2(z_2)], \\ -\int_0^s Y_n ds &= \mathrm{Re}[\Phi_1(z_1) + \Phi_2(z_2)]. \end{aligned}\right\} \tag{9}$$

By substituting Eq. (8) into Eq. (4), and obtained equations into Eq. (9), the equations for assigning the resultant stress on the boundary are obtained. Furthermore, the coefficients of the corresponding terms of $e^{im\theta}$ and $e^{-im\theta}$ ($1 \le m \le M$) are compared with each other, resulting in the following equations:

$$\left.\begin{aligned} A_1 + B_1 + \overline{A}_1 + \overline{B}_1 &= \frac{1}{a}(\alpha_1 + \overline{\alpha}_1), \\ \mu_1 A_1 + \mu_2 B_1 + \overline{\mu}_1\overline{A}_1 + \overline{\mu}_2\overline{B}_1 &= \frac{1}{ib}(\overline{\alpha}_1 - \alpha_1) = \frac{1}{a}(\beta_1 + \overline{\beta}_1), \\ \mu_1{}^2 A_1 + \mu_2{}^2 B_1 + \overline{\mu}_1{}^2\overline{A}_1 + \overline{\mu}_2{}^2\overline{B}_1 &= \frac{1}{ib}(\overline{\beta}_1 - \beta_1). \\ & \qquad (m=1) \end{aligned}\right\} \tag{10}$$

$$\left.\begin{aligned} A_m + B_m + \bar{t}_1{}^m\overline{A}_m + \bar{t}_2{}^m\overline{B}_m &= -\alpha_m, \\ \mu_1 A_m + \mu_2 B_m + \overline{\mu}_1\bar{t}_1{}^m\overline{A}_m + \overline{\mu}_2\bar{t}_2{}^m\overline{B}_m &= -\beta_m, \\ t_1{}^m A_m + t_2{}^m B_m + \overline{A}_m + \overline{B}_m &= -\overline{\alpha}_m, \\ \mu_1 t_1{}^m A_m + \mu_2 t_2{}^m B_m + \overline{\mu}_1\overline{A}_m + \overline{\mu}_2\overline{B}_m &= -\overline{\beta}_m. \\ & \qquad (m \ge 2) \end{aligned}\right\} \tag{11}$$

For the case of $m = 1$, there are only three equations for the four unknown quantities of the real and imaginary parts of A_1 and B_1, respectively, so these equations are unsolved. For this reason, the condition that the rigid body rotation is zero is additionally introduced, resulting in the following equation (Kawakubo et al., 1996)

$$(q_1 - \mu_1 p_1)A_1 + (q_2 - \mu_2 p_2)B_1 + (\overline{q}_1 - \overline{\mu}_1 \overline{p}_1)\overline{A}_1 + (\overline{q}_2 - \overline{\mu}_2 \overline{p}_2)\overline{B}_1 = 0. \qquad (12)$$

where

$$\left.\begin{aligned} p_1 &= a_{11}\mu_1^{\,2} + a_{12}, & p_2 &= a_{11}\mu_2^{\,2} + a_{12}, \\ q_1 &= \left(a_{12}\mu_1^{\,2} + a_{22}\right)/\mu_1, & q_2 &= \left(a_{12}\mu_2^{\,2} + a_{22}\right)/\mu_2. \end{aligned}\right\} \qquad (13)$$

By adding Eq. (12) to Eq. (10), A_1 and B_1 can be obtained completely.

3.0 Results and Discussion

In this paper, the shape which consists with uniform loading at the center and cosine curve at both edges is proposed as distribution of load on the contact area $\omega/2$. As shown in Figure 2, from center of loading platen, the uniform loadings whose width is $w_1/2$ are applied on both side. While, from both edge of uniform loading, cosine shaped loadings whose width is $w_2/2$ are applied on both side and loading is disappeared on the edge of contact area.

In this study, two sets of width shown in Table 1 are applied. Namely, 50% of contact area is covered with uniform loading in Case 1, 75% is in Case 2.

Table 1: Proportion of loading on boundary condition

	Width of uniform loading $w_1/2$	Width of cosine shaped loading $w_2/2$
Case 1	$\omega/8$	$\omega/8$
Case 2	$3\omega/16$	$\omega/16$

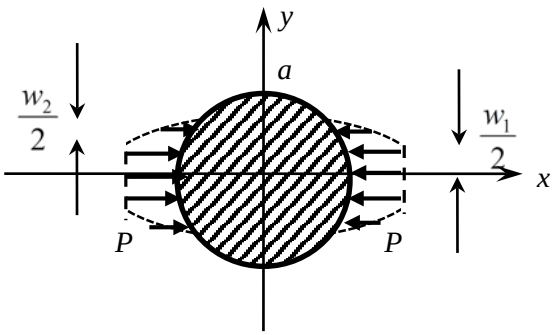

Figure 2: Boundary condition in this study

Fourier coefficients in Eq. (4) are expressed as shown in Eq. (14) for this problem.

$$\alpha_m = 0, \quad \beta_m = -ib_m . \tag{14}$$

b_m are able to be obtained through Fourier integral. The first equation in Eq. (4) is an odd function in this problem. Therefore, Fourier sine transform is able to be adopted for this problem. Furthermore, the first equation in Eq. (4) is able to be treated between 0 and $\pi/2$ because this equation is symmetry about the axis expresses the value of integration for resultant force. The Fourier integral for Case 1 is shown in Eq. (15).

$$\begin{aligned} b_m = \frac{2}{\pi}\Bigg[& \int_0^{\omega/8} \frac{2\theta}{\omega} \sin m\theta d\theta + \int_{\omega/8}^{\omega/4} \left\{ \frac{1}{4} - \frac{1}{4}\cos\frac{4\pi}{\omega}\theta \right\} \sin m\theta d\theta \\ & + \frac{1}{2}\int_{\omega/4}^{\pi-\omega/4} \sin m\theta d\theta + \int_{\pi-\omega/4}^{\pi-\omega/8} \left\{ \frac{1}{2} - C_1 \sin\frac{4\pi}{\omega}\theta - C_2 \cos\frac{4\pi}{\omega}\theta \right\} \sin m\theta d\theta \\ & + \frac{2}{\omega}\int_{\pi-\omega/8}^{\pi} (\pi - \theta)\sin m\theta d\theta \Bigg]. \end{aligned} \tag{15}$$

where

$$C_1 = \frac{1}{4}\cos\frac{4\pi}{\omega}\left(\pi - \frac{\omega}{4}\right), \quad C_2 = -\frac{1}{4}\sin\frac{4\pi}{\omega}\left(\pi - \frac{\omega}{4}\right). \tag{16}$$

The right side of Eq. (15) is calculated into Eq. (17).

$$\begin{aligned} b_m = \frac{2}{\pi}\Big(& B_{1m}^* + B_{2\,fm}^* + B_{2b1m}^* + B_{2b2m}^* + B_{3m}^* \\ & + B_{4\,fm}^* + B_{4c1m}^* + B_{4c2m}^* + B_{4b1m}^* + B_{4b2m}^* + B_{5\,fm}^* + B_{5bm}^* \Big). \end{aligned} \tag{17}$$

where

$$
\left.
\begin{aligned}
&B_{1m}^{*} = -\frac{1}{4m}\cos\frac{m\omega}{8} + \frac{2}{m^2\omega}\sin\frac{m\omega}{8},\ B_{2fm}^{*} = \frac{1}{2m}\sin\frac{3m\omega}{16}\sin\frac{m\omega}{16} \\
&B_{2b1m}^{*} = \frac{1}{8}\frac{\omega}{m\omega+4\pi}\left\{\cos\left(m+\frac{4\pi}{\omega}\right)\frac{\omega}{4} - \cos\left(m+\frac{4\pi}{\omega}\right)\frac{\omega}{8}\right\} \\
&B_{2b2m}^{*} = \frac{1}{8}\frac{\omega}{m\omega-4\pi}\left\{\cos\left(m-\frac{4\pi}{\omega}\right)\frac{\omega}{4} - \cos\left(m-\frac{4\pi}{\omega}\right)\frac{\omega}{8}\right\}, \\
&B_{3}^{*} = -\frac{1}{2m}\cos\left(m\pi-\frac{m\pi}{4}\right) + \frac{1}{2m}\cos\frac{m\pi}{4}, \\
&B_{4fm}^{*} = \frac{1}{4m}\left\{-\cos\left(m\pi-\frac{m\omega}{8}\right) + \cos\left(m\pi-\frac{m\omega}{4}\right)\right\}, \\
&B_{4c1m}^{*} = -\frac{\omega C_1}{2(4\pi+m\omega)}\left[\sin\left\{\left(\frac{4\pi}{\omega}+m\right)\left(\pi-\frac{\omega}{8}\right)\right\} - \sin\left\{\left(\frac{4\pi}{\omega}+m\right)\left(\pi-\frac{\omega}{4}\right)\right\}\right], \\
&B_{4c2m}^{*} = \frac{\omega C_1}{2(4\pi-m\omega)}\left[\sin\left\{\left(\frac{4\pi}{\omega}-m\right)\left(\pi-\frac{\omega}{8}\right)\right\} - \sin\left\{\left(\frac{4\pi}{\omega}-m\right)\left(\pi-\frac{\omega}{4}\right)\right\}\right], \\
&B_{4b1m}^{*} = -\frac{\omega C_2}{2(4\pi+m\omega)}\left[\cos\left\{\left(\frac{4\pi}{\omega}+m\right)\left(\pi-\frac{\omega}{8}\right)\right\} - \cos\left\{\left(\frac{4\pi}{\omega}+m\right)\left(\pi-\frac{\omega}{4}\right)\right\}\right], \\
&B_{4b2m}^{*} = \frac{\omega C_2}{2(4\pi-m\omega)}\left[\cos\left\{\left(\frac{4\pi}{\omega}-m\right)\left(\pi-\frac{\omega}{8}\right)\right\} - \cos\left\{\left(\frac{4\pi}{\omega}-m\right)\left(\pi-\frac{\omega}{4}\right)\right\}\right], \\
&B_{5fm}^{*} = \frac{2\pi}{m\omega}(-1)^{m+1} + \frac{2\pi}{m\omega}\cos\left(m\pi-\frac{m\omega}{8}\right), \\
&B_{5bm}^{*} = -\frac{2}{\omega}\left\{\frac{\pi}{m}(-1)^{m+1} + \frac{1}{m}\left(\pi-\frac{\omega}{8}\right)\cos\left(m\pi-\frac{m\omega}{8}\right) - \frac{1}{m^2}\sin\left(m\pi-\frac{m\omega}{8}\right)\right\}.
\end{aligned}
\right\} \quad (18)
$$

The Fourier integral for Case 2 is shown in Eq. (19).

$$b_m = \frac{2}{\pi}\left[\int_0^{3\omega/16}\frac{2\theta}{\omega}\sin m\theta d\theta + \int_{3\omega/16}^{\omega/4}\left\{\frac{3}{8}-\frac{1}{8}\sin\frac{8\pi}{\omega}\left(\theta-\frac{3\omega}{16}\right)\right\}\times\sin m\theta d\theta\right.$$
$$+\frac{1}{2}\int_{\omega/4}^{\pi-\omega/4}\sin m\theta d\theta$$
$$+\int_{\pi-\omega/4}^{\pi-3\omega/16}\left\{\frac{3}{8}+C_3\sin\frac{8\pi}{\omega}\theta+C_4\cos\frac{8\pi}{\omega}\theta\right\}\sin m\theta d\theta$$
$$\left.+\frac{2}{\omega}\int_{\pi-3\omega/16}^{\pi}(\pi-\theta)\sin m\theta d\theta\right]. \qquad (19)$$

where

$$C_3 = \frac{1}{4}\cos\frac{8\pi}{\omega}\left(\pi-\frac{\omega}{8}\right), \quad C_4 = -\frac{1}{4}\sin\frac{8\pi}{\omega}\left(\pi-\frac{\omega}{8}\right). \qquad (20)$$

Eq. (19) is also calculated into Eq. (17). For Case2, Constants in right side of Eq. (17) are shown in Eq. (21).

$$
\left.
\begin{aligned}
&B_{1m}^{*} = -\frac{3}{8m}\cos\frac{3m\omega}{16} + \frac{2}{m^2\omega}\sin\frac{3m\omega}{16},\ B_{2fm}^{*} = \frac{3}{4m}\sin\frac{7m\omega}{32}\sin\frac{m\omega}{32} \\
&B_{2b1m}^{*} = -\frac{1}{16}\frac{\omega}{m\omega+8\pi}\left\{\cos\left(m+\frac{8\pi}{\omega}\right)\frac{\omega}{4} - \cos\left(m+\frac{8\pi}{\omega}\right)\frac{3\omega}{16}\right\} \\
&B_{2b2m}^{*} = -\frac{1}{16}\frac{\omega}{m\omega-8\pi}\left\{\cos\left(m-\frac{8\pi}{\omega}\right)\frac{\omega}{4} - \cos\left(m-\frac{8\pi}{\omega}\right)\frac{\omega}{16}\right\}, \\
&B_{3}^{*} = -\frac{1}{2m}\cos\left(m\pi - \frac{m\pi}{4}\right) + \frac{1}{2m}\cos\frac{m\pi}{4}, \\
&B_{4fm}^{*} = -\frac{3}{8m}\left\{\cos\left(m\pi - \frac{3m\omega}{16}\right) - \cos\left(m\pi - \frac{m\omega}{4}\right)\right\}, \\
&B_{4c1m}^{*} = -\frac{\omega C_3}{2(8\pi+m\omega)}\left[\sin\left\{\left(\frac{8\pi}{\omega}+m\right)\left(\pi-\frac{3\omega}{16}\right)\right\} - \sin\left\{\left(\frac{8\pi}{\omega}+m\right)\left(\pi-\frac{\omega}{4}\right)\right\}\right], \\
&B_{4c2m}^{*} = \frac{\omega C_3}{2(8\pi-m\omega)}\left[\sin\left\{\left(\frac{8\pi}{\omega}-m\right)\left(\pi-\frac{3\omega}{16}\right)\right\} - \sin\left\{\left(\frac{8\pi}{\omega}-m\right)\left(\pi-\frac{\omega}{4}\right)\right\}\right], \\
&B_{4b1m}^{*} = -\frac{\omega C_4}{2(8\pi+m\omega)}\left[\cos\left\{\left(\frac{8\pi}{\omega}+m\right)\left(\pi-\frac{3\omega}{16}\right)\right\} - \cos\left\{\left(\frac{8\pi}{\omega}+m\right)\left(\pi-\frac{\omega}{4}\right)\right\}\right], \\
&B_{4b2m}^{*} = \frac{\omega C_4}{2(8\pi-m\omega)}\left[\cos\left\{\left(\frac{8\pi}{\omega}-m\right)\left(\pi-\frac{3\omega}{16}\right)\right\} - \cos\left\{\left(\frac{8\pi}{\omega}-m\right)\left(\pi-\frac{\omega}{4}\right)\right\}\right], \\
&B_{5fm}^{*} = \frac{2\pi}{m\omega}(-1)^{m+1} + \frac{2\pi}{m\omega}\cos\left(m\pi - \frac{3m\omega}{16}\right), \\
&B_{5bm}^{*} = \frac{2}{\omega}\left\{\frac{\pi}{m}(-1)^{m} - \frac{1}{m}\left(\pi - \frac{3\omega}{16}\right)\cos\left(m\pi - \frac{3m\omega}{16}\right) - \frac{1}{m^2}\sin\left(m\pi - \frac{3m\omega}{16}\right)\right\}.
\end{aligned}
\right\} \quad (21)
$$

4.0 Results and discussion

4.1 Boundary conditions

Figure 3 and Figure 4 show the relationship between the integral calculi about resultant force for the *x*-direction along the surface in the longitudinal axis and the number of terms used in Eq. (4) in the transverse axis. Number of terms *M*=20, 30, 50, 70 and 100 are used in these figures. It is observed that the convergence and the accuracy are improved as number of terms increases for each contact area. It is also seems that the convergence is faster as contact area is larger in both case. Table 2 shows the maximum

error causing on the surface that shows constant values of integral calculi about resultant force. It is observed that the maximum value decreases as the number of terms increases except the interval from *M* is from 50 to 70 when contact area is 4%. Fracture happens under contact area from 4.4 to 5.1% in Tage stone and 6.4% in cement modified soil (Aono *et al.* 2012). Therefore, calculations are carried out for contact area 4% and 8% in this paper and *M*=70 is adopted to obtain the enough accuracy.

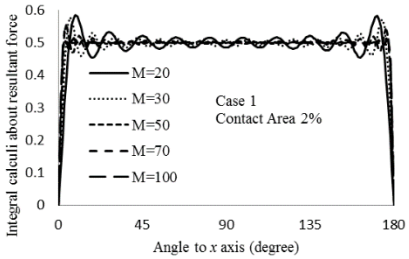

(a) Contact area 2%

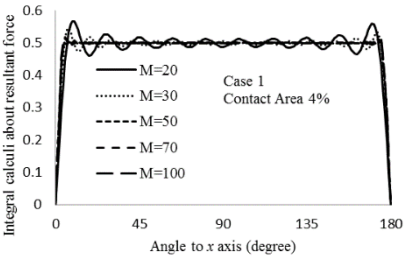

(b) Contact area 4%

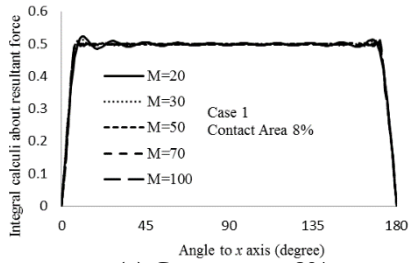

(c) Contact area 8%

Figure 3: Boundary condition under Case 1

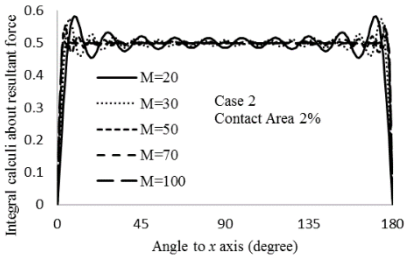

(a) Contact area 2%

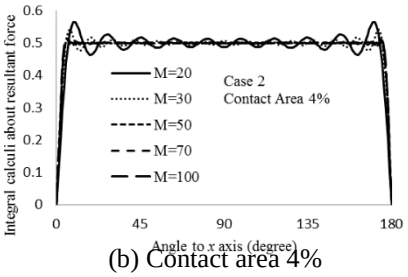

(b) Contact area 4%

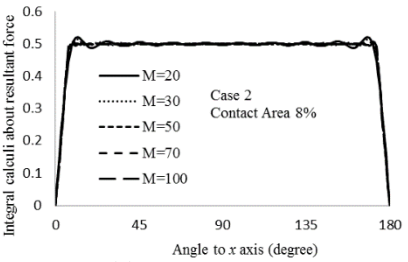

(c) Contact area 8%

Figure 4: Boundary condition under Case 2

4.2 Locus of deformation on the surface

Figure 5 and Figure 6 show the locus of deformation obtained from present result on the surface of disk around loading platen. Fig. 5 shows under Case 1, namely uniform loading covers on 50% of contact area. Fig. 6 shows under Case 2, namely uniform loading is covers on 75% of contact area. The locus of deformation is also obtained for uniform loading covering on whole contact area as shown in Fig. 7, and for concentrated force as shown in Figure 8. Figure 9 shows the locus of deformation obtained under uniform

Table 1: Error due to number of terms

(a) Case 1

Number of Terms	Contact Area		
	2%	4%	8%
M=20	16. 86	13. 57	4. 88
M=30	15. 43	9. 22	2. 33
M=50	11. 56	2. 76	1. 86
M=70	7. 10	4. 17	1. 47
M=100	2. 52	2. 10	1. 08

(b) Case 2

Number of Terms	Contact Area		
	2%	4%	8%
M=20	16. 71	13. 03	4. 22
M=30	15. 11	8. 51	3. 10
M=50	10. 93	2. 47	1. 70
M=70	6. 09	3. 45	1. 51
M=100	2. 48	1. 13	1. 03

loading covering on whole contact area. These figures show for the both case of contact area 4% and 8%. Furthermore, Figure 10 shows the locus of deformation obtained under concentrated force. The locus of deformation is shown at every one degree in the width of 20 degrees from the center of loading platen. The value of locus in each figure is multiplied by $0.05E_1a/P$ to draw these loci in this figure. In present results, the shape under loading platen appears flat surface after deformation. In addition, the deformation arises in the direction of loading under loading platen. While, the maximum value of locus arises at the center of loading platen under uniform loading though not clear. Under concentrated loading, the maximum value of locus arises at the center of loading platen and deformation arises to the center of contact area obviously. In all figures, the dent appears under contact area, namely, displacement within the contact area is larger than that around. However, it is common knowledge that any dents don't appear in actual behavior. Therefore, the results from these calculations are different from the actual behavior of specimen in diametrical loading test using flat loading platens. Although, it seems that the results from present study are more accurate than results from uniform loading covered with whole contact area or concentrated loading. In these studies, any tangential stresses generating along the loading platen are not taken account into. To improve the accuracy of study by authors, the theoretical model for tangential stresses generating along the loading platen, like the work by lavrov (2002), will be required.

4.2 Locus of deformation on the surface

Figure 5 and Figure 6 show the locus of deformation obtained from present result on the surface of disk around loading platen. Figure 5 shows under Case 1, namely uniform loading covers on 50% of contact area. Figure 6 shows under Case 2, namely uniform loading is covers on 75% of contact area. The locus of deformation is also obtained for uniform loading covering on whole contact area as shown in Figure 7, and for concentrated force as shown in Figure 8. Figure 9 shows the locus of deformation obtained under uniform loading covering on whole contact area. These figures show for the both case of contact area 4% and 8%. Furthermore, Figure 10 shows the locus of

deformation obtained under concentrated force. The locus of deformation is shown at every one degree in the width of 20 degrees from the center of loading platen. The value of locus in each figure is multiplied by $0.05E_1a/P$ to draw these loci in this figure. In present results, the shape under loading platen appears flat surface after deformation. In addition, the deformation

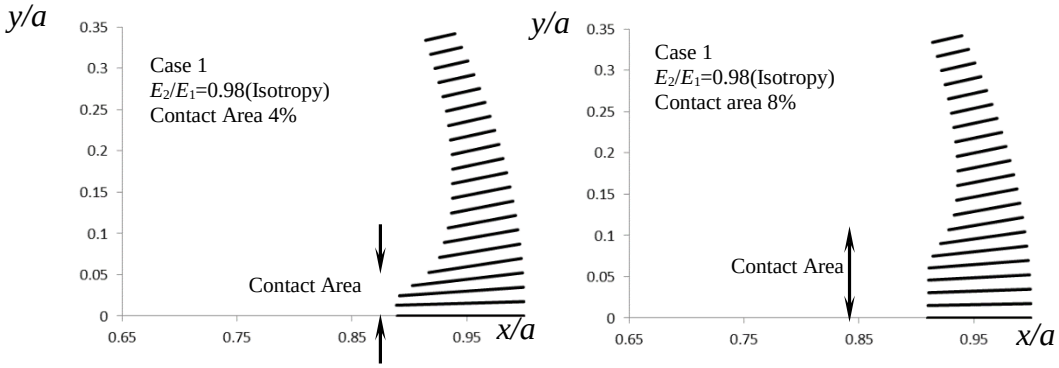

(a) Contct area 4% (b) Contact area 8%

Figure 5: Locus of deformation on surface under Case 1 in present study

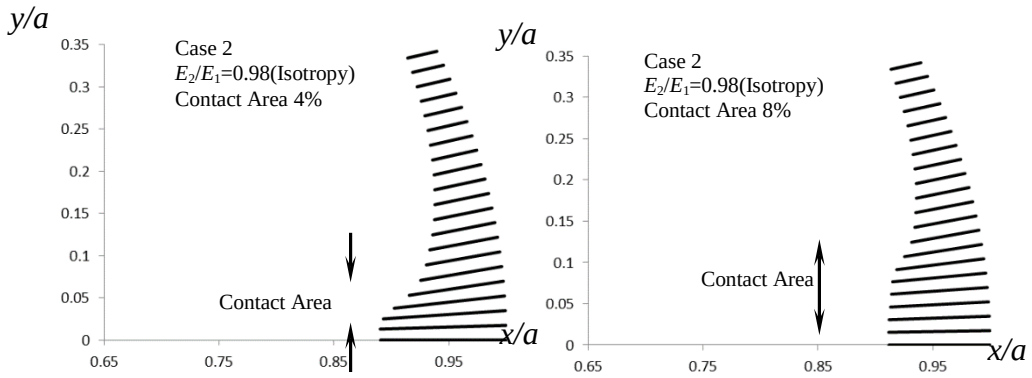

(a) Contct area 4% (b) Contact area 8%

Figure 6: Locus of deformation on surface under Case 2 in present study

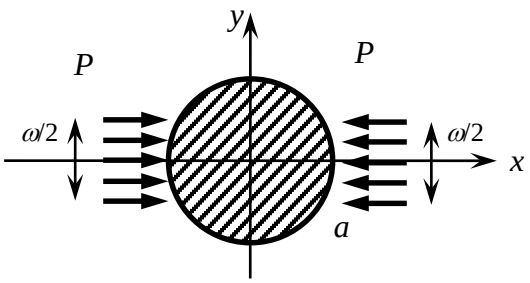

Figure 7: Scheme of uniform loading on whole contact area

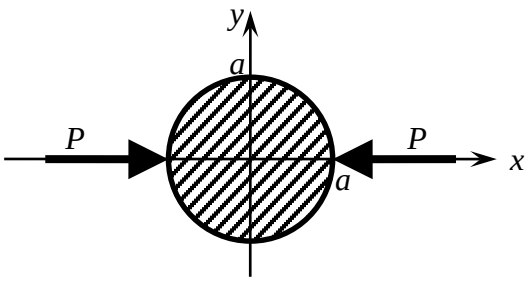

Figure 8 Scheme of concentrated loading

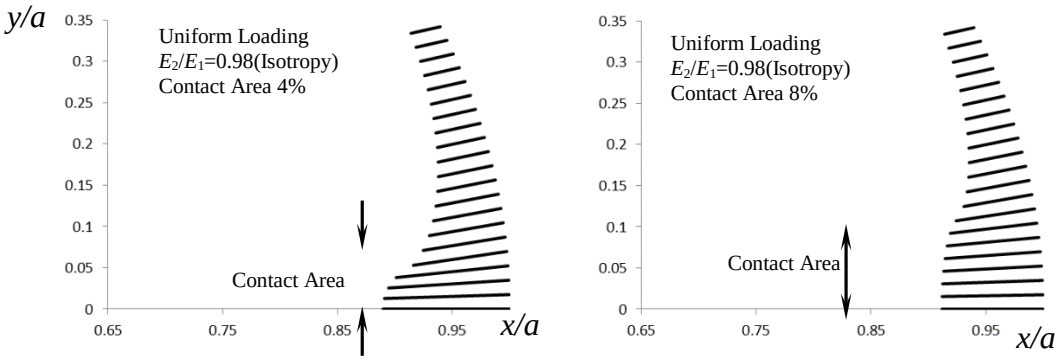

(a) Contct area 4% (b) Contact area 8%

Figure 9 Locus of deformation on surface under uniform loading

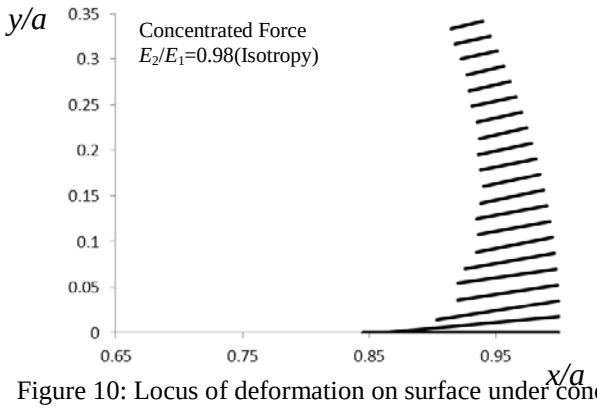

Figure 10: Locus of deformation on surface under concentrated force

arises in the direction of loading under loading platen. While, the maximum value of locus arises at the center of loading platen under uniform loading though not clear. Under concentrated loading, the maximum value of locus arises at the center of loading platen and deformation arises to the center of contact area obviously. In all figures, the dent appears under contact area, namely, displacement within the contact area is larger than that around. However, it is common knowledge that any dents don't appear in

actual behavior. Therefore, the results from these calculations are different from the actual behavior of specimen in diametrical loading test using flat loading platens. Although, it seems that the results from present study are more accurate than results from uniform loading covered with whole contact area or concentrated loading. In these studies, any tangential stresses generating along the loading platen are not taken account into. To improve the accuracy of study by authors, the theoretical model for tangential stresses generating along the loading platen, like the work by lavrov (2002), will be required.

4.3 Tensile stress generating on the loading radius

Figure 11 shows the comparison the distribution of tensile stress on the loading radius in isotropic specimen (E_2/E_1=0.98) between from present result, under uniform loading and concentrated force. The longitudinal axis means the normal stress to loading direction. This stress is normalized by the tensile strength for isotropic disk $P/(\pi a)$ shown in the specifications (Ulusay & Hudson, 2007). The transverse axis means the distance from center of the disk. This distance is also normalized by length of specimen's radius a. The uniform distribution of tensile stress appears under concentrated force that is used as the standard of measurement for tensile strength (Ulusay & Hudson, 2007). On the other hand, the maximum value of tensile stress appears at the center of specimen at first, the value of tensile stress decreases gently as the distance from center of specimen x/a increases secondly, decreases suddenly near the loading platen at last under Case 1, Case 2 and uniform loading covering on whole contact area. Almost same distribution of tensile stress appears under Case 1, Case 2 and uniform loading covering on whole contact area when the contact area is 4%. When the contact area is 8%, the tensile stress decreases suddenly at x/a is about 0.5 under Case 2 and uniform loading covering on whole contact area, while that happened at x/a is about 0.7 under Case 1.

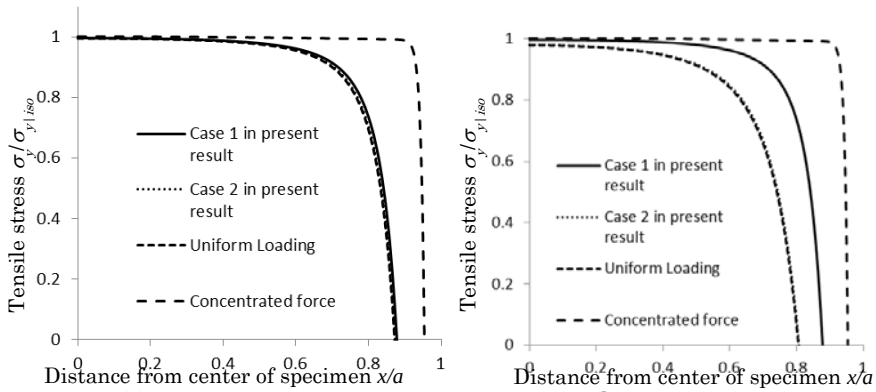

(a) Contct area 4% (b) Contact area 8%

Figure 11: Tensile stress on the loading radius in isotropic specimen

Comparisons the distribution of tensile stress on the loading radius are also carried out

for orthotropic specimen (E_2/E_1=1.5). Figure 12 shows when φ=0, namely the loading is carried out in softer axis. Figure 13 shows when $\varphi=\pi/2$, namely the loading is carried out in harder axis. Figure 14 shows when $\varphi=\pi/4$, namely the loading is carried out in the intermediate direction between harder and softer axis. When the loading direction is in principal elastic axis (i. e. φ=0, $\pi/2$), the obvious maximum value appears near the loading platen under concentrated force. While the maximum value appears at the distance from center of specimen x/a is about 0.7 under Case 1, Case 2 and uniform loading covering on whole contact area when the contact area is 4%. Furthermore, uniform distribution appears between x/a=0 to about 0.6, and the maximum value doesn't appear when the contact area is 8%. In all these figures, the value of tensile stress generating near the loading platen under concentrated force generating is largest, and those under other loadings are almost same. As shown in Figure 10, the obvious maximum value of displacement generate under concentrated force and this displacement is far different from the actual behavior in diametrical loading test using flat loading platen. Therefore, it seems that the distributions of tensile stress obtained from distributed load on loading platen are more reliable, especially near the loading platen.

When the loading is carried out in softer axis (φ=0), the value of maximum tensile stress is about 1.0 for 4% of contact area and about 0.95 for 8%. Therefore, the method to obtain the tensile strength for isotropic specimen is available in this loading direction and orthotropy ratio. When the loading is carried out in harder axis ($\varphi=\pi/2$), the tensile stress generating on the loading radius is smaller than that in softer axis because the deformation under loaded in harder axis is smaller than that in softer axis. The value of maximum tensile stress is about 0.82 for 4% of contact area and about 0.76 for 8%. Therefore, the tensile strength is estimated about 80% for the value obtained from the method for isotropic specimen.

When the loading is carried out in the intermediate direction between harder and softer axis, the maximum value of tensile stress generates at the center of specimen (i. e. x/a=0). Therefore, the tensile strength is estimated about 120% for the value obtained from the method for isotropic specimen.

5.0 Conclusion

Previous studies either used point, uniform or cosine shaped loading as boundary conditions for theoretical models for stress distribution in diametrical loading test. The present study adopts combination of loading consists of cosine shape and uniformly distributed load to satisfy the boundary conditions at the contact area between specimen and loading platens. At first, the boundary condition is verified using the proposed theoretical model and the number of terms in Fourier Series is set to 70 to obtain the adequate accuracy in calculation. Secondly, locus of deformation around the loading platen is shown in isotropic specimen and compared with some results from previous studies. It is shown that the flat deformation appears along the surface of loading platen

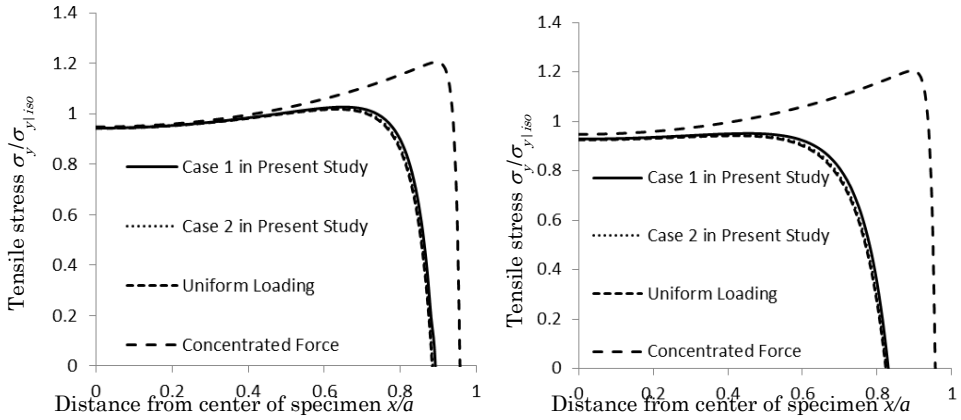

(a) Contct area 4% (b) Contact area 8%

Figure 12: Tensile stress on the loading radius in isotropic specimen

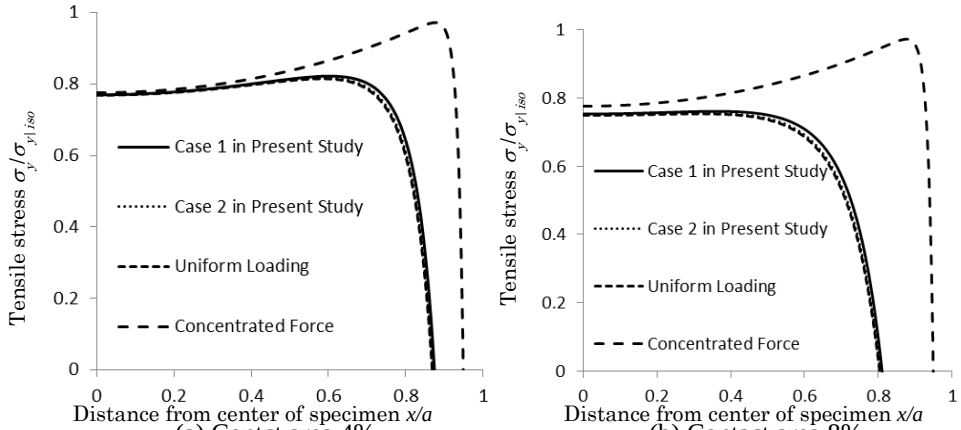

(a) Contct area 4% (b) Contact area 8%

Figure 13: Tensile stress on the loading radius in isotropic specimen

and the deformation of surface of specimen under the loading platen appears in the loading direction in present study. At last, the distributions of tensile stress along loading radius are calculated for selected orthotropy ratio, directions and contact areas, and compared with some results from previous studies. It is shown that the value of tensile stress generating near the loading platen in the result from present study, that is almost same as that from uniform loading on whole contact area, is smaller than that from concentrated force. Furthermore, the maximum value of tensile stress in orthotropic specimen from present study is almost same as that in isotropic specimen when loading is carried out in softer axis, and smaller than that when in harder axis and

larger than that in intermediate direction between softer and harder axis.
In these studies, any tangential stresses along the surface of loading platen or specimen are not taken account into. To establish the theoretical model for these tangential stresses and superpose on the theoretical model proposed in this study are future work for authors.

References

Aono, Y., Tani, K., Okada, T. and Sakai, M. (2012), "The mechanism of failure near the loading point in the splitting tensile strength test on Tage Stone" (in Japanese), *Proc. of 41th Rock Mech. Symposium in Japan*, 157-162.

Cauweleart, F. V. and Eckmann, B. (1994), "Indirect tensile test applied to anisotropic materials", *Materials and structures*, **27**, 54-60.

Chen, C. S., Pan, E. and Amadei, B. (1998) "Determination of Deformability and Tensile Strength of Anisotropic Rock Using Brazilian Tests", *Int. J. of Rock Mech. and Mining Sci.*, **35**, 43-61.

Claesson, J. and Bohloli, B. (2002), "Brazilian test: stress field and tensile strength of anisotropic rocks using an analytical solution", *Int. J. of Rock Mech. and Mining Sci.*, **39**, 991-1004.

Exadaktylos, G. E. and Kaklis, K.N. (2001), "Applications of an explicit solution for the transversely isotropic circular disc compressed diametrically", *Int. J. of Rock Mech. and Mining Sci.*, **38**, 227-243.

Exadaktylos, G. E. (2001), "On the constraints and relations of elastic constants of transversely isotropic geomaterials", *Int. J. of Rock Mech. and Mining Sci.*, **38**, 941-956.

Kawakubo, S., Tsutsumi, T. and Hirashima, K. (1996), "Stress and Displacement Fields for an Anisotropic Elliptical Disk Subjected to Arbitrary Loads at Boundary (in Japanese)", *Trans. JSME Series A*, **62**, 1626-1633.

Kukino, S. and Tsutsumi, T. (2014), Modification of boundary condition in theoretical model for diametrical compression test, *Proc. 4th International Symposium on Technology for Sustainability*, CD-ROM.

Lavrov, A. and Vervoort, A. (2002), "Theoretical treatment of tangential loading effects on the Brazilian test stress distribution", *Int. J. of Rock Mech. and Mining Sci.*, **39**, 275-283.

Lekhnitskii, S. G. (1968), *Anisotropic Plate*, 141, Gordon & Breach.

Lemmon, R. K. and Blackketter, D. M. (1996), "Stress Analysis of an Orthotropic Material under Diametral Compression", *Experimental Mech.* **36**, 204-211.

Markides, Ch. F., Pazis, D. N. and Kourkoulis, S. K. (2010), "Closed full-fill solutions for stress and displacements in the Brazilian disk under distributed radial load", *Int. J. of Rock Mech. and Mining Sci.*, **47**, 227-237.

Sokolnikoff, I. S. (1956), *Mathematical theory of elasticity*, 476, McGraw-Hill.

Tsutsumi, T. and Hirashima, K. (2000), "Analysis of Orthotropic Circular Disks and Rings under Diametrical Loading", *Structural Eng. and Mech.*, **9**(1), 37-50.

Tsutsumi, T. and Kukino, S. (2015), Distribution of Tensile Stress under Modified Boundary Condition in Theoretical Solution for Diametrical Compression Test, *Proc. 13th ISRM Congress*, CD-ROM.

Ulusay, R. and Hudson, J. A. (2006), *The complete ISRM suggested methods for rock characterization, testing and monitoring, 1974-2006*, 181-183.

POSSIBLE RE-UTILIZATION OF DEMOLISHED CONCRETE MATERIAL (DCM) IN STRENGTH DEVELOPMENT OF MARINE CLAY

Azimah Ayub[1], Nor Zurairahetty Mohd Yunus[1*], Muhammad Azril Hezmi[1], Nadiah binti Jamaluddin[1] Mohd Khairul Idham[1] & Haryati Yaacob[1]

[1] *Department of Geotechnics & Transportation, Faculty of Civil Engineering, Universiti Teknologi Malaysia, 81310 Skudai, Johor Bahru, Malaysia*

*Corresponding Author: *nzurairahetty@utm.my*

Emerging trend of using waste materials in soil stabilisation has been considered in present days. Currently, the use of coarser fraction of Demolished Concrete Material (DCM) has been used as a recycled aggregate in pavement construction but finer fractions are being left out still as a waste material. Hence, in the present study, efforts have been made to utilize these fines obtained from DCM as a soil stabilizer for improving the properties of Marine Clay to form the basis of a strong and reliable foundation for construction. Testing programme involves the determination of basic and engineering properties with and without various addition of DCM (5%, 10% and 15%) at curing periods of 0, 7, 28 and 60 days, respectively. The result shows that the strength of treated Marine clay increases with the increasing of DCM contents as time prolonged, which indicates the possibility of re-utilization of DCM in stabilising Marine clay.

Keywords: Demolished Concrete Material (DCM), Marine Clay, Strength

1.0 Introduction

Nowadays, the rapid development of a vigorous city in the world is inevitable while its influence to the land use proportion is a subject matter. It is undeniable that an array of expected problems such as the construction waste issue, distraction of land use, and the challenges of environmental sustainability will appear. On of them is the presence of unsuitable soil at the constuctions' particular area which then results in the unstable high rise building or failure for road pavements (Zhao et al.,2016 and Marto et al., 2016). Marine clay is considered as one of the problematic soils due to its poor soil properties and low unconfined compressive strength (Tanaka et al., 2001, Mohd Yunus et al., 2012, Al-bared, 2017). Therefore, lieu of this issue, soil stabilization is vital prior to any marine construction activities (Saeed et al,. 2013). Based on (Kumar et al., 2015) the process of soil stabilization helps to achieve the target properties of soil needed for the completion of construction activities. This is supported by ing (Hall, 2012), stabilising the soil for diverse landuse applications definitely helps in improving the soil strength, it is also more economical and gives better adjustments to the soil such as to its texture and durability.There are many additives which can be used in order to achieve soil stabilization

method including by recycling any waste materials (Sivrikaya et al, 2014; Modarres, 2015; Nosoudy, 2015).

On the other hand, at the construction site, the main solid waste generated are gravel, concrete, asphalt, bricks, tiles, plaster, masonry, wood, metal, paper and plastics (Abu Eusuf et al.,2012). According to Ajzen (1991), generally it is estimated that approximately 10% to 30% of waste disposed off in landfill originates from construction and demolition activities particularly in Canada. In Malaysia, this stressful issue being studied and had been conducted regarding the breakdown of waste in the central and southern region of Malaysia, which 28.34% of the total waste generated was contributed by construction and industrial waste-stream (Begum et al. 2007). Based on Nagapan et al. (2013), among main types of construction waste generated are concrete (12.32%), metals (9.62%), bricks (6.54%), plastics (0.43%), woods (69.10%) and other waste (2%). Hence, it could be perceived that concrete has quite a number of waste as ranked 2nd which is 12.32% behind woods waste which is 69.10%.

It has been estimated that only 20% to 30% of construction and demolished waste are being recycled according to the Southeast Regional Environmental Finance Centre (Abu Eusuf et al., 2012). Moreover, out of the 76% of solid waste that are collected in Malaysia, only 5% is recycled with 95% of waste are dumped at landfills (Syed Haidir and Agamuthu, 2012). Based on this statistics, it shows that there is an alarming need to recycle and reuse demolished concrete materials (DCM). By recycling or reusing demolished concrete it could help minimize environmental pollution due to the abundance of construction waste in landfills. Other than that, by using DCM, it will support sustainability efforts which is one of the movements that Malaysian government is trying to implement. In other countries like India, Japan and Canada, the reuse of DCM has been widely applied in various engineering field for years. For example, in India,coarse demolished concrete has been recycled to replace natural aggregate for sustainble subbase pavements (Radonjanin, 2010) while in Netherlands demolished concerete has been used for road construction also in coarse form (Husain and Assas, 2013; Hendriks, 2016). Eighty percent of coarse aggregate from any demolished buildings in Japan is being recycled for the new structure purpose as well as in renovation projects (Yee, 2012). However, based on review done by Kerni et al., 2015, there is no further research on the fines demolished concerete materials that has been yet discovered.

Therefore, it is vital to conduct a primary study specifically in Malaysia prior to any new development projects in the oceanic area. In lieu of this and along with the desire to reduce overflows of construction waste, stabilizing the marine clay with crushed fines fractions of DCM is an alternative available in the Geotechnical applications.

2.0 Materials and Testing Programme

The main materials used for this study are natural marine clay and demolished concrete materials which then will be added at different percentages of 5%,10%,15%, respectively to the soil. All of the testing is carried out according to each material used with the preparation process which complies to BS 1377: Part 2 - 9: 1990. Each of the samples are then being cured for 7, 28 and 60 days.

2.1 Marine clay

The marine clay is obtained in the construction area of Nusajaya, Johor Bharu as shown in Figure 1. It was collected from the depth of between two and three metres. The clay obtained contained a lot of organic matter, was greenish black in colour and had undesirable smell. The 2 mm marine clay used for test was air dried before any test had been conducted. The fresh and original marine clay deposited on the site was taken to the Geotechnical Laboratory of Universiti Teknologi Malaysia for further experimental works. Table 1 summarizes the properties of Marine clay used in this study while table 2 provides the chemical elements of marine clay according to Mohd Yunus et al,. (2012).

Figure 1: Deposited of marine clay at Nusajaya

Table 1: The summarisation of marine clay properties

Marine clay properties	Value
Natural water content	51.2
Specific gravity	2.26
Liquid limit	47.05%
Plastic limit	23.92%
MDD	1530 kg/m^3
Optimum moisture content	24%

Table 2: Summary of chemical elemnts forming Marine Clay (After Mohd Yunus et al., 2014)

Chemical elements	Amount (%)
Al	13.67
Si	21.91
K	2.02
Ti	2.06
Fe	5.11
Mg	0.78

2.2 The demolished concrete materials

Grade 30 demolished concrete blocks (as shown in Figure 2) were collected from the disposal site of Structural Laboratory, Faculty of Civil Engineering, Universiti Teknologi Malaysia. The demolished concrete was then being crushed and sieved up to 63µm for an efficient mix with the soil.

Figure 2: Gred 30 demolished concrete

2.3 Specimen Preparation

Soil samples which refer to marine clay were sieved through 2 mm mesh sieve in order to prepare samples for UCS. Distilled water was used during specimen preparation. All samples were prepared using 95% of the maximum dry density (MDD) and the corresponding optimum moisture (OMC) content in order to treat the samples before failure. The volume of the mold at which the samples where compacted and the MDD were used as the reference during sample preparation. The predetermined values of DCM were measured to the dry mass of marine clay. Marine clay and DCM were mixed thoroughly and then distilled water was added and mixed until homogeneity was achieved. The mixing period did not exceed 5 minutes to make sure that there was no loss in water content. The mix designs of DCM were 5, 10, and 15% at which three UCS samples were prepared for each percentage to avoid errors during the test. The compaction mold was designed, in particular, to be used for UCS and Triaxil tests samples with height to diameter ratio of 2:1 and was made from stainless steel. The mixture of marine clay and tiles was compacted inside the mould (76 mm height and 38 mm diameter) using hydraulic jack machine. A stainless steel plunger was used to extrude the samples from the mould. Samples were trimmed to remove the extra soil and wrapped with several layers of cling film in order to preserve the water content. Samples were placed inside air tight plastic containers and stored for curing inside a controlled humidity chamber. The humidity chamber temperature was 27 ± 2 C° and the humidity was 97% ± 2%. Samples were cured for 7, 14 and 28 days before testing.

3.0 Results and Discussion

The results show the shear strength of both untreated and treated marine clay after 7,28, and 60 days curing period with different percentage of DCM.

3.1 Unconfined compressive strength

Effect of shear trength on marine clay treated with DCM was determined based on different curing periods and various addition of DCM contents. Table 3 summarizes the value of shear strentgh for both treated and untreated marine clay at 5%,10% and 15% of DCM contents after selected curing period.

Table 3: Result of shear strength value with different curing period

Curing period	Percentage	q_u (kPa)
Untreated		88.1
0 days	5%	153.5
	10%	173.4
	15%	217.7
7 days	5%	163
	10%	210
	15%	249.35
28 days	5%	188.25
	10%	320.55
	15%	352.2
60 days	5%	292.1
	10%	327.8
	15%	403.6

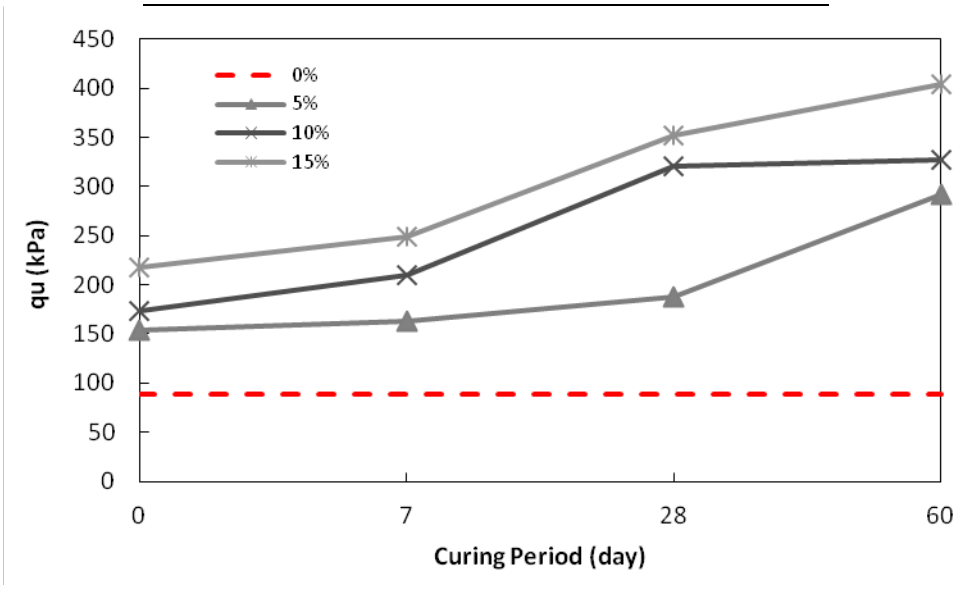

Figure 3: Effect of curing period on shear strength of DCM treated marine clay

The results of the UCS tests carried out on DCM-treated marine clay at different curing periods are shown in Figure 3. It can be seen that strength increases with addition of demolished concrete materials with a maximum value of 403.6 kPa in 60 days curing time. It can be seen also from Fig. 3 that the shear strength of all the treated specimens increases significantly compared to the strength of untreated Marine clay which is in agreement with previous study (Jain and Chawda, 2016). Basically, strength increases with higher curing periods. It has been found that, DCM can provide initial strength gained, where strength increased from 88.1 kPa to 153.5 with addition of 5% DCM contents immeditely (i.e. 0 day) after mixing it with marine clay. However, slight increase in shear strength was observed at 7 curing days as compared to 0 day. Significant increase in strength can be observed beyond 7 days for all of the specimen treated with DCM. Strength increased from (list the values at 7 days for all specimen at 5%, 10% and 15%) to (list the values at 28 days for all specimen at 5%, 10% and 15%) for specimens treated with 5%, 10% and 15% DCM content from 7 to 28 days, respectively. Investigation on strength development was continued at higher curing period of 60 days to observe long term stabilisation progress. Based on the result, it was found that, there was a slight increase in strength of specimens treated with 10% and 15% strength compared to 28 curing days.

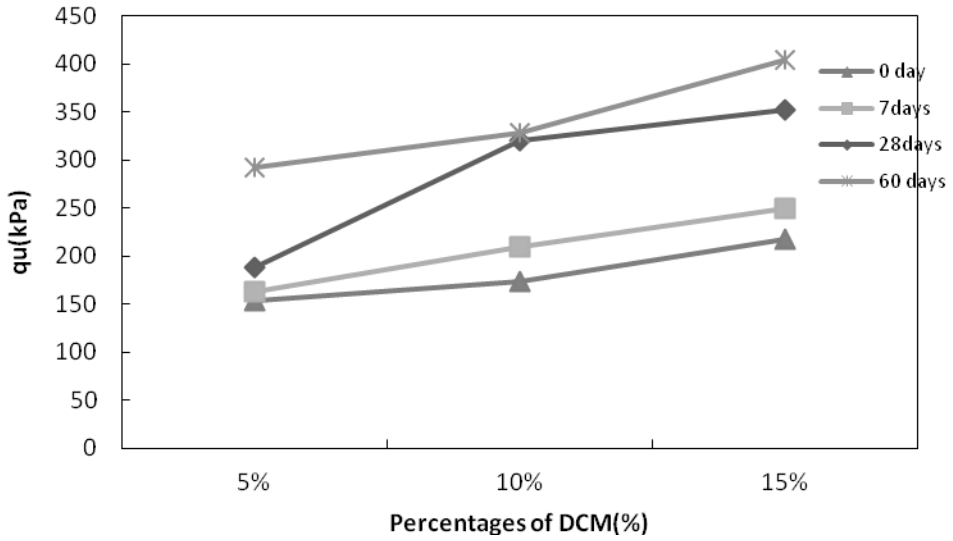

Figure 4: Effect of different DCM content on shear strength

The effect of DCM content on shear strength of marine clay is depicted in figure 4. There is a huge difference between untreated marine clay to 5% treated marine clay at 60 day curing time. It shows that at 60 day, the reaction between DCM and marine clay was getting better and helped in improving the marine clay strength even at 5%, as compared to other curing time. Other than that, the graph also illustrates that there is slightly diffrence between 5% DCM content and 10% DCM content for each curing period, which means, DCM acts more when more DCM contents are added.

This is happening because the frictional interaction between the soil and DCM which correlates to the fact that waste materials, particularly demolished concrete materials act as an effective stabiliser for marine clay soil. DCM obviously shows that it can be a great stabiliser to the

marine clay even at only 5% DCM content added to the clay. Then, the cementitous agent present in the recycled concrete reacted well with the clay itself as more curing time allocated. Based on the graph, at 15% DCM content increases from 28 day to 60 day that eventually potrays the highest strength compared to other curing period yet, according to Rana et al. 2016, concrete has better cementatious agent as compared to other materials like aggregate and marble tiles. However, a little difference between the strength is due to the a slight difference of DCM content. There is no significant increase might due to the only 5% of DCM being added to each of the samples. This is because DCM is less distributed into the marine clay which then resulting in poor workability as the air void in marine clay is not fully covered by the DCM content. This is even common to other stabilisation process where the strength development requires more cement additives to enhance more compressive strentgh as discussed by (Cong et al., 2014).

Table 4: Summary of percentage of strength gained within the specified curing time at different DCM content

Curing period	percentage	Strength gained (%)
0-7day	5%	10.73
	10%	41.54
	15%	35.93
7-28day	5%	28.66
	10%	125.48
	15%	116.74
28-60day	5%	117.877
	10%	17.25
	15%	58.34

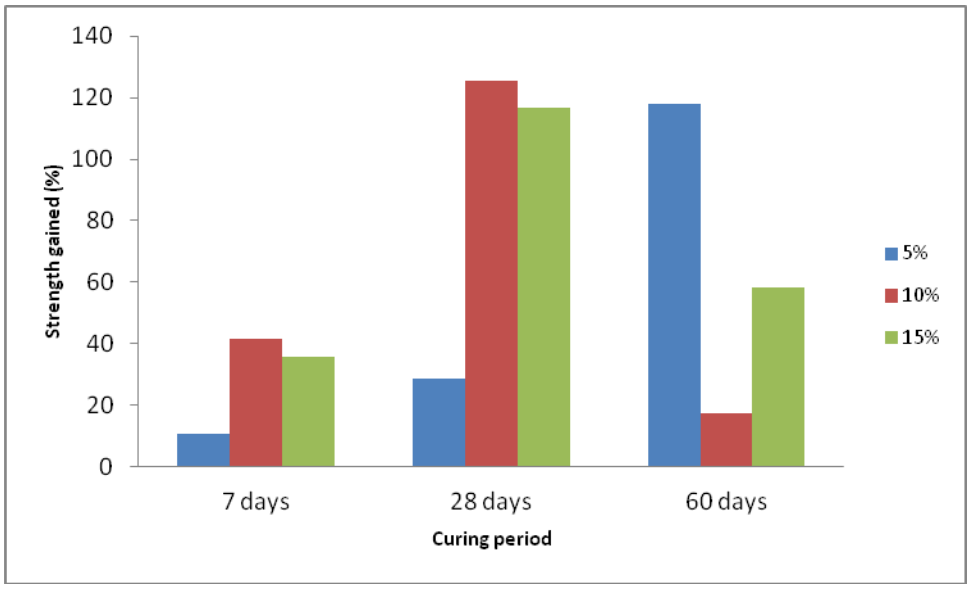

Figure 5: Strength gained at different curing period

Table 4 summarrizes the percentage of strength gained within the specified curing time at different DCM content. Based on figure 5, the maximum strength gained can be seen from 7 to 28 days and after 28 days. On the other hand, the strength starts to exhibits strength deduction as longer the curing time. It means that, in terms of curing time, demolished concrete materials require about 2 weeks to stabilise and react well with marine clay. However, different percentage of DCM potrays more strength increament. For example, at 5% DCM the strength shows consistence increment at each curing period. The results also show that the higher strength gained is at 10% of DCM within 7 to 28days of curing period. Slight strength increment is obviously gained at 15% of DCM content. 15% of DCM at 28days shows strength is then dropped from 116% to 58% at 60days. Hence, it can be considered that the DCM content works sufficiently with marine clay at 10% within 7 to 28 days curing time. After that, DCM no longer reacts with marine clay and act as a filler.

4.0 Conclusion

In this study, the effect of demolished concrete materials on marine clay has been determined. The comparison was made between treated and untreated marine clay at different percentages of DCM content and at different curing periods. Based on the obtained result and performed analysis the following deduction can be drawn:

1) Untreated marine clay resulted in considerably higher compressive strength than the corresponding untreated clay soil
2) The higher the amount of DCM content is, the higher the strength of treated marine clay is.
3) The highest increment of strength gained is at 10%.
4) Thus, the optimum DCM content sufficiently efficient to stabilise marine clay is considered at 10% DCM content after 7 to 28 curing days.

5.0 Acknowledgements

The authors gratefully acknowledged the financial support given by the Ministry of Education (MOE) under the Fundamental Research Grant Scheme (FRGS – Vot No. R.J130000.7822.4F885).

References

Abu Eusuf, M., Ibrahim, M. & Islam, R., 2012. The Construction And Demolition Wastes In Klang. *Journal of the Malaysian Institute of Planner*, X, pp.99–124.

Ajzen, I., 1991. The theory of planned behavior. *Orgnizational Behavior and Human Decision Processes*, 50, pp.179–211.

Al-bared, M.A.M., 2017. Review On The Geotechnical And Engineering Properties Of Marine Clay And The Suitable Common. *Review On The Geotechnical And Engineering.* (April), pp.5–8.

Begum, R.A. et al., 2007. Factors and values of willingness to pay for improved construction waste management - A perspective of Malaysian contractors. *Waste Management*, 27(12), pp.1902–1909.

Cong, M., Longzhu, C. & Bing, C., 2014. Analysis of strength development in soft clay

stabilized with cement-based stabilizer. *Computers and Chemical Engineering*, 71, pp.354–362. Available at: http://dx.doi.org/10.1016/j.conbuildmat.2014.08.087.

Hall, M.R., 2012. Soil stabilisation: materials, properties and techniques. , (March 2014).

Hendriks, C.F., 2016. Application of aggregates out of construction- and demolition waste in road constructions and concrete. *Civil Engineering Resource*, 6.

Husain, A. & Assas, M.M., 2013. Utilization of Demolished Concrete Waste for New Construction. *International Journal of Civil, Environmental, Structural, Construction and Architectural Engineering*, 7(1), pp.37–42.

Jain, M.A. & Chawda, M.A., 2016. Mr Archit Jain*, Mr Arpit Chawda MTech scholor, Assistant professor Department of civil engineering, RKDF SOE, Indore DOI : 10.5281/zenodo.155098. , 5(9), pp.715–719.

Kerni, V., Sonthwal, V.K. & Jan, U., 2015. Review on Stabilization of Clayey Soil Using Fines Obtained From Demolished Concrete Structures. *International Journal of Innovative Research in Science, Engineering and Technology*, 4(5), pp.296–299.

Kumar, R., Parkash, A.V. & Ash, R.H., 2015. Stability of Clay Soil Using Rice Husk Ash and Stone Dust. , 3(5).

Marto, A. et al., 2016. Stabilization Of Marine Clay Using Biomass Silica-Rubber Chips Mixture. *IOP Conference Series: Materials Science and Engineering*, 160, p.12084. Available at: http://stacks.iop.org/1757-899X/160/i=1/a=012084?key=crossref.30751df9049ff58c0c9f48fdd3f1906c.

Modarres, A. & Nosoudy, Y.M., 2015. Clay stabilization using coal waste and lime - Technical and environmental impacts. *Applied Clay Science*, 116–117, pp.281–288. Available at: http://dx.doi.org/10.1016/j.clay.2015.03.026.

Mohd Yunus, N.Z. et al., 2014. Undrained & Drained Behavior of Lime- Treated Organic Clay with Calcium. *EJGE*, 19(1596), p.17.

Nagapan, S. et al., 2013. Study of Site's Construction Waste in Batu Pahat, Johor. *Procedia Engineering*, 53, pp.99–103. Available at: http://dx.doi.org/10.1016/j.proeng.2013.02.015.

Radonjanin, V., 2010. Recycled Concrete as Aggregate for Structural Concrete Production. , pp.1204–1225.

Rana, A. et al., 2016. Recycling of dimensional stone waste in concrete : A review. , 135, pp.312–331.

Saeed, K.A.H., Kassim, K.A. & Yunus, N.Z.M., 2013. Characterization of Hydrated Lime-Stabilized Brown Kaolin Clay. , 2(11), pp.3722–3727.

Sivrikaya, O., Kiyildi, K.R. & Karaca, Z., 2014. Recycling waste from natural stone processing plants to stabilise clayey soil. *Environ Earth*, 71, pp.4397–4407. Available at: http://link.springer.com/article/10.1007/s12665-013-2833-x.

Syed Haidir, F. & Agamuthu, P., 2012. Municipal Solid Waste Management in Malaysia: Strategies in Reducing The Dependency on Landfills. *Journal of Chemical Information and Modeling*, 53, p.160.

Tamadher, T.A., Anuar, B.K. & Zamri, B.C., 2007. Stabilisation of Silty Clay Soil Using Chloride. *Journal of Engineering Science and Technology © School of Engineering, Taylor's University College*, Vol:2(No.1), pp.102–110.

Tanaka, H. et al., 2001. Characterization of Singapore, Bangkok, and Ariake clays. *Canadian Geotechnical Journal*, 38(2), pp.378–400. Available at: http://www.nrcresearchpress.com.libproxy1.nus.edu.sg/doi/abs/10.1139/t00-106#.VI-qjTGUeos.

Yee, K., 2012. Where Do Demolished Buildings Go？ *Building Research Institute,Japan*. Available at: http://www.kenken.go.jp/english/contents/topics/japan-journal/pdf/jj2011aug_30-33.pdf [Accessed March 31, 2017].

Yunus, N.Z.M., Wanatowski, D. & Stace, L.R., 2012. Effectiveness of Chloride Salts on the Behaviour of Lime-Stabilised Organic. , (0), pp.407–412.

Zhao, Y. et al., 2016. Effect of fines on the mechanical properties of composite soil stabilizer-stabilized gravel soil. *Construction and Building Materials*, 126, pp.701–710. Available at: http://linkinghub.elsevier.com/retrieve/pii/S0950061816315215.

EXPLORATION OF UNCULTURED BACTERIAL PHYLA IN BIOLOGICAL WASTEWATER TREATMENT SYSTEMS

Kyohei Kuroda[1]*, Masashi Hatamoto[2], Masayoshi Yamada[3], Masahito Yamauchi[3] & Takashi Yamaguchi[4]

[1] *Department of Chemical Science and Engineering, National Institute of Technology, Miyakonojo College, 473-1 Yoshio-cho, Miyakonojo, Miyazaki, Japan*
[2] *Top Runner Incubation Center for Academia-Industry Fusion, Nagaoka University of Technology, 1603-1 Kamitomioka, Nagaoka, Niigata, Japan*
[3] *Department of Urban Environmental Design and Engineering, National Institute of Technology, Kagoshima College, 1460-1 Shinko, Hayato-cho, Kirishima, Kagoshima, Japan*
[4] *Department of Science of Technology Innovation, Nagaoka University of Technology, 1603-1 Kamitomioka, Nagaoka, Niigata, Japan*

*Corresponding Author: *kkuroda@cc.miyakonojo-nct.ac.jp*

Abstract: *Biological wastewater treatment technology is widely applied for several wastewater types (e.g. industrial, agricultural, and municipal wastewaters) in the world. Achieving high treatment efficiency requires well-developed microbial community structures to ensure pollutant degradation. However, comprehensive understanding of biological wastewater treatment mechanisms is prevented because a wide range of uncultured microorganisms is present in the wastewater treatment systems. In this study, we performed analysis of a total of 54 aerobic, anoxic and anaerobic sludge samples collected from 17 different wastewater treatment reactors by high-resolution 16S rRNA gene sequencing (> 1 million sequence reads from 54 sludge samples) to understand the distribution patterns of uncultured phyla in different wastewater treatment systems. In doing so, we discover the ecological habitats of uncultured 10 bacterial phyla in biological wastewater treatment systems. We believe that the analyses we used in this study allowed us to evaluate not only the ecological distribution of uncultured microorganisms, but also microbial community development in biological wastewater treatment systems.*

Keywords: *biological wastewater treatment system, uncultivated microorganisms, microbial community analysis, 16S rRNA gene sequencing, phylogenetic analysis*

1.0 Introduction

Biological wastewater treatment systems are essential for the treatment of various types of wastewater. Activated sludge reactors, membrane bioreactors, and down-flow hanging sponge (DHS) reactors, all of which are types of aerobic wastewater treatment technology, are widely used and studied globally. Up-flow anaerobic sludge blanket

(UASB) reactors are also widely used; these can treat higher quantities of organic loading, have lower energy requirements compared with aerobic systems, and provide energy recovery in the form of methane gas production (Sato *et al*., 2007; Kleerebezem *et al*., 2003). Recently, the UASB reactor has been applied to the treatment of low-organic wastewater, psychrophilic wastewater, and wastewater that is toxic to microorganisms (Uemura *et al*., 2000; Lettinga *et al*., 2001; Veeresh *et al*., 2005). One disadvantage of UASBs is that a sludge-bulking phenomenon often occurs in the activated sludge and the UASB systems. The causative agent of this phenomenon might be filamentous bacterium. In particular, bacteria belonging to KSB3 and *Anaerolineae* are speculated to cause bulking, however, this mechanism remains unclear because these microbes are uncultivated (Yamada *et al*., 2007; Sekiguchi *et al*., 2001).

To elucidate this phenomenon, microbial community analysis based on 16S rRNA gene sequences, such as PCR-cloning, denaturing gradient gel electrophoresis, and terminal restriction fragment length polymorphism have been performed (Sekiguchi *et al*., 1998; Liu *et al*., 1997; Muyzer *et al*., 1993). In recent advances, researchers have developed a next-generation DNA sequencer that can perform high-throughput DNA sequences (>1 million reads per run). Researchers have used this latest technology to perform various types of microbial community analyses (Sundberg *et al*., 2013; Zhang *et al*., 2012). Additionally, these analyses have demonstrated that many kinds of uncultivated taxa are present in wastewater treatment sludge (Ye *et al*., 2011; Chouari *et al*., 2010).

As a result of recent developments in molecular biology, many microbial genomes have been analyzed, and their physiological functions have been estimated. Rinke *et al*. (2013) analyzed 201 uncultivated microorganism genomes, including those of 20 uncultured phyla, and estimated the relationships of each phylum, such as DPANN superphylum (Rinke *et al*., 2013). Previous studies have completely constructed the genome of WWE1, the group that is detected at an abundance rate >12% in mesophilic anaerobic digesters (Chouari *et al*., 2005; Pelletier *et al*., 2008). These studies have suggested that this organism may perform amino acid fermentation or propionate degradation along with hydrogen-utilizing microbes. However, a complete understanding of biological wastewater treatment mechanisms, such as the removal of organics and nutrients, is not possible because of the presence of several uncultivated and unknown microorganisms (Rinke *et al*., 2013; Dinis *et al*., 2011).

For this study, we analyzed a total of 54 aerobic, anoxic, and anaerobic sludge samples from 17 different reactors by 16S rRNA gene sequencing with the goal of understanding the distribution of uncultivated bacterial phyla in wastewater treatment systems. We then estimated environmental conditions of putative habitats based on distribution patterns. This study provides ecological information relevant to core microbial members and uncultured bacteria at the phylum level in biological wastewater treatment systems.

2.0 Materials and Methods

2.1 Sludge sample collection and DNA extraction

We collected wastewater treatment sludge samples from 17 wastewater treatment systems. We collected samples No. 1–16 from a pilot-scale UASB reactor that was treating municipal sewage at an ambient temperature (10–28°C) on different operational days (Days 91, 111, 167, 214, 255, 284, 335, 363, 379, 406, 421, 453, 537, 634, 699, and 747). The influent of the UASB reactor contained sulfate at a concentration of 40–150 mgS·L^{-1} of sulfate from day 98. The chemical oxygen demand (COD) concentration was approximately 300 mg L^{-1}. We collected samples No. 17–20 from a mesophilic digester that was treating rice husk (1000–2000 mgCOD·L^{-1}) at days 1, 34, 48, and 66. The seed sludge of this reactor was mesophilic UASB granular sludge that was treating food-industry wastewater. We obtained samples No. 21–23 from different heights of a mesophilic UASB reactor that was treating rubber-industry wastewater (approx. 13,000 mgCOD·L^{-1}). Sample No. 24 was thermophilic multi-staged-(MS-)UASB granule that was treating alcohol distillery wastewater. We collected sample No. 25 from a MS-UASB reactor that was treating molasses wastewater under thermophilic conditions (influent concentration: 17,000 mgCOD·L^{-1}), and we collected sample No. 26 from a mesophilic UASB reactor installed before No. 25 for post-treatment processing. We obtained samples No. 27–30 from a full-scale mesophilic UASB reactor that was treating alcohol-producing wastewater (300–2500 mgCOD·L^{-1}). This UASB reactor was recirculating DHS effluent for nitrogen removal before samples No. 29 and 30 were collected. We obtained samples No. 31–36 from an anaerobic/anoxic sequencing batch reactor (A_2SBR) at days 2, 33, 89, 152, 207, and 244. The influent wastewater of this reactor was from a DHS reactor that was treating sewage, in which the carbon:phosphorus ratio was maintained at 25:1 with acetate (approx. 100 mg COD·L^{-1}). We collected sample No. 37 from a sand filter that was treating the DHS effluent (sewage treatment) at an ambient temperature (10–28°C). We collected samples No. 38–45 from different up-flow sludge blanket reactors that were treating marine aquarium water for nitrogen removal. We obtained samples No. 46 and 47 from methane-oxidizing upflow fixed bed (UFB) sludge that contained nitrate and nitrite, respectively. We collected samples No. 48 and 49 from methane-oxidizing DHS sludge that contained nitrate and nitrite, respectively. Sample 50 was methane-oxidizing UFB sludge with ferric ion. We collected samples No. 51 and 52 from the top and bottom, respectively, of a DHS reactor installed after the UASB reactor (No. 21–23). We collected samples 53 and 54 from a DHS reactor that was treating mesophilic UASB effluent (No. 26). We performed DNA extraction using FastDNA Spin Kit for Soil (MP Biomedicals, Carlsbad, CA, USA), according to the manufacturer's protocol.

2.2 16S rRNA gene sequencing

We performed a PCR reaction with a universal forward primer of Univ515F (5′-GTGCCAGCMGCCGCGGTAA-3′) and a universal reverse primer of Univ806R (5′-

GGACTACHVGGGTWTCTAAT-3′) (Caporaso *et al*., 2012). The PCR reaction was performed under the following conditions: initial denaturation, 94°C for 3 min; denaturation, 94°C for 45 s; annealing, 50°C for 60 s; elongation, 72°C for 90 s; final elongation, 72°C for 10 min (Caporaso *et al*., 2012). We purified the PCR products using QIAquick PCR Purification Kit (QIAGEN, Hilden, Germany). We performed DNA sequencing using the MiSeq reagent Kit v2 (500 cycles) and MiSeq (Illumina Inc., San Diego, CA, USA).

2.3 Data Analysis

We analyzed all raw data using QIIME software package ver. 1.7.0 (Caporaso *et al*., 2010). To maintain the quality of observed 16S rRNA gene sequences, we trimmed the low quality DNA sequences (Phred quality score>30) using the fastx trimmer tool (http://hannonlab.cshl.edu/fastx_toolkit/). I used the paired-end assembler for Illumina sequences software package (PANDAseq) for assembly (Masella *et al*., 2012). We observed operational taxonomic units (OTUs) using UCLUST at 97% sequence similarity (Edgar, 2010). We identified the taxonomy of observed OTUs with the Greengenes database ver. 13_5 using blast (DeSantis *et al*., 2006; Altschul *et al*., 1990). We performed BLAST searches to confirm that observed OTUs were related species (http://blast.ncbi.nlm.nih.gov/Blast.cgi). We removed chimeric sequences using ChimeraSlayer (Haas *et al*., 2011). We constructed the phylogenetic tree based on 16S rRNA gene sequences using neighbor-joining and parsimony methods in ARB, using the Greengenes 16S rRNA gene database (Ludwig *et al*., 2004). The topology of the constructed tree was confirmed by 1000 bootstrap replicates (Felsenstein, 1985). The definitions of phylum and genus level analyses were performed according to QIIME scripts.

3.0 Results and Discussion

3.1 Distribution patterns of uncultured bacterial phyla

We performed microbial community analysis based on 16S rRNA gene sequences of 54 sludge samples from 17 wastewater treatment reactors using the next generation DNA sequencer. In this study, we observed a total of 1,041,539 sequence reads and approximately 9500–39,000 reads per sample. Based on the results of the 16S rRNA gene sequences from 54 sludge samples, we evaluated the distribution patterns of uncultured bacterial phyla. Using a bubble plot of bacterial phyla detection rates, we speculated on their habitats and functions (Figure 1). Based on the detected predominant OTUs (>1% maximum abundance rate in each sample), we constructed phylogenetic positions using 16S rRNA gene phylogenetic tree based on the Greengenes database (Figure 2).

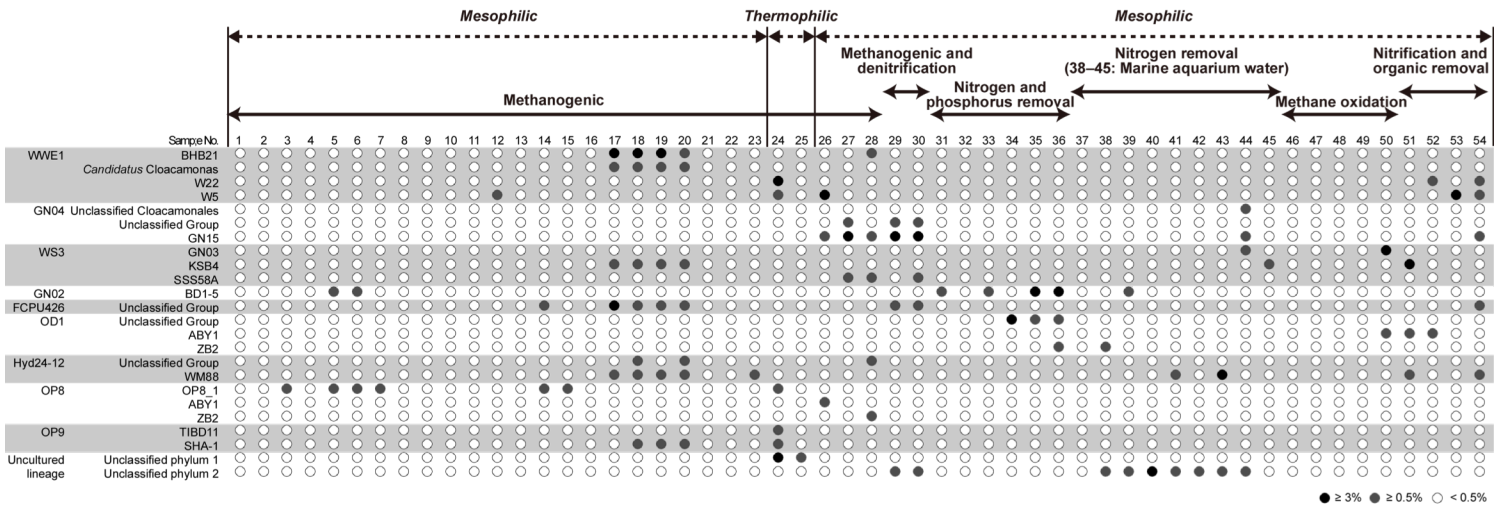

Figure 1: Detection rate of uncultured bacterial phyla from 54 wastewater treatment systems.
Black, gray, and white circles indicate ≥ 3%, ≥, 0.5%, and < 0.5% of detection rate, respectively.

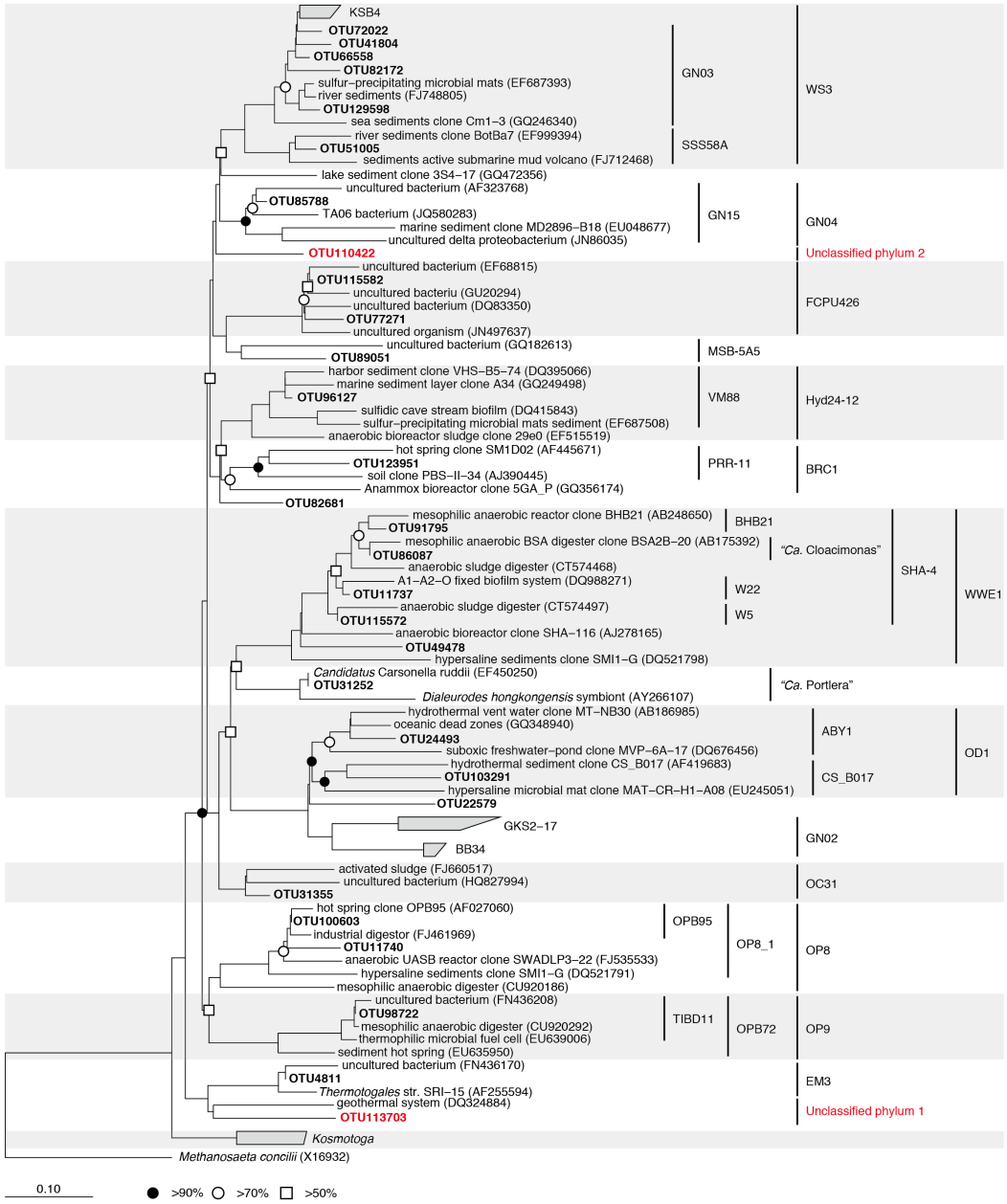

Figure 2: Phylogenetic tree representing predominant (>1% of maximum abundance rates in each environment) OTUs in 54 sludge samples using the neighbor-joining and parsimony methods based on 16S rRNA gene sequences. The solid circle, open circle, and open square indicate the bootstrap-supported probabilities at >90%, >70%, and >50%, respectively. The red highlights indicate the uncultured phylum clade in Fig. 1.

3.1.1 WWE1

The uncultured bacteria belonging to WWE1 ("*Ca*. Cloacimonetes") were detected at rates of approx. 6.5% and 8.2% in mesophilic rice husk digester sludge (No. 17–20) and mesophilic UASB sludge (No. 26), respectively (Figures 1 and 2). This phylum has been detected in anaerobic sludge, for example in anaerobic digesters (Chouari *et al*., 2005). According to the genus level analysis, "*Ca*. Cloacimonas" are only present in sample No. 18 at a rate of approximately 2.0% (Figure 1). Recent genomic analysis suggested that "*Ca*. Cloacimonas" may perform propionate degradation with hydrogenotrophic methanogens or amino acid fermentation (Pelletier *et al*., 2008). Clone cluster BHB21 was predominant in samples No. 17–20 at a rate of approximately 5.5% (Figure 1). This genus had an abundance rate of approximately 7.8% in sample No. 17 (seed sludge), while in sample No. 20, its abundance rate was approx. 2.8%. This indicates that BHB21 might favor the substrates derived from food-processing wastewater, because this seed sludge was collected from the UASB reactor that was treating this wastewater. Besides, several uncultured groups of WWE1 are present in thermophilic MS-UASB granule No. 24 (W22 group, 3.5%); mesophilic USB sludge that was treating marine aquarium water No. 44 ("*Ca*. Cloacimonales", 2.0%); mesophilic ("*Ca*. Cloacimonales", 2.0%); mesophilic DHS sludges No.52–54 and mesophilic UASB granules treating molasses wastewater No.26 (W5 group, 2.6% and 8.0%). Consequently, it is estimated with previous reports that most of uncultured group in WWE1 are present in anaerobic condition (Figure 1) (Chouari *et al*., 2005; Zhang *et al*., 2009).

3.1.2 GN04

Phylum GN04 was detected in UASB sludge samples No. 27–28 (4.0%), which were treating alcohol-producing wastewater and in sludge samples No. 29–30 (6.9%) (Figures 1 and 2), which were from the same reactor and were treating recirculated of DHS effluent. These findings indicate that the nitrogen components might be influencing the GN04 abundance rate because GN04 abundance increased following recirculation. Although GN04 was detected in high-sodium concentration environments, deep-sea methane seeps, and sediments from water storage tanks (Ley *et al*., 2006; Nunoura *et al*., 2012; Röske *et al*., 2012; Harris *et al*., 2013), no genomic analyses of GN04 have been reported to date. In high-salinity microbial mats, GN04 had a relatively high abundance (approximately 2.0%), and the maximum abundance rate was observed at a maximum depth of 49 mm in this mat (collected from a depth of 1–49 mm) (Harris *et al*., 2013). This environment has a high sulfur concentration because sulfate reduction occurs from the surface to a depth of 49 mm in the mat. These findings, along with those of previous reports, indicate that GN04 might be present under anaerobic or anoxic environments (Figure 1).

3.1.3 WS3

WS3 was widely detected in mesophilic UASB granules that were treating alcohol-producing wastewater (No. 27 and 28), denitrifying and methanogenic sludge (No. 29 and 30), mesophilic USB sludge that was treating marine aquarium water (No. 44 and 45), methane-oxidizing sludge with ferric ion (No. 50), and aerobic DHS sludge that

was treating industry wastewater (No. 51) (Figure 1). As indicated by genomic analysis, some taxa belonging to WS3 may utilize a wide range of sugar and amino acids; however, detailed information is not available (Rinke *et al*., 2013). The distribution patterns suggest that WS3 are widely present under anaerobic, anoxic, and aerobic conditions (Figure 1). Genus-level analysis of WS3 demonstrates that clone cluster group KSB4 was present in mesophilic USB sludge that was treating marine aquarium water (No. 44, 2.7%) and methane-oxidizing DHS sludge with ferric ion (No. 50, 3.2%). Additionally, the clone cluster group KSB4 was detected in mesophilic USB sludge (No. 45) and aerobic DHS sludge (No. 51) at rates of 1.7% and 3.4%, respectively (Figure 1). GN03 and KSB4 are likely aerobic or anoxic microorganisms because most of these taxa were not detected under anaerobic conditions. I also detected SSS58A group in the UASB reactor that was treating alcohol-producing wastewater (No. 27 and 28) at a rate of approximately 1.9%. Although this group was also detected in the same reactor in sludge that was treating recirculated DHS effluent, the abundance rate was lower (approximately 0.8%). These findings indicate that the SSS58A group could be anaerobes.

3.1.4 GN02 and OD1

GN02 and OD1 were detected in high abundances in A_2SBR sludge that was treating sewage (nitrogen and phosphorus removal) (Figures 1 and 2). In particular, I measured high abundance (approximately 8.6%) in samples No. 35 (operational day 207) and 36 (day 244), suggesting that these organisms are suitable for growth in a A_2SBR environment. In previous studies, researchers analyzed GN02 and OD1 genomes by single-cell genomics (Rinke *et al*., 2013; Wrighton *et al*., 2012). BD1-5 belonging to GN02 and OD1 might be strict anaerobes because they lack an electron transport chain and a tricarboxylic acid cycle (Wrighton *et al*., 2012). Additionally, OD1 may play an important role in the sulfur cycle under anaerobic conditions, as indicated by the distribution patterns of OD1 (Wrighton *et al*., 2012; Peura *et al*., 2012; Elshahed *et al*., 2005). Results of this study, along with those of previous studies, indicate that GN02 and OD1 may play a role in the removal of organics or in the sulfur cycle (Figure 1).

3.1.5 FCPU426 and Hyd24-12

FCPU426 was present in mesophilic anaerobic digester sludge that was treating rice husk (No. 17–20) at a rate of approximately 4.2% (Figure 1). However, the detection rate of FCPU426 decreased from >10% to 2.3% during operation. This indicates that FCPU426 favors substrates present in food-industry wastewater (Figure 1). Although FCPU426 has been highly detected in peat layers of northern wetlands (Serkebaeva *et al*., 2013), its metabolic functions remain unclear.

Hyd24-12 was present in high abundance in nitrogen removal sludge and aerobic DHS sludge (Figure 1). In particular, USB sludge that was treating marine aquarium water (No. 43) had a high abundance rate (approximately 4.0%, Figure 1). To date, Hyd24-12 has been observed in high-sodium environments, such as microbial mats and marine

sponges (Harris *et al*., 2013; Simister *et al*., 2012), indicating that Hyd24-12 can be optimally grown at high sodium concentrations.

3.1.6 OP8 and OP9

OP8 and OP9 were detected in high abundances in methanogenic sludge samples (Figure 1). In particular, abundance rates of these organisms were high (OP8, 2.2%; OP9, 3.4%) in thermophilic methanogenic sludge that was treating alcohol-distillery wastewater (No. 24). The distribution patterns of OP8 are consistent with those of a previous study, in which OP8 was detected in high-organic-loading wastewater treatment methanogenic sludge (Sekiguchi *et al*., 2006). The results of genome analyses of OP8 (OP8_1 group) and OP9 indicate that these microbes may be able to utilize wide ranges of amino acids and sugar (Rinke *et al*., 2013; Dodsworth *et al*., 2013). However, detailed information, such as the roles they play in the environment remains unknown.

3.1.7 Unknown lineage

Results of phylogenetic analysis using Greengenes ver. 13_5 indicated that there were two types of unknown lineages: unclassified phylum1 and unclassified phylum2, identified in thermophilic MS-UASB sludge (No. 24, 7.1%) and mesophilic USB sludge that was treating marine aquarium water (No. 40, 3.9%), respectively (Figures 1 and 2). Results of a blast search of the nr database demonstrated that the closest taxonomy of unclassified phylum1 was *Dictyoglomus turgidum* DSM6724 (NR_043385) in phylum *Dictyoglomus* (84%, 215/257 bp). *Dictyoglomus turgidum* is known to be a thermophilic, strictly anaerobic, and chemo-organotrophic organism (Saiki *et al*., 1985). Results of this study suggested that this unclassified phylum1 might play a role similar to that of the genus *Dictyoglomus*, given that this unknown taxonomy was observed in a thermophilic methanogenic sludge sample (Figure 1).

Unclassified phylum2 was observed in mesophilic USB sludge samples that were treating marine aquarium water (No. 39, 1.6%; No. 40, 3.9%; No. 44, 1.5%,) (Figures 1 and 2). This unknown taxonomy was most closely related to *Caldicoprobacter guelmensis* D2C22 (NR_109614) (87%, 220/254 bp), which is a hyperthermophilic, anaerobic, and xylanolytic organism (Yokoyama *et al*., 2010; Bouanane-Darenfed *et al*., 2011). This uncultured phylum2 is completely unknown because environments in this study would not support organisms with a certain type of physiology.

4.0 Conclusions

In this study, to investigate the putative habitats of predominant uncultured bacterial phyla in biological wastewater treatment systems, we performed high-resolution 16S rRNA gene sequencing of aerobic, anoxic, and anaerobic wastewater treatment sludges. We detected several candidate phyla, including WWE1, GN04, WS3, GN02, FCPU426, OD1, Hyd24-12, OP8, OP9, and unclassified phylotypes at the phylum level in the sludge sample. Additionally, we were able to estimate the putative habitats and

environmental conditions of these uncultured phyla by examining the distribution patterns in each wastewater treatment sludge sample. Although the roles of many of the uncultured microoganisms and the mechanisms responsible for sludge development in anaerobic bioreactors are still unknown, the results of this study can be applied in the evaluation and design of wastewater treatment systems. We believe that these results also contribute to elucidating the "*black box*" in anaerobic wastewater treatment systems.

5.0 Acknowledgements

This research was supported in part by the Japan Society for the Promotion of Science (JSPS). The authors thank Aqua and Soil Environmental laboratory in Nagaoka University of Technology for supporting the experiment and stimulating discussion.

References

Altschul, S.F., Gish, W., Miller, W., Myers, E.W. and Lipman, D.J. : Basic local alignment search tool, *J. Mol. Biol*., Vol. 215, No. 3, pp. 403–410, 1990.

Bouanane-Darenfed, A., Fardeau, M.L., Grégoire, P., Joseph, M., Kebbouche-Gana, S., Benayad, T., Hacene, H., Cayol, J.L. and Olliver, B. : *Caldicoprobacter algeriensis* sp. nov. a new thermophilic anaerobic, xylanolytic bacterium isolated from an Algerian hot spring, *Curr. Microbiol*., Vol. 62, No. 3, pp. 826–832, 2011.

Caporaso, J.G., Lauber, C.L., Walters, W.A., Lyons, D.B., Huntley, J., Fierer, N., Owens, S.M., Betley, J., Fraser, L., Bauer, M., Gormley, N., Gilbert, J.A., Smith, G. and Knight, R. : Ultra-high-throughput microbial community analysis on the Illumina HiSeq and MiSeq platforms, *ISME J*., Vol. 6, No. 8, pp. 1621–1624, 2012.

Caporaso, J.G., Kuczynski, J., Stombaugh, J., Bittinger, K., Bushman, F.D., Costello, E.K., Fierer, N., Pe, A.G., Goodrich, J.K., Gordon, J.I., Huttley, G.A., Kelley, S.T., Knights, D., Koenig, J.E., Ley, R.E., Lozupone, C.A., McDonald, D., Muegge, B.D., Pirrung, M., Reeder, J., Sevinsky, J.R., Turnbaugh, P.J., Walters, W.A., Widmann, J., Yatsuneko, T., Zaneveld, J. and Knight, R. : QIIME allows analysis of high-throughput community sequencing data, *Nat. Methods*, Vol. 7, No. 5, pp. 335–336, 2010.

Chouari, R., Paslier, D.L., Daegelen, P., Dauga, C., Weissenbach, J. and Sghir, A. : Molecular analyses of the microbial community composition of an anoxic basin of a municipal wastewater treatment plant reveal a novel lineage of *Proteobacteria*, *Microb. Ecol*., Vol. 60, No. 2, pp. 272–281, 2010.

Chouari, R., Paslier, D.L., Dauga, C., Daegelen, P., Weissenbach, J. and Sghir, A. : Novel major bacterial candidate division within a municipal anaerobic sludge digester, *Appl. Environ. Microbiol*., Vol. 71, No. 4, pp. 2145–2153, 2005.

DeSantis, T.Z., Hugenholtz, P., Larsen, N., Rojas, M., Brodie, E.L., Keller, K., Huber, T., Dalevi, D., Hu, P. and Andersen, G.L. : Greengenes, a chimera-checked 16S rRNA gene database and workbench compatible with ARB, *Appl. Environ. Microbiol*., Vol. 72, No. 7, pp. 5069–5072, 2006.

Dinis, J.M., Barton, D.E., Ghadiri, J., Surendar, D., Reddy, K., Velasquez, F., Chaffee, C.L., Lee, M.C.W., Gavirilova, H., Ozuna, H., Smits, S.A. and Ouverney, C.C. : In search of an

uncultured human-associated TM7 bacterium in the environment, *PLoS One*, Vol. 6, No. 6, pp. 1–8, 2011.

Dodsworth, J.A., Blainey, P.C., Murugapiran, S.K., Swingley, W.D., Ross, C.A., Tringe, S.G., Chain, P.S., Scholz, M.B., Lo, C.C., Raymond, J., Quake, S.R. and Hedlund, B.P. : Single-cell and metagenomic analyses indicate a fermentative and saccharolytic lifestyle for members of the OP9 lineage, *Nat. Commun.*, Vol. 4, No. 1854, doi:10.1038/ncomms2884, 2013.

Edgar, R.C. : Search and clustering orders of magnitude faster than BLAST, *Bioinformatics*, Vol. 26, No. 19, pp. 2460–2461, 2010.

Elshahed, M.S., Najar, F.Z., Aycock, M., Qu, C., Roe, B.A. and Krumholz, L.R. : Metagenomic analysis of the microbial community at Zodletone spring (Oklahoma): Insights into the genome of a member of the novel candidate division OD1, *Appl. Environ. Microbiol.*, Vol. 71, No. 11, pp. 7598–7602, 2005.

Felsenstein, J. (1985) Confidence-limits on phylogenies - an approach using the bootstrap. *Evolution* **39**: 783-791.

Haas, B.J., Gevers, D., Earl, A.M., Feldgarden, M., Ward, D.V., Giannoukos, G., Ciulla, D., Tabbaa, D., Highlander, S.K., Sodergren, E., Methé, B., DeSantis, T.Z., Consortium, T.H.M., Petrosino, J.F., Knight, R. and Birren, B.W. : Chimeric 16S rRNA sequence formation and detection in Sanger and 454-pyrosequenced PCR amplicons, *Genome Res.*, Vol. 21, No. 3, pp. 494–504, 2011.

Harris, J.K., Caporaso, J.G., Walker, J.J., Spear, J.R., Gold, N.J., Robertson, C.E., Hugenholtz, P., Goodrich, J., McDonald, D., Knights, D., Marshall, P., Tufo, H., Knight, R. and Pace, N.R. : Phylogenetic stratigraphy in the Guerrero Negro hypersaline microbial mat, *ISME J.*, Vol. 7, No. 1, pp. 50–60, 2013.

Kleerebezem, R. and Macarie, H. : Treating industrial wastewater: anaerobic digestion comes of age, *J. Chem. Eng.*, Vol. 110, No. 4, pp. 56–64, 2003.

Lettinga, G., Rebac, S. and Zeeman, G. : Challenge of psychrophilic anaerobic wastewater treatment, *Trends Biotechnol.*, Vol. 19, No. 9, pp. 363–370, 2001.

Ley, R.E., Harris, J.K., Wilcox, J., Spear, J.R., Miller, S.R., Bebout, B.M., Maresce, J.A., Bryant, D.A., Sogin, M.L. and Pace, N.R. : Unexpected diversity and complexity of the Guerrero Negro hypersaline microbial mat, *Appl. Environ. Microbiol.*, Vol. 72, No. 5, pp. 3685–3695, 2006.

Liu, W.T., Marsh, T.L., Cheng, H. and Forney, L.J. : Characterization of microbial diversity by determining terminal restriction fragment length polymorphisms of genes encoding 16S rRNA, *Appl. Environ. Microbiol.*, Vol. 63, No. 11, pp. 4516–4522, 1997.

Lozupone, C. and Knight, R. : UniFrac : a new phylogenetic method for comparing microbial communities, *Appl. Environ. Microbiol.*, Vol. 71, No. 12, pp. 8228–8235, 2005.

Ludwig, W., Strunk, O., Westram, R., Richter, L., Meier, H., Yadhukumar *et al.* (2004) ARB: a software environment for sequence data. *Nucleic Acids Res* **32**: 1363-1371.

Masella, A.P., Bartram, A.K., Truskowski, J.M., Brown, D.G. and Neufeld, J.D. : PANDAseq: paired-end assembler for illumina sequences, *BMC bioinfo.*, Vol .13, No. 31, pp. 1–7, 2012.

Mori, K., Yamaguchi, K., Sakiyama, Y., Urabe, T., Suzuki, K. *Caldisericum exile* gen. nov., sp. nov., an anaerobic, thermophilic, filamentous bacterium of a novel bacterial phylum, *Caldiserica* phyl. nov., originally called the candidate phylum OP5, and description of *Caldisericaceae* fam. nov., *Caldisericales* ord. nov. and *Caldisericia* classis nov., *Int J Syst Evol Microbiol*, 59(Pt 11):2894-8, 2009.

Muyzer, G., de Waal, E.C. and Uitterlinden, A.G. : Profiling of complex microbial populations by denaturing gradient gel electrophoresis analysis of polymerase chain reaction-amplified genes coding for 16S rRNA, *Appl. Environ. Microbiol.*, Vol. 59, No. 3, pp. 695–700, 1993.

Nunoura, T., Takai, Y., Kazama, H., Hirai, M., Ashi, J., Imachi, H. and Takai, K. : Microbial diversity in deep-sea methane seep sediments presented by SSU rRNA gene tag sequencing, *Microbes Environ*., Vol. 27, No. 4, pp. 382–390, 2012.

Pelletier, E., Kreimeyer, A., Bocs, S., Rouy, Z., Gyapay, G., Chouari, R., Rivière, D., Ganesan, A., Daegelen, P., Sghir, A., Cohen, G.N., Médigue, C., Weissenbach, J. and Paslier, D.L. : "*Candidatus* Cloacamonas acidaminovorans": Genome sequence reconstruction provides a first glimpse of a new bacterial division, *J. Bacteriol*., Vol. 190, No. 7, pp. 2572–2579, 2008.

Peura, S., Eiler, A., Bertilsson, S., Nykänen, H., Tiirola, M. and Jones, R.I. : Distinct and diverse anaerobic bacterial communities in boreal lakes dominated by candidate division OD1, *ISME J*., Vol. 6, No. 9, pp. 1640–1652, 2012.

Rinke, C., Schwientek, P., Sczyrba, A., Ivanova, N.N., Anderson, I.J., Cheng, J.F., Darling, A., Malfatti, S., Swan, B.K., Gies, E.A., Dodsworth, J.A., Hedlund, B.P., Tsiamis, G., Sievert, S.M., Liu, W.T., Eisen, J.A., Hallam, S.J., Kyrpides, N.C., Stepanauskas, R., Rubin, E.M., Hugenholtz, P. and Woyke, T. : Insights into the phylogeny and coding potential of microbial dark matter, *Nature*, Vol. 499, No. 7459, pp. 431–437, 2013.

Röske, K., Sachse, R., Scheerer, C. and Röske, I. : Microbial diversity and composition of the sediment in the drinking water reservoir Saidenbach (Saxonia, Germany), *Syst. Appl. Microbiol*., Vol. 35, No. 1, pp. 35–44, 2012.

Saiki, T., Kobayashi, Y., Kawagoe, K. and Beppu, T. : *Dictyoglomus thermophilum* gen. nov., sp. nov., a chemoorganotrophic, anaerobic, thermophilic bacterium, *Int. J. Syst. Bacteriol*., Vol. 35, No. 3, pp. 253–259, 1985.

Sato, N., Okubo, T., Onodera, T., Lalit, K.A., Ohashi, A. and Harada H. : Economic evaluation of sewage treatment processes in India, *J. Environ. Manage*., Vol. 84, No. 4, pp. 447–460, 2007.

Sekiguchi, Y., Kamagata, Y., Syutsubo, K., Ohashi, A., Harada, H. and Nakamura, K. : Phylogenetic diversity of mesophilic and thermophilic granular sludges determined by 16S rRNA gene analysis, *Microbiology*, Vol. 144, Pt. 9, pp. 2655–2665, 1998.

Sekiguchi, Y., Takahashi, H., Kamagata, Y., Ohashi, A., Harada, H. In situ detection, isolation, and physiological properties of a thin filamentous microorganism abundant in methanogenic granular sludges: a novel isolate affiliated with a clone cluster, the green non-sulfur bacteria, subdivision I, *Appl Environ Microbiol*, 67(12):5740-9, 2001.

Sekiguchi, Y. : Yet-to-be cultured microorganisms relevant to methane fermentation processes, *Microbes Environ*., Vol. 21, No. 1, pp. 1–15, 2006.

Serkebaeva, Y.M., Kim, Y., Liesack, W. and Dedysh, S.N. : Pyrosequencing-based assessment of the bacteria diversity in surface and subsurface peat layers of a northern wetland, with focus on poorly studied phyla and candidate divisions, *PLoS One*, Vol. 8, No. 5, pp. 1–14, 2013.

Simister, R.L., Deines, P., Botté, E.S., Webster, N.S. and Taylor, M.W. : Sponge-specific clusters revisited: a comprehensive phylogeny of sponge-associated microorganisms, *Environ. Microbiol*., Vol. 14, No. 2, pp. 517–524, 2012.

Sundberg, C., Al-Soud, W.A., Larsson, M., Alm, E., Yekta, S.S., Svensson, B.H., Sørensen, S.J. and Karlsson, A. : 454-pyrosequencing analyses of bacterial and archaeal richness in 21 full-scale biogas digesters, *FEMS Microbiol. Ecol*., Vol. 85, No. 3, pp. 612–626, 2013.

Uemura, S. and Harada, H. : Treatment of sewage by a UASB reactor under moderate to low temperature conditions, *Bioresour. Technol*., Vol. 72, No. 3, pp. 275–282, 2000.

Veeresh, G.S., Kumar, P. and Mehrota, I. : Treatment of phenol and cresols in upflow anaerobic sludge blanket (UASB) process: a review, *Water Res*., Vol. 39, No. 1, pp. 154–170, 2005.

Wrighton, K.C., Thomas, B.C., Sharon, I., Miller, C.S., Castelle, C., VerBerkmoes, N.C., Wilkins, M.J., Hettich, R.L., Lipton, M.S., Williams, K.H., Long, P.E. and Banfied, J.F. :

Fermentation, hydrogen, and sulfur metabolism in multiple uncultivated bacterial phyla, *Science*, Vol. 337, No. 6102, pp. 1661–1665, 2012.

Yamada, T., Yamauchi, T., Shiraishi, K., Hugenholz, P., Ohashi, A., Harada, H., Kamagata, K., Nakamura, K. and Sekiguchi, Y. : Characterization of filamentous bacteria, belonging to candidate phylum KSB3, that are associated with bulking in methanogenic granular sludges, *ISME J*., Vol. 1, No. 3, pp. 246–255, 2007.

Ye, L., Shao, M.F., Zhang, T., Tong, A.H.Y. and Lok, S. : Analysis of the bacterial community in a laboratory-scale nitrification reactor and a wastewater treatment plant by 454-pyrosequencing, *Water Res*., Vol. 45, No. 15, pp. 4390–4398, 2011.

Yokoyama, H., Wagner, I.D. and Wiegel, J. : *Caldicoprobacter oshimai* gen. nov., sp. nov., an anaerobic, xylanolytic, extremely thermophilic bacterium isolated from sheep faeces, and proposal of *Caldicoprobacteraceae* fam. nov., *Int*. *J*. *Syst*. *Evol*. *Microbiol*., Vol. 60, Pt. 1, pp. 67–71, 2010.

Zhang, H., Banaszak, J.E., Parameswaran, P., Alder, J., Krajmalnik-Brown, R. and Rittmann, B.E. : Focused-Pulsed sludge pre-treatment increases the bacterial diversity and relative abundance of acetoclastic methanogens in a full-scale anaerobic digester, *Water Res*., Vol. 43, No. 18, pp. 4517–4526, 2009.

Zhang, T., Shao, M.F. and Ye, L. : 454 pyrosequencing reveals bacterial diversity of activated sludge from 14 sewage treatment plants, *ISME J*., Vol. 6, No. 6, pp. 1137–1147, 2012.

CARBONIZED GREEN MUSSEL SHELL FOR LEAD REMOVAL

Nur Afifah A.Rahman, Shamila Azman & Mohd Ismid Mohd Said

Department of Environmental Engineering, Faculty of Civil Engineering, Universiti Teknologi Malaysia, 81310 Skudai, Johor Bahru, Malaysia

*Corresponding Author: *shamila@utm.my*

Abstract: Large amount of mollusc shell are usually disposed off and can create nuisance due to odor and its quantity. Therefore this study aims to explore the adsorption capacity of green mussel (*Perna viridis*) shell for lead removal in aqueous solutions.. The adsorbent was prepared from powdered green mussel shell carbonized at 600°C. The carbonization process was conducted for four hours and allowed to cool at room temperature. Characterization of pH, bulk density, moisture content and ash content was also conducted. The effect of various operational parameters such as concentration, pH, temperature and sorption time on the adsorption of heavy metals were investigated using batch process experiments. It is proven that green mussel shell can be used as a low cost adsorbent for the removal of heavy metals in aqueous solution. This shows that the adsorption of lead on the adsorbent involves chemisorption. Kinetic treatment of the results gave a pseudo-second order type of mechanism while the adsorption characteristics of the adsorbent followed the Freundlich adsorption isotherm. The results obtained proved that green mussel shells can be an alternative source of adsorbent materials.

Keywords: *Carbonization, green mussel shell, lead removal*

1.0 Introduction

Large tonnes of mussel shell are disposed illegally and dumped into public waters and reclaimed lands annually. The shell wastes are generated from fisheries industry. Only very small proportions of the shells are recycled as additives in animal husbandry, poultry farming, soil fertilizers and coating materials and fish fodders. Enormous amounts of these materials are dumped and become environmental burden (Vukovic *et al*., 2010 ; Du *et al*., 2011 and Alidoust *et al*., 2015). Therefore, alternative approaches for recycling waste mussel shells are needed. The ideal solution would be to convert the waste mussel shells to a product that is both beneficial and economically viable.

It is well known that various types of mollucs's shell have been used as natural adsorbent for nutrient and heavy metal (Odoemelam and Eddy, 2009; Du *et al*, 2012; Peña-Rodríguez *et al*., 2013; Yoshimura and Shiomi, 2014; Seco-Reigosa et al., 2014; Hossain *et al*, 2015 and Alidoust *et al*., 2015). It contains a large amount of organic compounds and macromolecules, that can form framework for other macromolecular components, strongly implying that it have a potential to be used as adsorbent. It consist of more than 95% of $CaCO_3$ with small amount of SiO_2, protein and polysaccharide (Liu *et al*., 2009 ;Du *et al*., 2012 and Lu *et al*., 2015). Shells are made up of three layers, i.e. hypostracum (the innermost layer), followed by ostracum (the basic shell building layer) and periostracum (the outermost layer) (Oladoja et al., 2013). All the layers have different microstructures. The strength and toughness of the shell are determined by the thickness of the individual layers and their microstructure. The periostracum is made of sclerotized proteins. These outermost shell layer, is not made of calcium carbonate, but of an organic material called conchin, a mixture of organic compounds, mostly of proteids. Conchin does not only make the outer shell layer, but is also embedded between the calcium carbonate crystals of deeper layers. The

prismatic layer, hypostracum is a form of aragonite, a type of calcium carbonate. It is composed of calcite prisms surrounded by a conchiolin matrix, with the prisms oriented at an angle to the surface. A possible solution would be to convert the waste shells into calcium-based alkaline adsorbent products. Depending on metal ion and concentration, the rate and degree of metal sequestration can vary greatly between shells of different species. This attribute may enable specific mollusk and certain highly mineralized crustacean shell materials to be used singly or in combination to selectively remove one or several different types of metal ions at different rates.

Heavy metals are an inherent component of the environment that can be a potential hazard to human beings and animals. It is one of the vital factors for decline in water quality that has an obvious impact on seafood diversity. In aquatic environment, minute quantities of some metals, such as copper, zinc, iron, manganese and nickel are essential for biological systems to function but their excessive concentration can be toxic to living organisms. Other metals such as cadmium, mercury, arsenic and lead are non-essential and therefore have toxic effects on living organisms (Heath, 1995 and Sany et al., 2013). The objective of this study to produce adsorbent from green mussel shell waste for lead removal.

2.0 Materials and Methods

2.1 Sample Collection And Preparation

Green mussel (*Perna virids*) shell waste were collected from Teluk Jawa, Johor, Malaysia. The shells were sorted to commercial size (60-80 mm), cleaned from mud and barnacles, washed thoroughly with tap water and rinsed with deionized water and oven dried at 105°C for 24 hours. Then, the shells were grinded using Wellmax grinder.

2.2 Carbonization

Carbonization of the shell was conducted using muffle furnace (Carbolite Sheffield England LMF 4) which allow limited supply of air. Carbonization was done at 600°C for four hours and allowed to cool at room temperature for 24 hours then kept in a sample container for future use.

2.3 Aqueous Lead Solution

Lead solution used for this study were analytical grade reagent from Merk, Germany (1000 mg/L). Working solutions of 10 mg/L were prepared from aliquots diluted to the appropriate concentration. The total concentration of lead in the aqueous solution was confirmed using Atomic Adsorption Spectrophotometer (AAS) from Perkin Elmer PinAAcle 900T.

2.3 Batch Adsorption Studies

Adsorption studies of lead on green mussel shell-derived adsorbent were carried out in batch mode. Adsorption experiments to study the effect of initial concentration were carried out by contacting 0.1 g of adsorbent with 30 mL of Pb solution (10 mg/L) at constant temperature (30^{o}C) in 250 mL Erlenmeyer flasks. The effect of initial concentration was then evaluated on various adsorbent for comparison. Removal percentage and adsorption capacity of lead by the mussel shell was calculated using equation 1 and 2.

% R = $(C_o - C_e)/ C_o$* 100 (1)

where C_o = Initial concentration (mg/L) and C_e= Final concentration(mg/L)

$$q_e = \frac{C_o - C_e \times V}{m} \quad (2)$$

q_e is the equilibrium adsorption capacity (mg/g), C_o and C_e are the initial and equilibrium concentrations of the heavy metal solution (mg/L), respectively, V is the volume of the heavy metal solution (mL/L), and m is the mass of the adsorbent (mg/g).

2.4 Charaterization of Adsorbent

The surface morphology of the raw and carbonized shells were analyzed using scanning electron microscope (Model JEOL JSM-6390LA). The Fourier transform infrared (FTIR) spectroscopy analysis was conducted using FTIR spectrophotometer (Model Shimadzu IRAffinity-1) in the range of 400-4000 cm^{-1} wavelength with 4 cm^{-1} resolution. FTIR characterization was used to determine the functional groups present on the surface of the samples.

2.5 Variation of dosage

Removal efficiency with respect to different adsorbent dosage experiments were performed by varying adsorbent at 10 mg, 30 mg, 50 mg, 100 mg and 200 mg in 30 mL of Pb solution (10 mg/L) at ambient temperature. For these experiment, the Erlenmeyer flask were agitated at 120 rpm using orbital shaker (PSU-10i, Grant Bio) for 4 hours to attain equilibrium with other variables kept constant.

2.6 Variation of agitation

Removal efficiency with respect to different agitation rates were performed at 90 rpm, 120 rpm and 150 rpm at 30 mL with Pb solution (10 mg/L) with 0.1 g adsorbent at ambient temperature. The experiment was conducted for 4 hours to attain equilibrium with other variables kept constant.

2.7 Variation of contact time

The effect of contact time on the removal of lead was determined by measuring the adsorbate (Pb) at 2, 4, 8, 16 and 24 hours and other variables were kept constant. The equilibrium was also determined.

2.8 Variation of initial metal ion concentration

In order to determine the removal efficiency with respect to adsorbate (lead) concentration, experiments were perfomed by varying adsorbate concentration of 0.5 mg/L, 2 mg/L, 6 mg/L, 8 mg/L and 10 mg/L at 8 hours with other variables kept constant.

2.9 Variation of pH value

To study the effect of pH on adsorbate (lead) removal, the solution was agitated at room temperature using orbital shaker at different pH at 3, 5, 7, 9 and 11 at 4 hours with other variables kept constant. 0.1 M HCl and 0.1 M NaOH solution was used for pH adjustment.

3.0 Results and Discussion

3.1 Characterisation of Adsorbent

FESEM micrographs and FTIR of the raw green mussel and carbonized green mussel adsorbent at 600°C are shown in Figures 1(a) and (b), respectively. From Figure 1(a), the FESEM micrograph shows presence of flaky sheet phase layer structure, rough and disordered surface with low porosity structure and rudimentary pores. Carbonization at 600°C resulted in presence of wide pores, relatively smooth with spherical particles of porous structure confirming occurrence of thermal decomposition. This activation process is dependent on the raw material which is composed mainly of calcium carbonate.

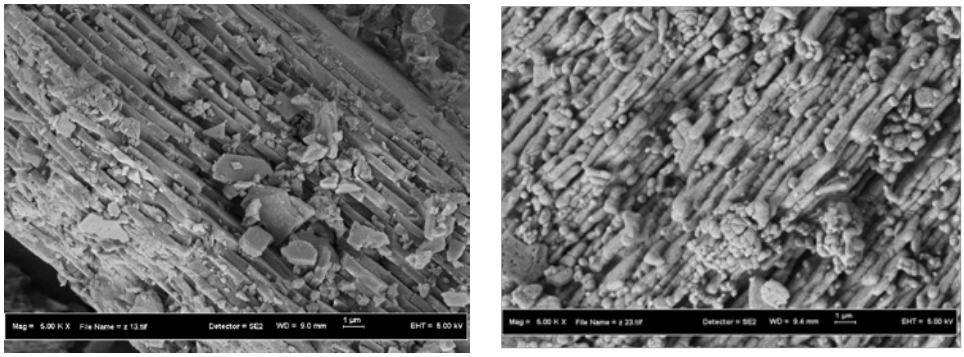

(a) (b)

Figure 1: FESEM micrographs of (a) Rraw green mussel shell, (b) Carbonized at 600°C

FTIR spectrums obtained for raw, carbonized adsorbent and adsorbent with lead have similar pattern. This indicated that green mussel adsorbed lead without changing its surface chemistry (Tan *et al*., 2013). The main functional groups responsible for adsorption process were the hydroxyls, carbonyls, carboxylic and amides (Durve & Chandra, 2014). Clear shifts were observed at wavenumber of 3452.00 cm^{-1} (raw adsorbent) to 3453.49 cm^{-1} (lead loaded), which indicated the surface -OH group was one of the functional group responsible for adsorption. The peak in the frequency range of 1000-1200 cm^{-1} is related to the C=O stretch (COOH) in amides, alcohol, carboxylic acids and esters. The peak at 1796.41 cm^{-1} in adsorbent and 1796.15 (adsorbent with lead) may be due to the graphite structure (C=C) of carbonized green mussel shell. The intensities of the C–O bands of $CaCO_3$ between 1500 and 500cm^{-1} were the strongest. C–O stretching vibration at 1440 to 1450cm^{-1}. The peaks at 1425.17 cm^{-1} and 1426.78 to 1428.11 cm^{-1} indicate the involvement of the H-C-H asymmetric and symmetric stretches and C-H alkanes stretch. These peaks are attributed to asymmetric stretch; out-of-plane bend and in-plane bend vibration modes for CO_3. The out-of-plane C–O bending vibrations at 710.45 cm^{-1} for carbonized adsorbent and 708.58 cm^{-1} for adsorbent with lead. At 470.48 cm^{-1} for adsorbent without heavy metal the band was assigned to Si-O stretching. Only raw adsorbent shift of these band indicated presence of Si-OH group. Naiya *et, al*. (2011) reported major shift of these band also indicated that Si-OH group is responsible for adsorption.

3.2 Variation of dosage

Higher dosage of green mussel shell show lead removal efficiency increased from 51% to 97% (refer Figure 2). The increase in adsorbent amount provides more chance for lead ions to adhere to the adsorbent surface due to increase in number of available adsorption sites and surface area. Pb has increase adsorption capacity from 1.5 to 2.9 mg/g. At dosage above 100 mg, the removal percentage of heavy metal is marginal. Experimental results, with regard to 30 mL of aqueous heavy metal solution, initial heavy metal concentration of 10 mg/L, adsorbent dosage of 100 mg and agitating speed of 120 rpm for 4 hours, produced optimal removal percentage of Pb which shows good effective adsorption capacity and adsorption percentage.

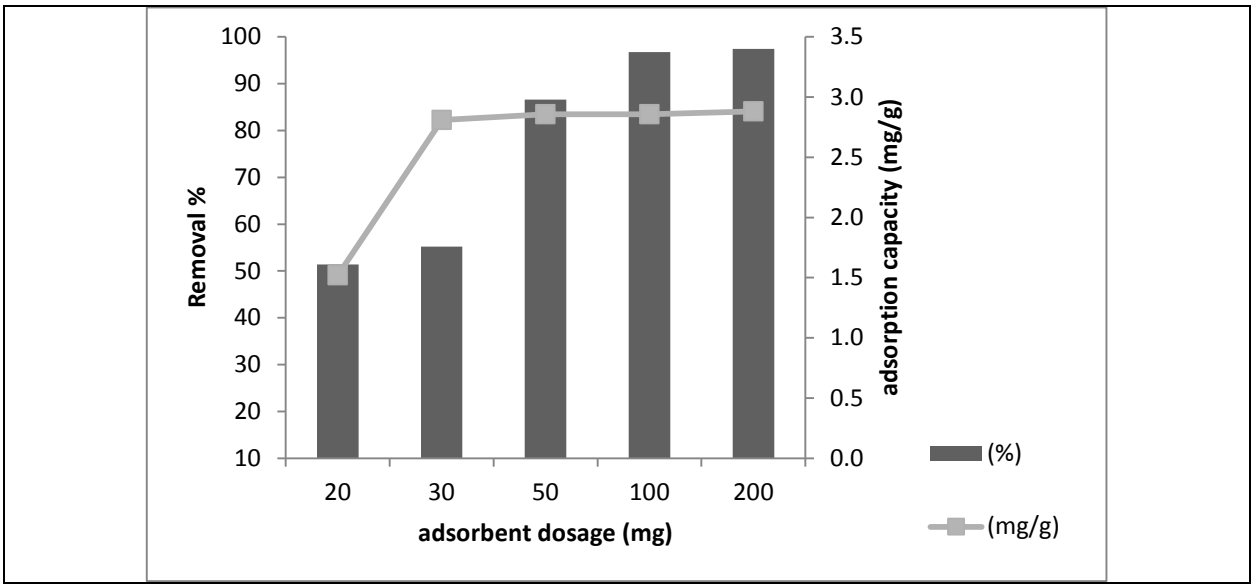

Figure 2 : Effect of adsorbent dosage on lead adsorption

3.3 Variation of agitation

Equilibrium time at suitable agitation speed is another important operational parameter for an economical wastewater treatment process. Figure 3, show that increase in agitation speed will increase removal efficiency until equilibrium adsorption was established. Agitation speed was kept at 90, 120 and 200 rpm at 4 hours respectively. Adsorption percentage for Pb was effective at 97 to 99% but the adsorption capacity was static at 2.8 mg/g. This study shows that equilibrium adsorptions were established within 120 rpm.

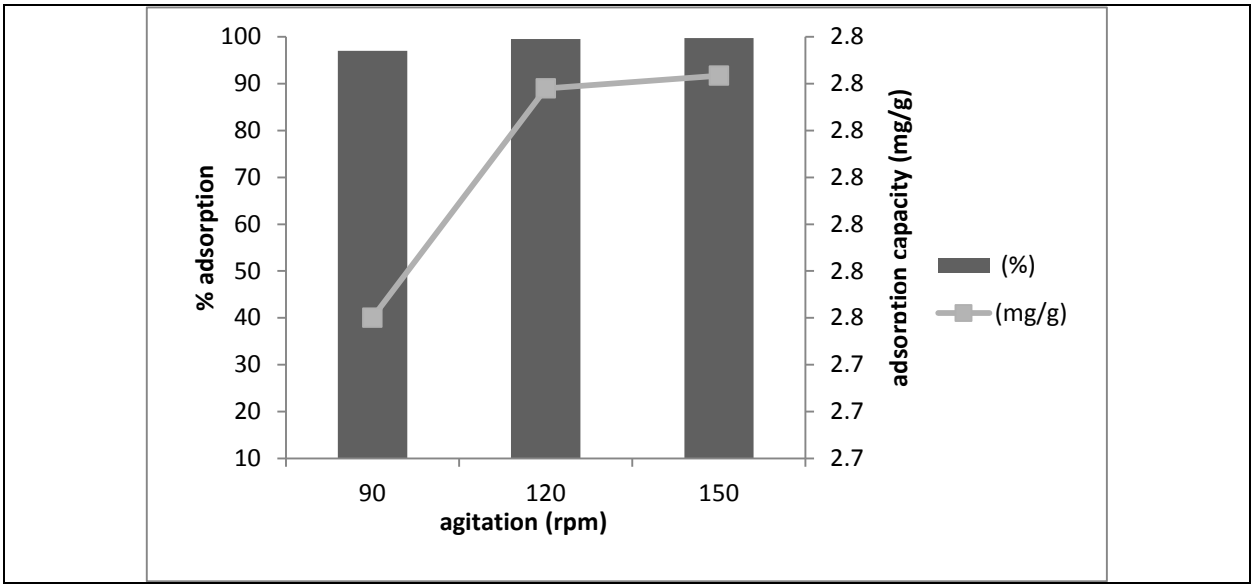

Figure 3 : Agitation at different speed

3.4 Variation of contact time

As shown in Figure 4, lead removal efficiency increased from 76% to 96 % with time. Larger amounts of lead ions were adsorbed by green mussel shell as the agitating time increases. This study shows Pb adsorption using green mussel was effective. It was observed that the removal percentage increased rapidly at the initial stages because more unsaturated surface and active sites were available on the adsorbent surface area. Usually, the metal ions create a monolayer on the adsorbent surface (Abbaszadeh et. al, 2016). Eventually the adsorbent surface area becomes gradually exhausted, and the sorption capacity decreased. Based on the results, lead uptake by green mussel shell was obtained after 8 hours, and the uptake trend increased and then become steady after 8 hours with Pb adsorption capacity 2.7 mg/g at equilibrium.

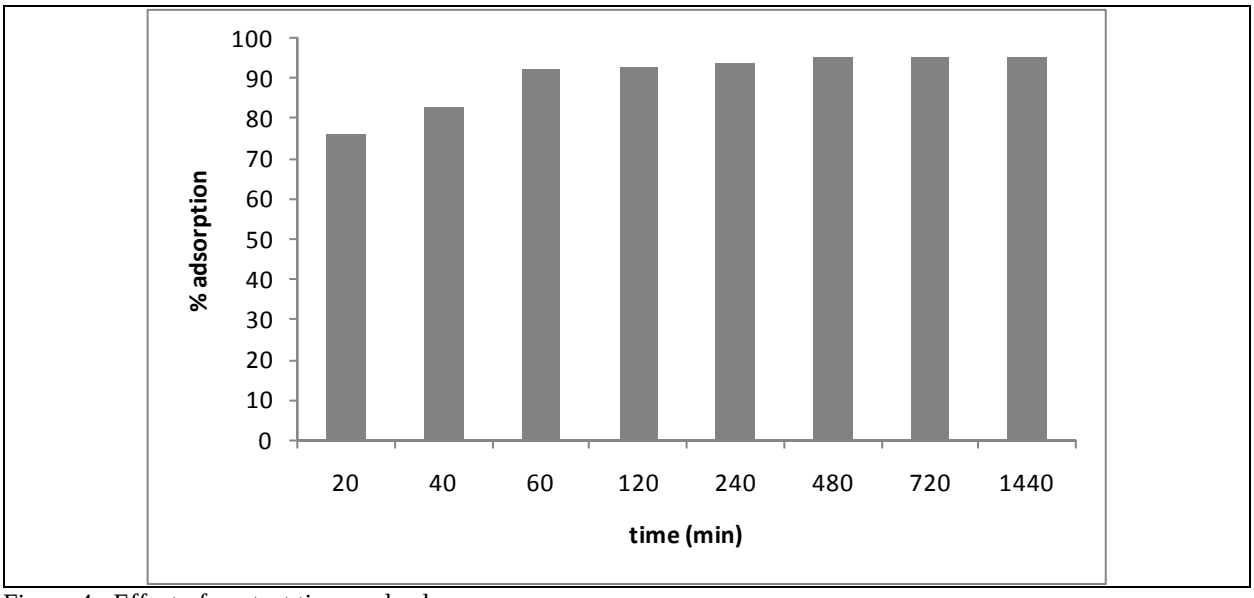

Figure 4 : Effect of contact time on lead

3.5 Variation in initial lead concentration

The removal efficiency of lead increased from 79 to 95 % (refer Figure 5) when the initial concentration was increased from 1 to 10 mg/L. The pattern can be predicted because higher initial concentration of metal ions intensifies the adsorption capacity (qe), however as the process proceeds, the high amount of adsorbate is confronted with limited (constant) availability of active sites on the adsorbent surface. The adsorption capacity for Pb was calculated as 2.6 mg/g. There is an increase in the adsorption when Pb concentration is increased. Correspondingly, at lower concentration, the ratio of metal ions over the adsorption surface is low. Therefore, the metal ions quickly adhere to the available adsorption sites, resulting in higher adsorption efficiency.

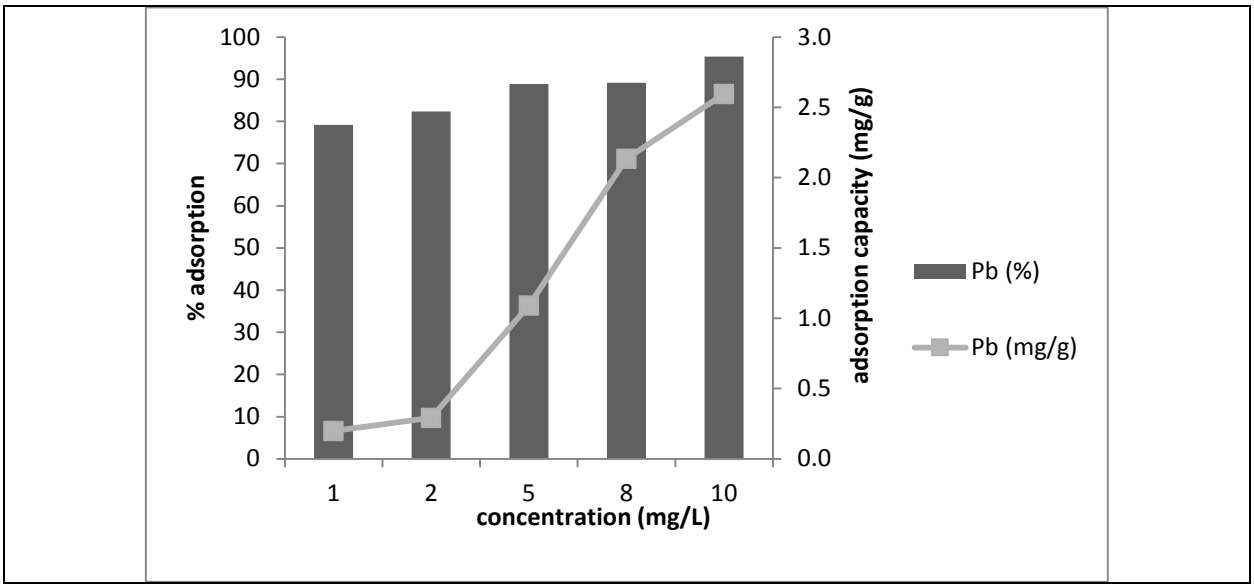

Figure 5 : Initial concentration of lead vs adsorption

3.6 Variation of pH value

Increase in pH shows increase in adsorption. The adsorption percentage shows that adsorption was best at both condition either acidic or alkaline. At pH 7 the adsorption percentage was reduced and equilibrium was reached at pH 9-11.

3.7 Adsorption model isotherm and kinetic

From Table 1, it can be seen that the green mussel shell has a maximum adsorption capacity of 1.94 mg/g to form a monolayer coverage for Pb. This isotherm is suitable for representing chemisorptions on a set of distinct localized adsorption site. However, the negative value of Langmuir constant indicated the inadequacy adsorption of heavy metal using green mussel shell as adsorbent. Freundlich isotherm is usually used for non-ideal adsorption on heterogeneous surfaces. The heterogeneity arises from the presence of different functional groups on the surface, and various adsorbent-adsorbate interactions. K_F values indicate that Pb with adsorption, K_F = 4.18. This model assumes that when the adsorbent concentration increases, the concentration of adsorbate on the adsorbent surface also increased and correspondingly, the sorption energy exponentially decreased over the completion of the sorption centre of the adsorbent. It is proven that the Freundlich model provides a better fit for explaining the adsorption of Pb onto all modified adsorbents.

Table 1: Adsorption isotherm parameters for Lead using Langmuir and Freundlich Isotherm

Adsorption Isotherm Model	**Parameter Value**
Langmuir Isotherm	
	Pb
Equation	y = 0.513x - 0.020

q_m (mg/g)	1.9493
K_L (L/mg)	-25.6502
R^2	0.999
Freundlich isotherm	
Equation	y = 1.605x +1.430
K_F (mg/g)(L/mg)$^{1/n}$	4.179
1/n	1.605
R^2	0.797

The linear forms of the pseudo-first-order and second-order equations, rate constants, expected lead uptake and correlation coefficients is shown in Table 2 and 3. For the pseudo first order model the correlation coefficient (R^2 =0.785) and the calculated lead uptake with this model is lower than the expected metal uptake for lead. this Indicate that the chemisorption process is not a first order reaction. The pseudo second order reaction in chemisorption is based on the sorption capacity on the solid phase. The correlation coefficient in the pseudo second order reaction (R^2 = 0.999) is high for Pb. k which is the pseudo-second-order rate constant is 6.42 min^{-1} and the calculated metal adsorption is much nearer to the expected value suggesting that the chemisorption process comply to pseudo second order model. The results indicate that the kinetic behaviour of Pb on green mussel shell as adsorbent can be satisfactorily explained with the pseudo-second-order sorption equation. Based on the assumption step, chemical sorption or chemisorption involving valency forces through sharing or exchange of electrons between adsorbent and adsorbate.

Table 2 : The pseudo-first–order parameter of Pb adsorption

Element / Parameter	**Pb**
equation	y = -0.426x - 1.064
q_e experiment	2.1465
q_e calculated	0.345
k_1	0.426
R^2	0.785

Table 3 : The pseudo-second–order parameter of Pb adsorption

Element / Parameter	**Pb**
equation	y = 0.466x + 0.035
q_e experiment	2.1465
q_e calculated	2.1459
k_2	6.2046
R^2	0.999

4.0 Conclusion

Green mussel shell was successfully used as a low-cost alternative adsorbent for the removal of lead. Since the shell are abundantly and locally available, it is economically viable for removal of heavy metal from aqueous solution. FESEM micrographs illustrated that carbonization treatment with 600°C developed porosity on the surface of the adsorbent. The FTIR spectrum obtained for the functional groups responsible for adsorption process like hydroxyls, carbonyls, carboxylic and amides. The relative study of adsorption percentage capacity, show that it can adsorb more than 99% of lead. The equilibrium adsorption data indicated that the equilibrium sorption fitted well with the Freundlich isotherm, displaying higher regression coefficient, R^2 value. The monolayer adsorption capacity of green mussel waste was found to be 1.94 mg/g. The adsorption kinetics can be well described by the pseudo-second-order model equation. Based on the results obtained, mussel shells has the potential to be an alternative and inexpensive adsorbent for Pb in aqueous solution.

5.0 Acknowledgements

The authors acknowledge the Universiti Teknologi Malaysia Research University Grant Vot 11H97 for financial assistance.

References

Abbaszadeh, S., Wan Alwi, S. R., Webb, C., Ghasemi, N., & Muhamad, I. I. (2016). Treatment of lead-contaminated water using activated carbon adsorbent from locally available papaya peel biowaste. *Journal of Cleaner Production*, 1–13.

Alidoust, D., Kawahigashi, M., Yoshizawa, S., Sumida, H., & Watanabe, M. (2015). Mechanism of cadmium biosorption from aqueous solutions using calcined oyster shells. *Journal of Environmental Management*, *150*, 103–10.

Du, Y., Lian, F., & Zhu, L. (2011). Biosorption of divalent Pb, Cd and Zn on aragonite and calcite mollusk shells. *Environmental Pollution*, *159*(7), 1763–8.

Du, Y., Zhu, L., & Shan, G. (2012). Removal of Cadmium from contaminated water by nano-sized aragonite mollusk shell and the competition of coexisting metal ions. *Journal of Colloid and Interface Science*, *367*(1), 378–382.

Durve, A., & Chandra, N. (2014). FT-IR analysis of bacterial biomass in response to heavy metal stress. *International Jouranl of Biotechology*, *112*, 386–391.

Hossain, A., Bhattacharyya, S. R., & Aditya, G. (2015). Biosorption of Cadmium by Waste Shell Dust of Fresh Water Mussel Lamellidens marginalis : Implications for Metal Bioremediation. *ACS Sustainable Chem. Eng.*, *3*(JAN), 1.

Liu, Y., Changbin, S., Xu, J., & Youzhi, L. (2009). The use of raw and acid-pretreated bivalve mollusk shells to remove metals from aqueous solutions. *Journal of Hazardous Materials*, *168*(1), 156–162.

Lu, J., Lu, Z., Li, X., Xu, H., & Li, X. (2015). Recycling of shell wastes into nanosized calcium carbonate powders with different phase compositions. *Journal of Cleaner Production*, *92*, 223–229.

Naiya, T. K., Singha, B., & Das, S. K. (2011). FTIR Study for the Cr (VI) Removal from Aqueous Solution Using Rice Waste. *International Proceedings of Chemical, Biological and Environmental Engineering (IPCBEE)*, *10*, 114–119.

Odoemelam, S. A., & Eddy, N. O. (2009). Studies on the Use of Oyster, Snail and Periwinkle Shells as Adsorbents for the Removalof Pb2+ Aqueous Solution. *E-Journal of Chemistry*, *6*(1), 213–222.

Oladoja, N. A., Ololade, I. A., Adesina, A. O., Adelagun, R. O. ., & Sani, Y. M. (2013). Appraisal of gastropod shell as calcium ion source for phosphate removal and recovery in calcium phosphate minerals crystallization procedure. *Chemical Engineering Research and Design*, *91*(5), 810–818.

Peña-Rodríguez, S., Bermúdez-Couso, A., Nóvoa-Muñoz, J. C., Arias-Estévez, M., Fernández-Sanjurjo, M. J., Álvarez-Rodríguez, E., & Núñez-Delgado, A. (2013). Mercury removal using ground and calcined mussel shell. *Journal of Environmental Sciences (China)*, *25*(12), 2476–2486.

Seco-Reigosa, N., Cutillas-Barreiro, L., Nóvoa-Muñoz, J. C., Arias-Estévez, M., Fernández-Sanjurjo, M. J., Álvarez-Rodríguez, E., & Núñez-Delgado, A. (2014). Mixtures including wastes from the mussel shell processing industry: retention of arsenic, chromium and mercury. *Journal of Cleaner Production*, *84*, 680–690.

Tan, I. A. W., Leonard, L. L. P., Rosli, N. A., & Ling, L. T. H. (2013). Derivation Of Oil Palm Shell-Based Adsorbent Using H2so4 Treatment For Removal Of Atrazine From Aqueous Solutions. *Malaysian Journal of Civil Engineering*, *25*(1), 45–57.

Vukovic, G. D., Marinkovic, A. D., Colic, M., Ristic, M. D., Aleksic, R., Peric-Grujic, A. A., & Uskokovic, P. S. (2010). Removal of cadmium from aqueous solutions by oxidized and ethylenediamine-functionalized multi-walled carbon nanotubes. *Chemical Engineering Journal*, *157*(1), 238–248.

Yoshimura, K., & Shiomi, H. (2014). Lead removal by scallop shell used for crystallization phosphorus removal. *Journal of the Society of Materials Science, Japan*, *63*(6), 442–445.

Precious Metals Extraction with Sulfur Function Supported on Methylacrylate-Styrene Copolymer

Minako Iwakuma*[1], Hirofumi Hanada[1], Yoshinar Baba[2]

[1]*National Institute of Technology, Miyakonojo College*
473-1 Miyakonojo City Miyazaki Prefecture, Japan
[2]*University of Miyazaki2, 1-1 Gakuenkibanadai Nishi Miyazaki City, Miyazaki Prefecture, Japan*

*Corresponding Author: *minako@cc.miyakonojo-nct.ac.jp*

Abstract: Newly extractant containing and pyridine sulfur atoms as ligand, methyl-2-chloroacrylate-*o*-(2-sthiomethylpyridyl)styrene (ATPS1 and ATPS2) were synthesized for palladium(II) and gold(III) over base metals. Extraction of metal ions by a batchwise method at 303K from the hydrochloric acid containing 0.1 milli molar metal ions was carried out. Paltinum(IV) and gold(III) were selectively extracted in whole concentration of hydrochloric acid with ATPS1. These results suggest that ATPS1 selectively extracted precious metals from chloride media. The palladium(II) extraction was found to be independent of copper(II) in the solution, even when they are present in 200-fold excess. Extraction equilibria can be achieved within 1h with ATPS1. the effect of concentration of H^+, Cl^-, and extractant on the Au(III) extraction with ATPS was studied. As a result, the extraction equilibria were described by protonation of pyridine and making ion pair with protonated pyridine and $AuCl_4^-$.

$$\overline{RSN} + H^+ + Cl^- \leftrightarrows \overline{RSN{\cdot}H^+} + Cl^- \; ; K_1 \; (1) \qquad \overline{RSN{\cdot}H^+} + AuCl_4^- \leftrightarrows \overline{RSN{\cdot}H^+ \cdot AuCl_4^-} \; ; K_2 \; (2)$$

The value of K_1 and K_2 were decided by nonlinear least-squares method and were given K_1=7.50 and K_2=8.93×10^7.

Keywords: *precious metals, extraction, polymer extractant, gold, palladium*

1.0 Introduction

Precious metals such as gold (III), palladium (II) and platinum(IV) are important metals in the fields of catalysts and the battery and electronic industries. The selective separation and recovery of precious metals from aqueous solutions are of great importance in hydrometallurgy and wastewater treatment. However, since the separation and purification of these metals are very difficult processes because of their chemical properties and the formation of many chemical species in chloride media, it is very important to develop a more efficient recovery process for their recovery and separation. In recent years, the development of solvent extraction as an alternative technique for precious metals removal has been reconsidered [1]. Since the separation and purification of these metals are very difficult processes because of their chemical properties and many chemical species in chloride media, it is very important to develop a more efficient recovery process for their extraction and separation [2,3] In this study, newly extractant containing pyridine and sulfur atoms as ligand, methylacrylate-(α -*o*-thiometylpyridyl)-styrene copolymer (ACS) was synthesized for precious metals over base metals.

2.0 Experimental

2.1 Reagent

Methylacrylrate-*α-(-o*-thiometylpyridil)-styrene copolymer (ATPS) was synthesized from methylacrylchloride-styrene copolymer[1)] and thiometylpyridine according to a conventional method. ATPS2 has molecular weight two times as large as ATPS1.

The reaction mixture was evaporated. Water and chloroform were added to the reaction mixture and then the two phases were separated with a separatory funnel. Chloroform phase was successively washed using 0.1 mol dm^{-3} hydrochloric acid mixed with sodium chloride as a salting out reagent, 1.0 mol dm^{-3} aqueous sodium hydroxide and distilled water. The final product was a viscous brownish liquid. Identification of the purified product was carried out using ^{1}H-NMR, ^{13}C-NMR and FT-IR spectra. The product was identified as ACS and its purity was 97% as measured by gas chromatography.

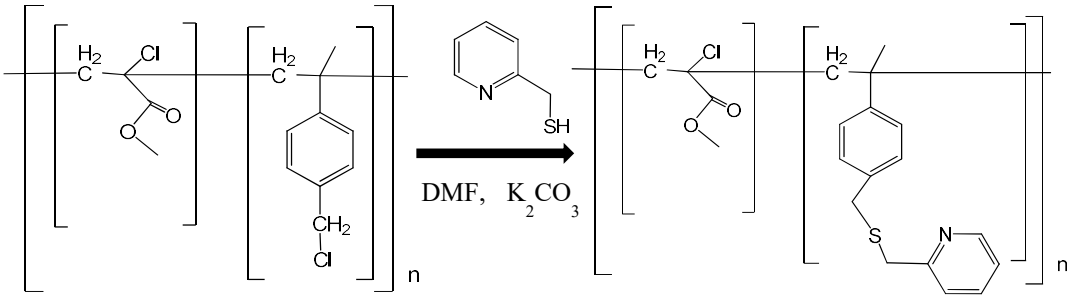

Scheme 1 Synthesis of methyl-2-chloroacrylate-*o*-(2-sthiomethylpyridyl)styrene copolymer.

2.2 Extraction of hydrochloric acid with ATPS1 and ATPS2

To elucidate the distribution behavior of extractant to both the aqueous phase and the organic phase, we examined the distribution of hydrochloric acid to the organic phase. The organic phase was prepared by extractant concentration 0.25wt%. The aqueous phase was prepared by changing the hydrochloric acid concentration from 1.0×10^{-4} to 5.0×10^{-3} mol dm^{-3}. Equal volumes of the aqueous and organic phases were placed in Erlenmeyer flask and the combination was shaken for 3 h. The concentration of hydrochloric acid in the organic phase was determined by acid-base titration with potassium hydroxide dissolved in ethanol.

2.3 Selectivity of Metal Ions with ATPS

The aqueous phase was prepared by dissolving metal chloride into hydrochloric acid. The organic phase was prepared by dissolving with chloroform. The initial concentration of each metal was about 1.0×10^{-4} mol dm^{-3}. Equal volumes of aqueous and organic phases were shaken in a flask at extraction operation. Equilibrium was reached within 24 hours at 303K in the extraction of metals from hydrochloric acid. The measurement of extraction equilibrium was carried out by a batchwise method. Equilibrium and initial concentrations of metals were determined by atomic adsorption spectrophotometer. Equilibrium and initial concentrations of hydrochloric acid were determined by an acid-base titration.

3.0 Results and Discussion

3.1 Charactaristic of ATPS1 and ATPS2

Table 1 shows the physical properties of ATPS1 and ATPS2. The weight and mean avarage molecurars of ATPS1 and ATPS2 were measured by size exclusion chromatography (Shimadzu LC-10), respectively. The density of ATPS1 and ATPS2 were measured by contact angle gauge(KYOWAKAIMEN DropMasters-401).

Table 1 Physical properties of ATPS1 and ATPS2

	weight average molecule weight	number average molecule weight	Interfacial tension mN/m
ATPS1	3.78×10^4	1.85×10^4	18.5
ATPS2	7.22×10^4	3.63×10^4	16.1

Fig.1 shows the extraction of hydrochloric acid with ATPS1 and ATPS2, respectively. Saturated amount of hydrochloric acid is q_{s1}=1.69mmol g^{-1} and equilibulium constant of adsorption is K_{ad1}=52.4 dm^3 mol^{-1} with ATPS1. Saturated amount of hydrochloric acid is q_{s2}=2.08 mmol g^{-1} and equilibulium constant of adsorption is K_{ad2}=21.5 dm^3 mol^{-1} with ATPS2. It is indicated that ATPS1 are similar character to ATPS2. Number and weight molecule weights are not relate to character.

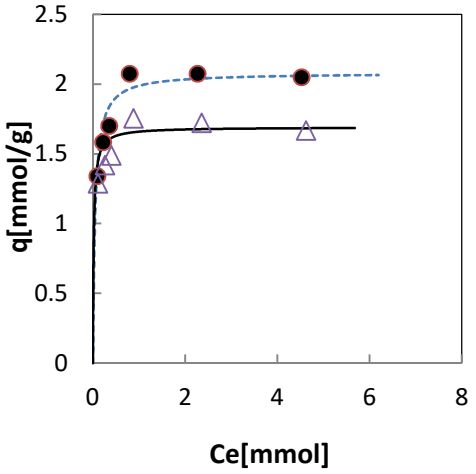

Fig.1 Effect of hydrochloric acid concentration on the extraction percent with ATPS1 and ATPS2.

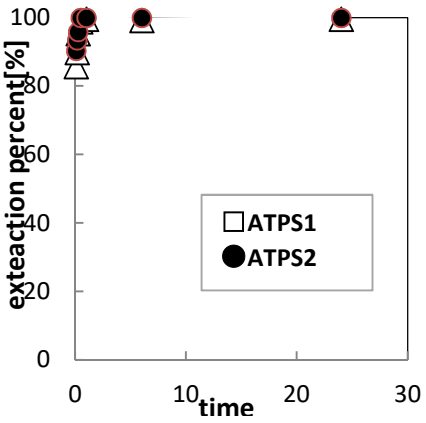

Fig.2 Effect of contact time on the extraction percentage of palladium(II) with ATPS1 and ATPS2.

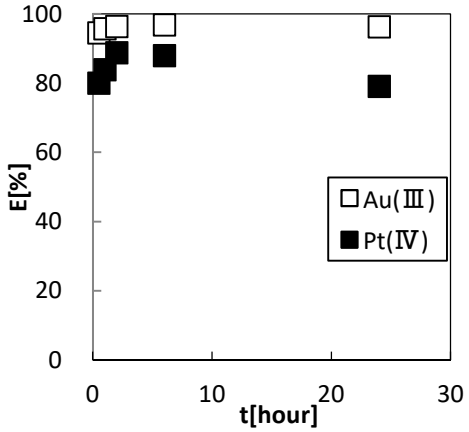

Fig.3 Effect of contact time on the extraction percentage of platinum(IV) and gold(III) with ATPS1.

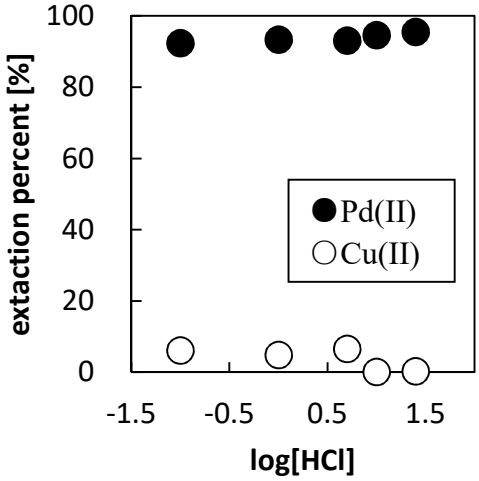

Fig.4 Effect of hydrochloric acid concentration on the extraction percent for various metal ions with ATPS1.

Fig.2 shows the contact time on the extraction percent of palladium(II) with ATPS1 and ATPS2. Extraction equilibria can be achieved within 15min with ATPS1 and ATPS2, respectively. The rate of uptake of both ions was quite rapid.

Fig.3 shows the effect of contact time on the extraction percentage of platinum(IV) and gold(III) with ATPS1. These results suggest that ACS selectively extracted precious metals from chloride media. Extraction equilibria can be achieved within 1h with ATPS1. At equilibrium, 98% of gold(III) and 90% of platinum(IV) were removed from the solution with ATPS1.

Fig.4 shows the experimental results on the selective adsorption of palladium(II) from the mixture prepared at 1 M containing 200-fold copper(II). As is clear from these results, the adsorption of palladium was independent of the contents of copper even if 200-fold iron and copper are coexisting in the mixture.

3.2 Selectiviry of Various Metals with ATPS1.

Fig.5 shows the effect of hydrochloric acid concentration on the extraction percent. Base metals such as copper(II), cobalt(II), nickel(II) and iron(III) were not extracted under these experimental conditions. ATPS1 exhibits the high selectivity for gold(III) and palladium(II) over the entire hydrochloric acid concentration range. Platinum(IV) was extracted in the high hydrochloric acid concentration region, while mercury(II) was extracted in the low hydrochloric acid concentration region.

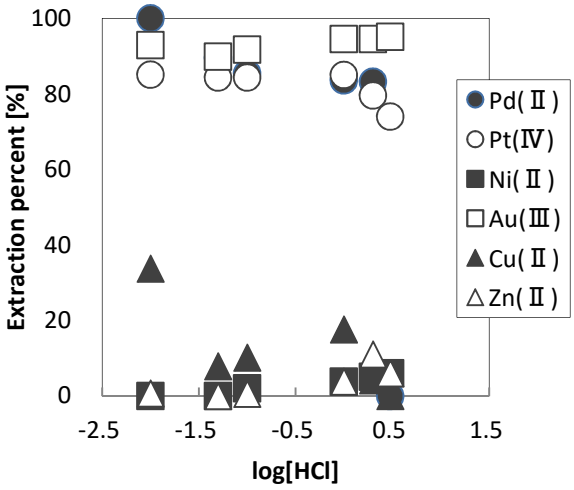

Fig.5 Selectivity of Pd(II) over Cu(II) in the adsorption from the mixture solution of Pd(II) and Cu(III) with ATPS1.

3.3 Extraction Eqilibrium of Gold(III) with ATPS1

Fig. 6 shows the effect of the hydrogen ion concentration on the distribution ratio of gold(III) at a fixed chloride ion concentration ($[Cl^-]$ = 0.5 mol dm^{-3}) with ATPS1. As it can be seen from this result, the distribution ratio increases with increasing hydrogen ion concentration. The plotted points lie on straight line with a slope of 0.4. The effect of the chloride ion concentration on the distribution ratio of gold(III) at a fixed hydrogen ion concentration ($[H^+]$ = 0.5 mol dm^{-3}) with ATPS1.(no figure) The distribution ratio is independent of the chloride ion concentration. Fig. 7 shows the effect of the extractant concentration on the distribution ratio of gold(III) with ATPS1. The distribution ratio increases with increasing extractant concentration with ATPS. The plotted points lie on straight line with a slope of 1. From these results, it can be concluded that gold(III) is extracted with ATPS1 by the following extraction reactions. As a result, the extraction

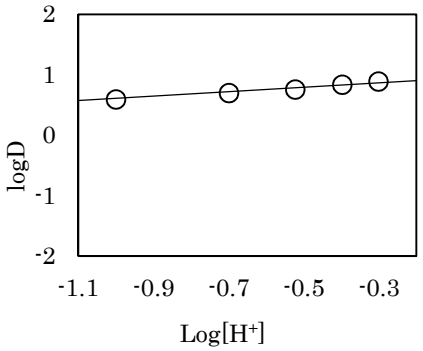

Fig.6 Effect of the hydrogen and ion concentration on the distribution ratio of gold (III) with ATPS1.

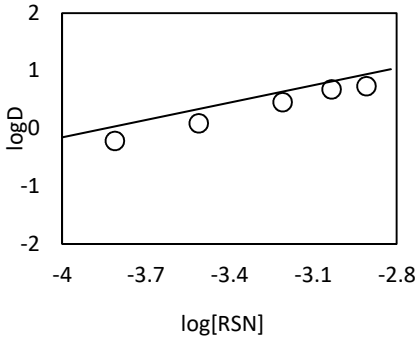

Fig.7 Effect of the extractant concentration on the distribution ratio of gold (III) with ATPS1.

equilibria were described by protonation of pyridine and making ion pair with protonated pyridine and $AuCl_4^-$.

$$\overline{RSN} + H^+ + Cl^- \leftrightarrows \overline{RSN{\cdot}H^+} + Cl^- \; ; K_1 \; (1)$$
$$\overline{RSN{\cdot}H^+} + AuCl_4^- \leftrightarrows \overline{{\cdot}\,AuCl_4^-} \; ; K_2 \; (2)$$

The value of K_1 and K_2 were decided by nonlinear least-squares method and were given K_1=7.50 and K_2=8.93×10^7, respectively.

4. 0 Conclusion

The extraction rate of precious metal with ACS serious were the following information was obtained;
1. Saturated amount of hydrochloric acid is q_{s1}=1.69mmol g^{-1} and equilibulium constant of adsorption is K_{ad1}=52.4 dm^3 mol^{-1} with ATPS1. Saturated amount of hydrochloric acid is q_{s2}=2.08 mmol g^{-1} and equilibulium constant of adsorption is K_{ad2}=21.5 dm^3 mol^{-1} with ATPS2.
2. ATPS1 selectively extracted precious metals for gold(III), platinum(IV) and palladium(II). Extraction equilibria can be achieved within 1h with ATPS1 from chloride media.
3. ATPS1 was a selective extractant for precious metals such as gold(III), palladium(II) and platinum(IV) from hydrochloric acid solution.
4. Extraction equilibria of ATPS1 and gold were described by protonation of pyridine and making ion pair with protonated pyridine and $AuCl_4^-$.

References

[1] G. V. K. Puvvada and D. S. R. Murthy *Hydrometall*., **58**, 185 (2000)
[2] A. T. Yordanov and D. M. Roundhill, *Coord. Chem. Rev.*, **170**, 93 (1998)
[3] Y. Baba, M. S. Hairi, K. Oguma, K Shiomori and Y. Kawano, *Solv. Extr. Dev. Jpn.*, **5**, 60 (1998)

FIRST FLUSH OF STORMWATER RUNOFF FROM URBAN RESIDENTIAL CATCHMENT

Alias, N[1]; Goonetilleke, A[2], Egodawatta, P[3]

[1]Senior Lecturer, Faculty of Civil Engineering, Universiti Teknologi Malaysia, 81310 UTM Skudai, Johor

[2]Professor, Science and Engineering Faculty, Queensland University of Technology, 4000 Brisbane, Australia

[3]Senior Lecturer, Science and Engineering Faculty, Queensland University of Technology, 4000 Brisbane, Australia

*Corresponding author: *noraliani@utm.my*

Abstract:
First flush is an important parameter when dealing with the urban treatment system as first flush is related to the most polluted part of the runoff. Therefore, first flush runoff can be treated and the rest of the runoff can be released to the receiving water. In this study, the existence of first flush from urban residential catchment was investigated. An urban residential catchment located in Coomera Waters, Gold Coast, Australia was selected as the study site. 23 storm events were sampled and analysed for three water quality parameters; total suspended solids (TSS), total phosphorus (TP) and total nitrogen (TN). Results show that, 83% of the storm events experienced TSS first flush which is the highest compared to TP (78%) and TN (65%).
.

Keywords: *First flush, urban residential catchment, urban treatment system, Total Suspended Solids, Total Nitrogen, Total Phosphorus*

1.0 Introduction

Stormwater quality is an important issue particularly in urban area as the polluted stormwater will impacts the quality of the receiving water. Therefore, mitigation approach is essential. First flush phenomenon is an important issue in urban stormwater management. In order to design an effective stormwater treatment facility, it is essential to have an in-depth understanding of the first flush behaviour. The existence of first flush is debated by researchers as several studies have observed the phenomenon while

other studies have not found the first flush existence (Han et al. 2006; Tiefenthaler et al. 2008, Alias et al. 2014(a,b)).

First flush is defined as an increased presence of pollutants in the early stage of the runoff hydrograph compared to the later stage of runoff. The existence of first flush will benefit stormwater management as a treatment system could be designed to treat the most polluted discharge volume and to release the remainder of the runoff.

This has implications in relation to the size of the treatment facility as it could be reduced, thus reducing the cost. Therefore, it is essential to have an in-depth understanding of the first flush phenomenon in order to design an effective stormwater treatment system. This study investigated the existence of first flush of stormwater runoff from urban residential catchment.

2.0 Materials and Methods

2.1 Study Site

Coomera Waters was selected as the study area. Three sub-catchments in Coomera Water; Sub-Catchment A, Sub-Catchment B and Sub-Catchment C were identified to monitor the first flush of the stormwater runoff. Coomera Waters is a new residential area located in Gold Coast and was developed around a 17 ha lake and natural wetlands and provided with Water Sensitive Urban Design (WSUD) in order to protect the natural waterways from being polluted by the stormwater runoff. The total area of Coomera Waters development is 496 hectares, which contains approximately 1,800 homes. Figure 1.0 shows the location of Coomera Waters while Figure 2.0 shows Sub-Catchment A, Sub-Catchment B and Sub-Catchment C.

Figure 1.0: The location of Coomera Waters, Gold Coast, Australia

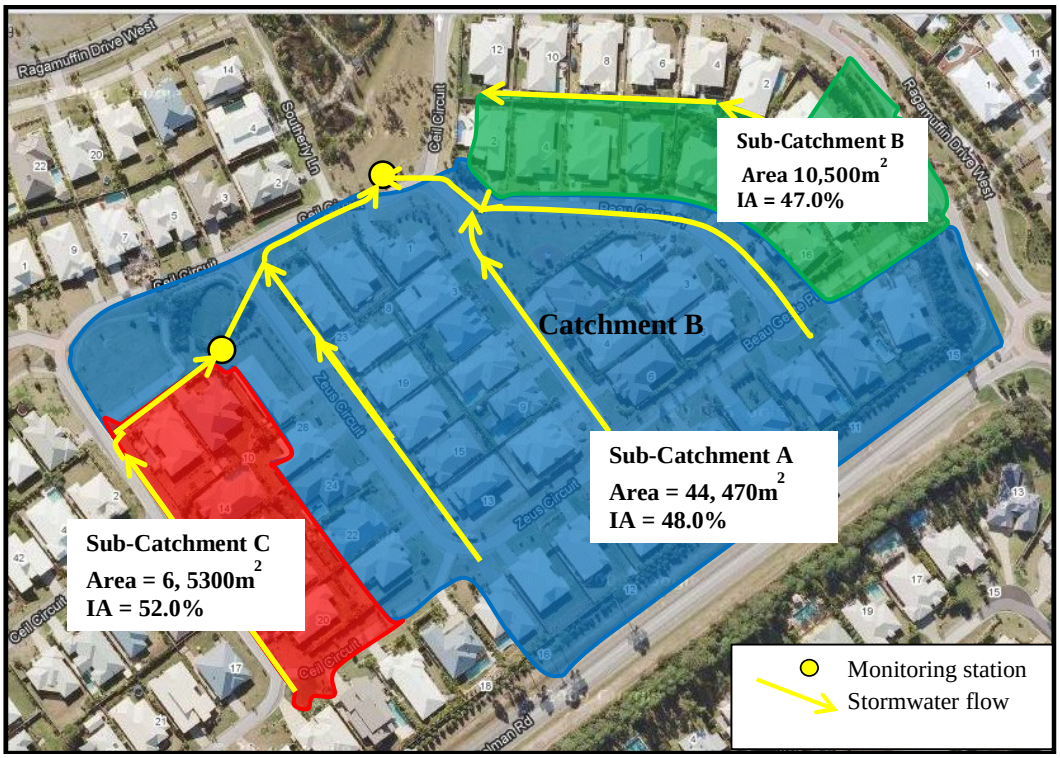

Figure 2.0: Location of Sub-Catchment A, Catchment B and Catchment C and its'characteristics

2.2 Sample Collection and Data Testing

Monitoring stations were installed at the outlet of the three catchments in order to collect stormwater runoff samples and to record rainfall-runoff data. Each of the stations contained an ISCO automatic water sampler, a Campbell Scientific data logger, a solar regulator and a RF radio as shown in Figure 3.0. The ISCO automatic water sampler was programmed to collect the water in 1L plastic bottles and up to 24 bottles can be collected. A V-notch weir was used to measure the runoff volume at the catchment outlet stormwater. 2 rain gauges were installed in two sub-catchments; Sub-Catchment A and Sub-Catchment C to record the rainfall. 23 storm events were sampled and analysed in order to determine occurrence of the first flush phenomenon Details of the sampling station are summarised in Table 1.0.

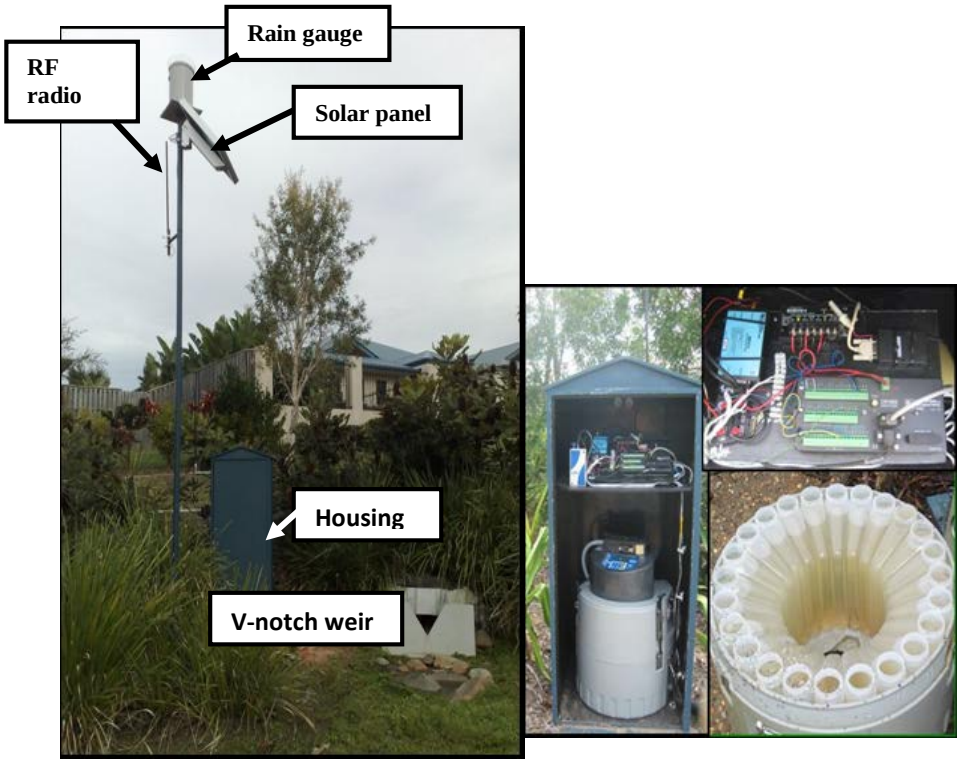

Figure 3.0: Monitoring Station at the catcment outlet

Table 1.0: Details of the monitoring stations at Sub-Catchment A, Sub-Catchment B and Sub-Catchment C (adapted from Parker (2010))

Monitoring stations	Sub-Catchment A	Sub-Catchment B	Sub-Catchment C
Collected sample	Down 1.4m x 1.4m x 2.8m access	Down 1m x 0.5m x 1m access	Attached to 300 mm drain pipe
Weir	90° weir	60° weir	70° weir
Logger	Campbell CR 1000	Campbell CR 211	Campbell CR 1000
Autosampler	ISCO 6712	ISCO 6712	ISCO 6712
Raingauge	yes		yes

Total Suspended Solids (TSS), Total Phosphorus (TP) and Total Nitrogen (TN) were selected for water quality parameters. These water quality parameters were chosen as these are most common water quality pollutants found in urban stormwater, particularly in residential areas and these are the primary pollutants treated by stormwater treatment devices (Alias, 2013).

2.2 First Flush Ocurrence

There are several approaches available in defining first flush. Most common definitions are concentration based first flush (CBFF), mass based first flush (MBFF), and empirically based first flush (EBFF). In this study, MBFF method was selected as the most appropriate method for defining the first flush.

As first flush is typically defined as the wash-off of a relatively higher pollutant load during the early part of the runoff event, the analysis of the variation of cumulative pollutant load (L) vs. cumulative runoff volume (V) formed the first phase of assessment (refer Figure 4.0). Typically, the first flush is considered to exist when the LV curve is above the bisector line (denoted as B line), particularly at the initial part of the runoff volume (Geiger 1987; Lee et al. 2002)**.** B line indicates the fraction of pollutant load washed-off from the surface with respect to the fraction of runoff volume exported from the catchment. Variation of LV versus V curve was used to derive first flush coefficients. In this regard, the mathematical equation presented in Equation 1 was used.

$$LV = V^{a} \qquad \text{Eq 1}$$

Where, a is the first flush coefficient which can be computed by linear regression using Equation 2:

$$lnM(t) = a\ ln\ V(t) \qquad \text{Eq 2}$$

a indicates the gap between the LV curve and B line and termed as strength of first flush

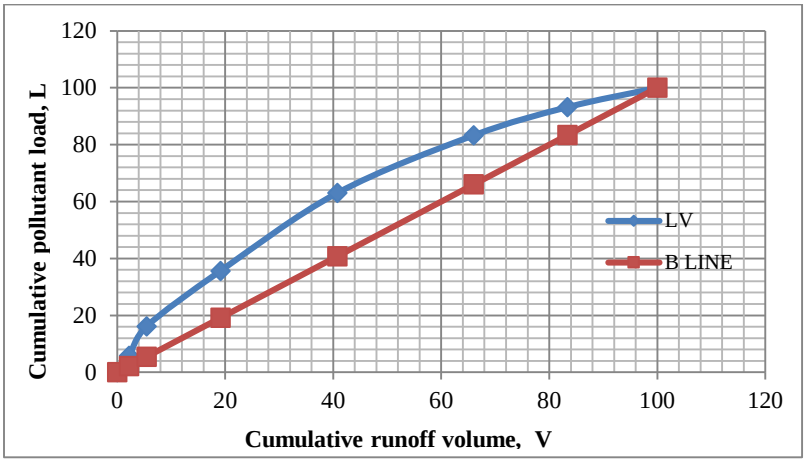

Figure 4.0: Cumulative pollutant load, L vs. cumulative runoff volume, V

3.0 Results and Discussions

Figures 5.0, 6.0, 7.0, 8.0, 9.0, 10.0, 11.0, 12.0 and 13.0 show the variation of LV curve for TSS, TN and TP of Sub-Catchment A, Sub-Catchment B and Sub-Catchment C, respectively.

As seen in the figures, there are variations in the LV curves. Most of the events exhibited first flush as the LV curve is above the bisector, B line which suggests the first flush existence. First flush phenomenon was observed for Event A6, A4 and A3 for TSS while the phenomenon was not observed for A9. First flush existence for TP was observed for most of the storm events except for Event A6. Similar trend also can be observed for TN in terms of first flush occurrence

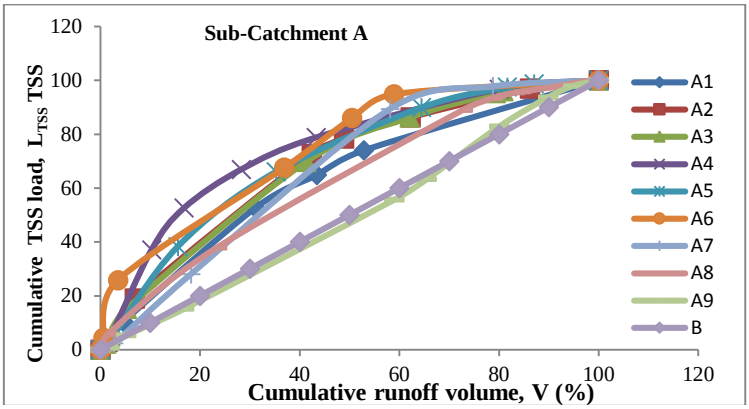

Figure 5.0: Variations of LV curves for TSS in Sub-Catchment A

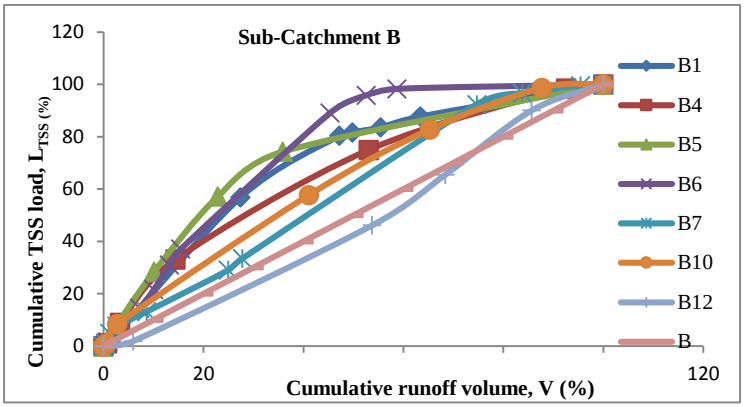

Figure 6.0: Variations of LV curves for TSS in Sub-Catchment B

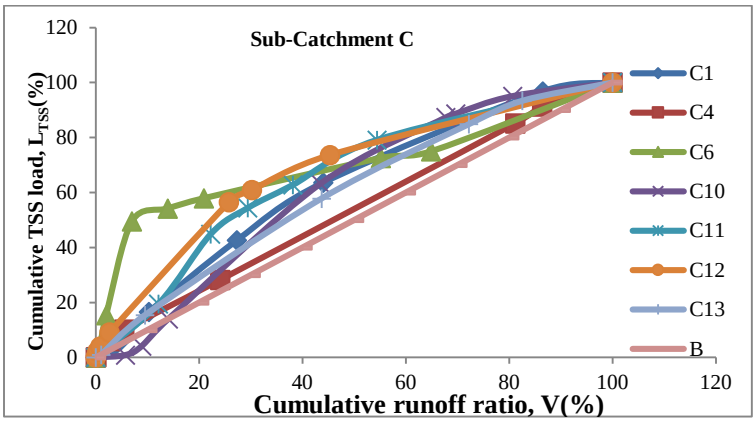

Figure 7.0: Variations of LV curves for TSS in Sub-Catchment C

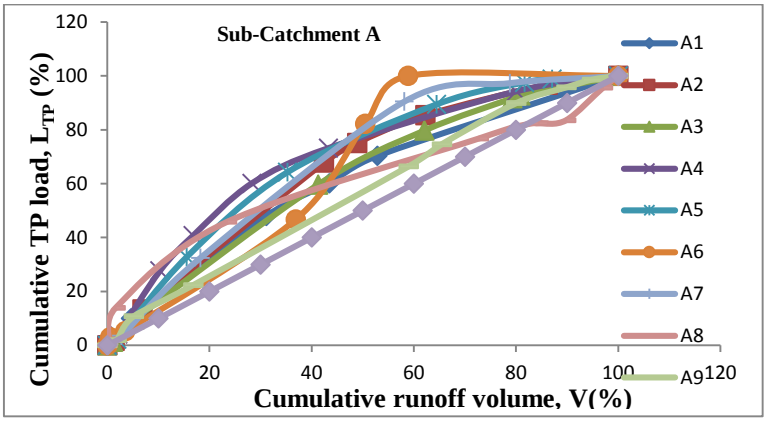

Figure 8.0: Variations of LV curves for TP in Sub-Catchment A

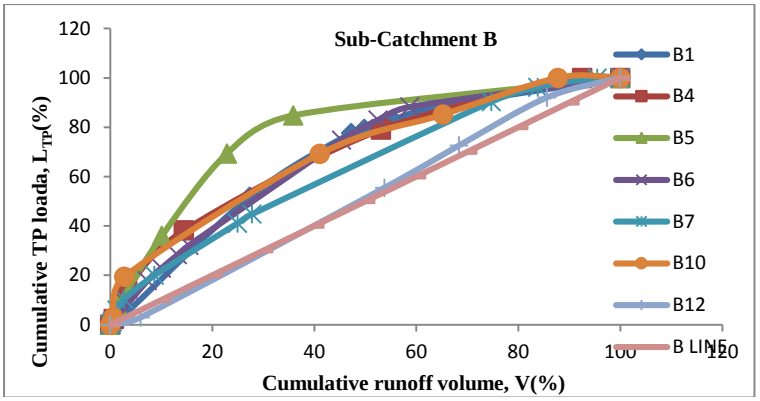

Figure 9.0: Variations of LV curves for TP in Sub-Catchment B

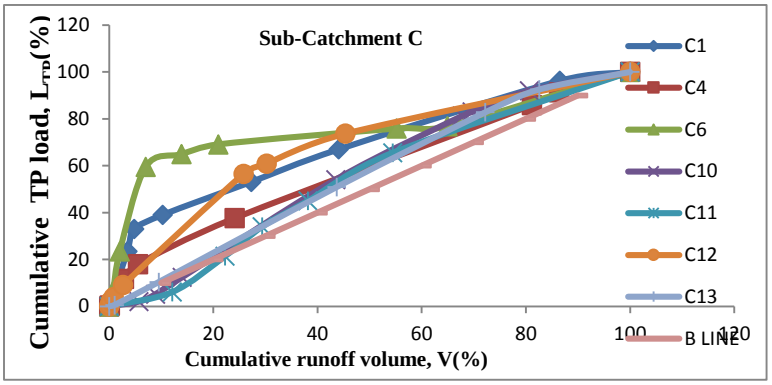

Figure 10.0: Variations of LV curves for TP in Sub-Catchment C

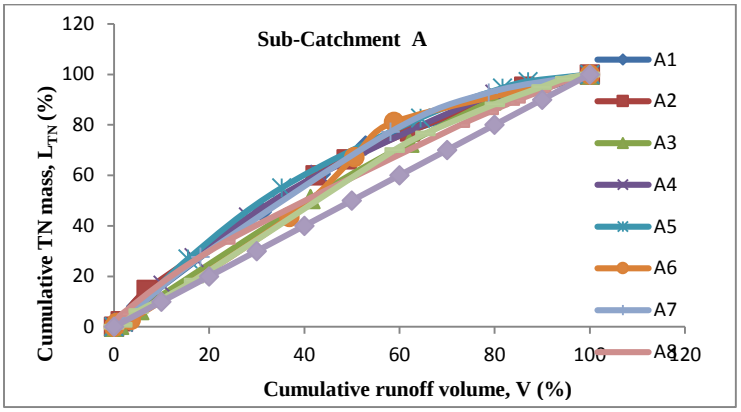

Figure 11.0: Variations of LV curves for TN in Sub-Catchment A

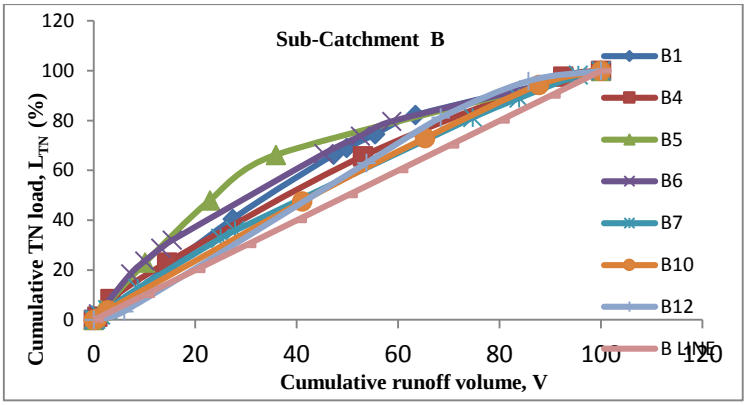

Figure 12.0: Variations of LV curves for TN in Sub-Catchment B

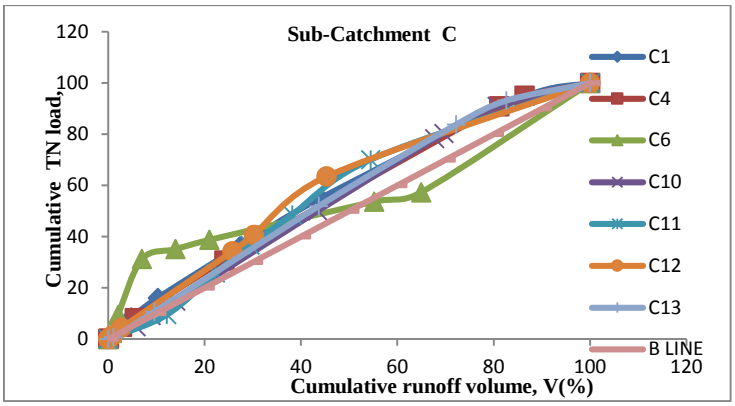

Figure 13.0: Variations of LV curves for TN in Sub-Catchment C

Table 2.0 lists the first flush occurrence for the three sub-catchments. According to Table 2.0, 78% to 86% of the selected storm events show the existence of first flush for TSS for the three catchments. However, TN has low percentage of storm events with the occurrence of first flush, which is between 57% and 71%. Among the three pollutants, TP has the widest range of storm events with first flush occurrence, which is between 57% and 89%. TSS has the highest first flush occurrence which is 83% , while TP with 78% and TN has the lowest first flush existence (65%).

Table 2.0: First flush occurrence in Sub-Catchments A, B and C

Pollutant		TSS		TP		TN	
Catchment	Total events	FF exist (no of events)	FF exists (%)	FF exist (no of events)	FF exists (%)	FF exist (no of events)	FF exists (%)
A	9	7	78	8	89	6	67
B	7	6	86	6	86	5	71
C	7	6	86	4	57	4	57
All	23	19	83	18	78	15	65

4.0 Conclusions

The results show that first flush occurrence varies within the storm events, type of pollutants and sub-catchments. 82.6% of the selected storm events experienced TSS first flush which is the highest compared to TP (78.3%). Among the three pollutants, TN has the lowest percentage of first flush existence where only 65.2% of the storm event experienced first flush.

Acknowledgement
The author would like to thank Malaysian Government and Universiti Teknologi Malaysia for supporting the author in terms of the finance during her Ph.D study.

References

Alias, N. (2013). First flush behaviour in urban residential catchment, PhD thesis, Queensland University of Technology, Australia.

Alias, N, Liu, A., Egodawatta, P., Goonetilleke, A. (2014a) Sectional analysis of the pollutant wash-off process based on runoff hydrograph, Journal of Environmental Management, 134 (2014) 63-69.

Alias, N, Liu, A., Egodawatta, P., Goonetilleke, A. (2014b) Time as the critical factor in the investigation of the relationship between pollutant wash-off and rainfall characteristic, Ecological Engineering, Volume 64, 301–305.

Geiger W. F. (1987). *Flushing effects in combined sewer systems.* Paper presented at the Proc. Fourth Int. Conf. on Urban Storm Drainage, Lausenne, 40-46.

Han Y., Lau S.-L., Kayhanian M. and Stenstrom M. K. (2006). Characteristics of highway stormwater runoff. Water Environment Research, 78(12), 2377-2388.

Lee J. H. and Bang K. W. (2000). Characterization of Urban Stormwater Runoff. *Water Research, 34*(6), 1773-1780.

Parker, Nathaniel. (2010) Assessing the effectiveness of Wate Urban Design in Southeast Queensland, Msc Thesis, Queensland University of Technology.

Tiefenthaler L. L., Stein E. D. and Schiff K. C. (2008). Watershed and land use-based sources of trace metals in urban stormwater. Environmental Toxicology and Chemistry, 27(2), 277-287.

REMOVAL OF COD MATTER, NITROGEN, AND PHOSPHORUS IN SEWAGE WITHOUT EXTERNAL AERATION BY UASB-DHS-A_2SBR SYSTEM

Takashi Yamaguchi[1]*, Masashi Hatamoto, Namita, Shinya Maki, Namita Maharjan & Takahiro Watari

[1] *Department of Science of Technology Innovation, Nagaoka University of Technology,*
[2] *Department of Civil and Environmental Engineering, Nagaoka University of Technology,*
1603-1, Kamitomioka, Nagaoka, Niigata, 940-2188, Japan

* Corresponding Author: *ecoya@vos.nagaokaut.ac.jp*

Abstract: Recently combination of down-flow hanging sponge (DHS) reactor and an up-flow anaerobic sludge blanket (UASB) reactor has been gaining interest as an innovative technology. DHS is a completely aerobic reactor with the porous sponge material for attached growth process for attaining higher SRT over 100 days favoring nitrification without any aeration. Meanwhile, anaerobic/anoxic sequencing batch reactor (A_2SBR) was reported to remove the phosphorus and nitrogen efficiently by using denitrifying phosphorus accumulating organisms.

Pertaining to this, the combined UASB-DHS- A_2SBR system was operated at average sewage temperature of 25 °C in summer and 10 °C in winter at the Nagaoka sewage treatment center in Japan to investigate the overall performance of this combined system. However, from the obtained data it was observed that the average SS (Suspended Solids), BOD (Biochemical Oxygen Demand) and COD (Chemical Oxygen Demand) removal rates in summer (winter) were 96% (88%), 97% (87%) and 92% (71%), respectively. Similarly, TKN and ammonium nitrogen removal rates in summer (winter) were 92% (37%), 88% (41%), respectively.

The A_2SBR performance showed that nitrate in effluent remained less than 5 mg/L as N throughout the study. Phosphorus removal as low as 1 mg/L as P was achieved under adjusting the pH of 7.4 ± 0.2. Despite the slight reduction in performance during the winter season it still meets the discharge standards for the wastewater treatment water discharge effluent to the river bodies. Therefore, proposed UASB-DHS-A_2SBR system without aeration could be a promisingly applicable technology for domestic wastewater treatment for next generation.

Keywords: *DHS, Sewage*

1.0 Introduction

The prevailing need of environmental sanitation has enticed many researches in the field of municipal wastewater treatment to find the better solution. In this advent, upflow anaerobic sludge blanket (UASB) has been proven to be effective for medium to high strength wastewater in tropical zones, subtropical zones and also in low ambient temperature (Takahashi *et al*., 2011; Foresti *et al*., 2006; Moawad *et al*., 2009).
As a best option for post treatment, an aerobic down-flow hanging sponge (DHS) unit was developed. DHS, a system developed by Professor Harada research team has significant capability to remove organic load due to its high retention of biomass by sponges having more than 90% void space (Tandukar *et al*., 2005, 2007; Onodera *et al*., 2013). The combined system of UASB-DHS has been considered as one of the most convincing technologies for municipal sewage treatment under variable conditions (Tandukar *et al*., 2006). Besides, it is economically advantageous over conventional activated system with respect to its less energy requirement. Nonetheless, further studies and findings confronted that this system was not able to remove nutrients well, even though satisfactory nitrogen removal was reported by Araki *et al*. (1999) and Tandukar *et al*. (2005). Therefore, anaerobic/anoxic sequencing batch reactor (A_2SBR) was chosen as suitable tertiary treatment unit for UASB-DHS.
Anaerobic/anoxic reactor is a single tank, same sludge based sequencing batch reactor. With the discovery of denitrifying phosphorus accumulating organisms (DNPAOs) simultaneous removal of nitrogen and phosphorus is possible with anoxic phosphorus uptake using nitrate/nitrite instead of oxygen as electron acceptors (Kuba *et al*., 1994, 1996). Under alternating anaerobic and anoxic conditions DNPAOs take up volatile fatty acids and store them as polyhydroxyalkanoates (PHAs) through hydrolysis of intracellular polyphosphate and glycolysis of glycogen under anaerobic conditions. In the anoxic condition, DNPAOs utilize nitrate as electron acceptor and utilize PHAs to generate energy for growth, glycogen synthesis and phosphate uptake (Mino *et al*., 1998; Tsuneda *et al*., 2006). In this retrospect, the integrated performance of emerging technology consisting UASB-DHS-A_2SBR was investigated. The objectives of the present work are to demonstrate the effect of seasonal variation on organic removal of UASB-DHS and evaluate the performance of A_2SBR as a tertiary treatment unit for nutrient removal from municipal wastewater.

2.0 Materials and Methods

2.1 Experimental Set- up of the pilot plant

Fig. 1 shows the schematic diagram of the experimental set up of a pilot scale municipal wastewater treatment plant in Nagaoka, Japan. The system consisted of reservoir (2000 L), UASB reactor (1178 L), DHS reactor (857 L) and A_2SBR reactor (200 L). DHS consisted of vertically aligned 10 boxes, which were stuffed with random polyurethane sponges. Sponge volume was 454 L and occupied 53% of the total volume of the reactor,

Each sponge was designed with plastic net ring of 33 mm × 33 mm wrapped in the polyurethane sponge cube of 33 mm.

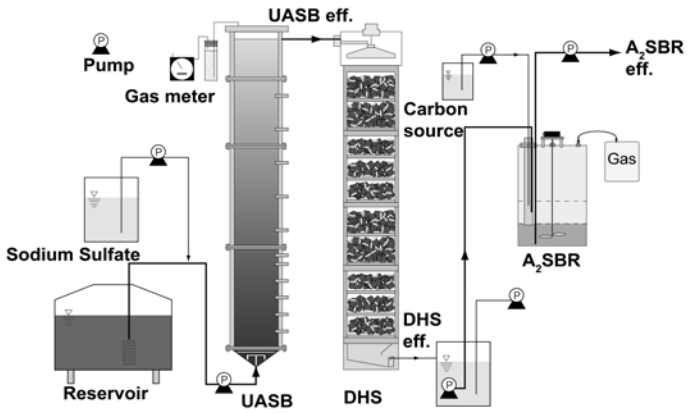

Fig. 1 Schematic diagram of a pilot-scale experimental setup of UASB-DHS-A_2SBR reactor installed in Nagaoka Sewage Treatment Center, Japan.

2.2 Operational conditions

The municipal wastewater after screening and grit removal was received from the combined sewer in a reservoir. 50 mg/L of sodium sulfate was added in wastewater to start up the sulfur-redox reaction in UASB for effective organic removal even at low temperature. All the systems were connected with peristaltic pumps to supply the influent to the respective units except UASB effluent, which was transferred to DHS by gravity.

The start-up of UASB and A_2SBR was done by the inoculation of the mesophilic digested sludge from the same sewage treatment center. The integrated system was operated for 600 days and the time period was categorized on the basis of ambient temperature of 15.1°C - 29°C as summer and 8°C - 15°C as winter. The hydraulic retention time (HRT) of UASB, DHS and A_2SBR was 8 h, 3.2 h and 12 h respectively. 50 mL of sodium acetate was used as carbon source in A_2SBR. At the initial phase of A_2SBR, anaerobic phase takes place where biomass uptakes carbon and releases phosphate into the system. It lasts up to 90 min. During anoxic phase, DHS effluent of 50 L is fed into the reactor and stirred continuously for 200 min. After that, the stirring is stopped and settling phase occurs for 60 min where the tank acts as a clarifier without any inflow or outflow. Finally, in the idle phase the clarified supernatant is discharged as treated effluent for 10 min.

2.3 Sampling and analytical methods

The performance of the whole system was monitored by the routine analysis of 24 h composite samples of sewage and UASB and grab samples of DHS and A_2SBR. The analysis was carried out twice a week. The parameters like temperature, dissolved oxygen (DO), oxygen reduction potential (ORP) and pH were measured regularly on site. Samples were preserved in an ice cool box at 4°C prior to analysis. The other parameters such as suspended solids (SS), chemical oxygen demand (COD_{Cr}), biological oxygen demand (BOD_5), total kjeldahl nitrogen (TKN), total phosphorus (TP), nitrites, nitrates etc. were analyzed according to the standard methods (APHA, 2005).

3.0 Results and Discussion

3.1 Performance of reactor for organic removal

Fig. 2 shows the time series of ambient temperature and organic treatment performance in terms of SS, COD_{Cr}, and BOD_5 over the time period of 600 days. The wastewater concentrations of SS 109 ± 64 mg/L in summer and 83 ± 24 mg/L in winter were decreased to 14 ± 19 mg/L and 22 ± 15 mg/L after being treated in UASB-DHS. Similarly, UASB-DHS showed total COD_{Cr} and BOD_5 concentrations of 41 ± 32 mg/L and 7 ± 7 mg/L in summer whereas 64 ± 35 mg/L and 15 ±10 mg/L in winter as shown in Table 1.

Similarly, the corresponding average SS, COD_{Cr} and BOD_5 removal efficiencies of the system in summer were 86%, 87% and 97% and the removals in the winter were 69%, 78% and 88% respectively. This result revealed that this process achieved significant organic removal in summer than in winter. The removal rates of UASB-DHS in this study were slightly higher than the studies by Machdar *et al*. (2000), Tandukar *et al*. (2006) and Mahmoud *et al*. (2010) with different generations of DHS reactors. But still, good organic removal even at low temperature in UASB-DHS could be attributed to the existence of sulfate-reducing bacteria capable of decomposing organic matter in UASB (Takahashi *et al*., 2011) and large amount of active biomass retained in DHS sponges (Tandukar et al. 2006). Furthermore, unlike other aerobic system, DHS possess a well pronounced advantage i.e. needlessness of external aeration thereby contributing in less energy requirement which has been well documented by Tandukar *et al*. (2005) and Tanaka *et al*. (2012) too.

There have been limited studies on the organic removal by A_2SBR. The average SS, COD_{Cr} and BOD_5 removals by A_2SBR were 79%, 86% and 97% in summer and 83%, 86% and 97% in winter, respectively. When the removal efficiencies of UASB-DHS and UASB-DHS-A_2SBR was compared no significant differences was highlighted. It was then confirmed that major organic removal was contributed by UASB–DHS. However, overall results of the final effluent from UASB-DHS-A_2SBR indicated good organic removal efficiency than other conventional municipal wastewater treatment systems.

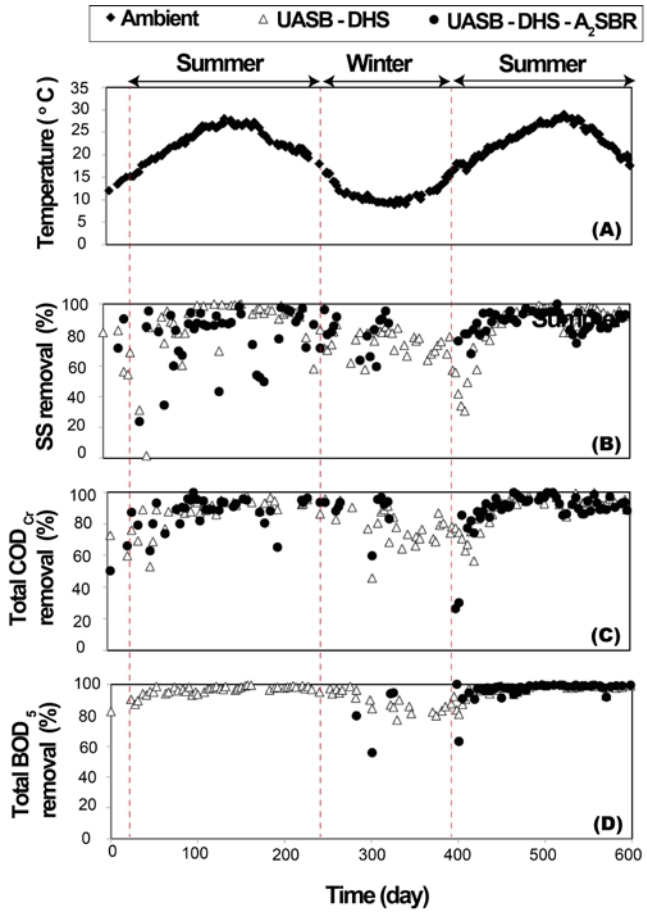

Fig. 2 – Time series of (A) ambient temperature recorded during the study, (B) SS removal rate, (C) Total COD_{Cr} removal rate and (D) Total BOD_5 removal rate.

Table 1- Summarized overview of process performance for organic removal

Parameters (mg / L)	Municipal wastewater (mg / L)	UASB-DHS eff. (mg / L)	UASB-DHS-A_2SBR eff. (mg / L)	UASB-DHS removal rate (%)	UASB-DHS-A_2SBR removal rate (%)
SS	109 ± 64 (83 ± 24)	14 ± 19 (22 ± 15)	21± 32 (14 ± 11)	86 ± 5 (69 ± 4)	79 ± 10 (83 ± 6)
Total COD_{Cr}	318 ± 108 (295 ± 97)	41 ± 32 (64 ± 35)	42 ± 41 (28 ± 12)	87 ± 5 (78 ± 3)	86 ± 5 (91 ± 2)
Total BOD_5	278 ± 12 (128 ± 55)	7 ± 7 (15 ± 10)	7 ± 11 (15 ± 8)	97 ± 2 (88 ± 2)	97 ± 3 (88 ±1)

Note: Values in parenthesis represent winter readings.

3.2 Effect of Contact Time and Initial Atrazine Concentration

The effect of contact time and initial atrazine concentration on adsorption of atrazine on oil palm shell-based adsorbent and activated carbon are shown in Figures 2 and 3, respectively. Batch adsorption experiments were carried out for 24 h to attain equilibrium. Figure 2 shows that the contact time necessary for adsorption of atrazine on oil palm shell-based adsorbent to reach equilibrium ranged between 150 to 240 min. However, for adsorption of atrazine on activated carbon, longer contact time of 24 h was required to achieve adsorption equilibrium, as shown in Figure 3. It could be seen that the adsorption rate at different concentrations was rapid in the first 15 min and steadily decreased with time until it gradually approached a plateau. The initial rapid uptake could be attributed to the availability of the number of free adsorption sites on the adsorbent and the higher concentration gradient created at the beginning of the adsorption process (Alam *et al*., 2004). As the atrazine loading on the adsorbent increased, the concentration gradient reduced and gave way to a much slower uptake. Furthermore, the atrazine uptake, qt increased with increasing in initial atrazine concentration. The amount of atrazine uptake at equilibrium, qe increased from 0.168 to 3.378 mg/g for oil palm shell-based adsorbent and from 5.392 to 30.734 mg/g for activated carbon, with the increase in the initial atrazine concentrations from 5 to 30 mg/L. The initial concentration provided an important driving force to overcome all mass transfer resistances of the atrazine between the aqueous and solid phases. Hence, a higher initial concentration of atrazine would enhance the adsorption process. Furthermore, the adsorption of atrazine could be described by three consecutive mass transport steps (Alam *et al*., 2007). Firstly, the adsorbate transferred through the solution to the adsorbent exterior surface, followed by adsorbate diffusion into the pores of adsorbent. Finally, the adsorbate was adsorbed into the active sites at the interior of the adsorbent particle. Thus, activated carbon showed a much better adsorption performance than oil palm shell-based adsorbent, which could be attributed to the higher porosity in activated carbon.

3.3 Performance of reactor for nutrient removal

The nutrient removal efficiency of UASB-DHS was improved after the introduction of A_2SBR. The removal efficiency of nitrogen and phosphorus of A_2SBR directly depended on DHS effluent. A_2SBR showed 52% of average phosphorus removal in both seasons and showed no distinct difference. However, TKN and NH_4^+ removal rates (data not shown) in summer were 92% and 88% and during winter the removal rates dropped almost to half of the summer performance rates to 37% and 41% respectively. This could be attributed to the effect of temperature in the activity of nitrifying bacteria which drops sharply below 15°C as the optimum temperature for their growth is within the range of 15°C-30°C (Shammas *et al*., 1986). Meanwhile, the behavior of microorganism responsible for nutrient treatment was also studied for better understanding of this system. For this, the profiling data of day 475 was taken as shown in Fig. 3. The microorganisms responsible for phosphorus removal in this process were

mostly considered as DNPAOs since other PAOs cannot thrive under simultaneous anaerobic and anoxic conditions. Within 90 min of the anaerobic phase, on one hand there was gradual decrease in carbon concentration from 126 mg/L to 24 mg/L while on the other hand there was increase of phosphate concentration from 3.8 mg -P/L to 36 mg-P/L. During this process, the COD_{Cr} uptake and phosphate release ratio was 0.8 which was in agreement with the range suggested by Lui *et al*. (1997) i.e. 0.04 –1.32, depending on the content of phosphorus in microorganism. While in the anoxic phase, after the addition of nitrate rich DHS effluent, the amount of phosphate uptake and nitrate removal was measured. However in winter season from day 301 to day 436 when temperature dropped to 11°C, nitrification rate significantly decreased in DHS (Fig. 4). Thus, external nitrate source ($NaNO_3$) was added in DHS effluent before feeding into A_2SBR to ensure the nitrate requirement for anoxic phase. As the reactor was configured airtight, it was obvious that nitrate acted as the electron donor. Eventually, the final effluent showed nitrate and phosphate concentration of 7mg/L and 1 mg/L respectively. The results clearly exhibited phosphorus uptake with simultaneous denitrification which is the requisite characteristics of DNPAOs. Hence, it can unanimously be propounded that DNPAOs presented a good phosphate and nitrate removal in this system. Yet this system is highly beneficial for lowering aeration cost and reducing sludge production (Kuba *et al*., 1997). Moreover, at the initial start-up period, pH and COD/P ratio varied and it was noticed that both nitrogen and phosphorus removal were unstable and unsatisfactory as indicated in Fig. 4. On day 195, pH and COD/P were maintained to 7.4 ± 0.2 and 20 respectively, which showed phosphate concentration as low as 1 mg-P/L. The corresponding average removal rate of 76% with the influent concentration of 1.9 mg-P/L to 9 mg-P/L without any external aeration. The optimum pH condition was maintained slightly alkaline in reference to Liu *et al.* (1996) who reported that an acidic pH has negative effect on both acetate uptake and P-release in anaerobic stage whereas alkaline pH tends to inhibit the uptake of acetate and stimulate P-release more than at acidic pH.

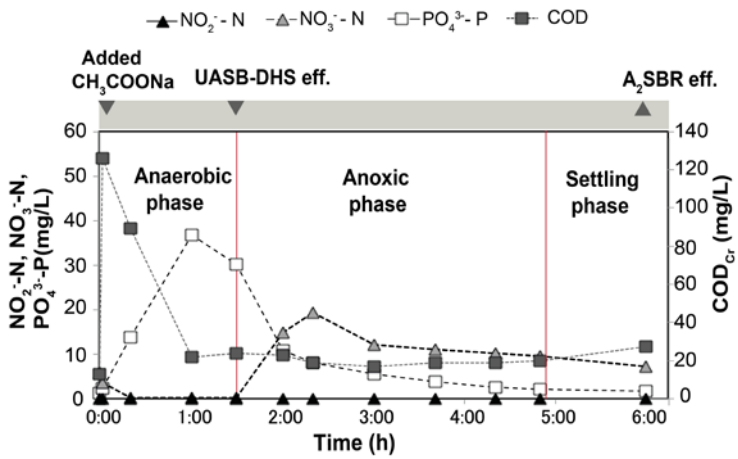

Fig. 3 Profiles of the concentrations of nitrite, nitrate, phosphate and COD during one cycle of A_2SBR operation.

Similarly, with the influent concentration of 9.2 mg-N/L to 25.5 mg-N/L corresponding nitrogen concentrations as low as 5 mg-N/L was achieved delivering average removal rate of 82%. This is due to the fact that the optimum pH for the denitrification is between 7.0 and 8.0 (Metcalf and Eddy, 2003) and henceforth the optimum pH of 7.4 ± 0.2 was maintained throughout the study.

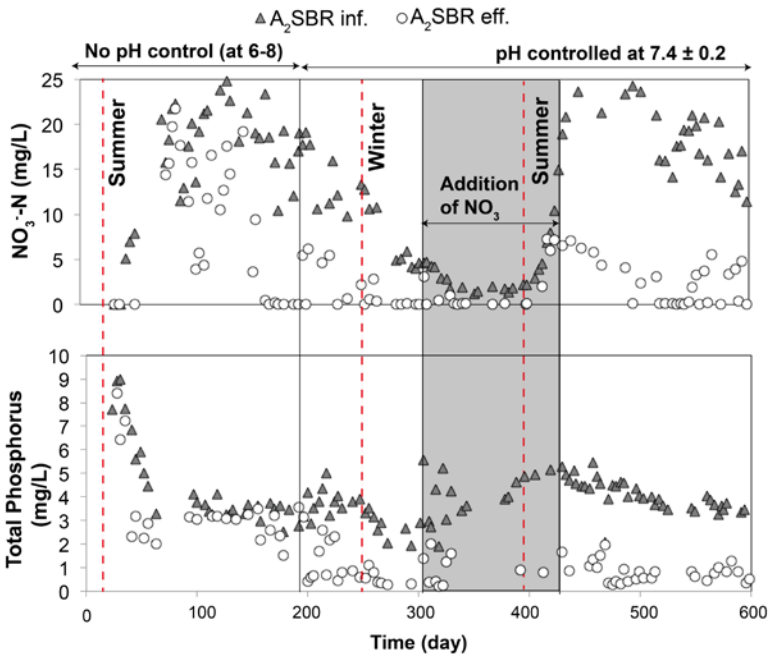

Fig. 4 Time series of nitrate and total phosphorus concentration showing effect of pH control in the system.

4.0 Conclusions

The overall performance of the integrated system of UASB-DHS-A_2SBR demonstrated good organic removal rates of sulfate containing municipal wastewater having COD/SO_4^{2-} average ratio of 4. The average SS, COD_{Cr} and BOD removal rates of 86%, 87% and 97% were obtained from UASB-DHS in summer. The average winter performances for the same parameters were 69%, 78% and 88% respectively. The TKN and NH_4^+ removal rates in summer were 92%, 88 % and during winter the removal rates dropped almost to half the summer performance rates to 37% and 41%. Under adjusting the pH of 7.4 ± 0.2 and COD/P of 20 at SRT of 50 days phosphorus removal as low as 1 mg-P/L was achieved and nitrate in effluent remained less than 5 mg-N/L throughout the operation showing removal efficiency of 76% and 82% respectively. Thus, this trio combination of anaerobic, aerobic and anaerobic/anoxic systems unambiguously ensures

no aeration requirement, low cost, less excess sludge, less area requirement with efficient nutrient removal capacity. The remarkable finding of this study was that the final effluent was in consistency with the discharge standards of municipal wastewater. Therefore, this proposed system could be an innovative solution for present prevalent wastewater treatment problems due to effective organic and nutrient treatment especially in hot climatic zones.

5.0 Acknowledgements

Authors are grateful to academic supports of Nagaoka Chuo Jouka Center for this study.

References

APHA (2005) Standard Methods for the Examination of Water and Wastewater, 22 nd ed. American Public Health Association, Washington D. C., USA.

Araki N., Ohashi A., Machdar I. and Harada H. (1999) Behaviors of nitrifiers in a novel biofilm reactor employing hanging sponge-cubes as attachment site. *Water Sci. Technol*., **39**(7), 23-31.

Converti A., Rovatti M. and Del Borghi M. (1995) Biological removal of phosphorous from wastewaters by alternating aerobic and anaerobic conditions. *Water Res*., **29**(1), 263-9.

Foresti E., Zaiat M. and Vallero M. (2006) Anaerobic processes as the core technology for sustainable domestic wastewater treatment: Consolidated applications, new trends, perspectives, and challenges. *Rev. Environ. Sci. and BioTechnol.*, **5**(1), 3-19.

Kuba T., Wachtmeister A., Van Loosdrecht M. and Heijnen J. (1994) Effect of nitrate on phosphorus release in biological phosphorus removal systems. *Water Sci. Technol*., **30**(6), 263–269.

Kuba T. M. C. M., Van Loosdrecht M. C. M. and Heijnen J. J. (1996) Phosphorus and nitrogen removal with minimal COD requirement by integration of denitrifying dephosphatation and nitrification in a two-sludge system. *Water Res.*, **30**(7), 1702-1710.

Kuba T. M. C. M., Van Loosdrecht M. C. M., Brandse F. A. and Heijnen J. J. (1997) Biological dephosphatation by activated sludge under denitrifying conditions: pH influence and occurrence of denitrifying dephosphatation in a full-scale waste water treatment plant. *Water Sci. Technol.* **36** (12), 75–82.

Liu W. T., Mino T., Matsuo T. and Nakamura K. (1996) Biological phosphorus removal process effect of pH on anaerobic substrate metabolism. *Water Sci. Technol*., **34**(1-2), 25-32.

Liu W. T., Nakamura K., Matsuo T. and Mino T. (1997) Internal energy-based competition between polyphosphate-and glycogen-accumulating bacteria in biological phosphorus removal reactors—Effect of PC feeding ratio. *Water Res.*, **31**(6), 1430-1438.

Machdar I., Sekiguchi Y., Sumino H., Ohashi A. and Harada H. (2000) Combination of a UASB reactor and a curtain type DHS (downflow hanging sponge) reactor as a cost-effective sewage treatment system for developing countries. *Water Sci. Technol.*, **42**(3-4), 83-88.

Mahmoud M., Tawfik A and El-Gohary F (2010) Simultaneous organic and nutrient removal in a naturally ventilated biotower treating presettled municipal wastewater, *J. Environ. Eng*., **136**(3), 301-307.

Metcalf and Eddy, Inc., 2003. Wastewater Engineering: Treatment and Reuse. McGraw-Hill Book Company, New York, USA,

Mino T, Van Loosdrecht M. C. M and Heijnen J. J. (1998) Microbiology and biochemistry of the enhanced biological phosphate removal process. *Water Res*., **323**(11), 193–207.

Moawad A., Mahmoud U. F., El-Khateeb M. A. and El-Molla E. (2009) Coupling of sequencing batch reactor and UASB reactor for domestic wastewater treatment. *Desalin*., **242**(1), 325-335.

Onodera T., Matsunaga K., Kubota K., Taniguchi R., Harada H., Syutsubo K., Okubo T., Uemura S., Araki N.,Yamada M.,Yamaguchi M. and Yamaguchi T. (2013) Characterization of the retained Sludge in a down-flow hanging sponge (DHS) reactor with emphasis on its low excess sludge production. *Bioresour. Technol*., **136**, 169-175.

Shammas N. K. (1986) Interactions of temperature, pH and biomass on the nitrification process. *J. Water Pollut. Con. F.*, **58**(1), 52-59.

Tanaka H., Takahashi M., Yoneyama Y., Syutsubo K., Kato K., Nagano A., and Harada H. (2012) Energy saving system with high effluent quality for municipal sewage treatment by UASB-DHS. *Water Sci. Technol.*, **66**(6), 1186 -1194.

Takahashi M., Yamaguchi T., Kuramoto Y., Nagano A., Shimozaki S., Sumino H., Harada H. (2011) Performance of a pilot-scale sewage treatment: an up-flow anaerobic sludge blanket (UASB) and a down-flow hanging sponge (DHS) reactors combined system by sulfur-redox reaction process under low-temperature conditions. *Bioresour. Technol*., **102**(2), 753-757.

Tandukar M., Uemura S., Machdar I., Ohashi A. and Harada H. (2005) A low-cost municipal sewage treatment system with a combination of UASB and the “fourth generation” Down-flow hanging sponge (DHS) reactors, *Water Sci. Technol*., **52** (1/2), 323–329.

Tandukar M., Machdar I., Uemura S., Ohashi A. and Harada H. (2006) Potential of a combination of UASB and DHS reactor as a novel sewage treatment system for developing countries: long- term evaluation, *J. Environ. Eng.*, **132** (2), 166–172.

Tandukar M., Ohashi A. and Harada H. (2007) Performance comparison of a pilot-scale UASB and DHS system and activated sludge process for the treatment of municipal wastewater, *Water Res*., **45** (10), 237–242.

Tsuneda S., Ohno T., Soejima K. and Hirata A. (2006) Simultaneous nitrogen and phosphorus removal using denitrifying phosphate-accumulating organisms in a sequencing batch reactor. *Biochem Eng J.*, **27**(3), 191–6.

IN SITU TRANSMISSION ELECTRON MICROSCOPE: DIRECT OBSERVATION OF GRAPHITIZATION OF METAL DOPED CARBON NANOFIBER

M. Zamri Yusop[1,*], Masaki Tanemura[2]

[1] *Department of Materials, Manufacturing and Industrial Engineering,, Faculty of Mechanical Engineering, Universiti Teknologi Malaysia, 81310 UTM Johor Bahru, Johor, Malaysia*

[2] *Department of Physical Science and Engineering, Nagoya Institute of Technology, Gokiso-cho, Shouwa-ku, 466-844 Nagoya, Japan.*

**Corresponding author: zamriyusop@utm.my*

Abstract: The structural modification of crystallinity of ion induced Copper (Cu) doped carbon nanofiber (CNF) was observed carefully by in-situ transmission electron microscopy (TEM) facilities during bias voltage on the CNF. The initial TEM observation of the Cu-doped CNF showing that it was consist mixture of amorphous carbon and very fine crystalline Cu structure which small Cu particles randomly dispersed and covered by amorphous carbon. The fibrous solid amorphous structures of ion induced CNF significantly changes to single crystalline encapsulated graphitic structure due to the Joule Heating with dramatic improvement of graphitization of CNFs from amorphous to crystalline. The latter structure significantly similar to multi-layered graphenes structure. Direct observation of in-situ TEM results will provide very useful information about the graphene structure formation and the critical information of solid phase reaction of graphene synthesis mechanism.

Keywords: *In-situ TEM observation, ion irradiation method, carbon nanofibers, joule heating.*

1.0 Introduction

The carbon nanomaterials such as carbon nanotubes (CNTs) (Iijima, 1991) , CNFs (Tanemura *et al.*, 2006) and graphene (Geim *et al.*, 2007) have attracted a significant interest as an efficient electron emitters due to their potential application in the future flat panel displays, electron beam instruments, x-ray sources etc (Wang *et al.*, 2001; de Jonge *et al*., 2005, Cheng *et al.*, 2006; Tan *et al*., 2004) . There are several advantages of the carbon nanomaterials based electron emitter such as very high aspect, sharp tip, chemical inertness etc. leading to restrain the applied voltage to emit electrons even at very low vacuum pressure (Rinzler *et al*., 1995). In general, CNTs and graphene are usually synthesized at high temperature growth process (Pan *et al*., 1998; Ren *et al*., 1998; Tanemura *et al*., 2001). On the contrary, ion induced CNFs can be fabricated at low temperature even at room temperature. Recent progresses have shown that ion induced CNFs can be directly fabricated on a transparent polymer surface (Ghosh *et al.*, 2010) and copper plate (Ghosh *et al*., 2011) also. Due to exceptional amorphous properties of CNFs, the fabrication of CNFs usually does

not need details information of temperature and annealing process. Graphene have similar synthesis method like CNTs which usually require high temperature process. The growth mechanism of CNTs and graphene still involve in details explanation in order to obtain perfectly desired properties of CNTs and graphene. The observation of graphitic structure of CNTs and graphene can be only performed under powerful microscope such as TEM and scanning transmission electrons microscope (STEM). However, the growth formation layer by layer of CNTs and graphene can be only observed by in situ TEM facilities that require external piezo devices equipped in the special TEM holder. In the previous work, we have discussed the formation of CNT from CNF using in situ facilities during field emission process. We believed that the graphitic formation could be controlled by in situ TEM facilities. Hence, in this work we challenged the direct observation of graphenes layers formation from Copper (Cu) incorporated CNF using in situ TEM facilities.

2.0 Experimental Setup

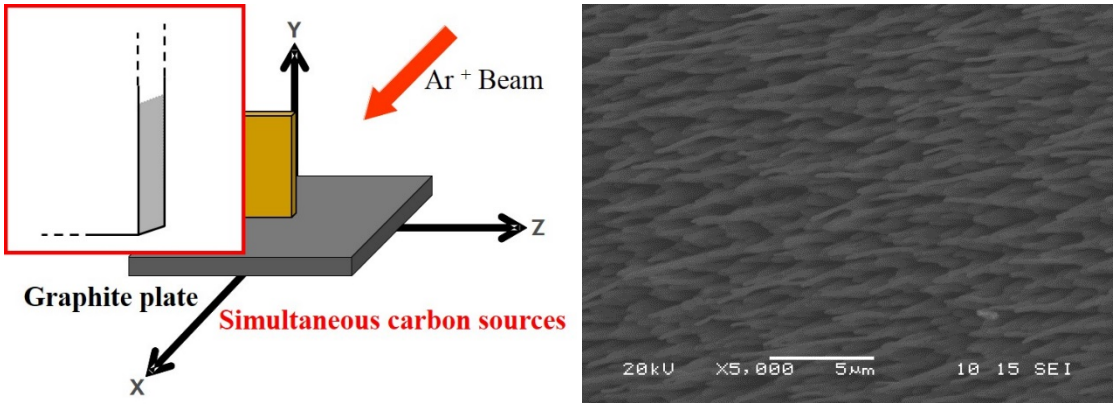

Figure 1. Schematic diagram of sample setup and the SEM image of the morphology of Fe-doped CNFs at the Cu foil edge after Ar^+ ion bombardment. The inset shows the marked area where CNFs were mostly grown.

We used a Kaufmann-type ion gun (Iontech. Inc. Ltd., model 3-1500-100FC) for growing CNFs. Samples employed were commercially available Copper foils having size 5 mm × 10 mm × 100 μ m and, and the edge of the foils were irradiated with argon ion (Ar^+) ions at room temperature. The growth mechanism of ion-induced CNFs was explained elsewhere in detail (Tanemura *et al*., 2004). For the Cu incorporated CNFs growth, an additional graphite plate, having size 15 mm × 10 mm × 1 mm, as a C supply was placed horizontally adjacent to the Cu foil and they were co-irradiated with Ar^+ at 45° from the normal to the surface for 45 minutes at room temperature (Figure 1). The oblique Ar^+ bombardment is known to be more suitable for the growth of ion induced CNFs than normal incidence (Tanemura *et al*., 2005). The diameter and ion beam energy employed for this experiment were 6 cm and 1 keV, respectively. The basal and working pressures were 1.5×10^{-5} and 2.0×10^{-2} Pa, respectively.

After sputtering, the morphology of the Cu incorporated CNFs grown on the edge of the Cu foils was carefully observed by scanning electron microscope [SEM (JEOL JSM-

5600)] and the crystallinity of the sample was examined by TEM (JEOL JEM-2010). We used a TEM sample holder (JEOL; EM – Z02154T) with a piezo-controlled tungsten (W) nanoprobe coated with gold (Au) to apply a bias voltage on the single composite CNF samples. The Cu foil was cut into 2 mm width and directly mounted on the TEM sample holder without any other post treatment.

3.0 Results and Discussion

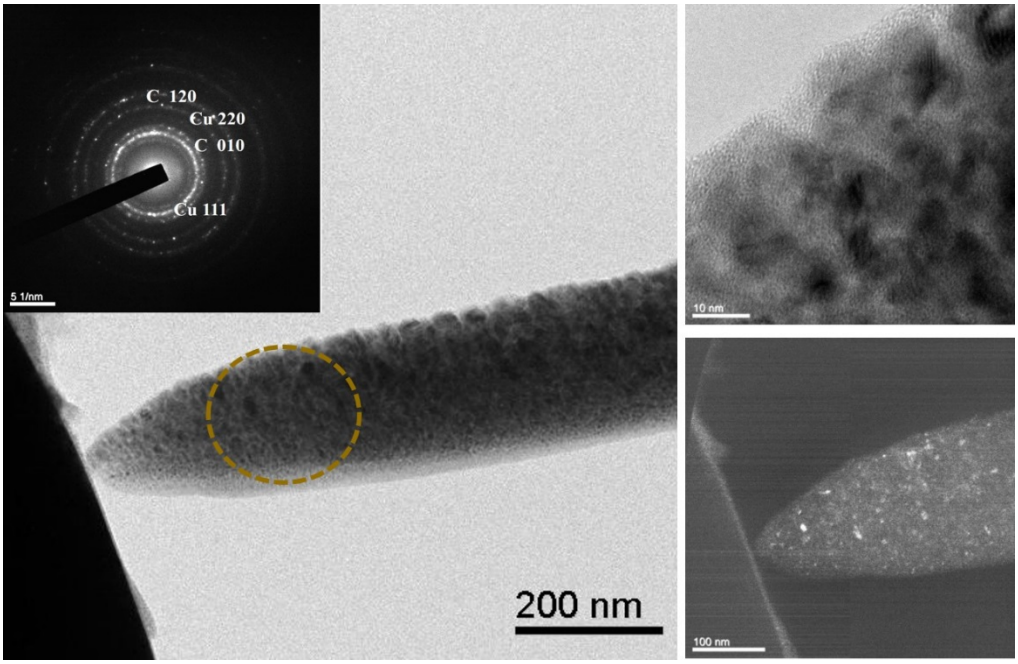

Figure 2. (a) TEM image of the intact structure of Cu incorporated CNF before bias voltage. (Inset show the selected area diffraction pattern). (b) The high magnification of TEM images of the fiber show the polycrystalline structure dispersed in amorphous carbon. (c) The dark field image shows the distribution of Cu particles in the carbon amorphous structure.

Figure 1 (b) shows the SEM image of Cu incorporated CNFs after ion irradiation. It should be noted that only single CNFs grew on respective cones and no CNFs grew without cone bases. The CNF was vibrating due to the charge effect from the TEM electron beam. During structure observation, we overcome this problem by contacting the nanoprobe with the CNF's tip. Figure 2(a-c) show the TEM images of Cu incorporated CNFs. The Cu incorporated CNFs was approximately 1 μm in length and 200 nm in diameter (Figure 2(a)). The inset image shows the selected area electron diffraction (SAED) pattern of the Cu incorporated CNF. From the SEAD pattern results it shows that Cu incorporated CNF consist of dominant diffraction spots of C 120, C 010, Cu 111 and Cu 220. Figures 2(b) shows the fibrous structures of the Cu incorporated CNF in high magnification at the fiber part revealing that dispersion of several polycrystalline nanostructures in the amorphous carbon matrix. Further investigation of dark field images from SEAD pattern indicated that Cu particles dispersed randomly in the amorphous carbon structure.

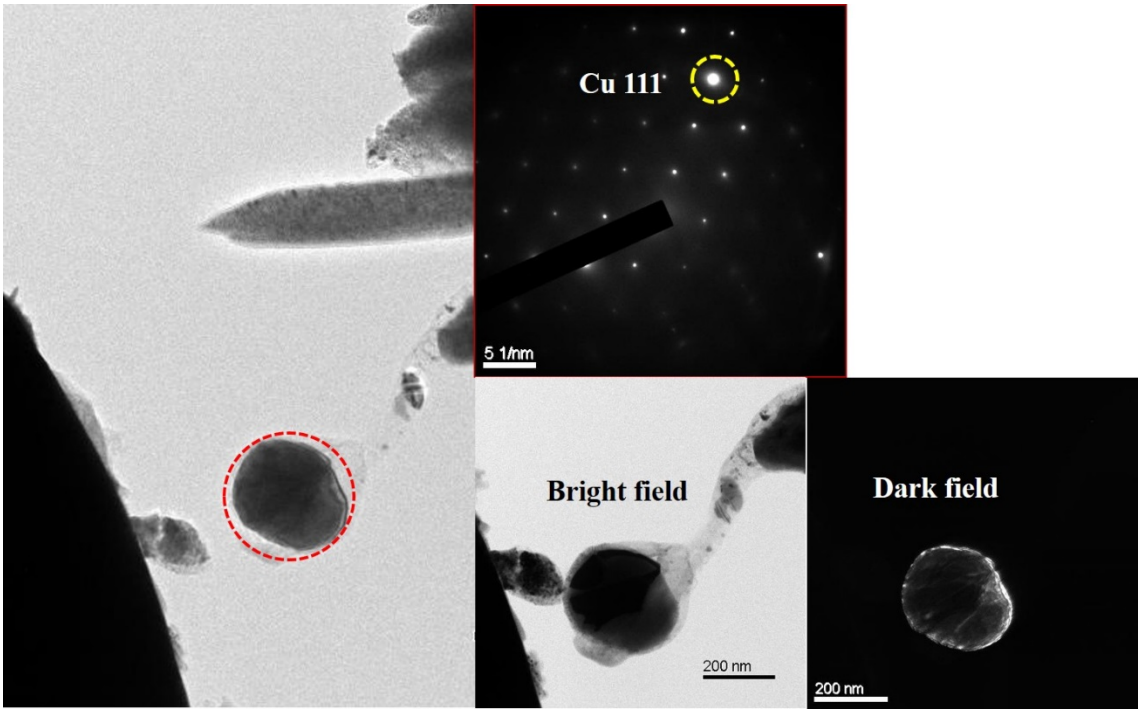

Figure 3 (a) The TEM image of Cu incorporated CNF after bias voltage. (b) The SAED pattern area that marked in figure 3(a) shows the crystalline structure of Cu 111. (c) The bright field image from the SAED results which clearly indicating metal crystalline (dark region) covered by graphitic layers formation (bright region) and (d) showing the dark field image from the SAED result that clearly shows area of the crystalline diffraction point from figure 3(b).

To investigate the structures transformations of Cu incorporated CNFs by bias voltage; we performed low applied bias voltage at 200 mV flow on metal incorporated CNF with additional 200 kΩ external resistor. The external resistor helps to reduce the shock damage at the CNF tip during applied bias voltage, hence proper structural transformation observable. The sample was observed at × 30k magnification in TEM. The gold (Au) coated tungsten (W) nanoprobe was slowly controlled by piezo driver to touch the Cu incorporated CNF tip. This also help to stabilize the CNF tip during the image capture process. The pressure in the specimen chamber was about 10^{-5} Pa during the applied bias. The structural transformation was captured using the CCD device and recorded using the computer software. The Cu incorporated CNF was transformed instantaneously after the applied bias voltage.

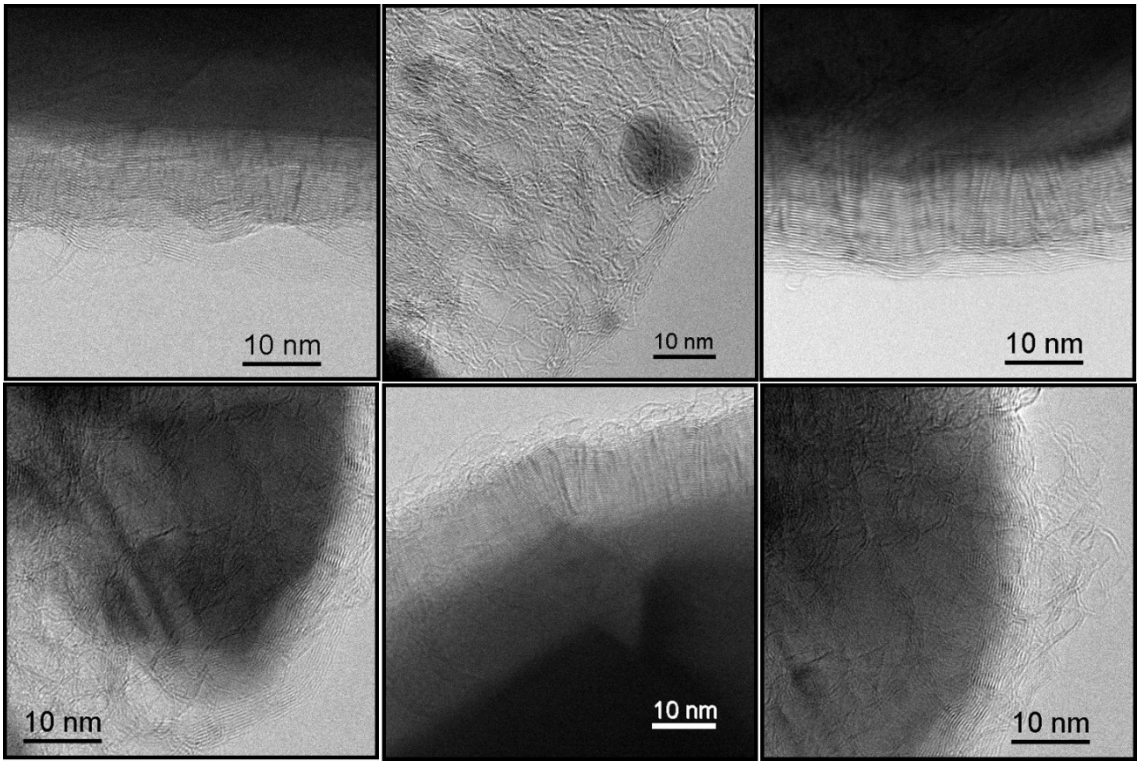

Figure 4 (a-f) The graphitic layer formation formed at the outer crystalline structure of Cu from the high magnification TEM. Most of the graphitic layers are around 10 – 13 nm.

Figure 3(a-d) shows the Cu incorporated CNF structure after the applied bias voltage. The Cu incorporated CNF significantly transformed into single crystalline particles encapsulated by graphitic layers after applied bias voltage due to the induced joule heating. The Cu nanoparticles from the fiber part of Cu incorporated CNF was agglomerated into huge sphere-like particles whilst amorphous carbon transformed into graphitic layers surrounding the agglomerated Cu particles (Figure 3(a)). This statement proven by the SAED pattern of round shape particle that clearly showed diffraction spots were single crystal of Cu 111 in figure 3(b). For further investigation, the bright field of the latter particle was taken using the SEAD spot clearly indicating that the graphitic formation covering the crystalline structure in figure 3(c). Finally, we can reconfirm that the crystalline area of the Cu 111 diffraction spot in figure 3(b) from the dark field image in figure 3(d). From figure 3(a-d) we understand that induced joule heating cause the Cu nanoparticles that randomly dispersed in the fibrous structure agglomerated and forming into large single crystalline structure of Cu 111. Both SAED pattern and dark field images also reconfirm that this result are not influence from the neighboring CNF part.

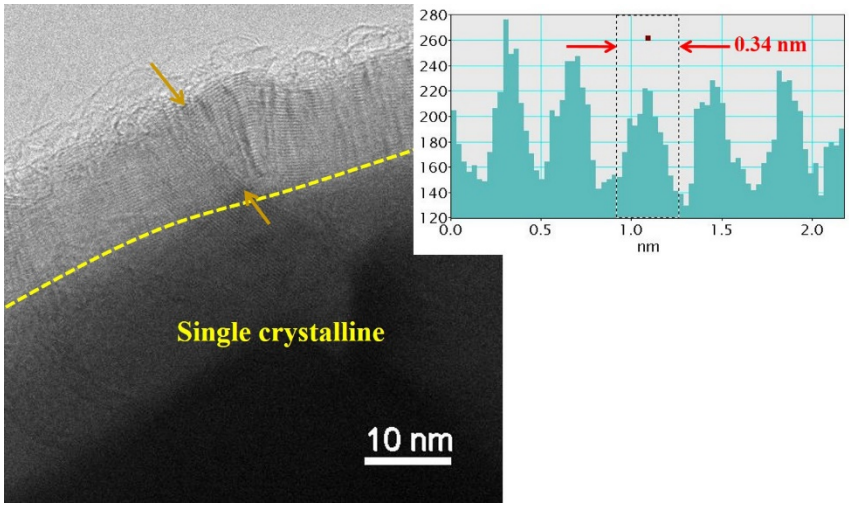

Figure 5 shows the distance profile result from figure 4 (e) indicating the bright region formation having thickness around 0.34 nm.

Figure 4(a-f) shows the high magnification TEM of the graphitic layers formation from figure 3(a). From these result we understand that most of the graphitic layers are around 10 – 13 nm. However, there a few sample shows very thin layers of graphene in less than two layers. Figure 4 (d) shows very fine formation of 10 layers graphitic structure. Figure 5 showing the distance profile result that indicating the layers thickness were around 0.34 nm. This distance value is similar to graphene thickness which we can confirm the formation of bright region in the TEM is graphitic layers formation. The distance profile also shows that the thickness formation were same for each layers which confirm there was no other carbide formation in the bright region.

In order to understand the effect of the Joule heating from the bias voltage we need to estimate the temperature rising during the applied voltage. According to Vincent *et al*. (2002), the temperature rising of 1-D object during current flow can be estimated using a resistive heating model. For a 1-D object like CNF, the temperature distribution equation is expressed as follows:

$$\Delta T(K) = T_L(K) - T_0(K) = \frac{RLI^2}{2\kappa A} \qquad (1)$$

where R is the metal resistivity of CNTs/CNFs (3.85×10^{-5} Ω.m), K is the thermal conductivity (20 W/mK), $A = \pi r^2$, the cross sectional area of a CNF and I is the current flow. In our present experiment, the length and radius of CNF`s tip was found to be 1000 and around 10 nm, respectively. The current flow was up to 1 μ A. The current would flow along the CNF from the tip part through outer surface and hence most of the structural change would occur from the outer layers (Wang *et al*., 2002). If the outer layer thickness is assumed to be 0.34 nm (corresponding to 1 layer thickness of graphene), the temperature of the outer layer during the applied bias voltage estimated from the above Equation (1) has been reached to $4.92 \times 10^{+2}$ K, which would be satisfy for the recrystallization temperature of CNF structure. So, generation of Joule heating during applied bias would be responsible for the structural change of the Cu incorporated CNF.

4.0 Conclusions

In summary, significant structural transformation of a Cu incorporated CNF fabricated on Cu foil was observed using in situ TEM facilities. After the applied bias voltage, the dramatic change in the Cu incorporated CNF structure from fibrous amorphous and/or very fine crystallites to single crystal encapsulated graphitic structure was observed. The randomly dispersed Cu nanoparticles was agglomerated and formed into single crystalline structure whilst amorphous carbon transformed into graphitic structure and covering the single crystalline particle. Joule heating would be responsible for the structural change of the Cu incorporated CNF.

5.0 Acknowledgement

The authors would like to acknowledge the financial support from the Malaysian Ministry Education and Universiti Teknologi Malaysia under GUP grant (Q.J130000.2546.12H54) and Higher Institution Centre of Excellent (HiCoE) grant. A part of the research work also has been done in Nagoya Institute of Technology.

References

Cheng, Y.; Zhang, J.; Lee, Y. Z.; Gao, B.; Dike, S.; Lin, W.; Lu, J. P.; Zhou, O. **2004,** *Development of a carbon nanotube based microfocus x-ray tube with single focusing electrode**, ReV. Sci. Instrum.,*** 75, 3264.

de Jonge, N.; Lamy, Y.; Schoots, K.; Oosterkamp, T. H. **2002,** High brightness electron beam from a multi-walled carbon nanotube., Nature 420, 393.

de Jonge, N.; Allioux, M.; Oostveen, J. T.; Teo, K. B.; Milne, W. I. **2005,** *Low Noise and Stable Emission from Carbon Nanotube Electron Sources.* Phys. ReV. Lett. 94, 186807.

Geim, A. K. and Novoselov, K. S. **2007,** *The rise of graphene*, Nature Materials, 6, 183 – 191.

Ghosh, P.; Zamri, M. Y.; Satoh, S.; Subramanian, M.; Hayashi, A.; Hayashi, Y.; Tanemura, M. **2010,** *Transparent and Flexible Field Electron Emitters Based on Conical Nanocarbon Structures.* J. Am. Chem. Soc. 132, 4034

Ghosh, P.; Zamri, M. Y.; Ghosh, D.; Hayashi, A.; Hayashi, Y.; Tanemura, M., **2011,** *Direct fabrication of aligned metal composite carbon nanofibers on copper substrate at room temperature and their field emission property*, Chem. Comm. 47, 4820–4822.

Iijima, S. **1991** *Helical microtubules of graphitic carbon* Nature**,** 354, 56.

Pan, Z. W.; Xie, S. S.; Chang, B. H.; Wang, C. Y.; Lu, L.; Liu, W.; Zhou, W. Y.; Li, W. Z. , **1998,** Very long carbon nanotubes Nature, 394, 631.

Ren, Z. F.; Huang, Z. P.; Xu, J. W.; Wang, J. H.; Bush, P.; Siegal, M. P.; Provencio, P. N. **1998,** Synthesis of large arrays of well-aligned carbon nanotubes on glass, Science, 282, 1105.

Rinzler, G.; Hafner, J. H.; Nikolaev, P.; Lou, L.; Kim, S. G.; Tomanek, D.; Nordlander, P.; Colbert, D. T.; Smalley, R. E. **1995,** *Unraveling Nanotubes: Field Emission from An Atomic Wire* Science, 269, 1550

Tan, T. T.; Sim, H. S.; Lau, S. P.; Yang, H. Y.; Tanemura, M.; Tanaka, J. **2006,** *X-ray generation using carbon-nanofiber-based flexible field emitters,* Appl. Phys. Lett. 88, 103105.

Tanemura, M.; Okita, T.; Tanaka, J.; Kitazawa, M.; Itoh, K.; Miao, L.; Tanemura, S.; Lau, S. P.; Yang, H. Y.; Huang, L. **2006** Room-Temperature Growth and Applications of Carbon Nanofibers: A Review**,** IEEE Trans. Nanotechnol. 5, 587.

Tanemura, M.; Iwata, K.; Takahashi, K.; Fujimoto, Y.; Okuyama, F.; Sugie, H.; Filip, V. **2001,** *Growth of aligned carbon nanotubes by plasma-enhanced chemical vapor deposition: Optimization of growth parameters,* J. Appl. Phys. 90, 1529.

Tanemura, M.; Okita, T.; Yamauchi, H.; Tanemura, S.; Morishima, R. **2004,** *Room-Temperature Growth of a Carbon Nanofiber on the Tip of Conical Carbon Protrusions,* Appl. Phys. Lett. 84, 3831.

Tanemura, M.; Tanaka, J.; Itoh, K.; Fujimoto, Y.; Agawa, Y.; Miao, L.; Tanemura, S. **2005,** *Field Electron Emission from Sputter-Induced Carbon Nanofibers Grown at Room Temperature,* Appl. Phys. Lett. 86, 113107.

Vincent, P.; Purcell, S. T.; Journet, C.; Binh, V. T. **2002,** *Modelization of resistive heating of carbon nanotubes during field emission,* Phys. Rev. B 66, 075406.

Wang, Q. H.; Yan, M.; Chang, R. P. H. . **2001,** *Flat panel display prototype using gated carbon nanotube field emitters,* Appl. Phys. Lett78, 1294.

Wang, Z. L.; Gao, R. P.; de Heer, W. A.; Poncharal, P. **2002,** *In situ imaging of field emission from individual carbon nanotubes and their structural damage.* Appl. Phys. Lett. 80 , 5, 856.

STEADY STATE CHARACTERISTICS OF NPC INVERTER WITH VOLTAGE BOOSTER

Eiichi Sakasegawa [1]*, Shota Waki[1] & Kichiro Yamamoto[2]

[1] *Department of Electrical and Electronics Engineering, National Institute of Technology, Kagoshima College, 1460-1 Shinko, Hayato, Kirishima, Kagoshima 899-5193, Japan*
[2] *Department of Electrical and Electronics Engineering, Kagoshima University, 1-21-40, Korimoto, Kagoshima 890-0065, Japan*

*Corresponding Author: *sakasegw@kagoshima-ct.ac.jp*

Abstract: This paper studies on steady state characteristics of neutral-point-clamped (NPC) inverter with voltage booster. The voltage booster controls not only DC link voltage but also neutral-point-potential. In this paper, the steady state characteristics of neutral-point-potential control is represented by both simulated and experimental results. A permanent magnet (PM) motor is used as a load. Furthermore, it is shown that the simulated results agree well with the experimental results.

Keywords: *Neutral-point-potential, NPC inverter, Voltage booster, PM motor, Compensation*

1.0 Introduction

In recent years, automotive manufacturers have released their Electric Vehicle (EV) and its market is increasing year by year. Conventional 2-level inverter with voltage booster is a major system for motor drive system of EV or Hybrid EV (Mizutani *et al*., 2015; Yamamoto *et al*., 2011). The reason of using the voltage booster is to obtain higher voltage than back-emf generated by the PM rotor magnets in high speed range (Morimoto *et al*., 2010). As a new technology, NPC inverter with voltage booster has been proposed for motor drive system of EV (Furuta *et al*., 2010) and wind power generation system (Yaramasu *et al*., 2014). The NPC inverter is widely used in industry or railway vehicle field. It has many advantages such as high capacity, low current distortion and high voltage in comparison with 2-level inverter (Nabae, Takahashi, Akagi,1981). On the other hand, the NPC inverter has a feature that the neutral-point-potential is fluctuated because of asymmetry of PWM waveform and individual difference of capacitors and switching devices. That may cause unbalance of the two capacitor voltages in the NPC inverter, and excessive voltage may break down switching devices (Ogasawara, Sawada, Akagi,1993). Therefore, it is very important to control the neutral-point-potential. The NPC inverter with voltage booster has a remarkable advantage that the voltage booster is able to control

not only DC link voltage but also neutral-point-potential. That makes NPC inverter free in terms of neutral-point-potential control and gives high control performance to the NPC inverter. This paper shows steady state characteristics of NPC inverter with voltage booster. It is shown that the simulated results agree well with the experimental results.

2.0 A NPC inverter system with voltage booster

Figure1 and Figure 2 show circuit configuration of the NPC inverter with voltage booster and block diagram of control system, respectively. Table 1 represents motor parameters used for simulation and experiments. This circuit topology originally has an ability to regenerate the electric energy. In this paper, however, the regenerative operation is not investigated. Therefore, DC supply with diode-bridge is used for the experiments. Surface permanent magnet synchronous motor (SPM) is used as a load. Output voltage of the NPC inverter is regulated by speed and current PI controller. There are many PWM methods for the NPC inverter, we decided to use the unipolar PWM method as a simple and easy method. The resistor 5Ω connected in series with the inductor suppresses the peak of the inductor current. Furthermore, a feedforward control is implemented for the suppression.

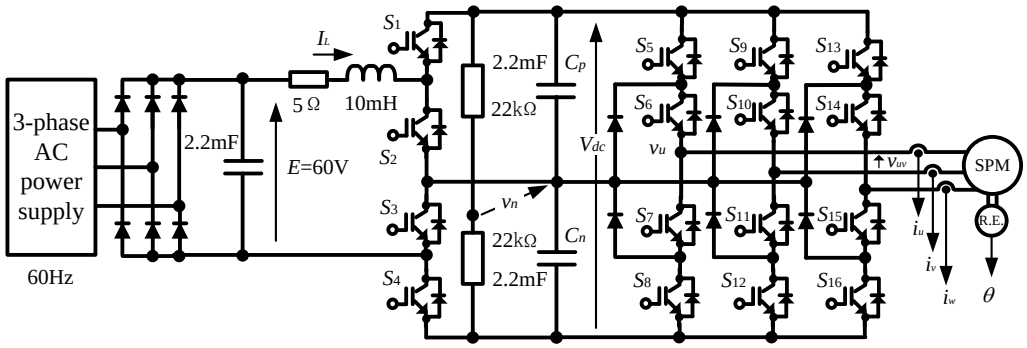

Figure 1. Circuit configuration of NPC inverter with voltage booster.

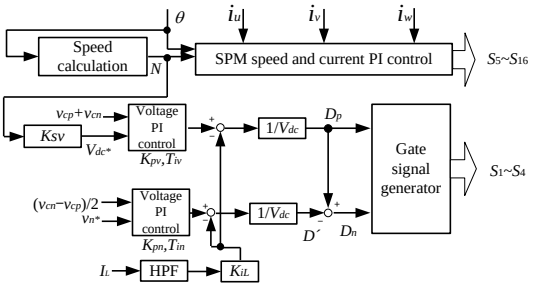

Figure 2. Block diagram of control system.

Table 1: Motor parameters

Motor rated output	120 W
Motor rated voltage	100 V
Motor rated speed	2500 rpm
Motor rated torque	0.47 N-m
Motor rated current	2 A
Stator resistance	2 Ω
Field flux	0.0457 Wb
Armature inductance	4 mH
Pole number p	8
Moment of inertia	0.00055 Kg-m^2

3.0 Control method of the system

3.1 Princple of DC link voltage and neutral-point-potential control

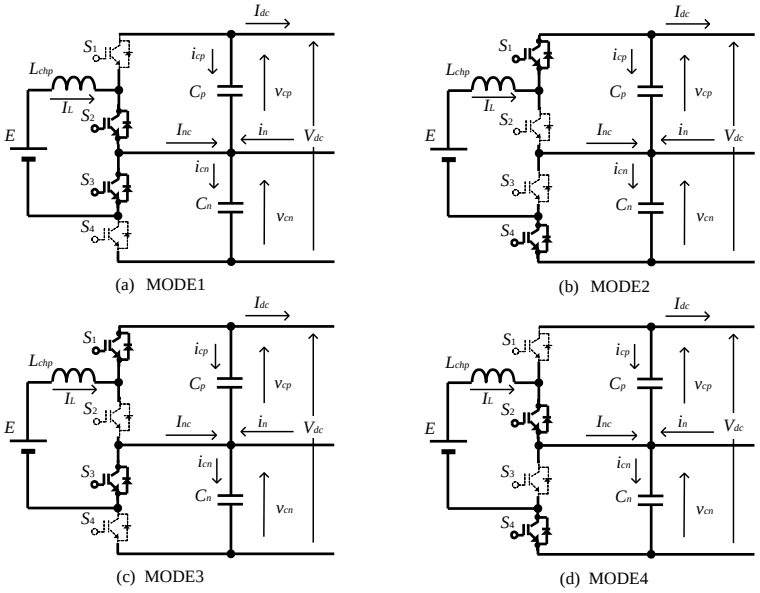

Figure3. Operating modes of voltage booster.
(a) S_2, S_3:ON, S_1, S_4:OFF. (b) S_1, S_4:ON, S_2, S_3:OFF.
(c) S_1, S_3:ON, S_2, S_4:OFF. (d) S_2, S_4:ON, S_1, S_3:OFF.

Figure 3 represents operating modes of the voltage booster. In this paper, we defined the voltage booster for NPC inverter as NPC voltage booster. SPM is connected to the NPC inverter although it is not seen in the Figure 3. Figure 3(a) illustrates MODE1 in which S_2, S_3 are ON and S_1, S_4 are OFF. In MODE1, magnetic energy is stored in the inductor. Figure 3(b) illustrates MODE2 in which S_1, S_4 are ON and S_2, S_3 are OFF. In MODE2, the inductor supplies the magnetic energy to the load, and boosts the DC link voltage. By cycling the two modes of MODE1 and MODE2, the NPC voltage booster operates as well as the conventional voltage booster. Figure 3(c) illustrates MODE3 in which S_1, S_3 are ON and S_2, S_4 are OFF. In MODE3, the inductor supplies the stored magnetic energy only to the upper capacitor C_p. Then, only upper capacitor voltage v_{cp} is boosted. Figure 3(d) illustrates MODE4 in which S_2, S_4 are ON and S_1, S_3 are OFF. Contrary to MODE3, in MODE4, the inductor supplies the stored magnetic energy only to the lower capacitor C_n. Then, only lower capacitor voltage v_{cn} is boosted. By selecting the MODE3 and MODE4 in accordance with the neutral-point-potential, each capacitor voltage can be controlled independently. The control method for DC link voltage can be explained as follows. For

the DC link voltage control, the duty factors for switching devices S_2 and S_3 are defined as D_p and D_n, respectively. MODE1 and MODE2 are used for boosting the DC link voltage when the neutral-point-potential is kept at 0V. At the situation, D_p equals D_n. Then, the DC link voltage is expressed as follows:

$$V_{dc} = E/(1 - D_p) \cdots\cdots (1)$$

Equation (1) coincides with that of the conventional voltage booster. On the other hand, when the neutral-point-potential is not 0V, MODE3 or MODE4 is used for compensating the neutral-point-potential variation. Figure 4 shows the principle of the PWM generation for controlling the neutral-point-potential with subharmonic modulation, and the situation is $v_{cp} > v_{cn}$. The T_s indicates the switching period. The duty factors should satisfy following condition to equalize each capacitor voltage. The condition is $D_p > D_n$. Then, ON-time of the S_2, D_pT_s, becomes longer than that of the S_3, D_nT_s. In other words, MODE4 appears during the time $D'T_s$ which is the time difference between D_pT_s and D_nT_s. In MODE4, the C_p discharges the electric energy to the load. On the other hand, The C_n charges the electric energy from the inductor. In this way, an unbalance between v_{cp} and v_{cn} are corrected. In the case of $v_{cp} < v_{cn}$, the duty factors should satisfy $D_p < D_n$ in a similar way.

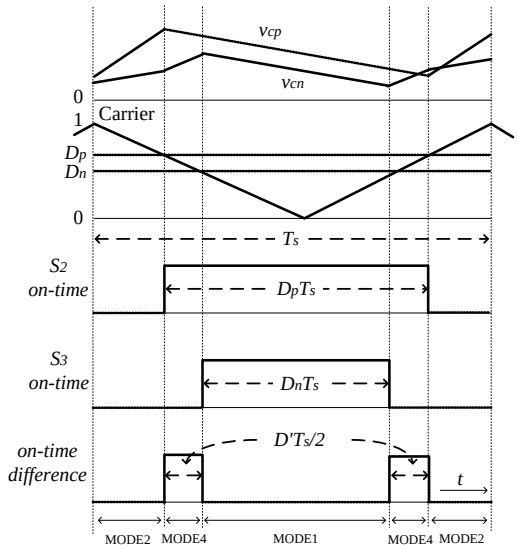

Figure 4. Principle of neutral-point potential control.

The fundamental equation of neutral-point-potential is given as follows:

$$v_n = (1/C)\int i_n dt \cdots\cdots (2)$$

where i_n represents neutral-point-current and C indicates C_p or C_n in Figure 3. Therefore, the capacitor voltage variations per switching period, Δv_{cp} and Δv_{cn} , are expressed as

follows:

$$\Delta v_{cp} = (I_L - I_{dc})(1 - D_p) / Cf_s \quad \cdots\cdots\cdots\cdots\cdots\cdots \quad (3)$$

$$\Delta v_{cn} = (I_L - I_{dc})(1 - D_n) / Cf_s \quad \cdots\cdots\cdots\cdots\cdots\cdots \quad (4)$$

where f_s represents the switching frequency. Both equations (3) and (4) show that it is possible to control each capacitor voltage independently by regulating the duties of the devices D_p and D_n, respectively. Using equations (1), (3) and (4), the system is able to control both the DC link voltage and the neutral-point-potential.

3.2 Verification of the control methods by simulation and experiment

We carried out the simulation of the motor drive system to confirm the effectiveness of the control methods investigated in previous section 3.1. We used an Electronic ciucuit simulation software package PSIM for simulation. The DC link voltage reference is decided so that the voltage is proportional to the motor speed, and the voltage matches the rated value of the motor voltage when the motor speed is rated value. Figure 5(a) represents the simulated results at rated speed and rated load. It can be seen that the DC link voltage is controlled to constant value 141V, and neutral-point-potential is kept at nearly 0V. Next, we carried out experiment of the motor drive system in the same condition to the simulation. We used a digital control system PE-expert3 from Myway-plus in experiment. Figure 5(b) shows the experimental results. It can be seen that the simulated results agree well with the experimental results. It can be presumed that the experimental waveform of phase current i_u contains the distortion due to cogging torque of the PM motor.

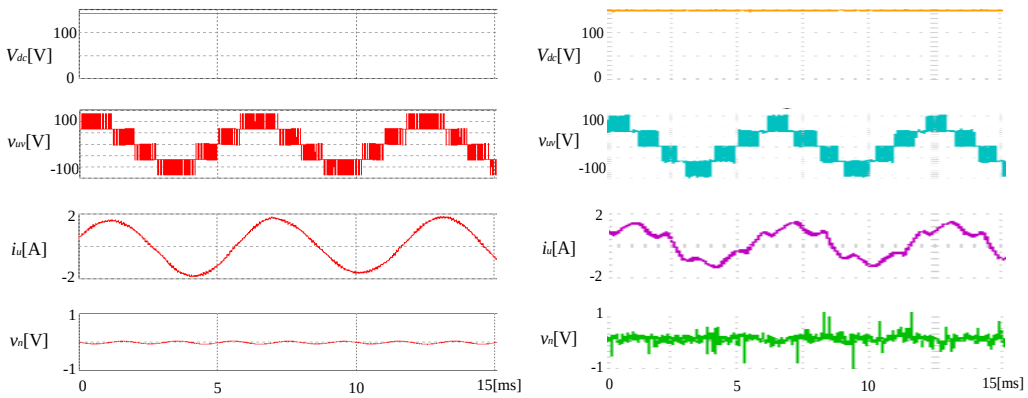

(a) Simulated results. (b) Experimental results.

Figure 5. Steady state characteristics of neutral-point-potential control.

4.0 Conclusions

This paper has investigated the control method for the DC link voltage and the neutral-point-potential of the NPC inverter with voltage booster. The steady state characteristics of the system have been demonstraed by both simulation and experiment. The simulated results agree well with the experimental results. The results both of simulation and experiment have demonstrated that the NPC voltage booster is able to control not only DC link voltage but also neutral-point-potential. Furthermore, effectiveness of the control method has been confirmed. This system is expected for application of motor drive system for high voltage class EV.

References

R. Mizutani, T. Tachibana, M. Morimoto, K. Akatsu, and N. Hoshi. (2015). *Electric Drive Technologies Contributing to Low-Fuel-Consumption Vehicles*, IEEJ Journal D , Vol.135, No.9:884-891 (in Japanese)

K. Yamamoto, A. Imakiire and K. Iimori. (2011). *PWM Inverter with Voltage Boosters with Regenerating Capability Augmented by Electric Double-Layer Capacitor*, IEEJ Journal D, Vol. 131, No.5: 671-678 (in Japanese)

M. Morimoto et al. (2010). *New Control Technology in Electric Vehicle*, NTS, 229 (in Japanese)

M. Furuta and T. Ohnishi. (2010). *NPC Inverter with Series Voltage Source Controlled by A Booster*, JIASC2010: 1-21 (in Japanese)

V. Yaramasu, and B. Wu. (2014). *Predictive Control of a Three-Level Boost Converter and an NPC Inverter for High-Power PMSG-Based Medium Voltage Wind Energy Conversion Systems*, IEEE Trans. PE., Vol.29, No.10: 5308-5322

A. Nabae, I. Takahashi and H. Akagi. (1981). *A New Neutral-Point-Clamped PWM inverter.* IEEE Trans. IA, Vol.1A-17, No.5: 518-523

S. Ogasawara, T. Sawada, and H. Akagi. (1993). *Analysis of the Neutral Point Potential Variation of Neutral-Point-Clamped Voltage Source PWM Inverters,* IEEJ Journal D, vol.113, No.6: 41-48. (in Japanese)

APPLICATION OF INTERNET OF THINGS IN MONITORING SWIMMING PERFORMANCE

Muhammad Ramdhan bin Mohd Suhaili[1], Kamaludin Mohamad Yusof[2] & N. Effiyana Ghazali[2]*

[1] *Advanced Telecommunication Technology (ATT) Research Group, Faculty of Electrical Engineering, Universiti Teknologi Malaysia, 81310 Johor Bahru, Johor Darul Ta'zim*
[2] *Department of Communications Engineering, Faculty of Electrical Engineering, Universiti Teknologi Malaysia, 81310 Johor Bahru, Johor Darul Ta'zim*

*Corresponding Author: *nurzal@utm.my*

Abstract: Wireless Sensor Network (WSN) in sports arena start to become popular as athletes and coaches realize the need of technology to obtain accurate measurement system that can be used to monitor the performance of athletes during tournaments as well as training session. Swimming is one of the most popular sport in the Olympic level. The major elements for monitoring swimmers' performance are stroke rate and time taken for each stroke. For that reason, this paper proposes electronic system to monitor swimmers' stroke rate and time taken per stroke wirelessly. There are three stages involve in this work which are developing sensor node, developing server node and developing monitoring application. Sensor node will send the raw data to the server node. Then, the server node process the data and store them in database. Finally, the process data which is the final results will be displayed on a simple web page Graphical User Interface (GUI). The GUI will display two graphs of stroke rate in real time which are stroke rate vs. time and time vs. stroke. As a result, coaches and swimmers will be able to view the stroke rate in real-time from poolside thus can use the available information to improve the swimmers' performance.

Keywords: *Wireless Sensor Network (WSN), stroke rate, performance, Graphical User Interface (GUI), real-time*

1.0 Introduction

Competitive swimming is one of the most popular sport at international level with events in freestyle, backstroke, butterfly and breaststroke. Swimming is an action oriented sport and just like others, implicate the sporadic application of force in which motion will be produced (Craig and Pendergast, 1979). When a great swimmer moving quickly through the water they seem so smooth and powerful. This is contributed by certain factors such as good rhythm and consistency. Rhythm can be improved by correct coaching and technique improvement. One of an important element in rhythm is called stroke rate.

Stroke rate is how many strokes a swimmer do per second counting both arms. By monitoring a swimmer stroke rate, swimmer overall performance can be improved (Craig and Pendergast, 1979). Presently, stroke rate is calculated manually by coach at the side of the pool by using a stopwatch. This can be difficult to do and not accurate. This project will tackle the overall lack in wireless automated training system for swimmer training regime by implementing wireless sensor network system.

Wireless Sensor Network (WSN) is attracted much attention in electronics engineering fields as its potential to create an impact on our society through its application. WSN able to act as a bridge between physical and virtual world. WSN is a type of network that capitalizes several sensor nodes which install in a certain area of activity. The sensor node should have integrated functions of calculating, sensing and wireless transmission (Choi *et al.*, 2010). Furthermore, WSN consists of spatially spread nodes armed with sensing devices to monitor and quantify attributes of the physical environment at different locales (Sandeep *et al.*, 2015). WSN required centralized nodes or master node that will act a server which will receive all information from other sensing nodes. Numerous research has been used Raspberry Pi in developing WSN where Raspberry Pi a cheap, credit card-sized, minicomputer (Gupta *et al.*, 2015). Among many of its application, WSN in sports field starts to become popular as athletes and coaches realize the need of electronics system to create a more accurate measurement system also to analyze the performance of athletes during tournaments but more importantly during a training session. By applying WSN in swimmer training environment, it will greatly improve swimmers' performance. Recently, the new Internet of Things (IoT) is being introduced everywhere. IoT is a system that links the real world and cyberspace via physical things that embed with several forms of smart sensors (Kraijak and Tuwanut, 2015).

There are a lot of swimming aspects can be considered in improving swimmers' performance however some aspects are very hard to improve such as stamina which requires hard and consistent training. Fortunately, some other aspects such as stroke rate are easier to improve by proper help from a coach and this project will look into it make this process easier. Last but not least is to do data transferring wirelessly in real-time. This is a revolutionize way of a monitoring system that makes available by WSN technology. Currently, lack of product with the usage of WSN in swimming sport is an issue. Therefore, monitoring swimmers' performance wirelessly is proposed.

2.0 Proposed Work

2.1 Overall Framework

The proposed work is divided into three stages which are developing sensor node, developing sensor network and developing monitoring application. The first two stages involve hardware development whilst the third stage is only software development. The constraint in the first stage is a size. The hardware should be as small as possible because it is a wearable device. The second part of the hardware is server node and its size can be

variable according to the type of device use which in this case in Raspberry Pi 2. Figure 1.0 shows an overall framework of this work.

Figure 1.0: Overall framework

In developing sensor node, it consists of microcontroller, sensor and transceiver. The sensors involve are accelerometer and gyroscope. Sensor node will be placed on swimmers' hand. This device responsible for sensing swimmers' stroke and time. The sensor that will be used is MPU-6050, where it will pass raw data to the microcontroller, Arduino Pro Mini (Pro Mini) and it will process the data. After that, microcontroller will pass it to a transceiver (nRF24L01+) for wireless data transmission toward server node. Next, the server node that uses Raspberry Pi 2 as its core will collect transmission data from the nRF24L01+ transceiver and process the data before it stores all information in the database.

The last part is software development which is monitoring application. The database handler used is MySQL. Afterward, Apache Web Server will be used to handle Hypertext Transfer Protocol (HTTP) request. Last but not least Hypertext Preprocessor (PHP) scripted will play role in creating Graphical User Interface (GUI) for end-user. In this work, GUI is intended to be the view from http://localhost either using Raspberry Pi 2 browser or another laptop connect to it.

Figure 1.1 shows an overview of general program flowchart that will be running on both sensor-node and server node. The sensor node focal function is to read data from the sensor and send it wirelessly while the server node key role is to receive the data, process it and store in the database.

2.2 Designing Sensor Node

An issue that need to consider is the size of the sensor. Pro Mini voltage output only give 5 V (Chen *et al.*, 2009) can be considered. However, both sensor and transceiver operate only take roughly 3.3 V input voltage. Hence, a voltage drop is required but instead of using voltage regulator which is bulky, another simpler solution will be used that is using General Purpose Plastic Rectifier to drop voltage. In this project 1N4001 diode will be used because it gives 1.1 V voltage drop (Bellar *et al.*, 1992), thus two of it will be used and resulted voltage is 2.8 V which is suitable for both sensor and transceiver.

One last part to be added is a switch that will be a program so if its value it's HIGH, the sensor will read data and if its value is LOW sensor will not read data and no transmission will be made. This switch will be label as Active Switch and its purpose is to make data reading more effective so when the device is in turn on the state but not in use, Active

Button can be used to shut down data reading. A 9V battery is used to power up the Pro Mini since Pro Mini can be supplied from 5-12 V on its raw input voltage pin (Chen *et al.*, 2009). In developing the sensor node, require devices are as follow:

(i) Arduino Pro Mini x 1
(ii) nRf24L01+ x 1
(iii) MPU-6050 x 1
(iv) 1N4001 diode x 2
(v) Slide switch x 1
(vi) 10k Ohm resistor x 1

The final circuit design is presented in Figure 1.1. It is noted a 10k Ohm resistor is fixed between slide switch and Pro Mini's GND pin.

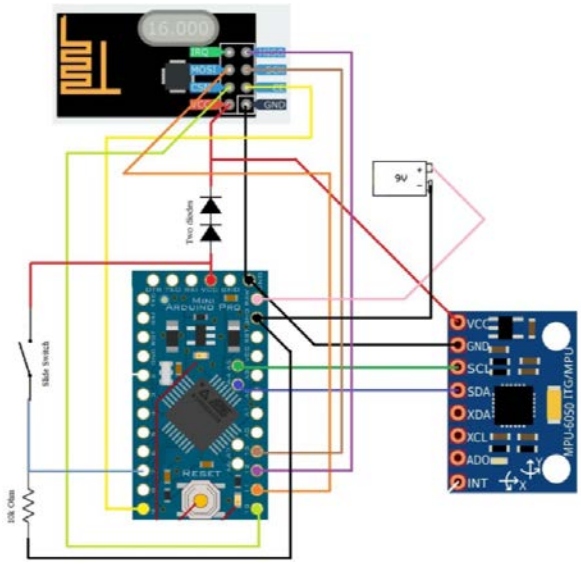

Figure 1.1: Final circuit design for sensor-node

2.2.1 Designing Sensor Node Program

This subtopic will present software design of Pro Mini. Software design is a task to convert consumer requirement into the embedded system so equipment works as user requirement. As mention before, sensor node main function is to read raw data, process it and pass through the transceiver to server node with Active Switch control sensor node function. The finalize flowchart of the program for sensor node is shown in Figure 1.2.

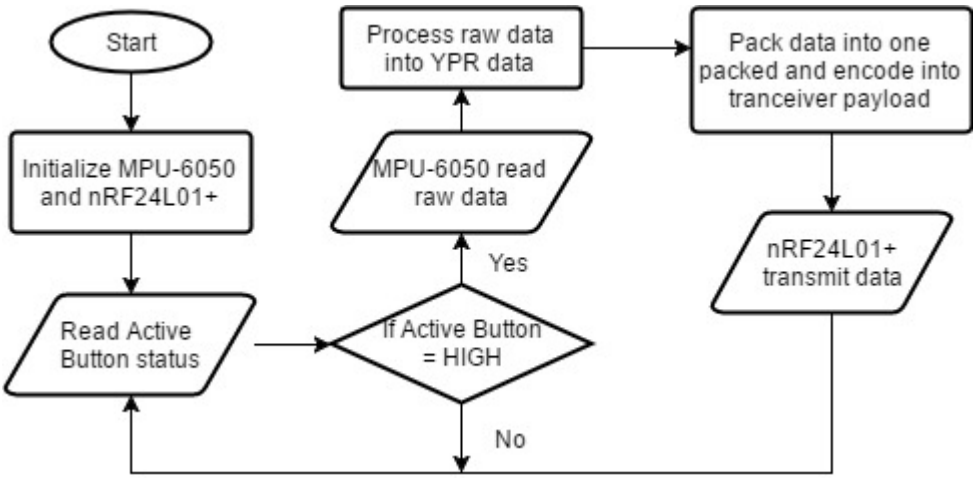

Figure 1.2: Sensor-node flowchart

2.3 Designing Server Node

The server node is the core element of this system, it will receive data, process it, record it in the database and also responsible for publishing the data to end-user. Hence, the choice of microcontroller or computer for this node this incredibly vital. For this work, Raspberry Pi 2 is chosen as server node computer. Next, another transceiver which is another nRF24L01+ is also required to receive data from sensor node. Figure 1.3 depicts the connection between Raspberry Pi 2 and nRF24L01+ as a server node.

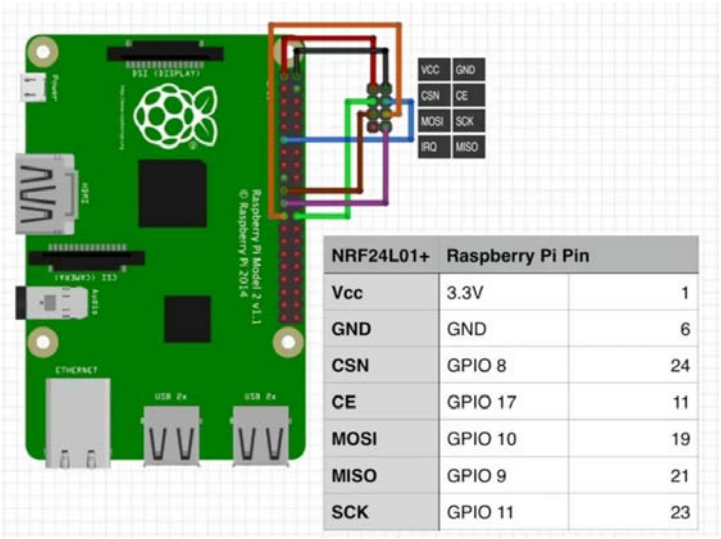

NRF24L01+	Raspberry Pi Pin	
Vcc	3.3V	1
GND	GND	6
CSN	GPIO 8	24
CE	GPIO 17	11
MOSI	GPIO 10	19
MISO	GPIO 9	21
SCK	GPIO 11	23

Figure 1.3: Raspberry Pi and nRF24L01+ connection

2.3.1 Designing Server Node Program

The server node is the core of this system thus it has the most complex program sequence for this project. There are two parts for the server node program as in Figure 1.4 which the first is data reading, process and storing which will be written in Python 3 and second part is a program for publishing data as GUI which will be written using PHP script. Both of the programming parts will be explained more in the next section.

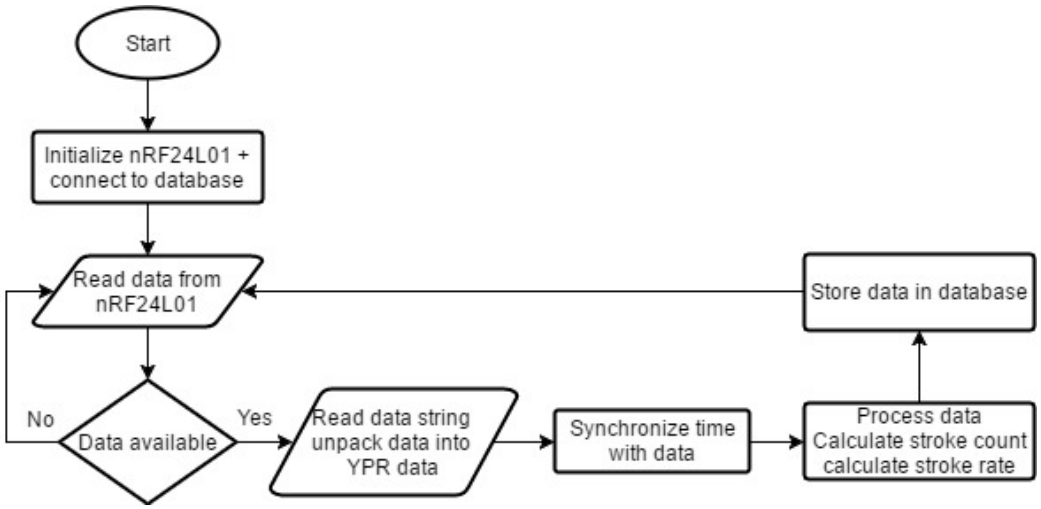

Figure 1.4: First part of the server node flowchart

2.4 Apache, MySQL, PHP and phpMyAdmin Installation

For the part of server node software development is transporting data into the database, manage the database and publish all information to end-user. There are three fundamental part for this stage, which is Apache as webserver, MySQL as a database manager and Hypertext Preprocessor (PHP) as a programming language to publish data in a web browser (Nixon, 2012).

Apache is one of the most famous web server (O'reilly, 2005). A web server is a system that process request through Hyper Text Transfer Protocol (HTTP) (Montulli, 2000). When a browser request a page, it goes to a web-server which is Apache, then Apache will pass the request to PHP and PHP will process the content, pass it to Apache and Apache will pass the content to the web browser. MySQL is an open-source database management system. A database can be briefly expressed as a repository for information. MySQL features a good level of security to its user (Zoratti, 2006). Database plays a very crucial role in this project as it is essential to store all recorded data such as stroke rate and time somewhere that can be accessed later. In this work, MySQL will be used to create and manage the database.

PHP is a scripting language, vigorously typed with no static type inspection or variable declarations, and is reinforced by an environment of hundreds of pre-defined, prepared to use libraries, modules and functions. Development in such an affluent environment is at a quicker pace; there is no requirement to compile, no need for complex build files, and PHP code can be interlaced directly with Hypertext Markup Language (HTML) code making it very easy to develop custom websites and web development frameworks (Kyriakakis *et al.*, 2016). PHP can easily fetch information from MySQL database. Thus, the web content for GUI will be written using PHP. Last to be mentioned is phpMyAdmin. It is a free-source instrument to easily handle and deal with MySQL database using the browser and it is written in PHP.

2.5 JpGraph Installation

For the purpose of presenting data through graph on GUI part, an add-on library needs to be added for adding the PHP ability to process and present a graph. JpGraph is a free-source library that allows PHP to process and display graphical object. Follow the following steps to add JpGraph library:

(i) On a PC, go to "http://jpgraph.net/download/" then, click "jpgraph3.5.0b1.tar.gz" to download the file.
(ii) Unpack the file using a program such as "7-Zip", again, unpack the subsequent ".tar" file using 7-Zip.
(iii) The result will produce a folder named "jpgraph-3.5.0b1". Rename the folder into "jpgragph".
(iv) Next, copy the folder into Raspberry Pi 2 using USB Flash Drive. Paste the folder into "/var/www/html/swim" directory. "/swim" directory will have to be made beforehand.

All this step will conclude JpGraph library installation on Raspberry Pi 2.

3.0 Results and Discussion

This section composes of obtained result and discussion from this project. A detailed explanation of hardware and software building process will be presented.

3.1 Sensor-node Prototype

Figure 1.5 and 1.6 show the final prototype of the development sensor node. It is a small, light and wearable device. To turn on the device, the 9V battery is required. Figure 1.7 shows Active Button. As discussed, the button is designed to control data reading from MPU-6050.

Figure 1.5: Sensor node prototype

Figure 1.6: Side view of the prototype

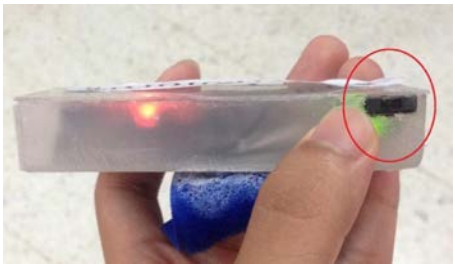

Figure 1.7: Active Button

As a summary, after turning on the device and set Active button state as true, the device will read data from MPU-6050, process it and send processed data to server node through the nRF24L01+ transmitter. Testing will be conducted again to ensure the device is fully working. If data can be read on the server node, we conclude that sensor node is working flawlessly.

3.2 Sensor Data Reading

The first part of the result that needs to be confirmed is MPU-6050 data. Without any adjusting, it will give raw data from accelerometer and gyroscope separately. Data read by the microcontroller from MPU-6050 sensor are viewed from Arduino IDE serial monitor from a PC. First raw data is viewed as shown in Figure 1.8. Then the processed data which is YPR code is uploaded and is viewed from the serial monitor as shown in Figure 1.9. Since Uno able to read YPR data, the MPU-6050 data reading stage is successful.

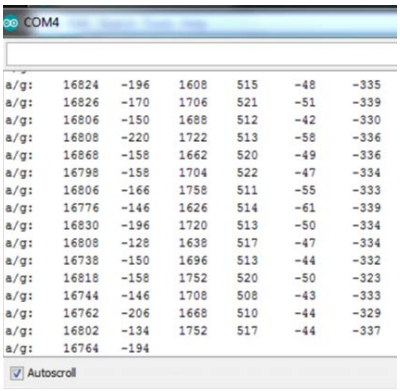

Figure 1.8: MPU-6050 raw data

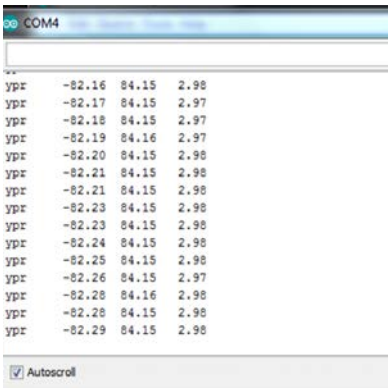

Figure 1.9: MPU-6050 YPR data

3.3 Stroke Rate Calculation

To calculate and measure stroke, an axis needs to be chosen as a reference, it can either YPR x, y or z-axis, in this prototype x-axis is chosen as a reference. To model a stroke sample, each time a-axis change its sign this constitute as half a stroke been done. Therefore, for the program to record a single stroke, x-axis sign need to change two times. The program will loop infinitely continue to record how many strokes has been done, which will be referred as stroke count until the system is turn off. Stroke rate is made up from two components which stroke count that has been discussed above and the other one is a time in term of a minute which Equation 1.0 shows stroke rate equation. Since the data from sensor node were sent at exactly 0.2-second interval the program will increment 0.2 seconds for each loop. Consequently, the program is able to accurately both monitor time and stroke count. The result is shown in Figure 1.10. With this outcome, stroke rate can be calculated using Equation 1.0.

$$Stroke\ rate = stroke\ count/min \qquad \text{Equation 1.0}$$

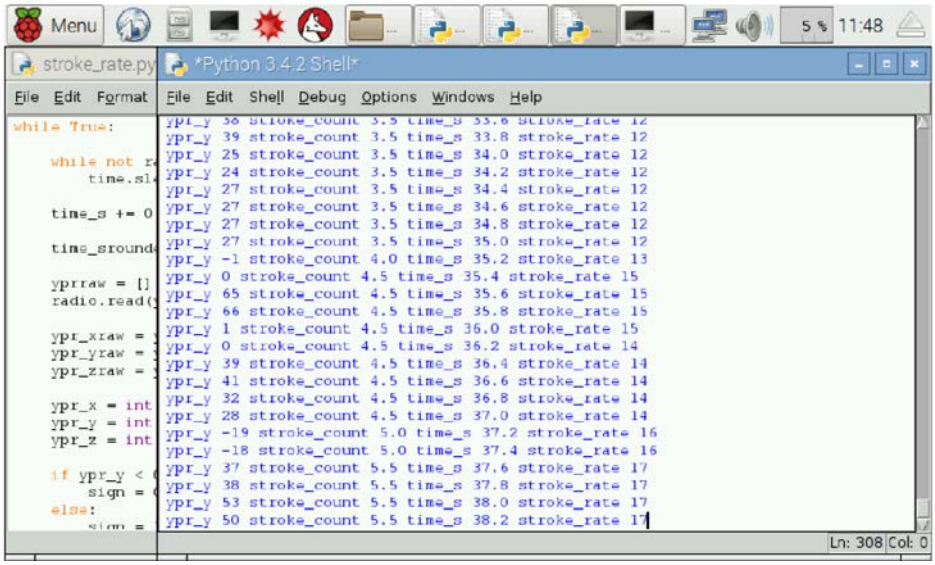

Figure 1.10: Stroke count, time (s) and stroke rate (stroke count/min) data

3.4 Time per Stroke Calculation

Another element in swimming performance that this system will monitor is time per stroke. Time per stroke is how many seconds it took for a swimmer to complete one stroke cycle. Figure 1.11 presented the resulted information.

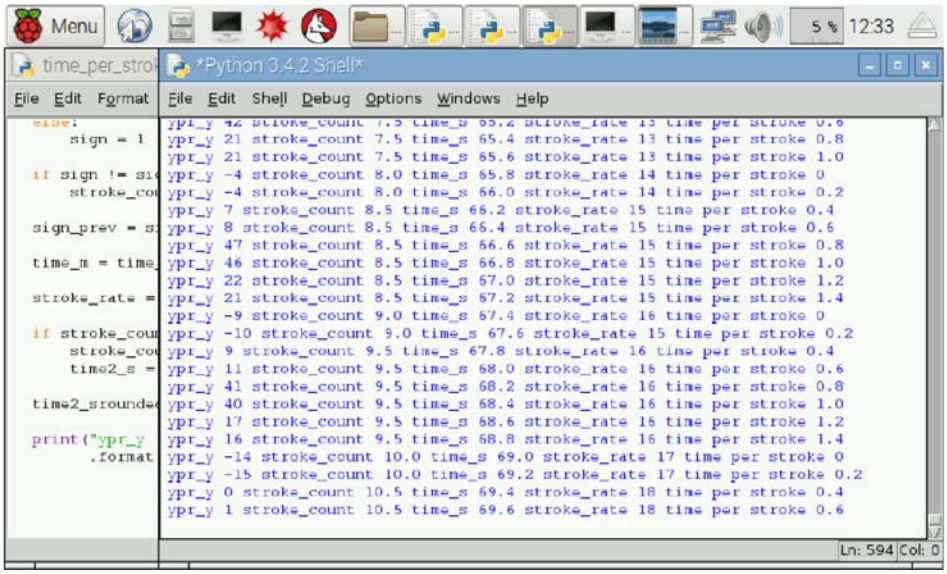

Figure 1.11: Stroke rate and time per stroke data

To do this, a new time variable, “time2” need to be introduced to the program on server node. This is because unlike “time” which will keep incrementing each time the programming run a loop, “time2” will be reset each time a new stroke count is recorded. Therefore, each time for each stroke will be recorded precisely.

3.4 Graphical User Interface

The final part of this work will address on GUI. The user interface is the only method through which a user can converse with certain software (Bajwa and Chaudhary, 2006). This will allow users such as coach or swimmer himself to view swimming performance data in real-time during training or after training session had ended. The GUI will be created to be viewed on the web browser and executed using PHP scripted. Then GUI can be viewed on Raspberry Pi 2’s browser address “localhost/swim”. GUI also can be the view from another laptop connecting to Raspberry Pi network via Ethernet cable. To do this, connect a laptop and Raspberry Pi 2 and then go to Terminal on Raspberry Pi 2 the type “hostname –I”, it will respond with an address for example “192.168.137.12”. Next, go to web browser and type the address such as “192.168.137.12/swim”. After that the browser should be able to access the system GUI. The GUI will display Stroke Rate data, Time per Stroke data and Stroke Rate vs. Time data are shown in Figure 1.12, Figure 1.13 and Figure 1.14.

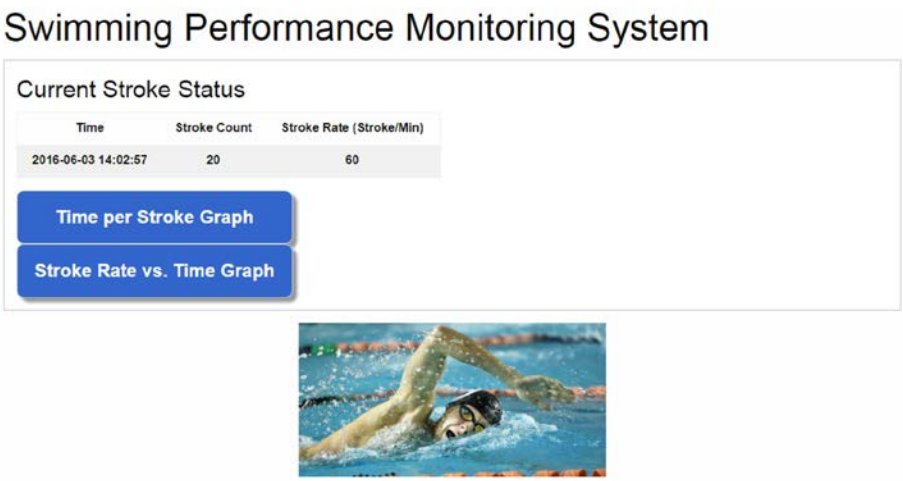

Figure 1.12: Main GUI

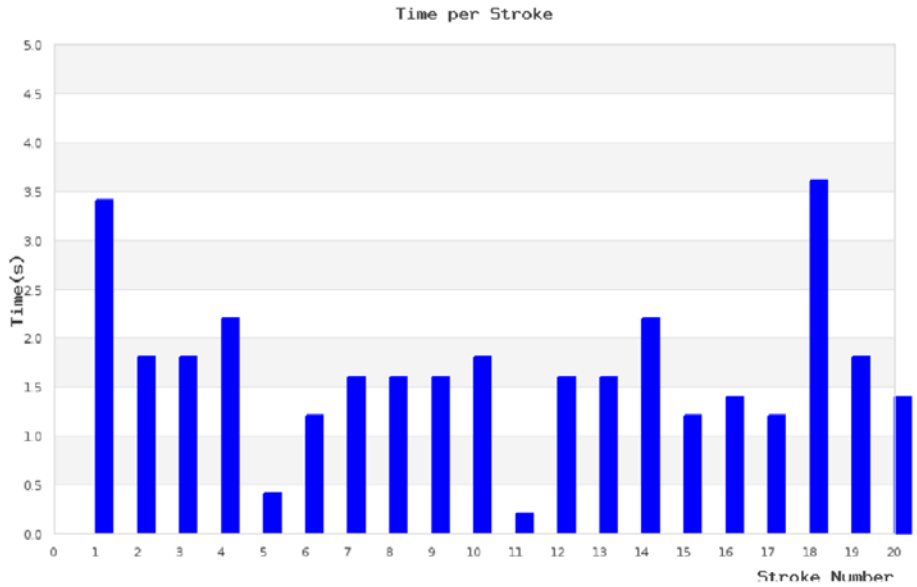

Figure 1.13: Time per stroke graph

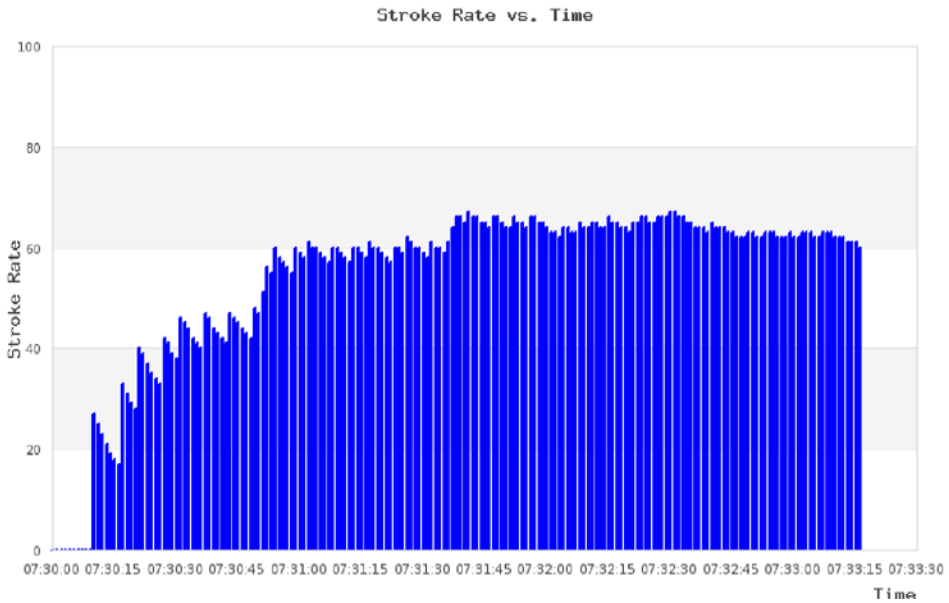

Figure 1.14: Stroke rate vs. time graph

The result obtained is very useful for a swimmer, as shown in Figure 1.12, the system calculates swimmer stroke rate for the current time as it will allow others such as coach see and analyze. Figure 1.13 shows swimmer stroke rate per time as swimmer continue to

swim as all the data had been recorded. After the swimming session has ended, a swimmer can review his performance by looking at the graph. This allows swimmer or coach to review the consistency of swimmer stroke rate. From this data, swimmer can decide what to do, to improve such as improving stamina. Figure 1.14, on the other hand, provide swimmer data on time they took per stroke, they allow the user to see the consistency of each stroke taken. In ideal form, a swimmer wants to have a flat graph which is consistency time for every stroke. Thus, from all the presented data, swimmer and coach able to monitor swimming performance to a good extent.

4.0 Conclusions

Swimming performance monitoring system entail three major parts. The first part is sensor node which integrated Arduino microcontroller, a sensor and transceiver. The subsequent part is server node which made of Raspberry Pi 2 minicomputer and a transceiver to receive data and process it. The final part is data publisher component which are a web server (Apache), database manager (MySQL) and publishes language PHP which is all integrated to publish necessary information to end-user through a web browser. The final result depicts the stroke count and stroke rate on GUI. The obtained result is useful to the coaches and swimmers to analyze the performance during training session or tournament.

5.0 Acknowledgements

The authors would like to thank all those who contributed toward making this research successful. The authors wish to express their gratitude to National Institute of Technology Kagoshima College for the sponsorship, Universiti Teknologi Malaysia for the financial support and Advanced Technology Telecommunication (ATT) Research Group for the advice of this work. (Vot number Q.J130000.2723.02K37).

References

Bajwa, I. S., and Chaudhary, M. A. (2006). *A Language Engineering System for Graphical User Interface Design (LESGUID): A Rule based Approach.* Paper presented at the Information and Communication Technologies, 2006. ICTTA'06. 2nd, 3582-3586.

Bellar, M., Watanabe, E., and Mesquita, A. (1992). Analysis of the dynamic and steady-state performance of Cockcroft-Walton cascade rectifiers. *IEEE transactions on power electronics, 7*(3), 526-534.

Chen, W., Nguyen, S. T., Coops, R., Oetomo, S. B., and Feijs, L. (2009). *Wireless transmission design for health monitoring at neonatal intensive care units.* Paper presented at the Applied Sciences in Biomedical and

Communication Technologies, 2009. ISABEL 2009. 2nd International Symposium on, 1-6.

Choi, Y.-S., Jeon, Y.-J., and Park, S.-H. (2010). *A study on sensor nodes attestation protocol in a Wireless Sensor Network.* Paper presented at the Advanced Communication Technology (ICACT), 2010 The 12th International Conference on, 574-579.

Craig, A., and Pendergast, D. R. (1979). Relationships of stroke rate, distance per stroke, and velocity in competitive swimming. *Med Sci Sports Exerc, 11*(3), 278-283.

Gupta, M. S. D., Patchava, V., and Menezes, V. (2015). *Healthcare based on IoT using Raspberry Pi.* Paper presented at the Green Computing and Internet of Things (ICGCIoT), 2015 International Conference on, 796-799.

Kraijak, S., and Tuwanut, P. (2015). *A survey on IoT architectures, protocols, applications, security, privacy, real-world implementation and future trends.* Paper presented at the Wireless Communications, Networking and Mobile Computing (WiCOM 2015), 11th International Conference on, 1-6.

Kyriakakis, P., Chatzigeorgiou, A., Ampatzoglou, A., and Xinogalos, S. (2016). Evolution of method invocation and object instantiation patterns in a PHP ecosystem.

Montulli, L. (2000). Persistant client state in a hypertext transfer protocol based client-server system: Google Patents.

Nixon, R. (2012). *Learning PHP, MySQL, JavaScript, and CSS: A step-by-step guide to creating dynamic websites*: " O'Reilly Media, Inc.".

O'reilly, T. (2005). What is web 2.0.

Sandeep, V., Gopal, K. L., Naveen, S., Amudhan, A., and Kumar, L. (2015). *Globally accessible machine automation using Raspberry pi based on Internet of Things.* Paper presented at the Advances in Computing, Communications and Informatics (ICACCI), 2015 International Conference on, 1144-1147.

Zoratti, I. (2006). *MYSQL security best practices.* Paper presented at the Crime and Security, 2006. The Institution of Engineering and Technology Conference on, 183-198.

THE EFFECTS OF DIFFERENCE METHODS OF BABYWEARING ON THE HUMAN POSTURE

Asha Hasnimy Mohd Hashim[1]*, Halijah Ibrahim[1], Zainal Abidin Zainuddin[1], Diyana Zulaika Abd Ghani[1] & Tiang Siew Ping[1]

[1] *Department of Educational Foundation and Social Science, Faculty of Education, Universiti Teknologi Malaysia, 81310 Skudai, Johor, Malaysia.*

*Corresponding Author: *asha@utm.my*

Abstract: Babywearing is the action or method of carrying an infant close against one's body in in a sling or another form of baby carrier. Although cultural differences is seen in babywearing style around the world, the purpose still the same. The present study investigates the effects of different method of babywearing in terms of babywearer's posture while walking. The participants (N = 20), aged between 20–35 years old (M=24.85, SD=2.13) were exposed to three conditions: babywearing without any carrier, babywearing with a soft-structured carrier, and babywearing with a wrap. The babywearer's posture was analysed after the participants walked on a treadmill for 1.6 km while carrying a 5-kg and 60-cm doll in the mentioned conditions. The babywearer's posture during walking were recorded and analysed. The statistical results show that the independent variable had significant effect on babywearer's posture ($p < 0.05$) especially in trunk and head. This implies that babywearing using soft-structured carrier and wrap able to reduce the forward lean posture thusable to improve the efficiancy of walking posture.

Keywords: *Babywearing, posture, walking*

1.0 Introduction

Babywearing is a method of holding or carrying baby close to individual body using carrying aids such as a long cloth, structured made of baby carrier like a bagpack and many more. In the industrialized world, babywearing has gained popularity in recent decades, partly under the influence of advocates of attachment parenting. The rationale underpinning the popularity of this mode of babywearing can vary from factors such as convinence to more complex psychosocial issues related to "mother-child bonding".

Studies shows that most parents or caregivers in throughout the world carry their baby with them for more than 50% of the day (Schön and Silvén, 2007). For example in African countries 96% of the time hold their baby (age of 3-4 months), 87% of the time when the baby turn 9-10 months and the duration of time decreased to 70% when baby

about to walk under age of 1 year old (Schön and Silvén, 2007). In many societies, children are carried until they are weaned, able to walk and keep up on their own, or the mother has another child. (Aryes, 1973, Kramer, 1998, Schön and Silvén, 2007 and Wall-Scheffler, 2007, Wu et. Al., 2016).

There are four main methods for carrying babies have been developed: front carry, back carry, side sling and no tools. The chosen babywearing carrier aids and techniques that were used depending on individual self-comfort based on this modes. For example the front wrap is using a long cloth that is tied around the carrier's body, thus forming a pouch to containing the child and activities and this most seen warm climates society South-east Asia (Wu, Huang and Wang, 2016). While the back position seems most widespread in Africa, Guatemala, Mexico and Nepal (Singh, 2009). The other mode of baby carry used cross-culturally is the side sling which is carried on the mother's hips and is suppored by a sling or shawl which most seen in Indonesian, Kung in Botswana and North East Zaire (.Blois, 2007). While those three modes of carrying are able to free the babywearer's hand for performing the task, the no tools carrying position is slightly more difficult. The child is carry on the babywearer's hip, back or even shoulders (if the child able to control their head and spine). This type of carrying required the use of babywearer's arms to support and stabilize the child's body.

Ergonomic load carrying evaluations are often found in backpacking. Study by Al-Khabbaz, Shimada and Hasegawa (2008) found that rectus femoris muscle activities increased progressively as the backpack load increase and trunk inclined backward with an increased backpack load. They also suggested that 20% body weight (BW) backpack or higher cause the most significant muscular and postural changes and should be avoided. A significant change was found in left erector spine muscles in 20% BW, but no significant heart rate was found (Baeur and Freivalds, 2009). Significant postural adaptations such as head forward bending and lumbar lordosis have been reported. When comparing the front pack and backpack, the backpack conditions demonstrated an increased forward head position, significant neck motion and hip flexion during walking; whereas, front pack conditions showed increased spinal extension and lumbar lordosis (Fiolkowski et al. 2006; Bettany-Saltikov and Cole 2012). Similar results were found when comparing front- and back-worn harness baby carriers (Kim and Yun 2013). As a result, the front pack allows the wearer to maintain a more upright posture and was recommended for load carrying.

In child development, the Center of Disease Control and Prevention (CDC, USA) reported that children around four months old would be able to hold a steady upright head position. Deppa and Allen (2014) indicated the concerns about baby suffocation using sling carrier when the baby is less than 4-month old. At around 6 months old, the child begins to sit without support, and around 12 months old, would be able to walk by holding onto furniture. Thus, it is reasonable to consider that children between 4 and 12 months would be the ages at which a babywearing aids would be most frequently used.

2.0 Materials and Methods

2.1 Participants

The present study involved 20 young female adults, aged between 20–35 years (M = 24.85, SD = 2.13). All of them were single and have no experience in babywearing. All the participants were healthy during the study and were free from any musculoskeletal injuries or diseases.

2.2 Methods

All the participants were exposed to three conditions: (1) babywearing without any carrier, (2) babywearing with a soft-structured carrier, and (3) babywearing with a wrap. The babywearing without any carrier is a condition in which the participants needed to hold the baby barehanded. Both the wrap and the soft-structured carrier were made from the same cloth material–Bebe Sachi Zen (diamond weaved). The difference between these two conditions is that the wrap was made of a long cloth (5.2 m) that can be used to tie the baby towards the babywearer's body using a front-cross carry technique, whereas the soft-structured carrier was a buckle carrier that resembled a backpack and was made by Snuggbaby Studio, Malaysia. In the three conditions, the baby was positioned facing towards each participant and carried near the participant's front torso (Figure 1). The baby was a 5-kg weighted doll that measured 60 cm in height (Touch-Needs, UK).

(a) (b) (c)

Figure 1: Babywearing conditions: (a) Babywearing without any carrier (WO) (b) Babywearing with soft structure carrier (SSC) (c) Babywearing with a wrap (W)

All the participants needed to walk on a treadmill for 1.6 km at their own pace in three days. On the first day, the participants were required to babywear with no carrier; on the second day, with a soft-structured carrier; and on the third day, with a wrap. The measurements were taken three days apart before the participants continued to walk in different babywearing conditions. The participant postures were obtained by using a IDS high speed camera (Imaging Development System GmBh, Obersulm, Germany) that was placed 3 meter away from participant in the sagittal plane. A reflective was attached to subjects body parts i.e., head, shoulder, hip knee and ankle. The data were analysed between absolute angles of the intial heel contact (heel strike) throughout the 1.6km walk using free online software Kinovea version 0.8.15 (https://www.kinovea.org) and Statistical Package for Social Science (SPSS) software version 16.0.

3.0 Results and Discussion

3.1 Results of different method of babywearing to human posture

The data obtained were analysed and presented in the following tables:

Table 1: Mean ± SD score for measured variables

	Without carrier (WO) (Mean ±SD)	Soft structure carrier (SSC) (Mean ±SD)	Wrap (W) (Mean ±SD)
Head	4.92 ± 0.40	1.20 ± 0.47	1.22 ± 0.42
Body	4.03 ± 0.55	0.67 ± 0.39	0.72 ±0.20
Hips	24.65 ± 1.90	24.45 ± 2.03	24.36± 2.10
Knee	9.52 ± 1.45	9.55 ± 1.89	9.56 ± 2.23
Ankle	22.12 ± 1.15	22.01 ± 1.89	22.00 ± 178

Table 2: Differences regarding the posture between three babywearing conditions

	(I)	(J)	Sig
Head	WO	SSC	0.000
	WO	W	0.000
	SSC	W	0.992
Body	WO	SSC	0.000
	WO	W	0.000
	SSC	W	0.853
Hips	WO	SSC	***
	WO	W	***
	SSC	W	***
Knee	WO	SSC	***
	WO	W	***
	SSC	W	***
Ankle	WO	SSC	***

*** Indicates no differences between those conditions in measured musculoskeletal area

Considering small sizes of our samples, we opted to use two parameter statistical test in order to compare the participant's posture of three conditions throughout the test. The results show that the independent variable had significant effect participant's posture ($p < 0.05$). The post-hoc analysis consistent with our hypothesis, it revealed that the three babywearing conditions were significant different one from another in the way we expected. By using babywearing aids, it able to maintain the angle of posture in head and body compared to without carrier.

3.2 Effect on head and body angle

Consistent with the previous studies, this study may provide further potential evidence regarding the angle of head and body with different conditions of babywearing. Results show participants who carry the doll without carrier tends to flex more of their head and body compared to babywearing aids. This is due to instability and uncertained centre of gravity from the load that been carried in arm. Whittle, (2002) mentioned that individual need to lean forward and flex the head to lower the center of gravity and maintain the body stability. Knapik et. al. (1996) study shows that the increament of body leaning forward while carry a front load due to three factors; fatigue, increased of loading and stability. By carrying the load using both arms, individual unable to maintan the stability while walking due to absence of arm swing compared to babywearing aids where boths arms were free. Thus it will contribute to instability of posture (Bruijn et. al., 2008; Pontzer et . al., 2009). In order to maintain the stability, individual need to change the posture by flexing the head and lean the body forward to maintan the posture (Filaire et. al., 2001; Grabowski et. al., 2004; Whitcome et.al., 2007).

These findings are considered important because they advocate further studies on the usefulness of appropriate babywearing in performing daily activities, considering the fact that none of the previous research can be used to test the hypothesis. The way the participants described their experience may represent a clue as to the appropriate babywearing that might induce a comfort state which, as in the case of using a soft-structured carrier or wrap, could play an important role in individual posture. In support of this assumption, it is important to mention that the association between comfort, perceived exertion and posture to babywearing has also been highlighted by other authors (Chao, Hsiao & Mao, 2014; 2016), and that our results did not reveal any significant differences between using a soft-structured carrier and using a wrap with regard to level of perceived exertion. This suggests that these two babywearing methods could produce similar effects on self-comfort and on the reduction of bad posture.

3.3 Hips, knee and ankle angle

The present study did not shows an significant differences between three condition of babywearing in terms of hips, knee and ankle angle while walking. Watson et. al. (2011) reported there are no changes in lower limb kinematic when carry a load at upper body.

The load that less than 30% of body weight will not make any changes to hips, knees and ankle angle (Sing and Kho, 2009; Devroey et. al., 2007).

4.0 Conclusions

These findings are considered important because they advocate further studies on the usefulness of appropriate babywearing in performing daily activities, considering the fact that none of the previous research can be used to test the hypothesis. The way the participants described their experience may represent a clue as to the appropriate babywearing that might induce a comfort state which, as in the case of using a soft-structured carrier or wrap, could play an important role in individual posture. In support of this assumption, it is important to mention that the association between comfort, perceived exertion and posture to babywearing has also been highlighted by other authors (Chao, Hsiao & Mao, 2014; 2016), and that our results did not reveal any significant differences between using a soft-structured carrier and using a wrap with regard to angle of measured posture. This suggests that these two babywearing methods could produce similar effects on self-comfort and on the reduction of bad posture while carrying a baby.

5.0 Acknowledgements

The authors acknowledge the research grants provided by Ministry of Education Malaysia (MOE) under Fundamental Research Grant Scheme (FRGS). We also would like to thank Bebe Sachi (Nurturing Concepts Sdn. Bhd.) and Snuggbaby Studio for being part of sponsoring this research.

References

Albert, M. V., & Kording, K. P. (2011), 'Determining Posture from Physiological Tremor', Experimental Brain Research, 215(3-4): 247-255.

Anisfeld E, Casper V, Nozyce M, Cunningham N. (1990), 'Does Infant Carrying Promote Attachment? An Experimental Study of The Effects of Increased Physical Contact on The Development of Attachment'. Child Development 61:1617-1627.

Arellano CJ, Layne CS, O'Connor DP, Scott-Pandorf M, Kurz MJ. (2009), 'Does Load Carrying Influence Sagittal Plane Locomotive Stability?', Medical Science Sports and Exercise, 41(3):620–627.

Attwells, R. L., Birrell, S. A., Hooper, R. H., & Mansfield, N. J. (2006), 'Influence of Carrying Heavy Loads on Soldiers' Posture, Movements And Gait', Ergonomics,49(14): 1527-1537.

Barr RG, McMullan SJ, Spiess H. (1991), 'Carrying as Colic Therapy: A Randomized Controlled Trial'. Pediatrics 87:623-630.

Blois, Maria (2007*).* Birth: Care of Infant and Mother: Time Sensitive Issues Best Practices in the Behavioral Los Altos: Institute for Disease Management.

Brick N, MacIntyre T, Campbell M. (2014) 'Attentional Focus In Endurance Activity: New Paradigms And Future Directions'. International Review of Sport and Exercise Psychology, 7(1): 106-134.

Chao Y. W., Hsiao R. H, Mao J W (2014), 'The Ergonomic Evaluations of Three Front Baby Carriers', Advances in Human Factors and Ergonomics 2014. Proceeding of the 5th AHFE Conference. 19-23 July 2014: 119 – 205.

Chao Y. W., Hsiao R. H, Mao J W (2016) 'Baby Carriers: A Comparison of Traditional Sling And Front-Worn, Rear-Facing Harness Carriers', Journal Ergonomics: 1-7.

Cong, X., Ludington-Hoe, S.M., Walsh, S., (2011). 'Randomized Crossover Trial of Kangaroo Care to Reduce Biobehavioral Pain Responses in Preterm Infants: A Pilot Study', Biological Research for Nursing, 13: 204-210

Craig, A.D. (2002) 'How Do You Feel? Interception: The Sense of The Physiological Condition Of The Body', Nature Review Neuroscience, 3: 655–666.

Ekkekakis P, Petruzzello S.J. (1999) 'Acute Aerobic Exercise and Affect: Current Status, Problems And Prospects Regarding Dose-Response', Sports Medicine, 28: 337–374.

Esposito, G., Yoshida, S., Ohnishi, R., Tsuneoka, Y., Rostagno, M.C., Yokota, S., Okabe, S., Kamiya, K., Hoshino, M., (2013), 'Infant Calming Responses during Maternal Carrying in Humans and Mice', Current Biology, 23(9):739–745

Filaire M, Vacheron JJ, Vanneuville G, Poumarat G, Garcier JM, Harouna Y, Guillot M, Tervers, Toumi H, Thierry C. (2001), 'Influence of the Mode of Load Carriage on The Static Posture of The Pelvic Girdle and the Thoracic and Lumbar Spine in-vivo', Surgical Radiology Anesthesia, 23(1):27–31.

Foster-Schubert, K., Alfano, C., Duggan, C., Xiao, L., Campbell, K., Kong, A., Bain, C., Wang, C.Y., Balckburn, G., McTiernan, A. (2012), 'Effect of Diet and Exercise, Alone or Combined, on Weight and Body Composition in Overweight-To-Obese Post-Menopausal Women', Obesity (Silver Spring, Md.), 20 (8): 1628–1638.

Gammie, S.C., (2013). 'Mother–Infant Communication: Carrying Understanding to a New Level', Current Biology, 23 (9): R341–R343

Harriet Hiscock (2010), 'Rock-A-Bye Baby? Parenting and Infant Sleep', Sleep Medicine Reviews, 14 (2):85–87.

Hunziker UA, Barr RZ. (1986). 'Increased Carrying Reduces Infant Crying: A Randomized Controlled Trial', Pediatrics, 77(5): 641-648

Hunziker, U. A., & Barr, R. G. (1986), 'Increased Carrying Reduces Infant Crying: A Randomized Controlled Trial', Pediatrics, 77(5): 641-648.

Imai, T., Moore, S. T., Raphan, T., & Cohen, B. (2001), 'Interaction of the Body, Head, and Eyes During Walking and Turning', Experimental Brain Research, 136(1): 1-18.

Johnson, R. F., Knapik, J. J., & Merullo, D. J. (1995), 'Symptoms during Load Carrying: Effects of Mass and Load Distribution during A 20-Km Road March', Perceptual And Motor Skills, 81(1): 331-338.

Kamal, N. A., Mohd Hashim, A.H., Ibrahim, H., Zainuddin, Z.A (2014), ‘ Perbezaan Kaedah Baby Wearing Terhadap Penggunaan Oksigen’, Journal of Physical Activity , Sports & Exercise, 2(2):21-26.

Knapik, J., Harman, E., & Reynolds, K. (1996), ‘Load Carriage Using Packs: A Review of Physiological, Biomechanical and Medical Aspects’, Applied Ergonomics, 27(3): 207-216.

Ludington-Hoe, S.M., (2013), ‘Kanggaroo Care as Neonatal Therapy, Newborn And Infant’, Nursing Review, 13(2): 73–75

Md Ghani, S.A., Mohd Hashim, A.H., Ibrahim, H., Zainuddin, Z.A (2014), ‘ Perbezaan Penggunaan Kaedah Babywearing Terhadap Penggunaan Tenaga’, Journal of Physical Activity , Sports & Exercise, 2(2):11-14.

Singh, T., & Koh, M. (2009). ‘Effects of Backpack Load Position on Spatiotemporal Parameters And Trunk Forward Lean’, Gait & Posture, 29(1): 49-53.

St. James-Roberts, I. (2007), ‘Helping Parents to Manage Infant Crying and Sleeping: A Review Of The Evidence And Its Implications For Practice’, Child Abuse Review, 16: 47-69.

Valizadeh, L., Ajoodaniyan, N., Namnabati, M., Zamanzadeh, V., Layegh, V. (2013), ‘Nurses' Viewpoint About The Impact of Kangaroo Mother Care on The Mother–Infant Attachment’, Journal of Neonatal Nursing, 19 (1): 38–43.

Wall-Scheffler C, Geiger K, Steudel-Numbers K. (2007), ‘Infant Carrying: The Role of Increased Locomotory Costs in Early Tool Development’. American Journal of Physical Anthropology, 133: 841–846.

Waltraud S, Nitsch P, Wassmer G, Roth B. (2002), ‘Cardiorespiratroy Stability of Premature and Term Infants Carried in Infant Slings’, Pediatrics, 110:879-883.

Westby, M.D., (2001) ‘A Health Professional’s Guide to Exercise Prescription for People with Arthritis: A Review of Aerobic Fitness Activities’, Arthritis Care & Research, 45: 501–11.

Whitcome KK, Shapiro LJ, Lieberman DE. (2007)., ‘Fetal Load and the Evolution of Lumbar Lordosis in Bipedal Hominins’, Nature 450: 1075–1078.

A PRELIMINARY STUDY ON EVOLUTIONARY DESIGN OF IMAGE PROCESSING PIPELINE USING HIERARCHICAL GRAPH STRUCTURE

Kazunari Minami[1], Masaki Maezono[2] & Satoshi Ono[1*]

[1] *Department of Information Science and Biomedical Engineering, Graduate School of Science and Engineering, Kagoshima University, 1-21-40, Korimoto, Kagoshima 890-0065, Japan*

[2] *Department of Information Engineering, Kagoshima National College of Technology, 1460-1, Shinkou, Hayato-cho, Kirishima, Kagoshima 899-5193, Japan*

*Corresponding Author: *ono@ibe.kagoshima-u.ac.jp*

Abstract: An image processing pipeline is an algorithm consisting of known primitive image processes for approximation of desired advanced functions. In general, the pipelines are designed by human experts in accordance with their domain knowledge and heuristics; however, it is essentially a pair of combinatorial optimization that finds an optimal arrangement of the primitive processes and numerical optimization of inner parameters in the primitive filters, requiring a considerable effort even for the experts. Therefore, this paper proposes an automatic design method of image processing pipelines that have graph structure using evolutionary computation (EC). Although the graph-structured pipeline approximates complicated image processing, EC tends to produce pipelines that have simple structure. Therefore, the proposed method iterates automatic graph-structured pipeline design and combines the obtained pipelines in a hierarchical structure so that the whole pipeline performed favorably. Experiments showed the proposed method could design better image processing pipeline than previous work.

Keywords: *Image processing pipeline design, genetic algorithm, evolutionary computation, graph-structured filter, hierarchical structure*

1 Introduction

Image processing and recognition techniques have been used in various fields. In general, a desired image processing algorithm is designed by combining known primitive image processes and such algorithm is called an image processing pipeline (or image processing chain, filter, etc.) . However designing an image processing pipeline is essentially a pair of combinatorial optimization that finds an optimal arrangement of the primitive processes and numerical optimization of inner parameters in the primitive filters, requiring considerable effort even for human experts.

Some methods have been proposeds for improving and automating image processing pipelines. Amongst them, Evolutionary Computation (EC) (Back *et al.*, 1997; Fogel, 2006) based approaches are promising that designs pipelines from scratch without doman knowledge; only pairs of input a desired output images (goal images) are needed, i.e., learning-based approach. EC-based methods approximates unknown image processing by an arrangemnt of known primitive image processing modules, and optimizes the arrangement so that its output images equals or as similar as possible the given desired output images.

The EC-based pipeline design methods are categorized by its structype types: list (Nagao and Masunaga, 1996; Rajua *et al.*, 2015), tree (Aoki and Nagao, 1999; Maezono *et al.*, 2006), and graph (Shirakawa and Nagao, 2007; Minami *et al.*, 2015; Ono *et al.*, 2016). The simplest one is list structure that simply applies known primitive image filters to an input image in turn. Tree structured pipeline allows using multiple inputs, e.g., color channels such as RGB and HSB. Genetic Algorithm (GA) (Goldberg, 1989) and Genetic Programming (G) (Koza, 1992) are mainly used to optimize list- and tree-structure, respectively. Graph-strucutred one reuses part of the pipeline by constructing a loop. The graph structure potentially has high flexibility; however, the graph-based method sometimes produces only lusterless filters that have too simple structure to produce images with sufficient quality especially when using many training images.

Therefore, this paper proposes an image processing filter design method that iteratively designs garph-structured pipeline in a hierarchical manner. That is, turning the the graph-based method's drawback of tending to generate simple structured filters to good account, the proposed method performs Genetic Algorithm (GA) based searches recursively and allows upper (later) search to use the designed partial filters in lower (earlier) searches as components to build a filter having sufficient performance. Experimental results have shown that the proposed method could design better image processing pipeline than that desgined by one GA-based search.

2 The proposed method

2.1 Basic Idea

This study presents an evolutionary design method for image processing pipeines. The proposed method is designed based on following ideas:

Graph-structured pipeline: the proposed method designs an image processing pipeline that have graph structure in which nodes correspond to known primitive filters and edges represent processing order. The graph structure essentially involves list and tree structures and allows representing feedback and loop structures. The proposed method designs the structure using GA rather than GP, preventing the *bloat* problem that solution size increases as the search progresses (Maezono et al., 2006). A derived image

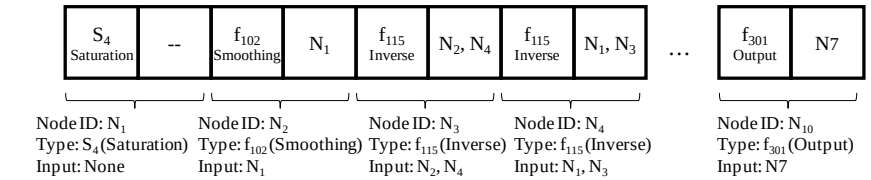

(a) Genotype

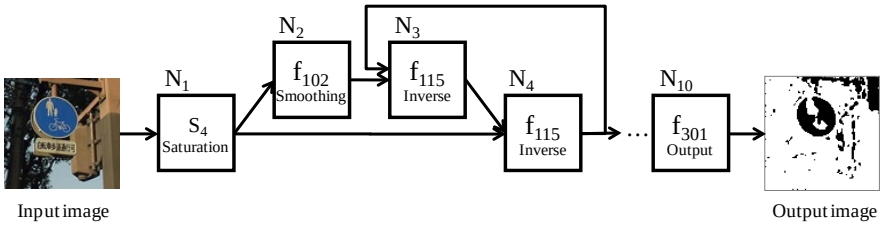

(b) Phenotype

Figure 1: Chromosome representation (Ono et al., 2016).

processing pipeline is human-readable and helps human experts to obtain new domain knowledge.

Hierarchical approach: graph-structured filters desinged by the *i*-th level search by GA, which are called as *functional filters*, are used in the same way as primitive filters in the (*i*+1)-th level search. In every search level, GA is performed several times so that designed filters compensate for each other. Therefore, the hierarchical approach allows the proposed method to design compensatory filters for each other and to combine them to build a better filter.

2.2 Chromosome Representation

The output of the proposed method is a image processing filter involving graph-structured pipeline. To find a solution with GA, the genotype and phenotype of a solution are represented as in Figure 1 on the basis of a previos work (Minami *et al.*, 2015; Ono *et al.*, 2016). A chromosome consists of a sequence of pairs involving two types of genes: a primitive filter identification number and a list of input arcs, as shown in Figure 1(a). A pair of genes is necessary in a genotype to compose a node and arcs connected to the node in a graph.

A phenotype is a graph that consists of nodes corresponding to primitive filters and arcs between nodes. Each primitive filter modifies an image obtained from a previous node connected to an incoming arc, and it sends its output image to the next nodes through outgoing arcs.

Unlike list- and tree-structured image filters, a graph-structured image processing pipeline requires a timescale to produce a consistent output image. In each step, all nodes apply their own filter to an input image and output the result to other filters. The filter graph stops when the number of steps reaches T_{step}, a parameter that was defined beforehand, and it outputs an image of an output filter node.

Tables 1 through 3 list the primitive filters used in this study. The filters are categorized into the following three groups according to the default number of input arcs: primitive filters without input arcs, with one input arc, and with two input arcs. Primitive filters without input arcs output the color componets of an input image, such as red, green, blue, hue, saturation, etc. Primitive filters with one input arc are simple, commonly used impage processing filters such as edge enhancement, binarization, etc. Primitive filters with two input arcs produce an output image with a specified operator such as subtraction, addition, average etc.

A node can have more input arcs than its primitive filters's number of default arcs; for instance, a node with a smoothing filter can have more than one input arc, and a node with an average filter can have more than two input arcs. In such cases, input arcs are prioritized in the reverse chronological order of input image update. In the opposite case, when a primitive filter whose defaur is two arcs has only one input arc, it simply outputs the input image, unchanged. Also, a node that have no input or no output arcs is ignored.

Some of the primitive filters have internal parameters, e.g., a binarization threshold, multiplier value, and addition value. Such internal parameters are initialized with a default value and are subsequently modified by mutation in GA processes.

A gene corresponding to a primitive filter node is represented as a set of integer values representing a primitive filter identification number and an internal filter parameter and a gene corresponding to an arc list is represente as a variable length list of interger values.

In the first level search, filters without input arc are put into a choromosome one by one, and the nodes involving them are locked, i.e., their primitive filter IDs cannot be changed during the search. Then, in the second level search and later, the filters generated by the previous level GAs are also put into the chromosome and their IDs are also not changed. Note that the ID fixation does not mean all the filters are necessarily used because some of them are not used when they does not have their output edge.

Objective function of this task is calculated by an averaged pixel-wise correspondance rate between given goal images and output images by an individual I as follows:

Table 1: Primitive filters without input arcs.

ID	Filter name	Inner parameter (default and range)	ID	Filter name	Inner parameter (default and range)
S_0	Red components	–	S_5	Brightnesscomponents	–
S_1	Green components	–	S_{50}	HLS Brightness	–
S_2	Blue components	–	S_{51}	Lab Luminance	–
S_3	Hue components	–	S_{52}	Lab a* components	–
S_4	Saturation components	–	S_{53}	Lab b* components	–

Table 2: Primitive filters with an input arc.

ID	Filter name	Inner parameter (default and range)			Inner parameter (default and range)
f_{101}	Edge emphasize	–	f_{122}	Min in neighbor	–
f_{102}	Smoothing	–	f_{123}	Max in neighbor	–
f_{103}	Edge extraction	–	f_{150}	Opening	3 (1-10)
f_{104}	Embossing Top	–	f_{151}	Closing	3 (1-10)
f_{105}	Embossing TopRight	–	f_{152}	Tophat	3 (1-10)
f_{106}	Embossing Right	–	f_{153}	Blackhat	3 (1-10)
f_{107}	Embossing BottomRight	–	f_{154}	Gradient	3 (1-10)
f_{108}	Embossing Bottom	–	f_{156}	Gaussian	3 (3-51)
f_{109}	Embossing BottomLeft	–	f_{157}	Sobel	–
f_{110}	Embossing Left	–	f_{158}	ScharrX	–
f_{111}	Embossing TopLeft	–	f_{159}	ScharrY	–
f_{112}	Binarization	128 (0-256)	f_{160}	Laplacian	–
f_{113}	Binarization	64 (0-256)	f_{161}	Canny	–
f_{114}	Binarization	192 (0-256)	f_{163}	SURF	–
f_{115}	Inverse	–	f_{169}	Zero wt threshold	128 (0-255)
f_{116}	Maximization	128 (0-256)	f_{170}	Noise reduction	–
f_{117}	Minimization	128 (0-256)	f_{180}	Fixed value	128 (0-255)
f_{118}	Multiplication	1.5 (1-5)	f_{181}	Convolution	0 (0-5)
f_{119}	Multiplication	0.5 (0.1-0.9)	f_{190}	Binarization Otsu	–
f_{120}	Addition	25 (0-255)	f_{191}	Guided filter	2 (1-3)
f_{121}	Subtraction	25 (0-255)	f_{192}	Normalize	–

Table 3: Primitive filters with two input arcs.

ID	Filter name	Inner parameter (default and range)	ID	Filter name	Inner parameter (default and range)
f_{201}	Abs of subtraction	–	f_{206}	Lower	–
f_{202}	Subtraction	–	f_{250}	And	–
f_{203}	Sum	–	f_{251}	Or	–
f_{204}	Avarage	–	f_{252}	Exclusive or	–
f_{205}	Higher	–			

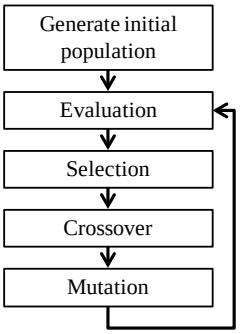

Figure 2: Process flow in each GA-based search.

$$f(I) = \frac{1}{N_{ti}} \sum_{k=1}^{N_{ti}} \left\{ 1 - \frac{\sum_{x=1}^{W_k} \sum_{y=1}^{H_k} w_k(x,y)\, \delta_k(x,y)}{\sum_{x=1}^{W_k} \sum_{y=1}^{H_k} w_k(x,y)} \right\} \quad (1)$$

$$\delta_k(\mathrm{x},\mathrm{y}) = \begin{cases} 1 & \text{if } |O_k(x,y) - T_k(x,y)| \geq \epsilon V_{max} \\ 0 & \text{otherwise} \end{cases} \quad (2)$$

where N_{ti} is the number of training images, and W_k are H_k are image width and height, and O_k, T_k, and w_k are given goal image, output image by individual I, and weight image whose pixel intensity represents the importance of the region in the goal image.

2.3 Process Flow

2.3.1 Pipeline Design Using Genetic Algorithm

Although the chromosome in the proposed method comprises a sequence of node information consisting of primitive filter ID, input edges, and inner parameter, general process flow of GA can be applied as shown in Fig. 2. First, an initial population is generated randomly. Then, individuals in the population are evaluated. To calculate the fitness function shown in Sec. 2.2, phenotype, i.e., an image processing pipeline, is implemented and applied to a given image sets. According to the obtained fitness values genetic operators such as selection, crossover, and mutation are performed to reproduce individuals in the next generation.

2.3.2 Hierarchization

The proposed method iteratively applies GA-based search shown in Sec. 2.3.1 to build an approximated image propcessing pipeline rather than simply applying the search just

once like previous work (Minami *et al.*, 2015; Ono *et al.*, 2016). Algorithm 1 describes the hierarchical framework of the proposed method.

Algorithm 1. Pseudo-code of the proposed algorithm.

1: **while** *level* ≤ $level_{max}$ **do**:
2: generate a filter using GA with the original training image set
3: **for** *filters* = 1 **to** N_{sup} **do**:
4: **if** *filters* = 1 **then**:
5: Make a derived training image set whose goal image is the difference between the original goal image and the output image of GA in line 2.
6: **else**:
7: Make a derived training image set whose goal image is the difference between the original goal image and the output image of GA in line 8.
8: Generate a filter using GA with the derived training image set.

An image processing filter designed by one GA-based search is called *a functional filter*. In the *n*-th level, functional filters generated from the first to $(n-1)$-th levels are used in the same way as the predetermined primitive filters, which are shown in Table 1, i.e., the functional filters are incorporated as a node when designing a new functional filter.

Also, in each level, GA-based search is performed more than one times to build functional filters that compensate with each other while varying goal images of a training image dataset, i.e., difference image between the original goal image and the output image produced by the filter designed in previous GA-based search.

In this study, functional filters derived in the earlier levels are used in the same way as the primitive filters without imput edge as shown in Figure 3, though the funcitonal filters can be used as primitive filters with an input edge. This is for the sake of simplification and improving computation speed; when evaluating solution candidates involving the functional filter, there is no need to apply the functional filter to the training image, i.e., its output image can be reused. Therefore, the computational cost of GA-based search in the second or later level is the same as the search in the first level, though the image processing pipeline becomes bigger and more complicated as the level increases.

In the first level, the first GA-based search in line 2 of Algorithm 1 corresponds to the search in previous work (Minami *et al.*, 2015; Ono *et al.*, 2016). In this study, N_{sup} is fixed to three, and the second and third GA-based searches aim at designing functional filters that eliminates misdetected regions by the functional filter designed by the first GA and that detect regions that cannot be extracted by the filter, respectively. Then, a goal image in a training dataset for the second GA is made by subtracting the region in the original goal image from that in the output of the functional filter by the first GA, and a goal image for the third GA is made by subtracting the region in the output of the first filter from that in the original goal. The weight image for the second GA is

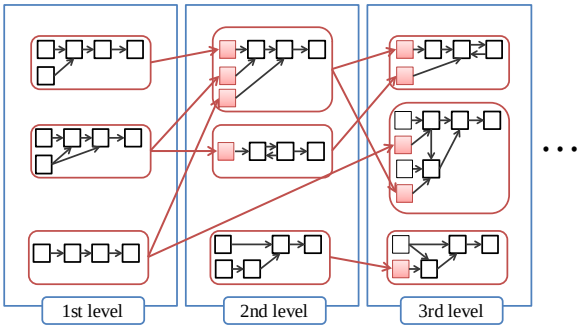

Figure 3: Example hierarchical filter.

generated so that the weight of the target region in the derived goal image become high, that of the region in the original goal moderately high, and the weight of the background almost zero, respectively. The weight image for the third GA is generated so that the weight of the detected region by the first GA becomes zero and the weight of the different region high, respectively.

In the second level, the three functional filters designed by the first level are used. If the two compensative functional filters would work properly, the first GA in the second level could produce a desirable filter that recognizes the target region with high accuracy. Actually, there often remains a gap between the given goal image and the output of the designed filter. In that case, the second and third GAs in the second level are peformed in the same way as those in the first level. The iteration stops when the output quality reaches some predetermined threshold or after $level_{max}$ times.

3 Evaluation

3.1 Experimental Design

To validate the effectiveness of the proposed method, experiments were conducted with the image dataset of "Segmentation of neuronal structures in EM stacks" in IEEE International Symposium on Biomedical Imaging (ISBI2012)[1] (Arganda-Carreras *et al.*, 2015). This dataset involves a full stack of EM slices (30 images with resolution of 512×512 pixels for 2×2 microns) and the goal images are binarized so that white for the pixels of segmented objects and black for the rest of pixels which correspond mostly to membranes, as shown in Figure 4(b).

To see the possibility whether the proposed method can improve its performance by iterating GA-based search in the hierarchical manner, all images are used for tranining rather than evaluating generaization performance by cross validation. Control

[1] http://brainiac2.mit.edu/isbi_challenge/home

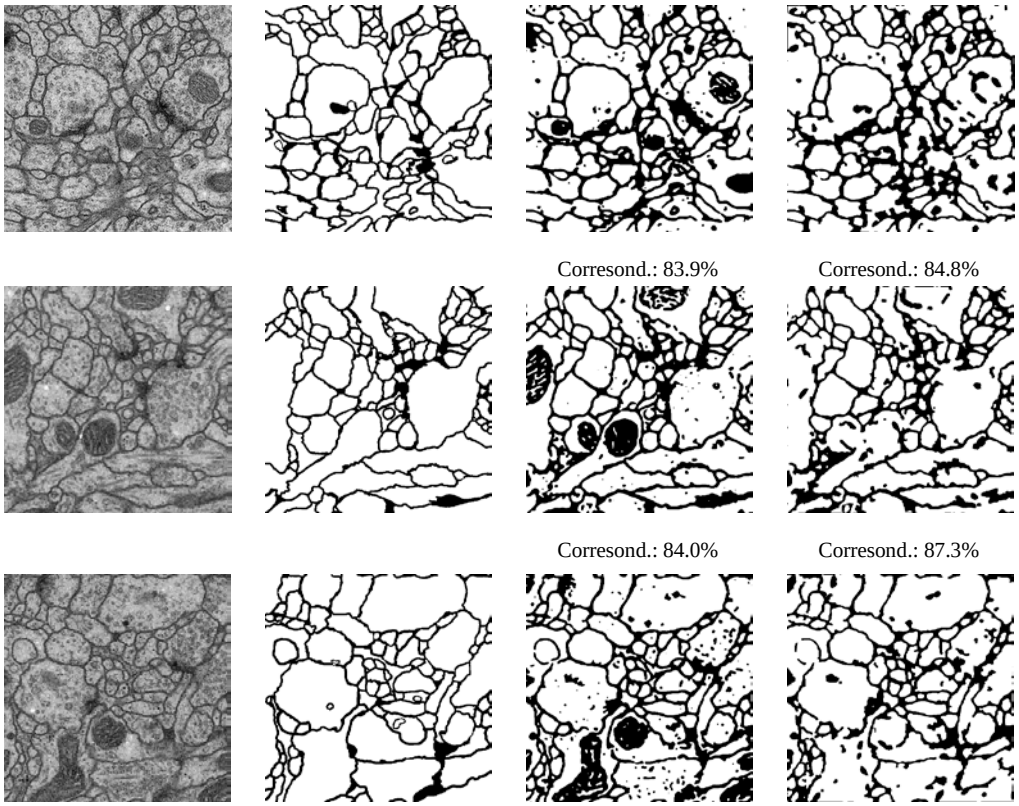

(a) Input images (b) Given goal images (c) Outputs of the 1st level (previous work) (d) Outputs of the 4th level (proposed method)

Figure 4: Example outputs of the filters designed by the proposed method.

parameters in GA were configured as follows. Minimal Generation Gap (MGG) was used as a generation alternation model (Satoh *et al.*, 1996). Population size, crossover rate, mutation rate were set to 50, 0.52, and 0.03, respectively. The choromosome length, which corresponds to the number of primitive filters used in a functional filter, and the number of steps T_{step} in each functional filter were set to 20 and 15, respectively. The GA-based search was iterated until level four, i.e., $level_{max} = 4$, and, in each level from the first to the third, GA was performed three times, i.e., $N_{sup} = 3$.

3.2 Experimental Result

Figure 4(c) and (d) show the output images by the functional filter $F_{1\text{-}1}$ designed by the first GA in the first level, which corresponds to previous work (Minami *et al.*, 2015; Ono *et al.*, 2016), and the output images of the filter $F_{4\text{-}1}$ designed by the GA in the

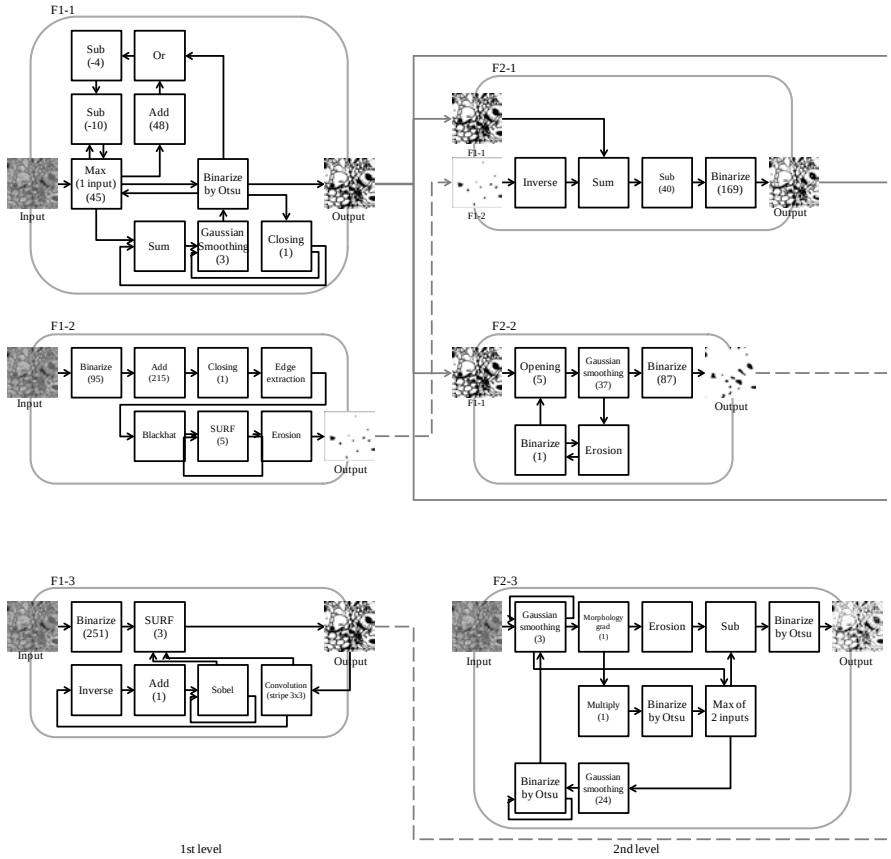

Figure 5: Designed image processing filter (1st and 2nd levels).

fourth level, which corresponds to the proposed hierarchical method, respectively. Although menbranes were basically extracted in the both results, the output of the previous work clearly involves nucleuses that should not be extracted whereas the output of the proposed method roughly eliminated them.

Figures 5 and 6 shows the whole filter structure designed by the proposed method. The first GA in the first level, which produced the images shown in Figure 4(c), successfully recognized membranes but inappropriately extracts nucleuses. The fucntional filter $F_{1\text{-}2}$ desgiend by the second GA in the first level adequately compensated eliminating the nucleus regions in some of training images, and also eliminated noises nearby menbranes by applying closing process. In the second level, the first GA search combined the two functional filters $F_{1\text{-}1}$ and $F_{1\text{-}2}$ obtained by the first and second GA in the first level, and the first GA in the thrid level also combined the three functional filters $F_{1\text{-}1}$, $F_{1\text{-}2}$, and $F_{2\text{-}1}$. As the iteration level increases, the generated filter gradually improved its output.

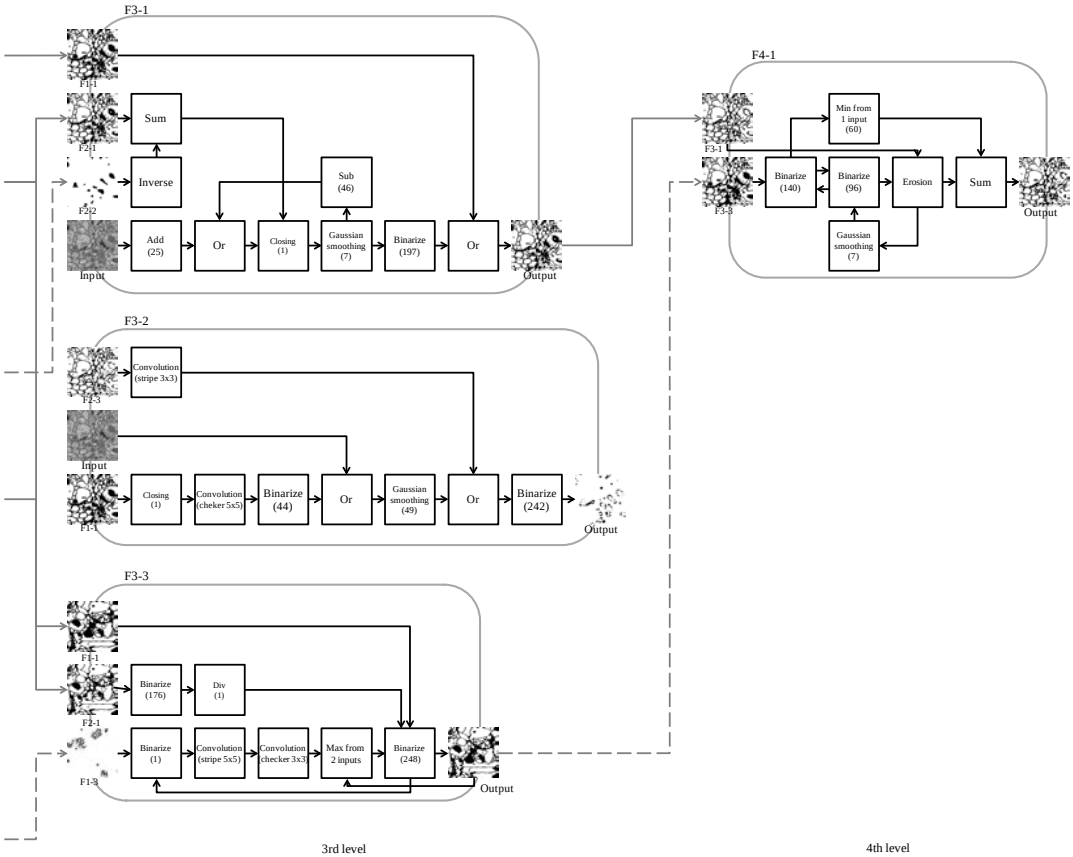

Figure 6: Designed image processing filter (3rd and 4th levels).

4 Conclusions

This paper proposes an image processing filter design method that combines known primitive filters to build a graph-structured image processing pipeline. The proposed method takes a hierarchical approach to improve the filter's performance, i.e., iteratively applying GA-based search and desgined functinal filters are used in the later search in the same way as the given primitive filters. It is also the advantage that the generated pipeline can be easily converted into a C++ language code, i.e., directly editable and executable format.

Experimental results showed that the proposed method could design the filter that produced better output image by iterating GA than the output of the filter designed by one GA-based search, which corresponds to previous work. Although the results showed the proposed hierarchical approach achieved small improvement, it is still in its infancy and has much room to improve.

In future, we plan to add more primitive filters; segment-wise processes would improve the output image quality and help to simplify filter structure.

5 Acknowledgements

This work was partially supported by JSPS KAKENHI Grant Number 23700272 and SCOPE (142110001) of Ministry of Internal Affairs and Communications (MIC), Japan.

References

Aoki, S. and Nagao, T. (1999). *Automatic construction of tree-structural image transformation using genetic programming*. In: Proceedings of the 1999 International Conference on Image Processing (ICIP-99). 1: 529–533.

Arganda-Carreras, I., Turaga S. C., Berger D. R. et al. (2015). *Crowdsourcing the creation of image segmentation algorithms for connectomics*. Frontiers in Neuroanatomy. 9: 142

Back, T., Fogel, D. B. and Michalewicz, Z. (1997). *Handbook of evolutionary computation*. New York: Oxford.

Fogel, D. B. (2006). *Evolutionary computation: toward a new philosophy of machine intelligence*. John Wiley & Sons.

Goldberg, D.E. (1989). *Genetic Algorithms in Search, Optimization, and Machine Learning.* Addison Wesley, Reading.

Koza, J. (1992). *Genetic Programming: On the Programming of Computers by Means of Natural Selection*. MIT Press.

Maezono, M., Ono, S. and Nakayama, S. (2006). *Automatic Parameter Tuning and Bloat Restriction in Image Processing Filter Generation Using Genetic Programming*. Transactions of Japan Society for Computational Engineering and Science, 20060021 (in Japanese).

Minami, K., Shiba, Y., and Ono, S. (2015). *Watermark Extraction Algorithm Design by Graph-Based Genetic Algorithm for Detecting Illegally Replicated Two-Dimensional Barcodes*. International Symposium on Artificial Life and Robotics, 438-443.

Nagao, T. and Masunanga S. (1996). *Automatic construction of image transformation processes using genetic algorithm*. In Proc. Int'l Conf. Image Processing, 731–734.

Ono, S., Maehara, T., and Minami, K. (2016). *Coevolutionary Design of a Watermark Embedding Scheme and an Extraction Algorithm for Detecting Replicated Two-dimensional Barcodes*, Applied Soft Computing, 46: 991-1007.

Rajua, R., Maula, T. and Bargiela, A. (2015). *Multiple Image Processing Chain Analysis for Membrane Detection – Optimization Outcome*. J. Comp. Sci. Comm. 1(2): 1-11.

Satoh, H., Yamamura, M., and Kobayashi, S. (1996). *Minimal generation gap model for gas considering both exploration and exploitation*. In: Proc. Int'l Conf. Soft Computing, 494–497.

Shirakawa, S. and Nagao, T. (2007). *Genetic Image Network (GIN): Automatically Construction of Image Processing Algorithm*. In Proc. Int'l Workshop on Advance Image Technology.

SYNTHESIS OF SiC USING ATMOSPHERIC PRESSURE NON-THERMAL PLASMA TECHNOLOGY

Marwan Hafeedh Yuonus[1], Aminudin Haji Abu[2], Shahrouz Zamani Khalajabadi[2], Norizah Redzuan[3] , Norhayati Ahmad[3]& Raja Kamarulzaman Raja Ibrahim[1*]

[1] *Laser Centre, Physics Department Faculty of Science, Universiti Teknologi Malaysia,*
[2] *Malaysia-Japan International Institute of Technology, Universiti Teknologi Malaysia,*
[3] *Faculty of Mechanical Engineering, Universiti Teknologi Malaysia.*

*Corresponding Author: *rkamarulzaman@utm.my*

Abstract: In this study, Dielectric Barrier Discharge Non-thermal Plasma technique (DBD-NTP) is used to deposit SiC films on the silica Multimode optical fiber at 10-30 seconds of deposition time. FTIR and FE-SEM equipped with EDS were used to characterize the deposited SiC films. It is found the thickness of deposited films on silica fibers is about 90 to 260 nm after 10-30 seconds of deposition. The homogeneous and uniform SiC film was obtained for the samples coated by 10 seconds of deposition time. The results indicate the DBD-NTP could be an appropriate technique for coating of optical fiber with SiC films.

Keywords: *Dielectric Barrier Discharge, Non Thermal Plasma, SiC film, Multimode Fiber*

1.0 Introduction

Silicon carbide (SiC) is considered as a promising material for the fabrication of high-temperature pressure sensors, owing to its mechanical robustness and chemical inertness at elevated temperatures. In addition, the electrical characteristics of SiC reveal a wide band gap, a low leakage current, and a high-breakdown electric field that making it was a better candidate for high-temperature electronic applications than silicon [1,2]. Simple and low-cost technique such as Dielectric Barrier Discharge-Non Thermal Plasma (DBD-NTP) represents a unique alternative for the synthesis of SiC. To the best of our knowledge, SiC growth on the optical fiber via DBD-NTP method has not been explored extensively. Thus, DBD-NTP method used to deposit of SiC films on the unclad section of the optical fiber in this study.

2.0 Materials and Methods

The deposition of SiC was carried out in a custom-built Dielectric Barrier Discharge Non-thermal Plasma system (DBD-NTP). The SiC was deposited from a mixture of between the Tetraethylorthosilicate (TEOS) vapor and Methane gas (CH_4). The schematic diagram of the experimental set-up is shown in Figure 1. The setup consists of a gas delivery system, plasma reactor and electrical measurement system. In the DBD reactor, the discharged plasma was generated in a cylindrical glass tube with an inner diameter of 10 mm and length of 150 mm. A graphene layer was wrapped on the outer surface of the glass tube and acts as the outer electrode, whereas a galvanized steel wire coated with zinc layer was used as the inner electrode (ground electrode). Both electrodes were connected to an AC high voltage source (PVM/DDR Plasma Dielectric Barrier Corona Driver, AC voltage 0-40 kV and frequency 20-70 kHz variable). The high voltage and current probes were used to measure applied voltage and current. The probes connected to a PC based Oscilloscope (PicoScope, ADC-216, Pico Technology) to record voltage and current reading and display on the PC. Microstructure, thickness and chemical composition of deposited films were investigated using FE-SEM (JEOL JSM 6380LA) equipped by EDX. A Fourier Transform Infrared Spectrometer (FTIR, SHIMADZU-IRAffinity-1S), was used to analyze the chemical bonding as well as to determine of the composition of multimode optical fiber (MMF) before and after deposition of SiC films.

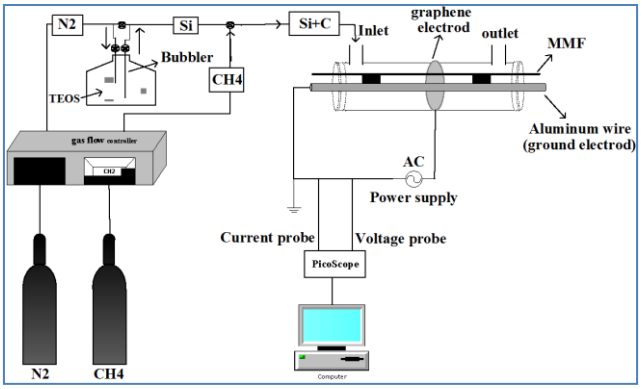

Figure 1: A schematic diagram of the experimental setup of SiC deposition on the MMF in DBD-NTP.

3.0 Results and Discussion

Figure 2(a) displays the typical EDX spectra of MMF system without and with the SiC films. By 10 sec of deposition, the film which formed on the MMF is mainly composed of Si, C and O, as well as the corresponding atomic percentage (at.%) are 31.1%, 13.3%

and 55.6%, respectively. However, the EDX spectra without SiC film composed of Si and O only.

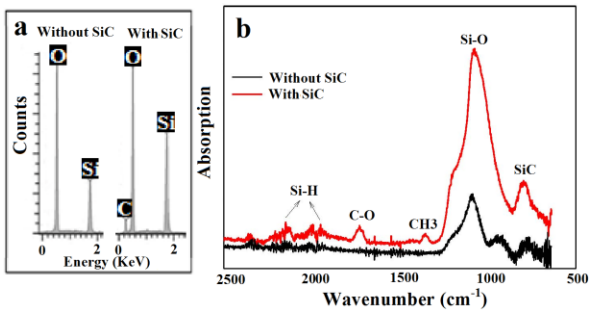

Figure 2: (a) EDX spectra scanned and (b) FTIR absorbance spectra on the MMF sensor at 10 sec of deposition

It can infer that the deposited layer on the MMF sensor is SiC. The presence of O in the surface of samples can be caused by the surface contamination which occured during the preparation of sample using a non vacuum technique. By 10 sec of deposition, a higher amount of C (13.3at.%) was obtained on the sample compared to those of after 20 and 30 sec of deposition time. Figure 2(b) indicates FTIR spectra of MMF with and without SiC film. The peak at 798 cm^{-1} corresponds to the stretching mode of the SiC bond [3,4]. The spectrum around 1000 cm^{-1} represents the stretching mode of the C-O bond. However, the weak peaks at 1366–1740 cm^{-1} referred to wagging, rocking and bending motions of type CH2 and CH3, which have the same tendency. The peaks that appeared at 2150–2300 cm^{-1} referred to stretching vibrations of Si-H bond [3,5,6].

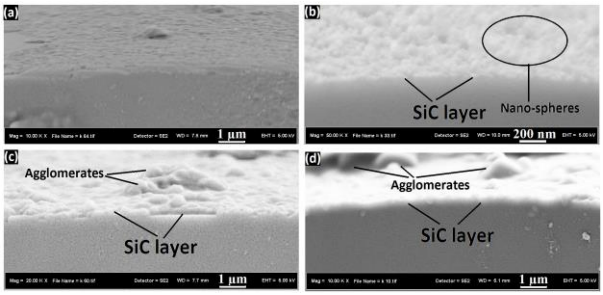

Figure 3: FE-SEM images of the SiC layer produced by DBD-NTP method, (a) MMF sensor without the SiC layer, MMF sensor with the SiC layer (b) after 10 seconds (c) 20 sec and (d) 30sec of deposition.

Figure 3 shows the FE-SEM images of the MMF sensors before and after SiC deposition. As can be seen, the formation of SiC films consisting spherical particles on the surface of optical fiber sensors is proved. A homogenous and uniform SiC film with ~95 nm of thickness is formed after 10 sec of deposition. By increasing of deposition time from 10 to 30 seconds the thickness of SiC increased to ~250 nm and the homogeneity of SiC

layer and particle size of nano-spheres decreased as some agglomerates observed on the samples deposited for 20 and 30 seconds.

4.0 Conclusions

1) EDX analysis indicate the formation of SiC film on the optical fibers using DBD-NTP technique
2) According to the FE-SEM images, the SiC formed on the optical fibers has uniform and homogenous microstructure consisting nano-spheres
3) FTIR results confirm chemical bonding energy of SiC on the surface of optical fibers after 10 sec of deposition
4) DBD-NTP is an appropriate technique for SiC coating optical fibers

5.0 Acknowledgements

This work was supported by Universiti Teknologi Malaysia under contract research grant 4C044 and Ministry of Higher Education under FRGS Grant 4F552 and 4F808.

References

M. Mehregany, and C. A. Zorman. (1999). *SiC MEMS: opportunities and challenges for applications in harsh environments.* Thin Solid Films 355–356, 518-524.

P. G. Neudeck, R. S. Okojie and C. Liang-Yu. (2002). *High-temperature electronics - a role for wide bandgap semiconductors?* Proceedings of the IEEE. 90(6), 1065-1076.

M. Künle, T. Kaltenbach, P. Löper, A. Hartel, *et al.* (2010). *Si-rich a-SiC:H thin films: Structural and optical transformations during thermal annealing*. Thin Solid Films. 519(1), 151-157.

Karbovnyk, P. Savchyn, A. Huczko, M. C. Guidi, *et al.* (2015). *FTIR studies of silicon carbide 1D-nanostructures.* Materials Science Forum: Trans Tech Publications Ltd. 821, 261.

T. Kaneko, D. Nemoto, A. Horiguchi and N. Miyakawa. (2005). *FTIR analysis of a-SiC:H films grown by plasma enhanced CVD.* J Cryst Growth. 275(1–2), e1097-e1101.

C. E. Viana, N. I. Morimoto and O. Bonnaud. (2000). *Annealing effects in the PECVD SiO2 thin films deposited using TEOS, Ar and O2 mixture*. Microelectronics Reliability. 40(4–5), 613-616.

POSTER PRESENTATIONS

Study on analysis model of R/C members aimed at evaluating residual deformation

National Institute of Tech, Kagoshima College Shimotsuru Shoma Kawasoe Atsuya

1. Academic background

Research on seismic isolation and damping structure has advance, and it is adopted mainly for high importance and high-rise building. But the base isolation / damping structure is very expensive. It is rare to be adopted for buildings such as facilities, apartment, houses etc. Since the 1995 Hyogo ken Nanbu Earthquake, the Great East Japan Earthquake of 2011 and the Kumamoto earthquake of last year, the activity is in the active phase of the earthquake near the Japanese archipelago A simple and inexpensive construction method is required to suppress the damage after the earthquake and to be able to use it continually. Reforced concrete construction (hereinafter referred to as RC construction) and the steel-framed earthquake-resistant structure are characterized by the surrender of the structure at the time of the earthquake Since the vibration energy is absorbed by damage, damage and deformation will remain after the earthquake. The reduction of these will be an important future task of the earthquake resistant structure. The upper main bar of the beam is made high strength reinforcing bar and the lower end main bar is made of ordinary rebar By doing so, after the ordinary rebar digested , Demonstrating that secondary rigidity by high strength reinforcing bars can be demonstrated and the residual deformation after the earthquake can be suppressed. However, if the high strength reinforcing bars are increased, although the residual deformation suppressing performance is improved, the secondary rigidity becomes large and large The shear force increases in the deformation zone, and the shearing design of the beams and the design of the pillars become severer remains.

2.Purpose of research

In order to continue to use the reinforced concrete building (hereinafter referred to as RC) building after a major earthquake, it is important to suppress not only the damage of the parts but also the residual deformation. It is a case of a large earthquake , We are aiming to minimize the damage to the structure and suppress the residual deformation angle to an extent that does not cause problems in use.

Specifically, we aim to develop an RC structure in which the residual interlayer deformation angle remains within 1/400 radian even if it receives a large earthquake reaching a maximum interlinear deformation angle of 1/50 rad. As a result of previous studies, It is clarified that by using the high strength reinforcing bars at the upper end, the entire frame can have the same hysteresis characteristics as the vibration damping structure by exhibiting the secondary rigidity throughout the beam.In this study, We proposed an analytical model of beam members aimed at evaluation of deformation. We developed an analytical model of beam using high strength reinforcing bars for a part of the upper end muscle and verify the analytical model.

3. Specimen to be analyzed and analysis model

The specimen to be analyzed is shown in Figure 1. The conventional specimen N - No.2 uses only ordinary rebar. In the improved specimen H - No.4, the upper end muscle is ordinary rebar, High strength reinforcing bars are placed at a position 50 mm from the upper end and the lower end muscles are all ordinary rebar with shearing force applied to the beam parts through the stubs provided at both ends of the beam. The two hydraulic jacks , The stubs at both ends are applied so as to move in parallel up and down. When unloading from the peak, quasi - static force is assumed assuming free vibration.

An analytical model of the specimen is shown in Figure 2. The plastic hinge is modeled by a multi spring (MS), the rotation of the material edge by withdrawal of the main reinforcement is a rotational spring, and the deformation due to the shear slip is modeled with a shear spring Other elements are elastic The restoring force characteristic of the reinforcing bar in the MS was a modified Ramberg-Osgood type and the restoring force characteristic of the concrete was a curve rigidity reducing model. The restoring force characteristic of the rotating spring was a slip rigidity reducing type, the restoring of the shear spring The force characteristic was a trilinear slip type.

In order to model the withdrawal of the reinforcing bar with a rotating spring as shown in Figure 3 (a), the rotation angle due to the extraction of the reinforcing bar is temporarily replaced with a virtual beam (hereinafter referred to as a virtual beam) shown in Figure 3 (b) MS is modeled in the same way as plastic hinge. The length Lv of the virtual beam is set so as to be the rotation angle due to extraction of the reinforcing bar caused by the bending moment of the beam end at the time of yield. Finding The relationship between the bending moment M and the rotation angle rθ of the beam and the modeled rotating spring is shown. The model of the rotating spring is modeled based on the load-deformation relation of the virtual beam. Figure 5 shows the restoring force characteristic The shearing spring was set so that the amount of shear sliding became 1/3 of the bending deformation of the beam. The restoring force characteristic of the shear spring was the slip model (FIG. 6).

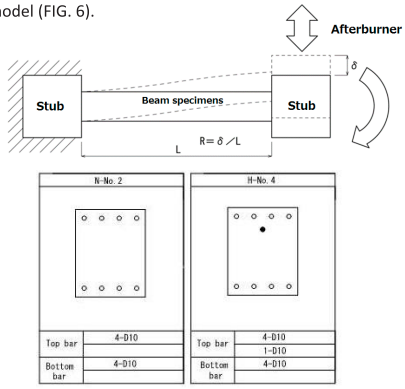

Figure 1 basic shape of the specimen and loading method

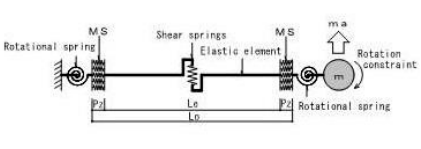

Figure 2 beam model of specimen

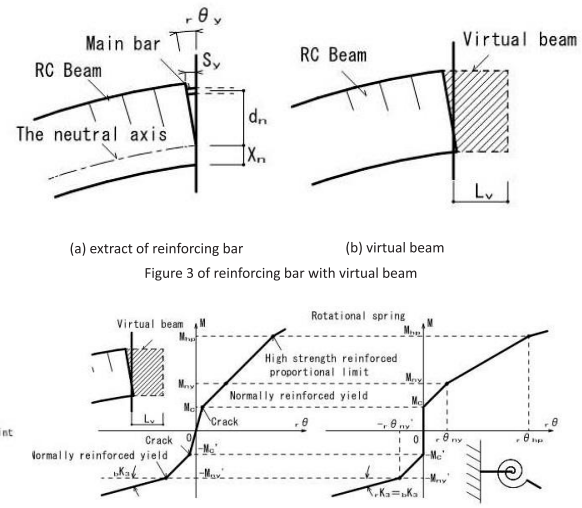

(a) extract of reinforcing bar (b) virtual beam

Figure 3 of reinforcing bar with virtual beam

Load - displacement relationships

Figure 4 virtual beam and rotational spring

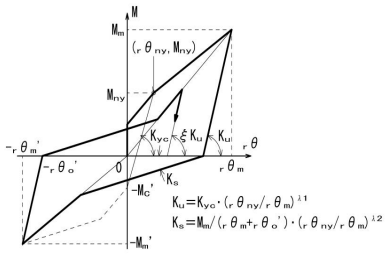

Figure 5 Rotational spring force characteristics
Slip stiffness reduction type

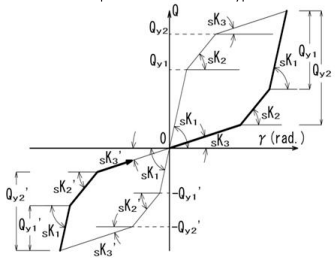

Figure 6 Trilinear slip model
Shear characteristics of spring

4.Comparison of analysis result and experiment result

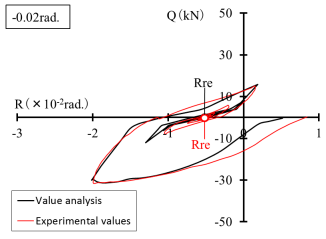

(a) shear force-deformation relation

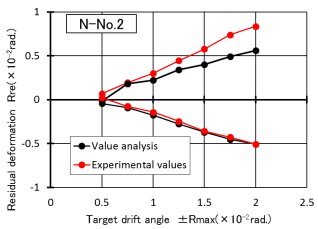

(b) residual deformation-target drift angle relationships

Figure 7-1 N-No.2

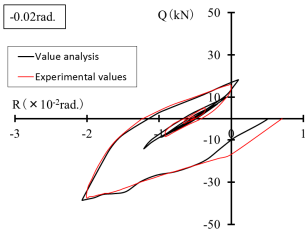

(a) shear force-deformation relation

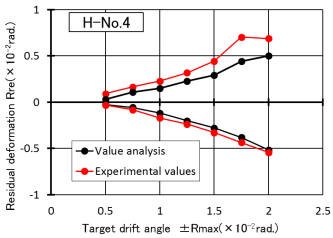

(b) residual deformation-target drift angle relationships

Figure 7-2 H-No.2

- The shape of the loop by experiment was reproduced roughly by analysis.
- The relationship between the target deformation angle and the residual deformation angle was underestimated in the experimental results in some cases, but the target deformation angle in the conventional beam (N - No.2) and the modified beam (H - No.4) The larger it is An increase in residual deformation could be reproduced.
- Using high strength reinforcing bars, it is possible to reduce the amount of shear slip.
- The analysis value of the residual deformation angle Rre decreases as the ratio of the high strength reinforcing bars increases, similarly to the experimental values.

Process performance of 20ºC UASB and non-heating DHS system treating actual soy-sauce wastewater

○Atsushi TOBO, Masayoshi YAMADA
(National Institute of Technology, Kagoshima College)

Introduction

・In soy sauce manufacturing factories, in many cases they use groundwater that is stable at a temperature of 16 to 20 ℃ throughout the year for manufacturing and cleaning. If this can be used for maintaining the temperature of the UASB reactor, it is possible to suppress the power required for maintaining the temperature. Therefore, in this study, we conducted a continuous treatment experiment of soy sauce production wastewater under low temperature (20 ℃) condition using UASB - DHS system combining UADB reactor and DHS (Down - flow hanging sponge) reactor.

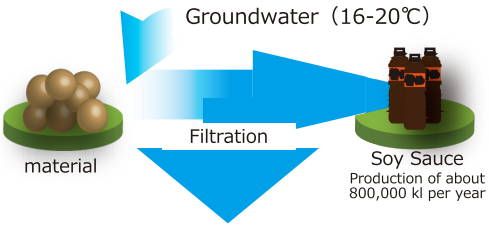

Soy Sauce Production Wastewater
- High COD concentration (100,000 - 150,000mgCOD/L)
- Organic wastewater with a stench

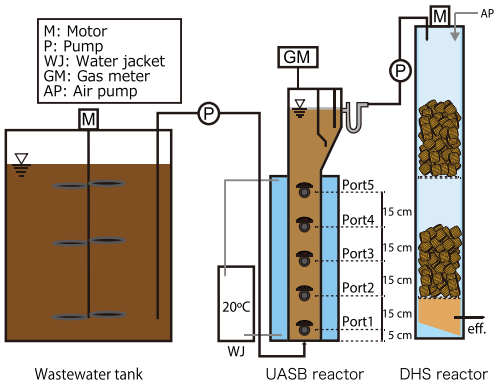

Method

Soy Sauce Production Wastewater

Dilution

- **24% NaOH**
- **Antifoaming agent (0.02%/wastewater)**

UASB-DHS system

・Operating condition

	Days	OLR (kgCOD/m³/day)	COD conc. (mgCOD/L)	HRT (hr)
Phase1	0~25	4.3±0.8	4300±700	27
Phase2	26~66	12.7±3.0	4400±600	9
Phase3	67~210	16.4±3.0	4600±1000	6

・Soy Sauce Production Wastewater composition

pH		4.80
SS	(mg/L)	10,075
VSS	(mg/L)	4,335
VSS/SS	(%)	43
CODcr total	(mg/L)	108,000
soluble	(mg/L)	100,000

VFA accounts for about 50% of COD

VFA	%
Acetate	48.3
Propionic	23.6
i-Butyric acid	4.1
n-Butyric acid	11.7
i-Valeric acid	9
n-Valeric acid	3
i-caproic acid	0.3

Result

Previous studies
Treatment of synthetic Soy Sauce production wastewater

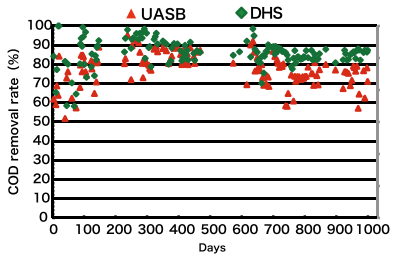

COD removal rate : Under Max OLR 26±3.6kgCOD/m³/day condition, COD removal rate in DHS was 87±7%

COD mass balance

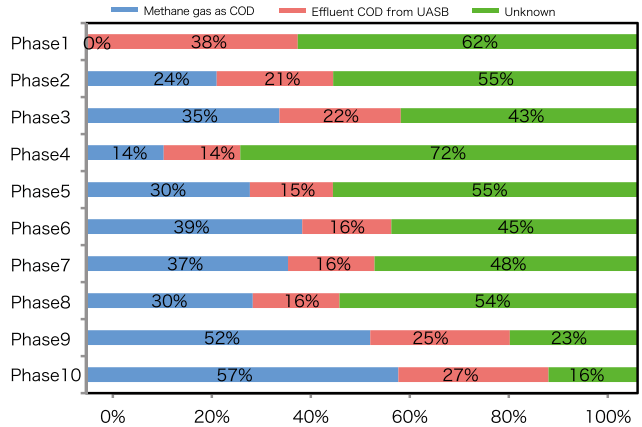

Treatment of actual Soy Sauce production wastewater

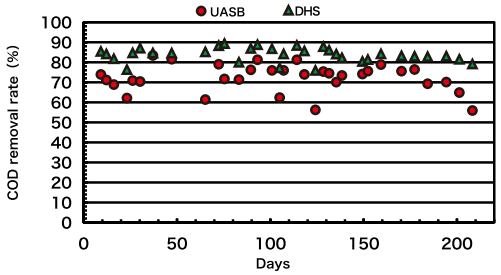

	COD removal rate (%)	
	UASB	DHS
Phase1	69±5	82±4
Phase2	74±9	85±1
Phase3	72±7	84±4

UASB-DHS system performed stable processing

Conclusion

・UASB-DHS system under Max OLR 26±3.6kgCOD/m³/day condition, COD removal rate in UASB was 72±7% and in DHS was 87±7%.

Future outlook on research

- Increase influent COD concentration and perform high load operation
- research the inhibition of sodium ions on treatment

Study on cultivation of mushrooms using fermented bagasse and brown sugar shochu lees

Hiroto Yamasaki[1], Masahito Yamauchi[1]

[1]National Institute of Technology, Kagoshima College

1.Introduction

Brown sugar shochu is an alcoholic spirit produced in the Amami Islands in southern Japan. The waste lees (deposits of dead and residual yeasts and other particles) from shochu production amount to 10,000 t per year1). A feature of shochu lees is the high potassium (K) content (5,200 mg per 100 g dry weight)2). Brown sugar is imported for shochu production because of its low cost, however, the drawback of this practice is the generation of excess K. The lees are usually sprinkled on local sugarcane fields where K accumulates in the soil. This excess K is likely to reduce sugar production by the cane, risking local basic industries. The bagasse fibers that remain after sugar extraction amount to 100,000 t per year and have been used as fuel. Therefore, in order to stimulate the local economy and stabilize sugar cane production in the Amami Islands, it is essential to devise new, high value-added products based on the lees and bagasse byproducts of shochu production.The combined usage of these two shochu by-products for the production of edible mushrooms provides a solution to the problems mentioned above.For this study we chose the cloud ear mushroom, which grows in warm regions, as a trial product. We used the jew's ear mushroom to test growth media containing fermented bagasse and lees, and compared the results with those of mushrooms grown on more conventional growth media.

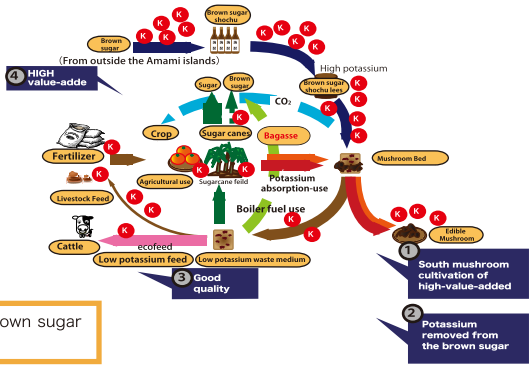

Purpose

We development resource circulation system by jew's ear mushroom production with bagasse and brown sugar shochu lees lower the K content as culture media in agricultural field Amami Island.

2. Materials and Methods

Medium Condition

Moisture Percentage：Adjusted to 65%

Test Strain ：Jew's ear fungus No.89 (Mori industry(LTD))

Culture Condition：Temperature 22±2℃
Humidity 75±5%
Lighting only at the time of work , 70 days

Conditions：Temperature24±1℃
Humidity 90％ or more
Fluorescent 9 h/ day Lighting

Harvest：Pileus is changed to a flat dish-shaped on the cup is more than 8cm size.

Test Itemes

- Weight of fruiting body (groceries , raw)
- Fungus around the number of the days
- The number of days since scraped bacteria to harvest
- The total cultivation dates
- General constituent (fluiting body)
- Inorganic component (fluiting body)
- Dietary fiber (fluiting body)

Table 1 Medium blemding conditions

	Test group	Media composition (dry weight %) Base materials FB	BLTS	BSSL	Nutirition RB	Other SF	Packed weight (g)	Water content*1 (%)
1	FB+BSSL*2	85.0		10.0				64.2
2	FB+RB	75.0			20.0		800	64.2
3	BLTS+							
4	BSSL		85.0	10.0		5.0	1,300	63.5
5							800	
6	BLTS+RB		75.0		20.0		1,300	65.2

FB:Fermented Bagasse , BSSL:Brown Sugar Shochu Lees
RB:Rice Bran , BLTSD:Broad Leaf Tree Sawdust

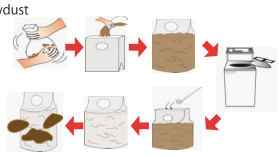

3.Results and Discussion

Yield results of mushroom culture tests

	Test group	Yield (raw) (mean±standard deviation) (g/bag)	The yield per 10g medum (g)
1	FB+BSSL	444.1±18.2	5.6
2	FB+RB	389.6±28.5	4.9
3	BLTS+BSSL	343.9±21.5	4.3
4		400.1±25.0	3.1
5	BLTS+RB	364.7±20.4	4.6
6		545.4±29.8	4.2

FB : Fermented Bagasse, BSSL : Brown Sugar Shochu Lees, RB : Rice Bran, BLTS : Broad Leaved Tree Sawdust

・The highest yields were observed in test group 1.

・Test group 3 and 5, showed similar yields with one another.

・Comparing the yields from 10g of each medium, group 1showed the highest: 5.6 g, followed by groups 2 and 5 in order.

・Fermented bagasse is not very absorbent, which increases its volume in packed media when combined with brown sugar shochu lees. Therefore, their combined usage decreases their packed weight by 40% when compared with media containing broad-leaved tree sawdust.

The main nutritional components

	Test group	protein	lipid	carbonhydrate	ash	dietary fiber
		(g/100g dry weight)				
1	FB+BSSL	9.3	0.3	87.3	3.1	82.8
2	FB+RB	11.6	0.4	84.7	3.3	79.9
6	BLTS+RB	14.2	0.4	81.8	3.6	78.5

FB : Fermented Bagasse, BSSL : Brown Sugar Shochu Lees, RB : Rice Bran, BLTS : Broad Leaved Tree Sawdust

・The mushrooms grown in the media with the fermented bagasse and brown sugar shochu lees tended to contain less protein, more carbohydrates, and slightly less ash when compared with the samples from group 6, which were grown in broad-leaved tree sawdust and rice bran. Cloud ear mushrooms contain high levels of dietary fiber; they suppress cholesterol absorption from the intestinal tract and prevent arteriosclerosis4). The mushrooms grown in the media containing fermented bagasse and brown sugar shochu lees contained more dietary fiber than the samples grown in broad-leaved tree sawdust and rice bran.

The β-glucan contents of the fruit bodies

	Test group	β-glucan (g/100g dry weight)
1	FB+BSSL	41.8
2	FB+RB	37.3
6	BLTS+RB	31.6

FB : Fermented Bagasse, BSSL : Brown Sugar Shochu Lees, RB : Rice Bran, BLTS : Broad Leaved Tree Sawdust

・The amount of β-glucan increased with the use of fermented bagasse; furthermore, it increased with brown sugar shochu lees as the nutrient supplement, resulting in 30% higher levels than those in group 6.

The mineral components

	Test group	Na	P	K	Ca	Mg
		(mg/100g dry weight)				
1	FB+BSSL	25	202	1,180	34	113
2	FB+RB	20	308	1,289	35	122
6	BLTS+RB	29	367	1,290	43	161

FB : Fermented Bagasse, BSSL : Brown Sugar Shochu Lees, RB : Rice Bran, BLTS : Broad Leaved Tree Sawdust

In particular the K, being one third of the ash, is resolved more efficiently than the other mineral components. Test group 1 contained K levels of 1,800 mg/100 g dry weight. The fruit bodies assimilated 530 mg per bed; that is, 30% of the K was assimilated by the cloud ear mushrooms. This suggests that cloud ear mushroom cultivation on fermented bagasse and brown sugar shochu lees could be an alternative practice that would prevent the high K accumulation in soil resulting from lees dumping.

4. Conclusions

1) Bagasse and brown sugar shochu lees can be used as the base material and nutrient supplement for jew's ear mushroom production. In particular, we have shown that brown sugar shochu lees can increase yields when compared with rice bran as the nutrient supplement.
2) The fiber contents in mushrooms grown in media containing fermented bagasse and brown sugar shochu lees are greater than those of mushrooms grown in other media. Additionally, the β-glucan contents of these mushrooms are higher. Our result suggest that mushrooms grown in such media could serve as a high value-added local product in the Amami Islands.
3) The cloud ear mushrooms resolved the K levels by 30% in the media containing fermented bagasse and brown sugar shochu lees. This is a potential solution to the high K problem caused by sprinkling the lees on local soils.

Characteristic Measurement of Gait with Plural Sensor

National Institute of Technology, Kagoshima College, AEI1
TOYOHIRA Lab
Konosuke Isomichi, Takayuki Toyohira

Background

Acceleration / angular acceleration sensor
TSND121

- hard to synchronize
- expensive (¥70,000)

Can not get a lot of data

Develop efficiency analysis system

System

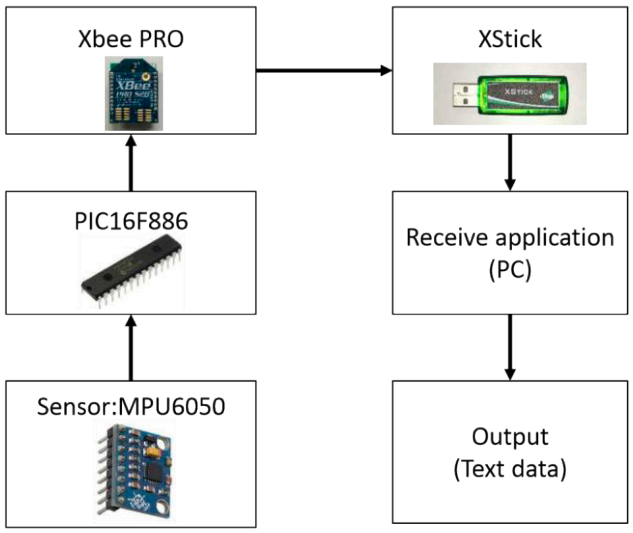

Development Process

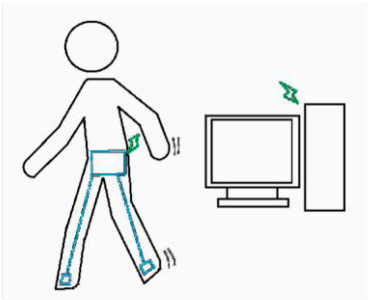

System image

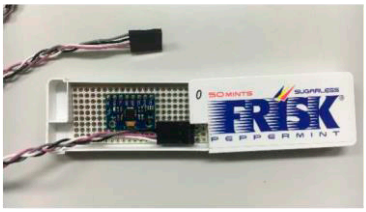

Measuring components with MPU6050

SG8002
(External oscillator to increase speed
In data communication)

Result

Measurement test

To Improve Performance

to make gait phase analysis

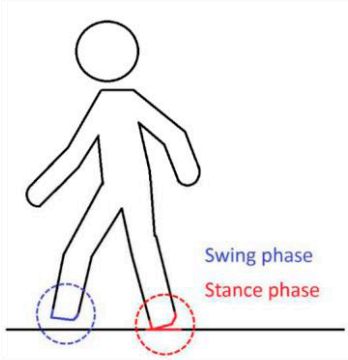

Pressure Sensor
FSR-400

Study on the Flight Acceleration Measurement for Flyer Acceleration Using the Intense-pulsed Electron Beam

Takuma ITO / Kenji KASHINE (National Institute of Technology, Kagoshima College)

Introduction

High-density ablation plasma is produced when we irradiate the Intense-pulsed Electron Beam to a solid target. A solid target is accelerated as a flyer by the reaction pressure which produced ablation plasma. The purpose of our study is evaluate the reaction pressure using this flyer acceleration. We designed the flyer velocity measuring device using the laser fence method. We tried to measure the flight acceleration of a sheet metal in small vacuum chamber.

Method of Flyer Acceleration

When irradiate the charged particle like the intense-pulsed ion beam or electron beam to a solid target, high temperature and high-density ablation plasma is produced and expands. Using this expands reaction pressure of the ablation plasma, we can accelerate a target with high-speed.

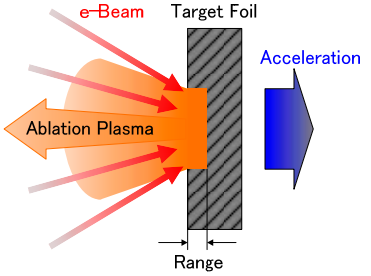

Fig.1 Schematic of producing the ablation plasma and the flyer acceleration

Method of Flyer Velocity Measurement

The laser fence method was carried out to measure the flyer velocity. For flyer position sensing, a narrow laser light and a detecting photodiode were used. We can evaluate the flyer velocity and it's flight acceleration by the time lag of each photodiode signal that flyer cuts a laser light.

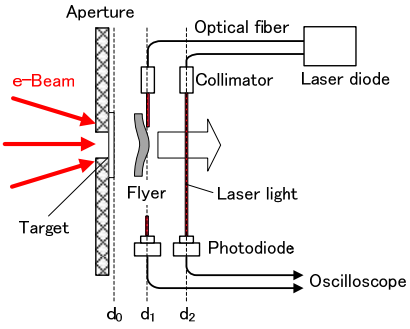

Flyer : aluminum (10 mm × 10 mm × t0.1 mm)

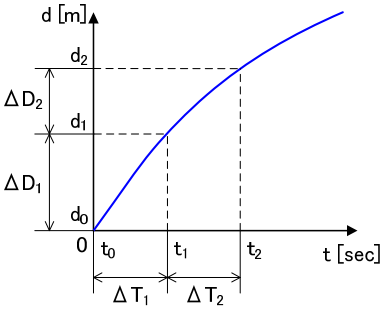

Fig.2 Outline of the velocity measurement method

Design of the Detector using Optical fiber

For evades a large electromagnetic noise produced by the ablation plasma, we use the optical fiber and fiber collimators. The fiber collimator can be a light filter which only path through the laser light.

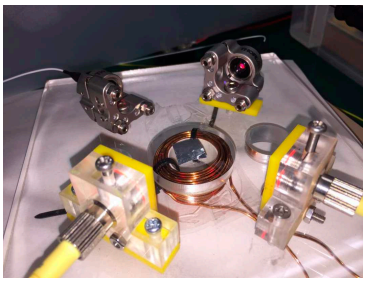

Fig.3 Photograph of the detector used in our study

Evaluation of the Velocity Measurement System

For evaluate check the performance of our measurement system, the trial experiment was carried out. In this trial experiment, a sheet metal flyer was accelerated by the electromagnetic force. We can evaluate the flyer velocity and it's flight acceleration by the time lag of each photodiode signal that flyer cuts a laser light.

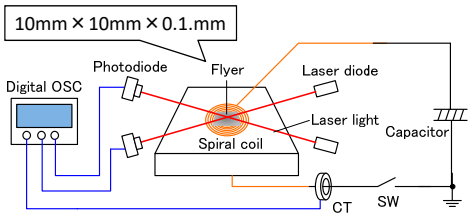

Fig.4 Outline of a flyer acceleration by the electro-magnetic force

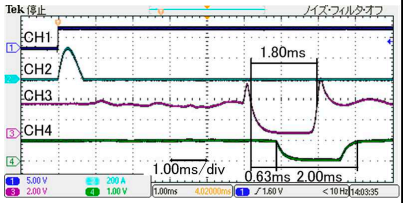

CH1:Arduino trigger voltage	5.00V/div
CH2:Pulse current	200A/div
CH3:1st photocoupler voltage	2.00V/div
CH4:2nd photocoupler voltage	1.00V/div

Fig.5 Waveforms of detectors (in air)

Conclusion

We designed a velocity measurement system for using our study.
We tried to measure the sheet-film flyer velocity using the simulated accelerator.

Future Plan

- We'll measure the flyer velocity which has more higher velocity. Also, we'll find the problems of our measurement system and estimate the flight acceleration of the flyer.
- We'll use our velocity measurement system in the Pulsed Power Generator "ETIGO-II" which can generate the pulsed electron beam. (Nagaoka University of Technology)

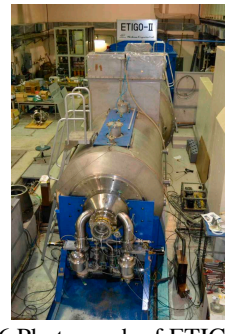

Fig.6 Photograph of ETIGO-II

Research on Discrimination Threshold of Motor Imagery Using Simple EEG Headset

National Institute of Technology, Kagoshima College
Advanced Electrical and Information Systems Engineering
Daiki Kashiwada, Yozo Tamari

1. Introduction

- Using many electrodes are necessary to obtain high accuracy by single measurement

Multiple Electrodes

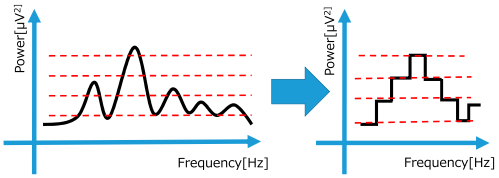

Fig.1 Using many electrodes

- Previous study was reported possible to detect 1 bit information from 1 channel EEG signal as a Fig.2 [1]

Single Electrode

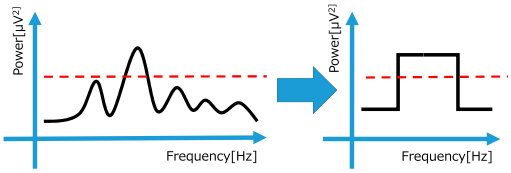

Fig.2 Using single electrode

Purpose:
Discrimination Threshold of Motor Imagery using Simple EEG Headset

2. Environment

Fig.3 EEG Headset

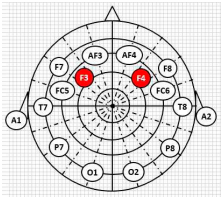

Fig.4 Headset's Electrode

- EEG Headset(Emotiv EPOC) made by Emotiv company
- EEG Headset specification
  Sampling rate:128Hz
  Dynamic range:8400μV(peak to peak)

3. Measurement method

- Measurement time is 15 seconds.
- This study measures EEG during right-hand movement imagery and relax.

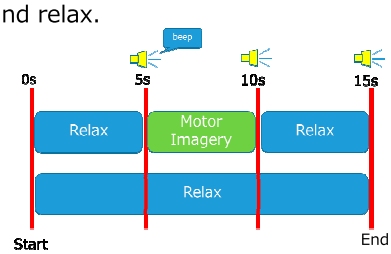

Fig.5 Flow of the experiment

4. Analysis method

- This analysis uses EEG data on F3 and F4 electrodes.
- These results are obtained by converting the section of 3~4 seconds, 8~9 seconds, and 13~14 seconds in EEG data by use of Fast Fourier Transform(FFT).

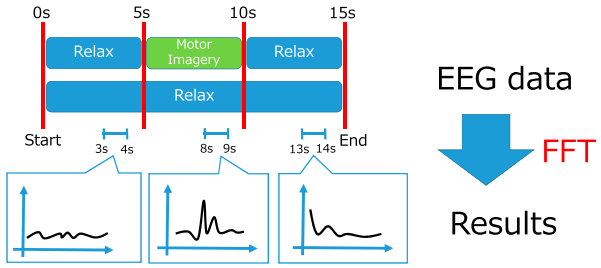

Fig.6 Image of the analysis

5. Results

Fig.7~9 show Fast Fourier Transform results of Relax and Motor Imagery. These data are taken the average of ten measurements.
In the following graphs' frequency range show between 8Hz and 30Hz because we focus on alpha and beta waves.

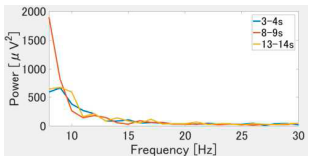

Fig.7 FFT result of Motor Imagery on F3

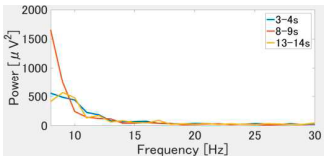

Fig.8 FFT result of Motor Imagery on F4

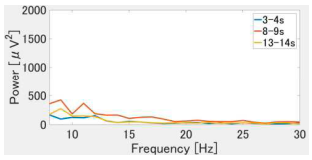

Fig.9 FFT result of Relax on F3

Frequency component of 8Hz during Motor Imagery is larger than that of Relax.

6. Conclusion

Frequency component of 8Hz during Motor Imagery is larger than that of Relax.

7. Future tasks

- Investigating effect of other Motor Imagery tasks
- Testing for personal difference of EEG

8. Reference

[1] S.Kanoh, R.Scherer, T.Yoshinobu, N.Hoshimiya, G.Pfurscheller, "A Basic Study on Brain-Computer Interface to Detect Foot Movement Imagery from EEG", IEICE, Technical Report MBE, 370, pp.9-12(2006).

Blood cells separation by using frequency dependence of dielectrophoretic force

Yasuhiro Kamimura, Takao Suda
Department of Advanced Electrical and Information Systems Engineering, Natl. Inst. Tech. Kagoshima College

1. Introduction

・Blood test is important for Clinical examination.
・Usually, Flow Cytometry method is used for a blood test
・Flow Cytometry Analyzer with sorting function is large and expensive.

Our purpose : the development of a small and inexpensive blood-cell-sorter using dielectrophoretic force

Our previous work

Erythrocytes and Leucocytes were separated by "negative" dielectrophoretic force in micro flow channel(fig 1.1).

Problem :
The throughput is low.

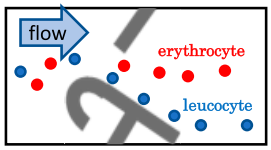

Fig 1.1 The example of blood cells separation by using difference of perpendicular direction dielectrophoretic force

In this research

We try to improve the throughput by another method using the difference of dielectrophoretic force between Erythrocytes and Leucocytes by the frequency of applied electric field(fig 1.2).
We observed frequency dependence of the dielectric force acting on red blood cells and white blood cells in low electric conductivity solution.

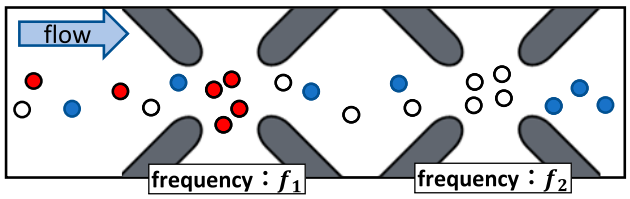

Fig 1.2 Schematic views of blood cells separation by using frequency dependence of dielectrophoretic force

2. Theory

・Dielectrophoretic force (DEP)
DEP is a phenomenon in which a force is exerted on a dielectric particle when it is subjected to a non-uniform electric field.

The direction of DEP dependent on the permittivity of a particle and a space around particle.

Positive-DEP : $\varepsilon_p > \varepsilon_s$

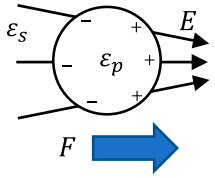

$$F = 4\pi\alpha^3\varepsilon_s Re\left[\frac{\varepsilon_p^* - \varepsilon_s^*}{\varepsilon_p^* + 2\varepsilon_s^*}\right] E \cdot \nabla E$$

$$\varepsilon_s^* = \varepsilon_s - j\frac{\sigma_s}{\omega}$$
$$\varepsilon_p^* = \varepsilon_p - j\frac{\sigma_p}{\omega}$$

Negative-DEP : $\varepsilon_p < \varepsilon_s$

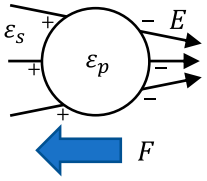

α : The radius of the particle
ε_p : The permittivity of the particle
ε_s : The permittivity of the suspending medium
σ_p : The conductivity of the particle
σ_s : The conductivity of the suspending medium
ω : The radian frequency of the electric field
E : The electric field

$$R_e\left[\frac{\varepsilon_p^* - \varepsilon_s^*}{\varepsilon_p^* + 2\varepsilon_s^*}\right] = R_e[\mathrm{k}(f)].$$

When $R_e[\mathrm{k}(f)]$ is zero, the frequency is called crossover frequency.

The crossover frequency depends on complex permittivity of particle and suspending medium.

If the conductivity of the suspending medium increase , the crossover frequency also increase (fig 3.1).

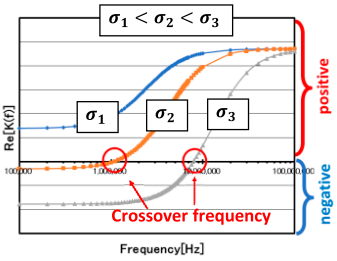

Fig 3.1 the example of frequency characteristics when changing in conductivity

3.Experimental method

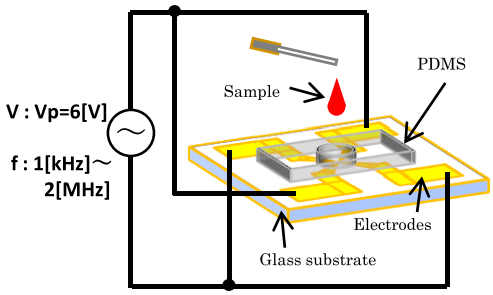

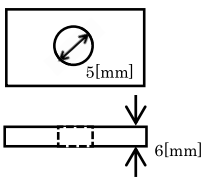

PDMS shape

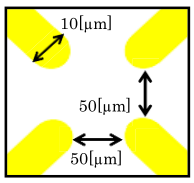

Shape of electrode tip

Fig 3.1 experimental device

Sample :
Small amount of blood is collected by self blood collector. And that is gravity settled in a Hematocrit tube. Buffy court (about 2[μl]) is picked out and mixed in low conductivity solution (about 2[ml]).

Low conductivity solution :
①**PBS** :
KCl:5[mM] , NaCl:90[mM], $NaH_2PO_4 2H_2O$:40[mM], $Na_2HPO_4 12H_2O$:9.5[mM]
②**Glucose solution** :
D-Glucose 300[mM]

① : ② = 1 : 99
conductivity : 0.02[S/m]

4.conclusion

erythrocyte

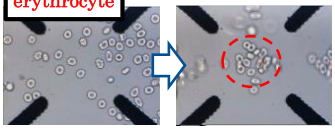

Fig 4.1 Vpp=12[V] , 50[kHz]

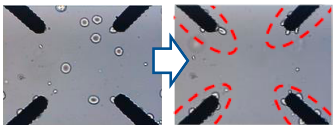

Fig 4.2 Vpp=12[V] , 150[kHz]

leucocyte

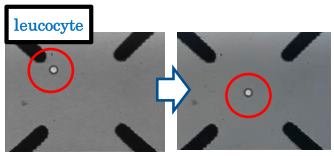

Fig 4.3 Vpp=12[V] , 1[kHz]

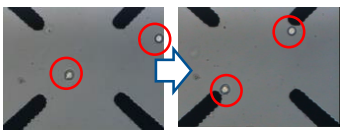

Fig 4.4 Vpp=12[V] , 80[kHz]

Result

・When conductivity is about 0.02 [S/m] , crossover frequency are as follows.
Erythrocyte : **90[kHz] or more**
Leucocyte (Neutrophil) : **80[kHz] or more**
・At around 90[kHz] , erythrocyte near the electrode receive positive DEP. After contacting electrode , that receive negative DEP and move toward the electrode center.

Future task

・Search of the crossover frequency other than Neutrophil.
・Examination of the blood cell separation in micro flow channel.
・Search of the conductivity suitable for separation.

A study on improving performance of P300speller for the input in Japanese

National Institute of Technology, Kagoshima college Advanced Electrical and Information Systems Engineering, Chosei Sha, Yozo Tamari

1. Back ground

- P300speller is input characters system with P300[1].
- The interface is characters matrix.
- The user has to find each letter from all the characters while row and column are flushing.
- Issue
  - ➢ Input speed is slow
  - ➢ Input Japanese is not easy[2]

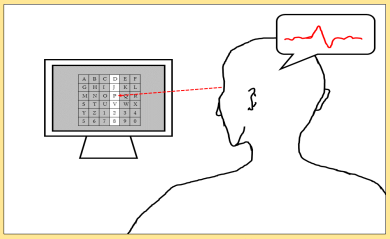

Fig.1. P300speller

2. Purpose

We propose a new interface of P300 speller, therefore we aim to be easy and to be quick for input Japanese.

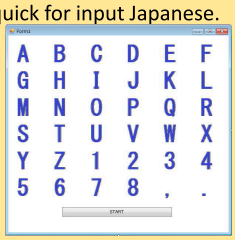

(a) Ordinary Interface

(b)Novel Interface

Fig.2 P300speller interface

3. Analysis

Comparison all combination of each row and column EEG data.

$column6 \times row6 = 36combination$

A	B	C	D	E	F
G	H	I	J	K	L
M	N	O	P	Q	R
S	T	U	V	W	X
Y	Z	1	2	3	4
5	6	7	8	,	.

(a) Ordinary Interface

$column4 \times row3 = 12combination$

あ	か	さ
た	な	は
ま	や	ら
	わ	

(b)Novel Interface

Fig.3 Number of combination at these interface

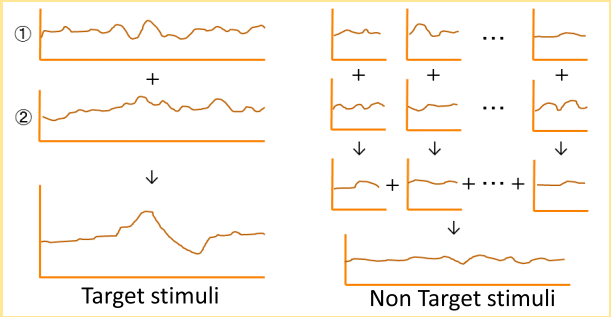

Fig.4 Analysis method

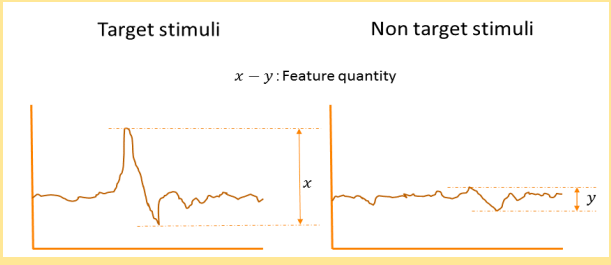

Fig.5 Comparison method

If the target stimuli is input character, it is able to estimate that feature quantity will be maximum.

4. Experimentation

Setting input characters : Ordinary interface is “O” and novel interface is “な”.

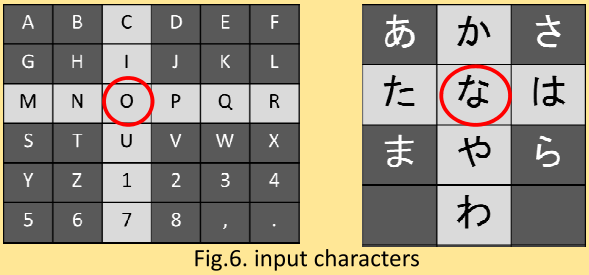

Fig.6. input characters

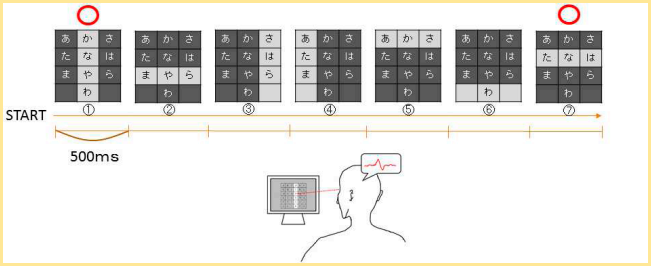

Fig.7. The flow of experimentation

Each stimuli are flush during 500ms and recorded 1 sequence EEG data.

6. Results

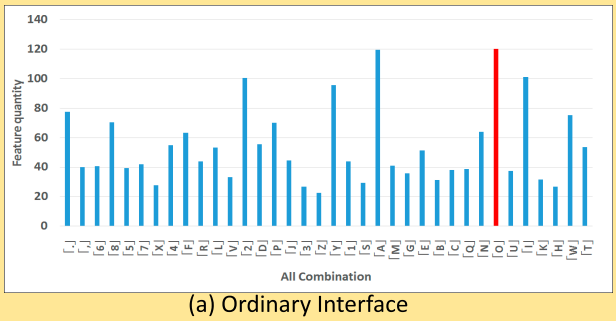

(a) Ordinary Interface

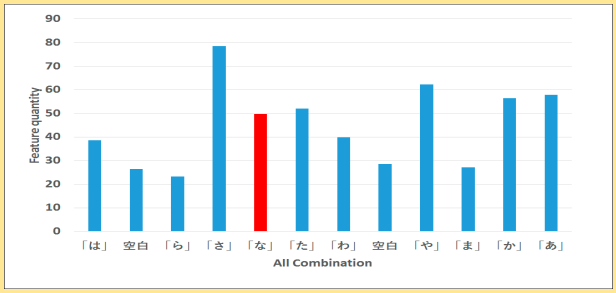

(b)Novel Interface

Fig.8. The result of experimentation

Ordinary interface can distinguished input character, however novel interface was cannot. Number of data in novel interface is fewer than that in ordinary interface, therefore input speed was improved.

7. Conclusion

7.1. Discussion

Input speed with novel interface system is faster than that with ordinary interface system, however the novel system is difficult to distinguish input characters in this present specification.

7.2. Future tasks

- Improving the novel interface
- proposing any new algolithm to distinguish characters

8. References

[1] L. Farwell and E. Donchin: “Talking off the top of your head: toward a mental prosthesis utilizing eventrelated brain potentials”, Electroencephalography and clinical Neurophysiology, 70, 6, pp. 510-523 (1988).

[2] Yoshikawa,Yamamoto,Kawai,Furuhashi：”Evaluation of practical usage with P300 speller”, Fuzzy System Symposium 30 pp.274-277(2014).

Cutting force and surface profile in end milling of CFRP

National Institute of Technology, Kagoshima College
Takahiro Inatomi, Kenji Shimana

1. Introduction

●CFRP is watched as a structure materials for a car and an airplane. “CFRP” is the abbreviated name for “Carbon fiber Reinforced plastics”. It’s excellence corrosion resistance and specific strength. The mileage can be reduced by applied the body of a car and aircraft.

●But, the CFRP is too hard material. Because the tool for processing tends to worn away. So, the surface roughness will be increase. Currently, CFRP is used in various fields. Therefore, improvement in machining accuracy is required.

●In this research, CFRP was side cut with 27 cutting conditions. So, I measured cutting force and surface profile in each cutting conditions. From the measurement results, I investigated the suitable cutting speed and feed rate for CFRP processing.

2. Method of cutting

Fig.1 Machining center

Table.1 Cutting conditions

Tool	Square end mill
Teeth number	8
Tool diameter [mm]	6
Spindle speed [min-1]	4000, 6000, 8000
Feed rate [mm/min]	400, 500, 600
Cutting depth [mm]	0.2, 0.6, 1.0

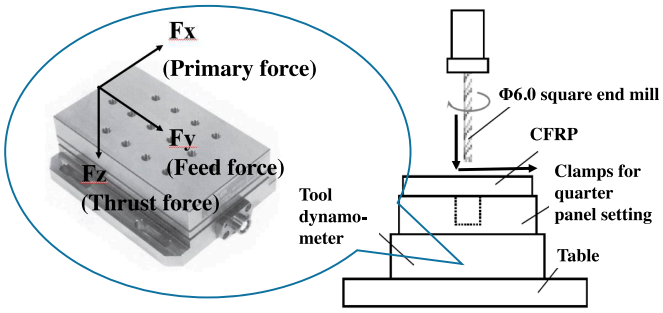

Fig.2 Method of cutting

3. Measuring instrument

(a) Non-contact type

(b) Contact type

Fig.3 Measuring instrument

4. Experimental results

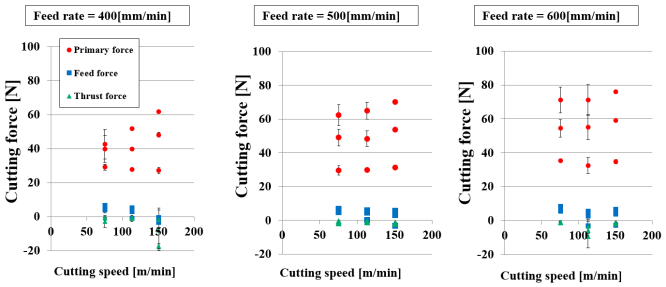

Fig.4 Relation between cutting speed and cutting force

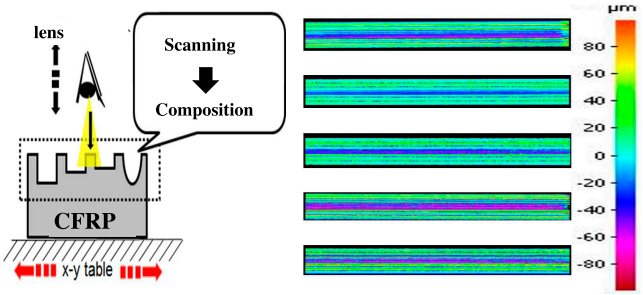

Fig.5 Surface profile

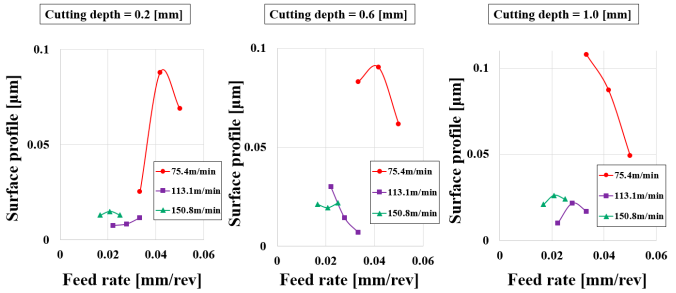

Fig.6 Relation between feed rate and surface profile

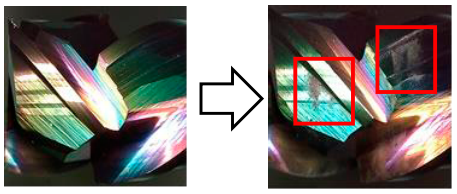

(a) Before press (b) After press

Fig.7 State of square end mill

5. Conclusions

(1)When the cutting speed is low, the cutting force is low. However, the surface roughness is large, and machining accuracy is bad.

(2)When the cutting speed is low, that is, when the spindle speed is low, the machining accuracy deteriorates. This was presumed that the cutting powder of CFRP was clogged in the grooves of the worn cutter, and the machining accuracy was deteriorated.

In the future, I need to investigate further.

Control for the inverted two-wheeled vehicle using the SIRMs fuzzy model constructed by learning algorithm

National Institute of Technology, Kagoshima College
Masashi Kawazoe , Kazuya Kishida

1. Introduction

Most of self-tuning fuzzy systems, which are automatically constructed from learning data, are based on the steeped descent method. However, this approach often requires a large convergence time and gets stuck into shallow local minimum. One of it's solutions is to use fuzzy rule modules with a small number of inputs such as SIRMs and DIRMs. In this study, in order to show the effectiveness of a SIRMs fuzzy model constructed by learning algorithm, control experiment for the inverted two-wheeled vehicle is performed.

2. SIRMs fuzzy model constructed by learning algorithm

SIRMs fuzzy model

SIRMs (Single Input Rule Modules) fuzzy model proposed by Yubazaki et al is constructed modules which has only a single input variable in the antecedent part. The summation of the products of the importance degree and the fuzzy inference result of each module is then taken as the output of model. Therefore, we can reduce the number of rules compared to conventional model. Fig.1 shows conventional model and SIRMs model, which x_i is input variable, h_i is each importance degree, and y_0 is output of model. SIRMs model show good performance in linear problem but doesn't always in nonlinear problem.

Learning algorithm

SIRMs fuzzy model constructed by learning algorithm is based on steepest descent method. And, the membership function is a function differentiated sigmoid function. A membership value of the antecedent part μ_{ij} for input x_j is expressed as:

$$\mu_{ij} = M_{ij}(x_j) \tag{1}$$

$$M_{ij}(x_j) = e^{-\frac{1}{2}\left(\frac{x_j - c_{ij}}{b_{ij}}\right)^2} \tag{2}$$

Where j is a rule number, M_{ij} is a membership function, and w_j is the weight. Let c_{ij} and b_{ij} denote the center and width values of M_{ij} respectively. Then the inference result of each rule group is expressed as:

$$y_j^0 = \frac{\sum_{i=1}^{n} \mu_{ij} w_{ij}}{\sum_{i=1}^{n} \mu_{ij}} \tag{3}$$

The inference output y* of fuzzy inference is calculated by:

$$y^* = \sum_{j=1}^{m} h_j y_j^0 \tag{4}$$

Where h_j is importance degree.

The inference error $E(t)$ is calculated by:

$$E(t) = \frac{1}{2}(y^* - y^r)^2 \tag{5}$$

Where y^r is a desirable output. Then c_{ij}, b_{ij}, w_j and h_j are updated by:

$$\beta(t+1) = \beta(t) - K_\beta \frac{\partial E}{\partial \beta} \tag{6}$$

$$\beta \in \{c_{ij}, b_{ij}, w_{ij}, h_j\} \tag{7}$$

Where K is a learning coefficient.

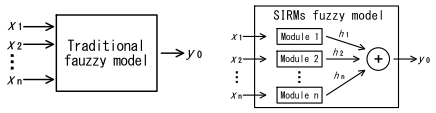

(a) Traditional fuzzy model (b) SIRMs fuzzy model

Fig. 1 Fuzzy models

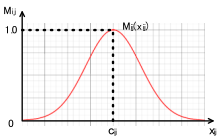

Fig. 2 Membership function

3. Control experiment for the inverted two-wheeled vehicle

Controlling method for the inverted two-wheeled vehicle

Fig.3 shows the schematic diagram of the controlling method for the inverted two-wheeled vehicle. In this study, we considered the angle, angular velocity and moving speed of the vehicle body are input data and the number of pulse to the motors is output data. Further, the experiment was performed in a level place.

Constructed SIRMs fuzzy model

Fig.4 shows the constructed SIRMs fuzzy model. We set nine membership functions for each of the angle, angular velocity and moving speed of the vehicle body, which is an input variable, and inferred every input. After that, we calculated the total sum of inference results of each rule group with importance degrees set to about 1, and determined the output value. This time, each inference rule was created by trial and error based on the knowledge of the researcher, and the SIRMs fuzzy model constructed by learning algorithm based on these inference rules.

Control experiment for the inverted two-wheeled vehicle

As a result of the experiment, the two-wheeled vehicle maintained stable inverted state. Also, it was confirmed that even if disturbance is given, the balance is maintained and the inverted continues while the two-wheeled vehicle was in the inverted state.

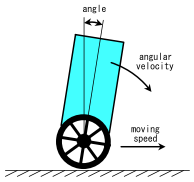

Fig. 3 Schematic diagram of the controlling method for the vehicle with two wheels.

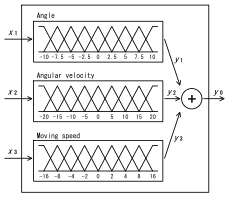

Fig. 4 Constructed SIRMs fuzzy model

4. Conclusion

In this study, in order to show the effectiveness of a SIRMs model, control experiment for the inverted two-wheeled vehicle is performed. As a result of the experiment, the two-wheeled vehicle applied the SIRMs fuzzy model maintained stable inverted state. In the future work, we would like to compare the SIMRs fuzzy model constructed by learning algorithm and by trial and error.

Compositional dependence of microstructure and martensitic transformation of CuZr shape memory alloys

Department of mechanical engineering of National Institute of Technology Kagoshima College : Takuya Kunishi, Hitoo Tokunaga

Introduction

[Results of previous research and expected application Areas]

- Cu-Zr binary alloys (alloys composed of two elements, Cu and Zr) are shape memory alloys(SMA).The shape memory effect of Cu-Zr alloy is caused by martensitic transformation .Cu-Zr alloy has attracted attention as a new functional material. Application range of practical SMA is limited to a temperature range of 100 degrees or less.
- Cu-Zr SMA is expected for application of temperature sensors and actuators in operation at exceeding 100 ℃.It can be expected to reduce the size and weight of the device, save energy, improve safety.

[objective] Control of the shape recovery temperature of Cu - Zr alloy. Effect of alloy composition (Cu/Zr ratio, third element) on crystal structure and shape recovery temperature

Experimental procedure

[Materials]

Cu - Zr alloy is fabricated using an arc melting furnace.

- Conditions

Degree of vacuum: R.pump 12[Pa] , D.pump7.2[Pa]
Number of melting: 3 times
Melting time: 60[s]

Table.1 The composition (nominal) and mass of elements

At(%)	Zr(g)	Cu(g)	Total(g)
$Zr-50Cu$	7.012	4.868	11.880
$Zr-45Cu$	7.849	4.453	11.302
$Zr-55Cu$	6.643	5.655	12.298

[Sample and Specimen]

- Cut out 2 sheets of 1-3 [mm] thick from the button type ingot by a precision shearing machine. Then apply emery polishing.(Fig1(A)→Fig1(B))→for XRD, SEM
- Cut out a disk (d=5[mm],m=0.1-0.3[g]) from one cut out plate by a wire electric discharge machine. Then polished with sandpaper.(Fig1(B)→Fig1(C)) →for DSC

[Analysis method]

- XRD(θ-2θ X-ray Diffraction analysis, Rigaku X-RAY DIFFRACTOMETER)

→Analysis of crystal structure
[Conditions] X-ray : Cu-Kα 40[kV]/20[mA]
Analysis angle(2θ) : 20-60[°], step : 0.02[°]

- DSC(Differential scanning calorimetry, Shimadzu DSC-60)

→Measurement of thermal characteristics
[Conditions]
Analysis temperature : 50-350[℃], Sampling time : 0.2[s],
Acceleration speed : 10[℃/min], Atmosphere : Air

- SEM(Scanning electron microscopy, JSM-6010LA)

→Distribution observation of material composition
(Observation of part A and B)
[Condition]
Acceleration voltage : 10.0[kV], Working distance : 10[mm]

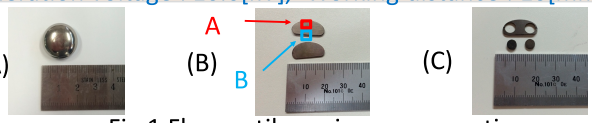

Fig.1 Flow until specimen preparation

Result and discussion

[XRD results]

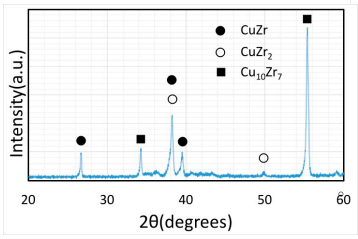

(a) Zr-45Cu

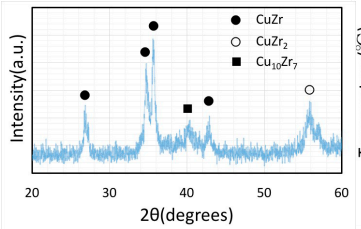

(b) Zr-50Cu

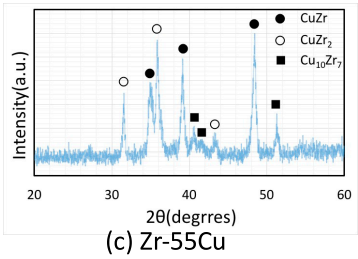

(c) Zr-55Cu

Fig.2 XRD results

[DSC results]

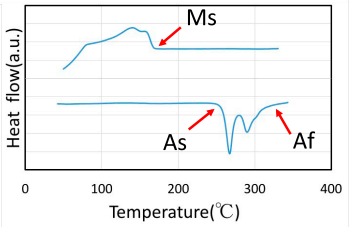

Fig.3 DSC results of Zr-50Cu

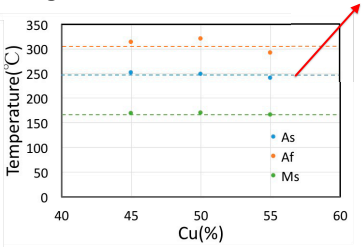

Fig.4 Thermal characteristics

[SEM results]

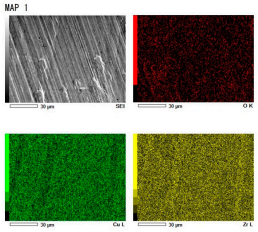

Fig.5DSC results of Zr-55Cu

[Results and discussion]

- XRD

It was confirmed that CuZr was formed, but since other compounds coexisted, heat treatment is necessary.
$CuZr_2$ increased in Zr rich and $Cu_{10}Zr_7$ increased in Cu rich, indicating that there is composition dependence.

- DSC

Endothermic and exothermic reactions due to martensitic transformation were observed.
The shape recovery temperature of CuZr alloy does not depend on composition.

- SEM

From the SEM test, it was found that there was no extreme distribution bias, but a finer composition distribution could not be observed. It is necessary to review the conditions and methods of observation.

[Summary]

・According to the results of XRD and DSC, changing the composition affects the kind of the intermetallic compound, and the amount of exothermic heat per unit weight in Zr - 50 Cu is the highest.
→With the composition of only Zr and Cu, shape recovery temperature can not be controlled.

[Plans]

Review the conditions and methods of SEM observation.
Add third element to Zr - Cu alloy and evaluation

References : C.A. Biffi,A.Figini,A.Tuissi : influence of compositional ratio on microstructure and martensitic transformation of CuZr shape memory alloys

9-11 May 2017　2nd ISEED2017 in RGB Kagoshima

Observation of Circular Cylinders Behavior on In-line Flow-induced Vibration

Department of Mechanical Engineering, National Institute of Technology Kagoshima College,
Shintaro SATO and Satoru ODAHARA

1. Purpose of Research

In-line Flow-induced Vibration is a resonance phenomenon in which the elastic column vibrates when natural frequency of the elastic column matches the frequency of the symmetrical vortex generated in the elastic column's wake, as shown Fig.1. This phenomenon occurred in the thermometer well of the secondary cooling system pipe of the fast breeder reactor "Monju" in 1995, and a sodium leakage accident was occurred, as shown in Fig.2. The purpose of this research is to experimentally reproduce the in-line flow-induced vibration and clarify the vibration characteristics.

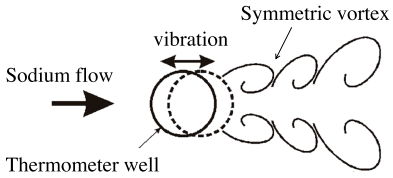

Fig. 1 Symmetric vortex.

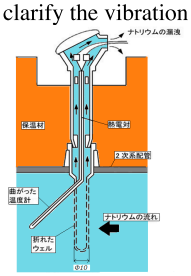

Fig. 2 Thermometer well of "Monju".

2. Experimental Equipment

In order to reproduce the In-line flow induced vibration, a self-made closed loop water experiment and a high speed camera was used to photograph and analyze the vibration of the cylinder, as shown in Fig.3 and Fig.4.

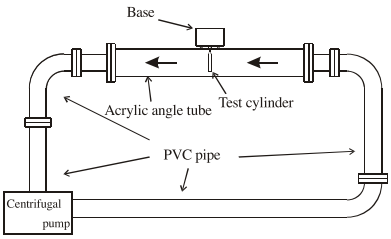

Fig. 3 Closed loop water flow equipment.

Fig. 4 High speed camera (KEYENCE VW-9000)

3. Experimental Method

According to Fig. 5, since the range of the dimension velocity at which In-line flow-induced vibration caused by a symmetric vortex occurred is V_r = 1.0 ~ 2.5, the flow velocity is set within that range. Using the closed loop water experiment of Fig. 3, water is caused to flow through a test cylinder of D = 13mm to generate In-line flow-induced vibration, as shown in Fig. 6. Tip of the vibrating cylinder was photographed with a high-speed camera and its moving image was analyzed to measure the amplitude of the vibration, as shown in Fig.7. Arrangement of cylinder is also shown in Fig.7. Fig.8 shows photographed test cylinders.

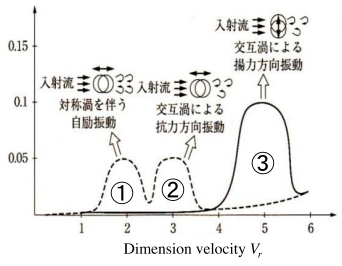

Fig. 5 Schematic of dimension velocity of flowing fluid and dimension amplitude.

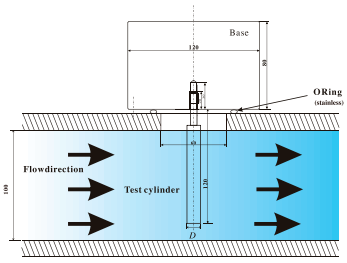

Fig. 6 Test section of closed loop water flow equipment.

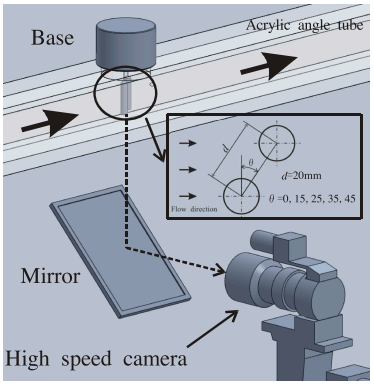

Fig. 7 Arrangement of test cylinder.

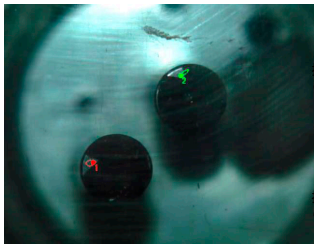

Fig. 8 Picture of vibrating cylinder.

4. Experimental Result and Consideration

Fig. 9 shows the relationship between the dimension amplitude δ/D and the dimension velocity V_r for each angle θ of the arrangement of cylinder. δ/D is a dimension amplitude obtained by dividing the vibration amplitude δ by the test cylinder diameter D. In the region of V_r = 1.0 ~ 2.5, δ/D tended to decrease as the θ increased. As the θ increases, the cylinder spacing seen from the projected surface in the flow direction decreases, so that the interference of symmetric vortices of each of the two cylinders becomes large and the emission of the symmetric vortex is hindered and the vibration amplitude is suppressed .

Table 1 shows the vibration phases of two cylinders for each V_r and θ. The phase between two cylinders became π as the angle θ of the cylinder arrangement increased.

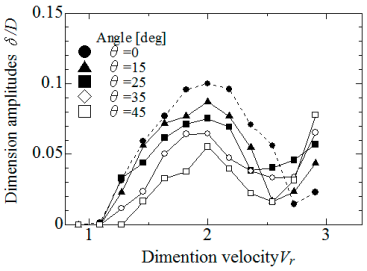

Fig. 9 Relationship between dimension amplitude and dimension velocity V_r.

Table 1 vibration phases of two cylinders for each V_r and θ.

V_r	θ = 0°	θ = 15°	θ = 25°	θ = 35°	θ = 45°
1.091137					
1.272993	0	0	0	π	
1.454849	0	0	0	π	π
1.636706	0	0	0	π	π
1.818562	0	0	π	π	π
2.000418	0	0	π	π	π
2.182274	0	0	π	π	π
2.36413	0	π	π	π	π
2.545987	0	π	π	π	π

5. Conclusions

(1) In-line flow-induced vibration occurred by setting the condition of the dimension flow velocity at V_r = 1.0 ~ 2.5.
(2) The vibration amplitude decreased as the angle θ of the arrangement of the cylinder increased at V_r = 1.0 ~ 2.5.
(3) The phase between two cylinders became π as the angle θ of the cylinder arrangement increased at V_r = 1.0 ~ 2.5.

Reference : Satoru ODAHARA and etc.; Fatigue Failure by In-line Flow-induced Vibration and Fatigue Life Evaluation, Transactions of the Japan Society of Mechanical Engineers Ser. A, Vol.70, No.690, 2004-2.

In-process Measurement of Tool Temperature in Machining

○ Keisuke Sawada, Shinichi Yoshimitsu
National Institute of Technology, Kagoshima College

1. Introduction

In-process monitoring and measuring of spindle power, cutting force, cutting and vibration have been proposed to monitor the cutting state. The temperature of the tool during cutting is very high and constantly changing. We examined the usefulness of the tool temperature changes as a signal to monitor the cutting state. The monitoring of tool temperature will be used for detecting the tool wear and tool breakage. In this experiment, the tool temperature was measured in turning by using a thermocouple as a fundamental approach.

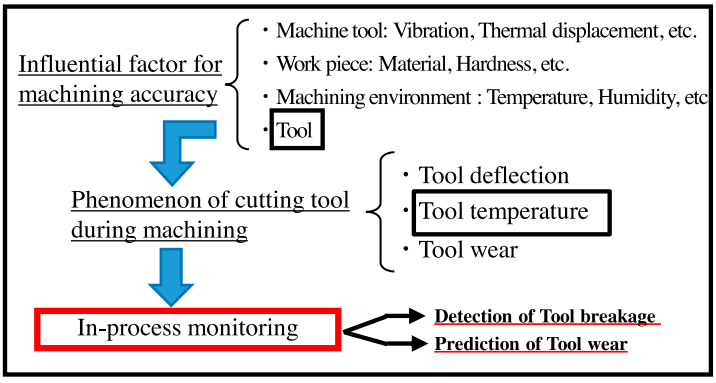

2. Experimental Method

Figure 1 shows the experimental setup. The electromotive force obtained from the thermocouple is converted to temperature by the data logger and the measurement data is sent to the PC. In order to investigate the relationship between cutting force and tool temperature, a dynamometer was installed. Insert tool was used for the experiment. Insert is a triangular chip of cermet (Fig.2). The thermocouple was installed by spot welding. Figure 3 shows the position of the thermocouple. Table 1 shows the cutting conditions. We applied them to the turning of the solid round bar in the experiment.

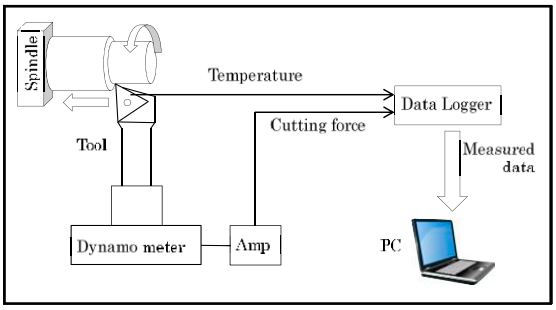

Fig.1 Experimental setup

Fig.2 Image of tool

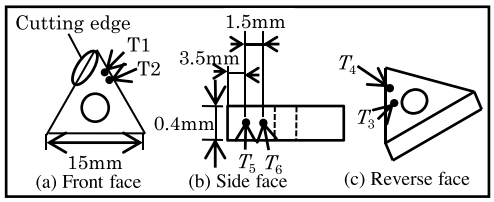

Fig.3 Measurement points of tool

Table 1 Cutting conditions

Tool	Cermet (TiCN) TNGG160408R-UM
Work	S25C
Cutting length L mm	200
Cutting speed V m/min	75, 100, 125
Feed rate f mm/rev	0.25, 0.35, 0.45
Cutting width t mm	0.5, 0.75, 1.5

3. Experimental Result

Figure 4 shows the temperature data of each measurement points obtained by the experiment. It is understood that the closer to the cutting edge the measurement point is, the higher the temperature is. It can be seen from Fig. 5 that the temperature increases as the feed rate increases. Figure 6 shows that the cutting speed is not significantly related to the temperature change within the range of the cutting condition of this time. Figure 7 shows the temperature change for each time when a cutting fluid is applied during lathe turning. The temperature of the tool is lowered by the effect of the cutting fluid in about 120 seconds from the start of cutting.

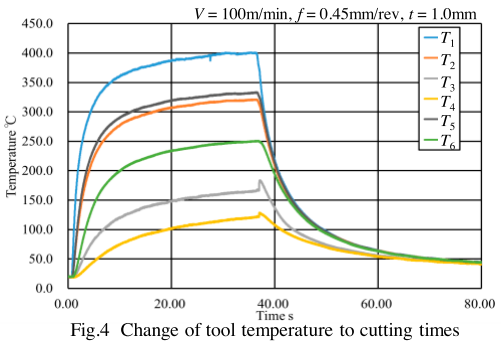

Fig.4 Change of tool temperature to cutting times

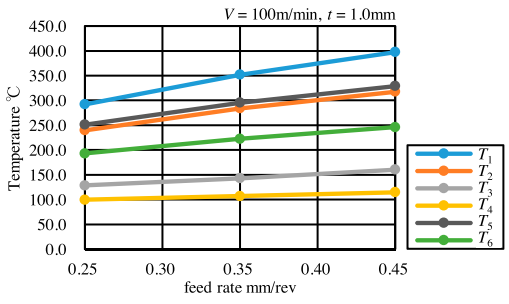

Fig.5 Relationship between feed rate and tool temperature

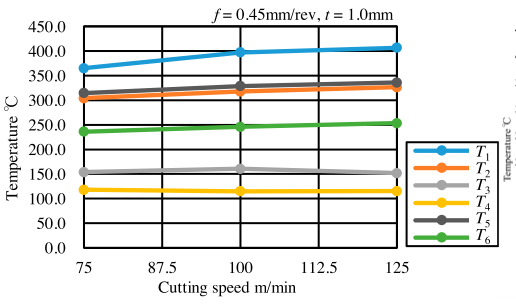

Fig.6 Relationship between cutting speed and tool temperature

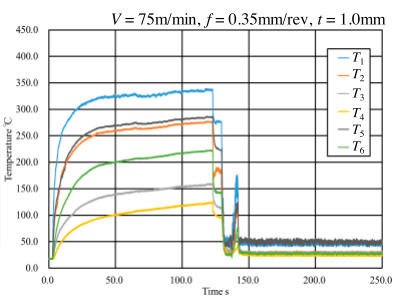

Fig.7 Change of tool temperature to cutting times

Study on control of the inverted pendulum

National Institute of Technology, Kagoshima College
Advanced Mechanical and Electronic Control Systems Engineering
Koki Shimono , Chikara Miyata

1. Background and objective

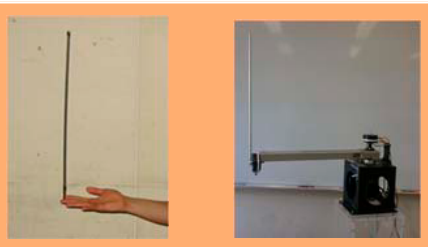

Fig.1 Control of an inverted pendulum

An inverted pendulum can be thought as a physical model for playing a stick on a hand, and it is often used as a model to learn control theory. In order to stand up and stabilization the pendulum, it is necessary to control two objects (arm position and pendulum angle) by one output. Therefore, classical control theory can not deal with, modern control theory or fuzzy control theory is used.

The aim of this study is to control the pendulum using fuzzy control theory.

2. Fuzzy inference

In fuzzy inference, fuzzy rule is made from the expression "if A then B", we call A an antecedent part, B a consequent part. A fuzzy set is a set which represent degrees belonging to a certain range.

By handling ambiguous information and empirical rules, we can control close to the human's sense and it does not require a strict mathematical model. In this study, the linear fuzzy inference method is used.

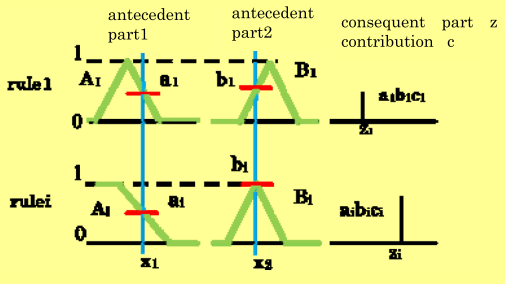

$$z_0 = \sum_{i=1}^{n} (a_i \cdot b_i \cdot c_i \cdot z_i) \Big/ \sum_{i=1}^{n} (a_i \cdot b_i \cdot c_i)$$

Fig.2 Linear fuzzy inference method

3. Creating of fuzzy rules

A part of the created fuzzy rules is shown in Table.1. Each rule is composed of four antecedent parts, one consequent part, and one contribution.

In the rule creating procedure, firstly, we created a rule to keep the pendulum upright. After that, we added the arm position correcting rules and swinging rules.

Table.1 Example of fuzzy rules

rule	arm position	pendulum angle	arm velocity	pendulum angular velocity	consequent part	contribution
0	5	1 ZR	5	1 ZR	0	3
1	5	4 NM NS	5	1 ZR	-70	1
2	5	4 PS PM	5	1 ZR	70	1
⋮	⋮	⋮	⋮	⋮	⋮	⋮

4. Experimental result

We conducted control experiments to stand up and stabilization the pendulum using the created fuzzy rules. As a result, 28 of 30 times succeeded. In addition, We verified whether stand up control is possible even when the pendulum is L-shaped and the center of gravity is shifted. As a result, we succeeded in control like the straight pendulum.

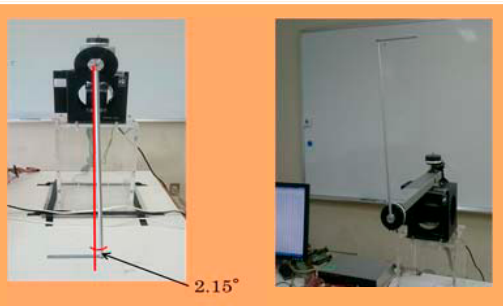

Fig.3 Experiment with L-form pendulum

5. The plan for study

We are planning to analyzed the movement of the pendulum using USB camera and to control the pendulum from these data.

Optimal Design of an Open-Type Magnetically Shielded Room for Magnetic Resonance Imaging Composed of Magnetic Material Plates

Satoru Temma, Koshi Goto, Yuya Tuboyama and Kiyotaka Kamata,
National Institute of Technology, Kagoshima College

1. Outline

Background of this study

Magnetic resonance imaging (MRI) generates a strong magnetic field during operation (Fig.1). In order to prevent malfunction of medical equipment in the hospital, need to reduce the leakage flux density to less than 0.5 mT outside the MRI room. Therefore, we are enclosing the entire MRI room with ferromagnetic walls.

However, the small space enclosed by the walls of the MSR may add to patients' stress and discomfort associated with the MRI diagnosis, which may lead to unstable or unreliable diagnostic results. In order to obtain stable diagnostic results, need to reduce such stress on the patient, an open type magnetically shield room would be most useful. In this study, the optimal design of an open-type magnetically shielded room for MRI composed of magnetic material plates was examined using 3-D linear magnetic-field analysis.

The principle of MRI

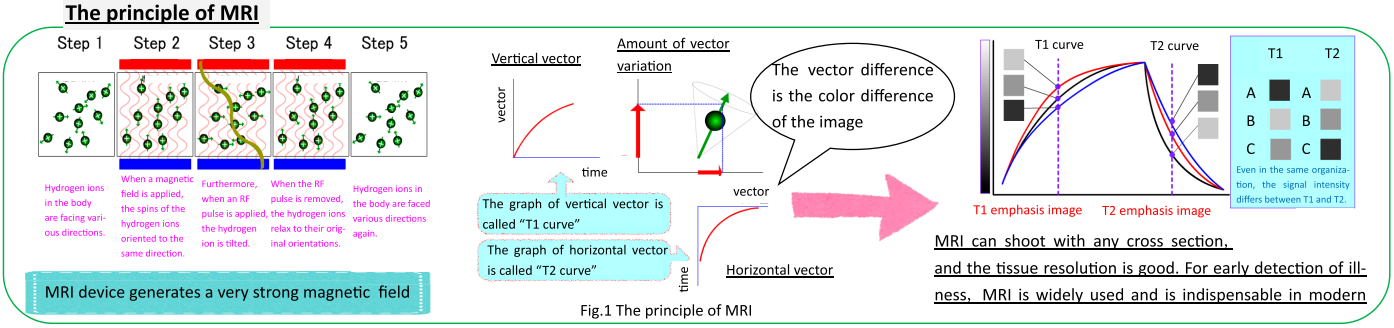

Fig.1 The principle of MRI

MRI can shoot with any cross section, and the tissue resolution is good. For early detection of illness, MRI is widely used and is indispensable in modern

2. Analysis method

Fig.2 shows the analysis model of a magnetically shielded room. Making use of symmetry, the analysis was performed using one quarter of the full room size.

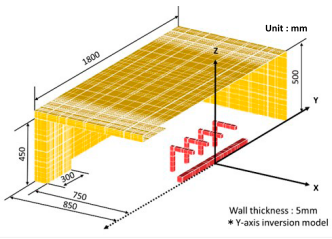

Fig.2 Analysis model

Analysis conditions

- Shield size : 750 ×300 ×450
- Wall thickness : 5 mm
- Permeability : μ = 3, 000
- Magnetic field : 1.5 T
- Analysis plain : Y = -1, 000 mm , Z = 75 mm

(1)Consideration of shield shape

Fig.3 shows analysis model of the magnetically shield.

Fig.3(C) shows the suggestion model examined in the present study.

we compare this model with the other shield model.

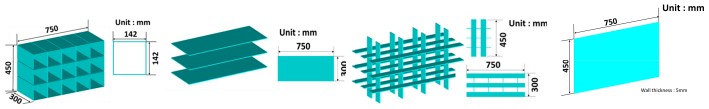

(A) Square Model (Model A) (B) Strip Model of (Model B) (C) Suggestion model (Model C) (D) Closed model (Model D) ＋(E) No shield model (Model E)

Fig.3 Magnetically shield model

(2)Influence of air gaps

In order to increase the shielding effect of our suggested model, air gaps were included in the analysis model in the Y axis direction (Fig.4), with the aim of further reducing the leakage magnetic field by passing it through air.

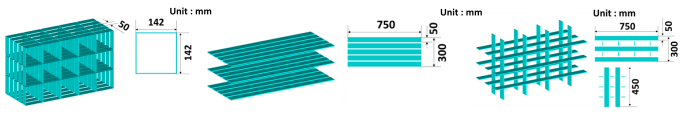

(A) Square Model (Model A) (B) Strip Model of (Model B) (C) Suggestion model (Model C)

Fig.4 Magnetically shield model (air gaps)

3. Analysis result

(1)Consideration of shield shape

The Fig.5 shows the fluctuation of the leakage magnetic field in the X axis direction at Y = -1,000 mm and Z = 75 mm. As shown in fig.5, our suggested model provided effective and stable shielding at all positions. To investigate the reason, we compiled a magnetic field vector distribution diagram, shown in Fig.6.

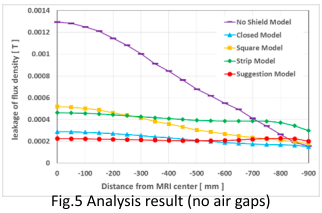

Fig.5 Analysis result (no air gaps)

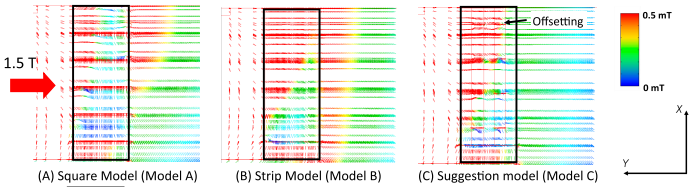

(A) Square Model (Model A) (B) Strip Model (Model B) (C) Suggestion model (Model C)

(D) Closed Model (Model D) (E) No shield model (Model E)

＊The inside of the black frame is magnetically shield.

We were able to clarify the high shielding effect of the suggestion model.

Fig.6 Vector distribution diagram (no air gaps)

(2)Influence of air gaps

Fig.7 shows the shielding effect due to air gaps in the magnetic shield. Moreover, Fig.8 shows vector distribution diagram of the suggestion model. From Fig.7 and Fig.8, it can be confirmed that by adding air gaps, the shielding effect has been improved for suggestion models.

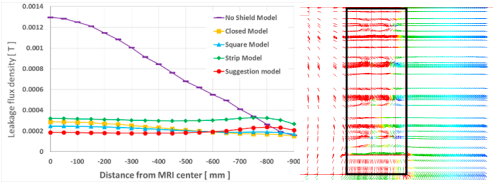

Fig.7 Analysis result (air gaps)

Fig.8 Vector distribution diagram (Model C, air gaps)

The leakage magnetic field could be further reduced by incorporating air gaps into the magnetic shielding.

Jet Flow Issuing from Deforming Nozzle

National Institute of Technology, Kagoshima College,
Advanced Mechanical and Electronic Control Systems Engineering,
Grade 2, Masato Higashi
Adviser : Takahide Tabata, National Institute of Technology,
Kagoshima College, Mechanical Engineering

INTRODUCTION

In the industry, the jet has been applied to many fluidic machinery because the jet provides some useful characteristics between diffusion effect and heat transfer effect. Moreover, industry field requires a variety of the spread of the jet in each flow field. However, the study on feedback control of the jet diffusion hasn't been investigated well. The purpose of this work is to control the jet diffusion by using deforming nozzle. **As the first step, the jet velocity by PIV(Particle Image Velocimetry)-method and flow condition were measured.**

EXPERIMENTAL APPARATUS AND CONDITIONS

Figure 1 shows coordinate systems. Also, reference diameter De , reference velocity U_{max} , and the Reynolds number Re are important parameters.

Experimental apparatus are consisted of the seeding system ①, the blower ②, the plenum chamber ③ to reduce the turbulence minimally, the LASER light system to irradiate in xOy-plane ④, the high speed camera ⑤, and the PC system ⑥ as shown in Fig. 2.

Next, the experimental conditions are shown in Table 1, 2, and 3. The calculated $Re = 6.97 \times 10^3$ ($= DeU_{max} / \nu$) based on kinetic viscosity $\nu = 1.49 \times 10^{-5}$[m^2/s] is non-dimensional number which shows flow condition, laminar flow or turbulent flow. And the velocity data were measured by using PIV in turbulent flow.

Here, shapes of nozzle exit were circular and square, and the effects of nozzle shape on the flow field were investigated.

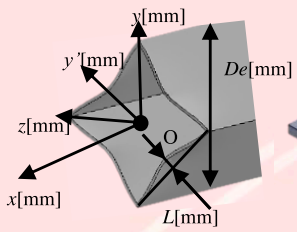

Fig. 1 Coordinate Systems

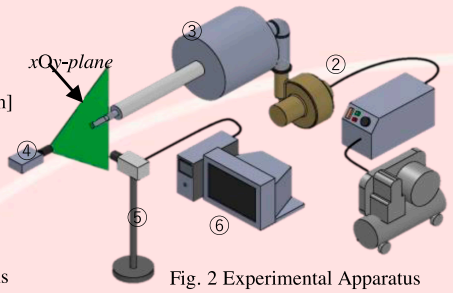

Fig. 2 Experimental Apparatus

Table 1 Experimental Conditions

Working Fluid	Air
Nozzles	Circular, Square
Maximum Velocity U_{max}	1.76 [m/s]
Reference Diameter De	6.97×10^3 [-]
Reynolds Number Re	59 [mm]

Table 2 Camera Conditions

Scale Factor	0.501 [mm/pixel]
Sampling Frequency	1000 [Hz]
Exposure Time	1/1500 [s]
Sampling Number	1301 [Sheet]

Table 3 Calculation Conditions

Calculation Method	Recursive Cross-correlation
Search Window	48×48 [pixel]
Inspection Window	28×28 [pixel]
Overlap	50 [%]

RESULT AND DISCUSSION

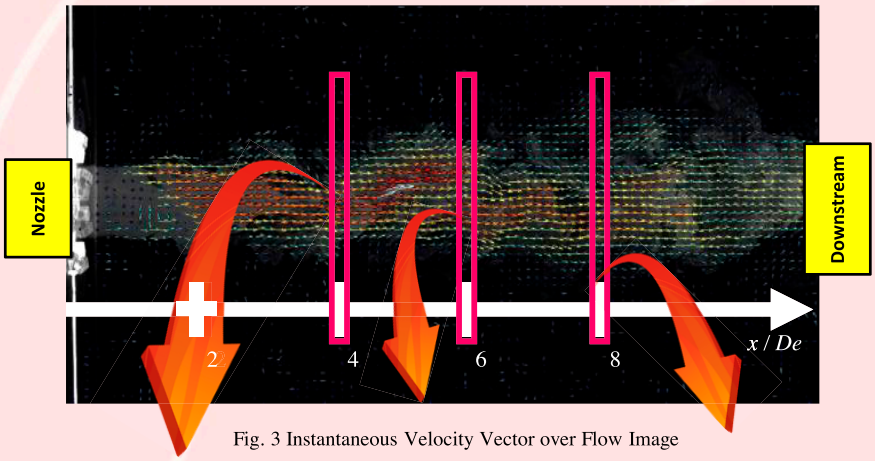

Fig. 3 Instantaneous Velocity Vector over Flow Image

Figure 3 shows instantaneous velocity vectors obtained from the flow image in xOy-*plane* as an example. The nozzle exit is shown in Left side in Fig. 3 and the jet issue to the right one, downstream. As shown in Fig.3, white area indicates the jet and black area indicates the surrounding air. At the location of $x / De \approx 2$ [-], the surrounding air is rolled to the jet by the roll-up vortex which is caused by viscosity. Furthermore, in the region of x/De from 6 to 8, the surrounding air is induced to center of the jet and the mixing the surrounding one and the jet is developed.

Figure 4 shows the velocity distributions at the downstream locations, x/De, 4, 6, and 8 [-]. It has been found that at the location of $x / De = 8$, comparing with the case of the circular nozzle jet, the square nozzle jet has higher velocity in the share layer. It indicates the square nozzle jet rolls up the more surrounding air than the circular nozzle one.

Finally, to evaluate the spread of the jet quantitatively, the half value widths are determined from the velocity distribution showing in Fig. 4. Here, the larger half value width indicates the promotion of the jet diffusion. Fig. 5 shows the variations of half value width in downstream direction to investigate the effect of the Re [-] on the jet diffusion. It has been clarified that in the downstream location, x/De from4 to 8, the half value width and its increase rate depend on the Re [-].

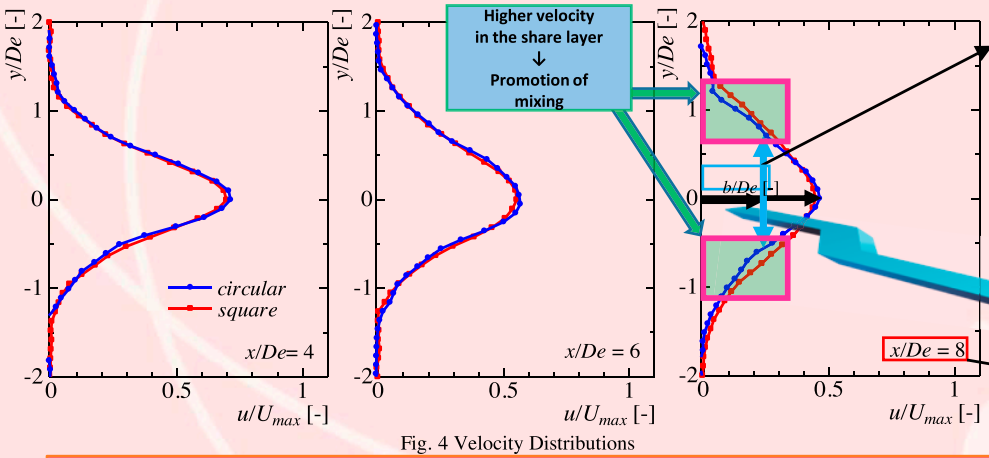

Fig. 4 Velocity Distributions

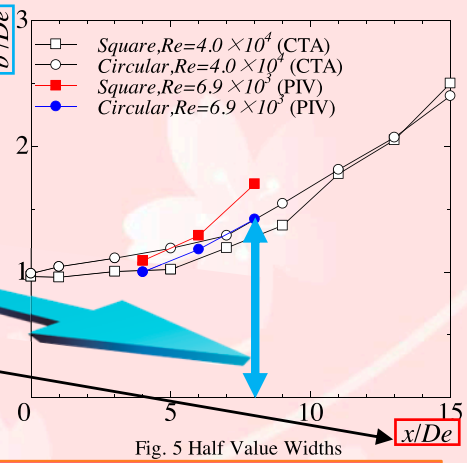

Fig. 5 Half Value Widths

CONCLUSION

In order to investigate the jet diffusion, the velocity measuring of the jet issuing from circular nozzle and square one were performed by the PIV. And the half value widths were determined from the obtained velocity distributions. As a result, the following conclusions have been obtained

- In the downstream location, x / De from 6 to 8, the rolled surrounding air is induced to the center of the jet by the viscosity. (by Fig. 3)
- In $x / De = 8$, in comparison with the circular nozzle jet, the square nozzle jet has higher velocity in the share layer. (by Fig. 4)
- In the measured range, x/De, half value width and its increase rate depend on the Re [-]. (by Fig. 5)

Create a bird's eye view by use of remote sensing image

National Institute of Technology,Kagoshima College
Advanced Mechanical and Electronic Control Systems Engineering
Ryota Funai, Chikara Miyata

Research background and purpose

Because the resolution of the bird's-eye view we made previously was 10 m, the image became dim when spread. In this research, we create high resolution color images from grayscale image of resolution 2.5 m (PRISM image) and color image of resolution 10 m (AVNIR-II image). Also we create high-precision bird's eye view by adding the altitude data. As the altitude data, we use the fundamental Geospatial data of the geospatial Information Authority of Japan.

Fig1. Bird's eye view （previously low resolution)

Satellite image and altitude map

In this research, we use satellite images of the advanced land observing satellite (ALOS). Three types of sensors PRISM, AVNIR - II and PALSAR are set in the ALOS. We use PRISM images and AVNIR-II images. Orbit altitude is 691.65 km.

PRISM image → Grayscale image of resolution 2.5 m

AVNIR-II image→ Color Images of resolution 10 m

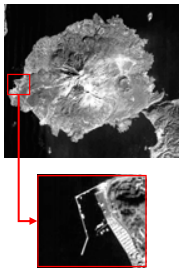

Fig2. PRISM Image

Fig3. AVNIR-II Image

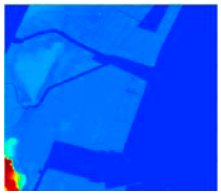

Fig4. Altitude map

Longitude/Latitude distance of the fundamental geospatial data is 0.2sec (5m). We made an altitude map from the fundamental geospatial data.

Pan-sharpen process

The pan-sharpen process is a process to creating pseudo color image with high resolution from grayscale image with high resolution and color image with a slightly lower resolution. In this research, the pan-sharpen process was performed as follows.

1) Convert AVNIR-II image from RGB image to HSI image.
2) Replace intensity of HSI image with PRISM image.
3) Convert HSI image which replaced to RGB image.

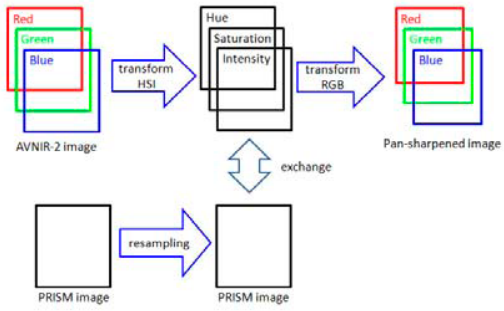

Fig6. Pan-sharpen process

Geometric correction

Geometric correction is to adjust the number of pixels, position and range so that images overlap. We set Grand Control Points (GCPs) for both images to make geometric correction. As shown in Fig. 5, I set 13 GCPs for each image. Then, resampling was carried out using the following affine transformation formula.

$$\begin{cases} P = aX + bY + c \\ L = dX + eY + f \end{cases}$$

X, Y is the coordinate of PRISM image and P, L is that of AVNIR - II image. The coefficients a ~ f were obtained by the least squares method.

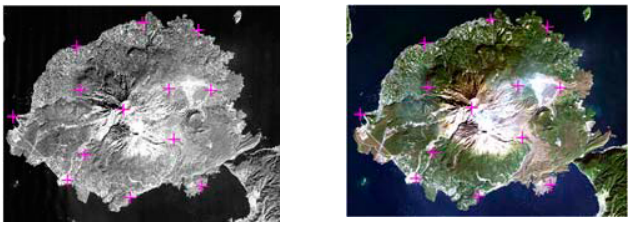

Fig5. GCP settings (13 GCPs)

Images of pan-sharpen process

Fig7.PRISM Image

Fig8.AVNIR-II Image

Fig9.Pan-sharpened Image

The plan for study

- Adjust the coordinate of the satellite image and the fundamental geospatial data by resampling.
- Interpolate the altitude at each lattice position whose distance is 2.5m from the fundamental geospatial data.
- Create a bird's eye view by the following.
  - XY plane → pan-sharpened image
  - Z axis → altitude data
- Examination of the usage.

Natural convection heat transfer from a vertical array of heated plates placed in a vertical channel

Kagoshima National College of Technology 2AMS10 Daisuke Horiwaki , Toshiyuki Misumi

1. Introduction

Natural convection heat transfer from heated plates set in a vertical array in a vertical channel were investigated analytically. As the result of this study, the average heat transfer coefficients from the plates in the array obtained from numerical analysis were summarized by non-dimensional parameters.

2. Analysis method

In numerical analysis, A domain containing the entire array of heated plates was handled. Air was used as the working fluid. Assuming two-dimensional laminar flow, the momentum, and energy equations in the domain were solved by the analysis software, ANSYS-CFX. The analysis were performed on two plates set in a vertical with height either L=20, 30, 50 mm placed at G=5 mm to 70 mm intervals that were heated with heat flux q_w =50, 100, 150 W/m^2. The plate row was placed in a vertical channel of width b =10, 20, 40, 60, 100 mm.

・Continuity equation

$$\frac{\partial u}{\partial x}+\frac{\partial v}{\partial y}=0 \tag{1}$$

・Momentum equation

X direction $$\rho\left(\frac{\partial u}{\partial t}+u\frac{\partial u}{\partial x}+v\frac{\partial u}{\partial y}\right)=-\frac{\partial p}{\partial x}+\mu\left(\frac{\partial^2 u}{\partial x^2}+\frac{\partial^2 u}{\partial y^2}\right) \tag{2}$$

Y direction $$\rho\left(\frac{\partial v}{\partial t}+u\frac{\partial v}{\partial x}+v\frac{\partial v}{\partial y}\right)=-\frac{\partial p}{\partial y}+\mu\left(\frac{\partial^2 v}{\partial x^2}+\frac{\partial^2 v}{\partial y^2}\right)-\rho g \tag{3}$$

・Energy equation

$$\rho c_p\left(\frac{\partial T}{\partial t}+u\frac{\partial T}{\partial x}+v\frac{\partial T}{\partial y}\right)=\lambda\left(\frac{\partial^2 T}{\partial x^2}+\frac{\partial^2 T}{\partial y^2}\right) \tag{4}$$

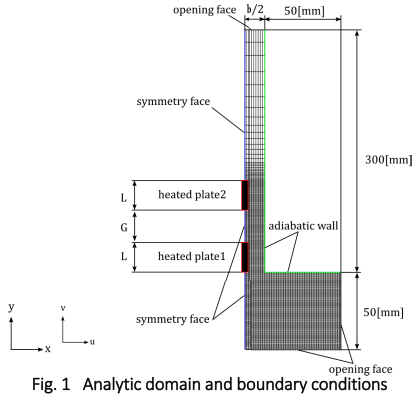

Fig. 1 Analytic domain and boundary conditions

3. Analysis result

3.1 Temperature and velocity distribution in a vertical channel

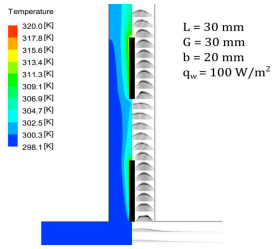

Fig.2 Temperature distribution and velocity vectors

The fluid in the channel is heated by the heated plates and ambient fluid flows from the channel entrance due to the chimney effect. The fluid heated by the first plate flows into the second plate while changing the velocity distribution. After that, the heated fluid flows toward the channel outlet.

3.2 Stream-wise velocity distribution at the bottom of heated plate when the channel width b is changed

the maximum velocity of the Y direction velocity v flowing into each plate is highest in b = 20 mm when the channel width b is changed from 10 mm to 100 mm.

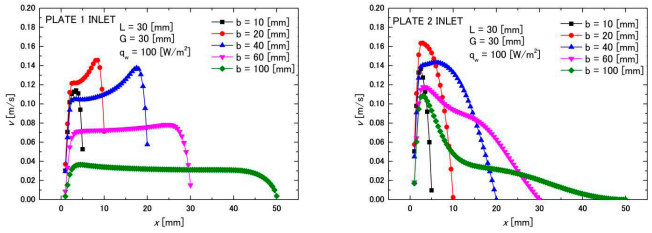

(a) First-plate (b) Second-plate

Fig.3 Stream-wise velocity distribution around the heated plates

3.3 Stream-wise velocity distribution at the bottom of heated plate when the plate spacing G is changed

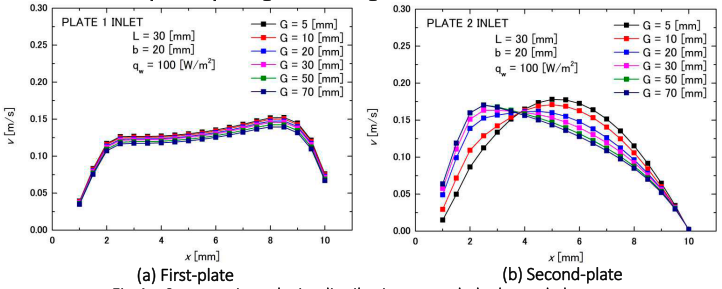

(a) First-plate (b) Second-plate

Fig.4 Stream-wise velocity distribution around the heated plates

The distribution of the Y direction velocity v flowing into the first plate decreases as the plate spacing G increases. Also the distribution of the Y direction velocity v flowing into second plate increases near the flat plate.

3.4 Temperature distribution at the bottom of heated plate when the plate spacing G is changed

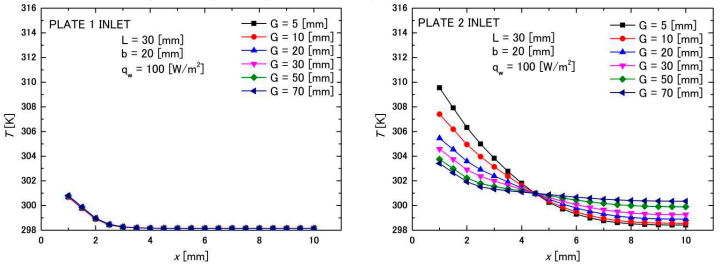

(a) First-plate (b) Second-plate

Fig.5 Temperature distribution around the heated plates

As the temperature of the fluid heated by the first plate diffuses horizontally as it flows upward, the temperature of the fluid flowing into the second plate decreases as the plate spacing G increases.

3.5 Average heat transfer coefficients

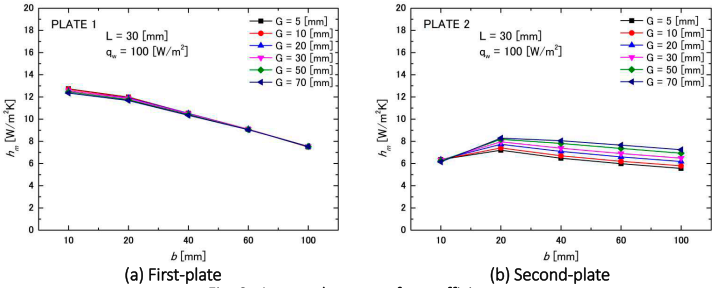

(a) First-plate (b) Second-plate

Fig. 6 Average heat transfer coefficients

Under the influence of the velocity and the temperature distribution in a channel, the average heat transfer coefficients of the first plate reaches the maximum value in b=10 mm and the second one does so in b=20 mm. Also plate spacing G increases, the average heat transfer coefficients of the first plate decreases slightly, whereas the average heat transfer coefficients of the second plate increases.

3.6 Non-dimensionalization

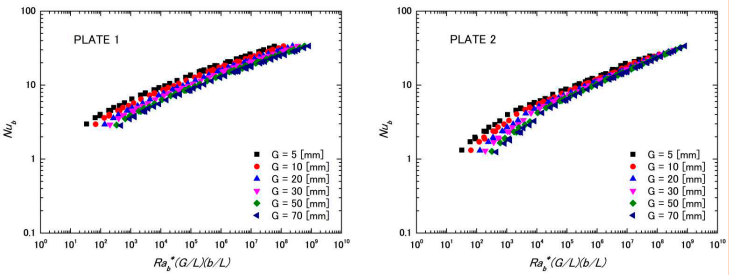

(a) First-plate (b) Second-plate

Fig. 7 Average nusselt numbers Nu_b from each plate plotted with $Ra_b^*(G/L)(b/L)$.

Since the average heat transfer coefficients of each flat plate is greatly influence by the plate height L, the plate spacing G, the channel width b, heat flux q_w, non-dimensional parameters that dominate heat transfer characteristics of these flat plates were investigated. From Fig.7, when the average nusselt number Nu_b is arranged by $Ra_b^*(G/L)(b/L)$, it is distributed on almost one curve for every plate spacing G.

4. Future task

Heat transfer and flow characteristics around each plate are examined by numerical analysis when three heated plates are placed in a vertical channel.

Investigation of transparent conductive multilayer film with Ag

Yuichiro Maeda [1], Yukio Yoshimura[2], Atsushi Nitta[3]

1 Advanced Mechanical and Electronic Control Systems Engineering, National Institute of technology, Kagoshima College
2 Shirasu Development Laboratories, Regional Resources Division, Kagoshima Prefectural Institute of Industrial Technology
3 Department electronic Control Engineering, National Institute of technology, Kagoshima College

Introduction

Transparent conductive film

Resistivity : 1×10^{-3} [Ω・cm] or less
Visible transmittance : 80 [%] or more

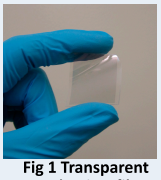

Fig 1 Transparent conductive film

- Low resistivity and high transmittance of transparent conductive films are in demand in many electronic devices such as solar cells , flat display and light emitting diodes.
- There is increasing attention paid to flexible device.

A flexible transparent conductive film is required.

Problems

- Indium Tin Oxide (ITO) is not strong against bending.
- ITO is expensive.
- Low temperature process is required for film formation.

Approach to AZO/Ag/AZO multilayer structures.

AZO/Ag/AZO

- Low cost
- AZO is strong against bending
- Ag Resistivity : 1.59×10^{-6} [Ω・cm]

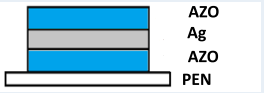

Fig 2 AZO/Ag/AZO multilayer structures

Target

Fabrication of a flexible transparent conductive film comparable to ITO.

Experimental methods

AZO : RF magnetron sputtering
Ag : Electron beam evaporation
Substrate : PEN

Cleaning with UV/O_3
↓
AZO : Sputtering
↓
Ag : E-beam evaporation
↓
AZO : Sputtering

Table 1. Deposition conditions

RF magnetron sputtering	
Sputtering pressure [Pa]	0.4
RF power [W]	40
Ar flow rate [sccm]	5
Substrate temperature [℃]	50
Target to substrate distance [nm]	150
Electron beam evaporation	
Chamber Pressure [Pa]	2.4×10^{-4}
Accelerating voltage [kV]	7
Emission current [mA]	50
Substrate temperature [℃]	50
Evaporation source to substrate distance [nm]	440

Change methods

- AZO thickness (70 nm ,100nm)
- Ag thickness (8 - 15 nm)

Evaluation method

- The electrical resistivity and optical transmittance of the resulting AZO/Ag/AZO films were measured by using digital multimeter (Iwatsu : VOAC7521-H) and a spectrophotometer (Hitachi high technologies : U-3900) in the range of 400 nm - 800 nm, respectively.
- The crystallinity and crystal orientation of the films were examined by X-ray diffraction (Rigaku : Ultima Ⅳ).

Result

AZO layer (100 nm)

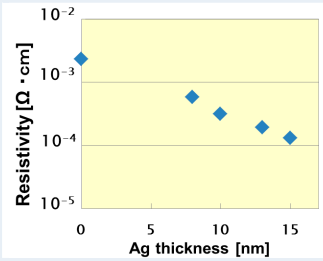

Fig 3. The resistivity of multilayers films at various Ag thickness. (AZO:100 nm)

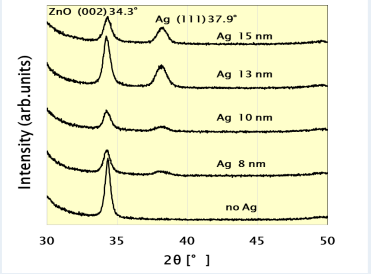

Fig 4. XRD patterns of the multilayers films as a function of Ag layer thickness. (AZO:100 nm)

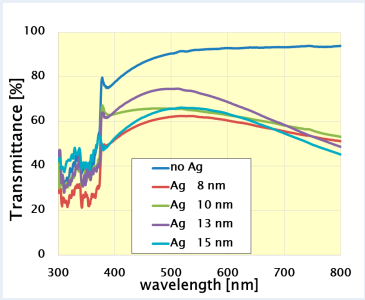

Fig 5. The transmittance of multilayers films at various Ag thickness (AZO:100 nm)

Table 2. The average transmittance and Composition ratio (O/Zn) (AZO: 100nm)

AZO thickness [nm]	Ag thickness [nm]	Average transmittance [%]	Composition ratio (O/Zn)
100	0	90.2	0.522
	8	57.8	0.498
	10	62	0.483
	13	65.2	0.425
	15	59	0.467
50	0	90.8	0.914

- The resistivity decreased with the increasing of Ag layer thickness ,but the crystallinity of AZO wasn't improved.
- The transmittance greatly decreased in the near infrared region.
- Oxygen defect was generated in AZO.

↓

- Heat is not transmitted to the entire film at 50 ℃ . So, we aimed at solving the heat conduction problem by thinning the AZO layers.

- Ag 8 and 10 nm films were deposited as separate islands randomly distributed and the separated islands would scatter the incident light. Thus reduced light transmittance.

AZO layer (70 nm)

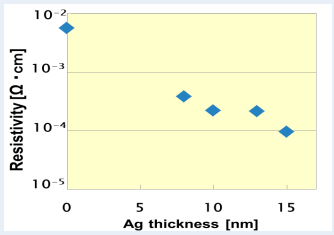

Fig 6. The resistivity of multilayers films at various Ag thickness. (AZO:70 nm)

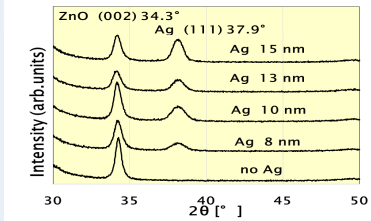

Fig 7. XRD patterns of the multilayers films as a function of Ag layer thickness. (AZO:70 nm)

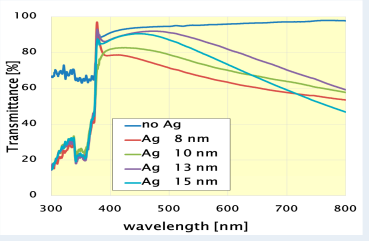

Fig 8. The transmittance of multilayers films at various Ag thickness. (AZO:70 nm)

Table 3. The average transmittance and Composition ratio (O/Zn) (AZO: 70nm)

AZO thickness [nm]	Ag thickness [nm]	Average trans-mittance [%]	Composition ratio (O/Zn)
70	0	95.3	0.762
	8	66.1	0.646
	10	71.9	0.716
	13	81	0.626
	15	74	0.704

- The resistivity similarly decreased with the increasing of Ag layer thickness.
- Oxygen deficiency was improved by thinning the AZO layers. Therefore, the transmittance increased, but the transmittance greatly decrease in the near infrared region.

Conclusion

The resistivity decreased with the increasing of Ag layer thickness, but the crystallinity of AZO wasn't improved. This finding indicates that the resistivity is greatly affected by Ag carrier. Oxygen deficiency was improved by thinning the AZO layers. Therefore, the transmittance increased.

In this study, the resistivity of 2.16×10^{-4}[Ω-cm] and the average transmittance of 81 [%] were achieved for the Ag layer thickness of 13 nm. But, the transmittance greatly decreased in the near infrared region.

Driving control of vehicle using SNIRMs fuzzy model constructed by leaning algorithm

National Institute of Technology, Kagoshima College
Yuto Watase, Kazuya Kishida

1. Introduction

Most of self-tuning fuzzy systems, which are automatically constructed from learning data, are based on the steeped descent method. However, this approach often requires a large convergence time and gets stuck into shallow local minimum. One of its solutions is to use fuzzy rule modules with a small number of inputs such as SIRMs and SNIRMs. The purpose of this study is to show the effectiveness of a SNIRMs model by a real vehicle. To apply this model, numerical simulations for function approximation using SNIRMs model is performed.

2. SNIRMs fuzzy model

SNIRMs fuzzy model

SNIRMs (Small Number of Input Rule Modules) fuzzy model proposed by Miyajima et al is constructed modules which has a single or a double input variable in the antecedent part. The summation of the products of the importance degree and the fuzzy inference result of each module is then taken as the output of model. Fig.1 shows conventional model and SNIRMs model, which x_i is input variable, h_i and h_{ij} are each importance degree, and y_0 is output of model. SNIRMs model show better performance than SIRMs in nonlinear problem.

Learning algorithm for SNIRMs fuzzy model

In order to learn parameters, we constructed self-tuning SNIRMs fuzzy system from learning data based on SDM (Steepest Descent Method). The objective function E is defined to evaluate the inference error between the desirable output y and the inference output y*.

$$E = \frac{1}{2}(y^* - y)^2 \qquad (1)$$

In order to minimize the objective function E, each parameter β is updated based on SDM.

$$\beta(t+1) = \beta(t) - K_\beta \frac{\partial E}{\partial \beta} \qquad (2)$$

where t is iteration time and K_β is a constant.

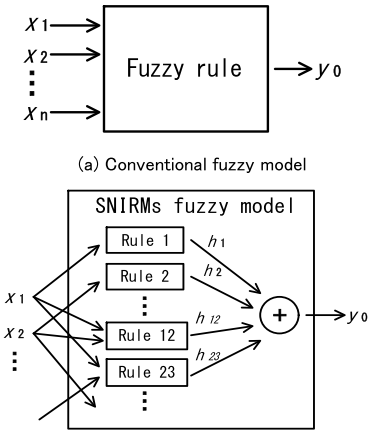

(a) Conventional fuzzy model

(b) SNIRMs fuzzy model

Fig. 1 Fuzzy models

3. Numerical simulation for function approximation

Numerical simulations for function approximation using SNIRMs model is performed as pre-test to control a real vehicle. This simulation uses four systems specified by the following functions with four dimensional input domains $[0,1]^4$ for (3) and (4) and $[-1,1]^4$ for (5) and (6). The simulation condition parameters are the number of partitions for fuzzy inference rules is three, the numbers of learning and testing data are 512 and 6400, respectively. All data are uniformly selected from the input space.

$$y = \frac{(2x_1 + 4x_2^2 + 0.1)^2}{37.21} \times \frac{(4\sin(\pi x_3) + 2\cos(\pi x_4) + 6)}{12} \qquad (3)$$

$$y = \frac{\sin(2\pi x_1) \times \cos(x_2) \times \sin(\pi x_3) \times x_4 + 1.0}{2.0} \qquad (4)$$

$$y = \frac{(2x_1 + 4x_2^2 + 0.1)^2}{74.42} + \frac{(4\sin(\pi x_3) + 2\cos(\pi x_4) + 6)}{446.52} \qquad (5)$$

$$y = \frac{(2x_1 + 4x_2^2 + 0.1)^2}{74.42} + \frac{(3e^{3x_3} + 2e^{-4x_4})^{-0.5} - 0.077}{4.68} \qquad (6)$$

Table 1 shows the results. In each box, three numbers from the top to the bottom show MSE (Mean Squared Error) of training($\times 10^{-3}$), MSE of testing ($\times 10^{-3}$), and the number of parameters, respectively. The result of simulation is the average value from ten trials. The results show that SNIRMs model is superior in terms of the number of parameters to conventional model and superior in terms of accuracy to SIRMs model.

Table. 1 The result of simulation for function approximation

		(3)	(4)	(5)	(6)
Conventional Fuzzy Model	MSE for learning($\times 10^{-3}$)	0.01	0.07	0.08	0.07
	MSE for testing($\times 10^{-3}$)	0.03	0.14	0.14	0.14
	The number of parameters	729	729	729	729
SIRMs Fuzzy Model	MSE for learning($\times 10^{-3}$)	1.60	10.69	1.40	3.34
	MSE for testing($\times 10^{-3}$)	1.80	10.71	1.62	3.75
	The number of parameters	40	40	40	40
SNIRMs Fuzzy model	MSE for learning($\times 10^{-3}$)	0.09	1.22	0.01	0.01
	MSE for testing($\times 10^{-3}$)	0.14	2.69	2.69	4.81
	The number of parameters	162	162	162	162

4. Conclusion

In this study, in order to show the effectiveness of a SNIRMs model, numerical simulations for function approximation using SNIRMs model constructed by leaning algorithm is performed. As a result of the simulation, we speculate that SNIRMs model is suited for controlling a real vehicle. In the future work, we would like to apply this model to a real vehicle.

ALGAL GROWTH EFFECTS OF ELUATE FROM A CHELATING AGENT AND ITS STRUCTUAL ANALYSIS

○Shogo Kimura[1], Yusuke Fuyuno[1], Katsuhiko Takenaka[2], Toshiyuki Takahashi[3]

[1] Materials Engineering Advanced Course, National Institute of Technology (NIT), Miyakonojo College, [2] Department of Materials Science and Technology, Nagaoka University of Technology, [3] Department of Chemical and Engineering, NIT, Miyakonojo College (Email : mttaka@cc.miyakonojo-nct.ac.jp)

Introduction

Microalgae have attracted attention for use as biofuels because they do not compete for food resources as corn and sugar corn production might. Nevertheless, the growth rate of microalgae is lower than that of bacteria. It remains a challenge to use microalgae as a stable fuel source. This study investigated a method to grow microalgae effectively, particularly examining effects on *Parachlorella kessleri* (*Chlorella kessleri*) by eluate from a commercial resin for immobilized metal ion adsorption chromatography. In addition, chemical properties of the eluate were analyzed using UV/IR spectrometry and GC-MS.

○Application of microalgae

Green Bio	Red Bio	White Bio
• Functional Food • Water Purification	• Medical supplies • Nutrients	• Bio fuel • CO_2Fixation material

Fig.1 Wide application of microalgae.

Microalgae are used for a wide range of application. They are categorized as Green Bio related to food and environmental, Red Bio related to health care and White Bio related to energy and industry.

White Bio is not yet put to practical use , but it has attracted attention for use as the solution about an energy issue.

Materials and Methods

Materials

○***Parachlorella kessleri* (*Chlorella kessleri*)**

This is the model organism representing microalgae.

○**Sesamol** (Liu *et al.*, *Food Chem.*, 2015)

This is one of an algal growth factor. Methanol was used as a solvent in this study.

○**Eluate from a commercial resin**

Commercial resin for immobilized metal ion adsorption chromatography was used in this study.

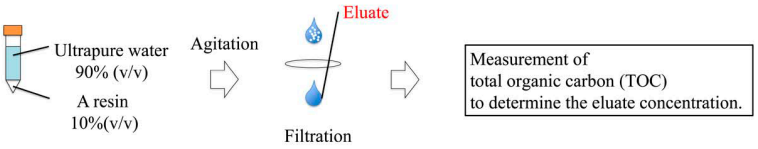

Methods

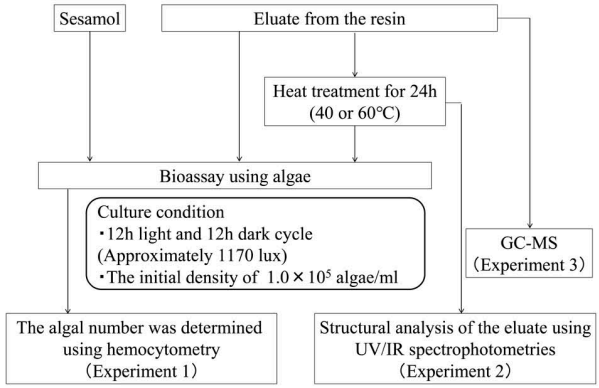

Result and Discussion

Experiment 1

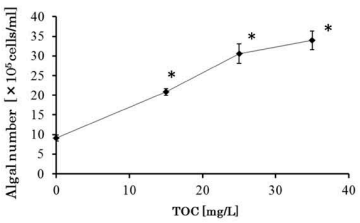

Fig. 2 Relation between eluate concentration and algal growth.

* shows statistical difference between control and each test sample using t-test.

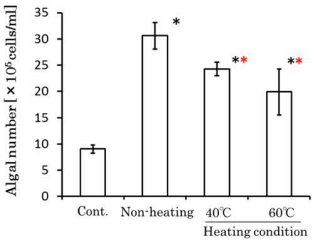

Fig. 4 Thermal tolerance of the eluate.

* shows statistical difference between control and each test sample using t-test.

* shows statistical difference between non-heated condition and each test sample using t-test.

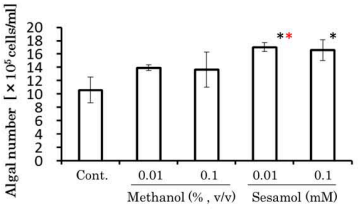

Fig. 3 Relation between sesamol concentration and algal growth.

* shows statistical difference between control and each test sample using t-test.

* shows statistical difference between methanol control and each test sample using t-test.

After treatment of algae with the eluate, the algal growth increased concentration-dependently. Especially, the algal number at the highest concentration of eluate in this study was 3 times as much as the control. Moreover, the proliferative effect of the eluate on algae was greater than that of sesamol.

The heated eluate decreased the proliferative effect on algae.

⇨ The proliferative effect of eluate on algae is greater than that of sesamol. Heat treatment of the eluate decreased its effect.

Experiment 2

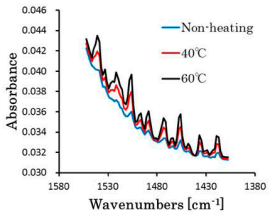

Fig .5 Structural analysis of the eluate using IR spectrophotometry.

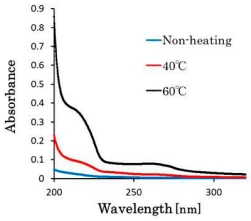

Fig .6 Structural analysis of the eluate using UV spectrophotometry.

The absorbance of the heated eluate at 1400 - 1600 cm^{-1} increased temperature-dependently.

The absorbance of the heated eluate in UV region increased temperature-dependently.

⇨ The decreased proliferative effect by heated treatment might result from the conformational change of the biologically active substances in the eluate.

Experiment 3

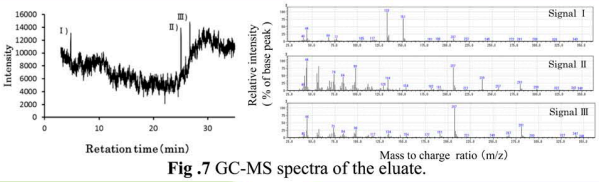

Fig .7 GC-MS spectra of the eluate.

Three signals were detected in a GC spectrum. These signals were subjected to MS analysis. However, the similarity search using data obtained from GC-MS could not identify any candidate molecule.

⇨ The result indicates that the eluate contained several components or that the GC process decomposed the entity in the eluate to several chemicals. To identify the entity in the eluate, further analysis such as LC-MS is needed.

Conclusion

- **The eluate increased algal growth concentration-dependently, and this proliferative effect of the eluate was greater than that of sesamol.**
- **Heat treatment changed the biologically active substances in the eluate into the inactive conformation, resulting in decrease of its proliferative.**
- **GC-MS analysis of the eluate couldn't identify any candidate component.**

Assessment of phytoplankton such as microalgae using an automated cell counter

Takuya Tsukada[1], Kouichiro Murakawa[2], Toshiyuki Takahashi[2]
[1] Materials Engineering Advanced Course, National Institute of Technology (NIT), Miyakonojo College, Japan.
[2] Department of Chemical and Engineering, NIT, Miyakonojo College, Japan. (E-mail:mttaka@cc.miyakonojo-nct.ac.jp)

Introduction

Microorganisms have generally fast growth. They as liquid samples can be easily handled. Therefore, microorganisms have been widely used for productions of pharmaceuticals and fermented food, and for an electrical production using biomass. To use microorganisms in several ways, it is important to grasp cell densities of interest and the cell state in each culture. Although a cell counter plate like a hemocytometer has been used to determine cell densities, it requires a skilled user for accurate determination of cell densities. This study paid attention to an automated cell counter. This study aimed to evaluate usefulness of an automated cell counter on assessing microbes because commercially available automated cell counters are optimized to detect cultured animal cells (≧10 μm) rater than microbes (<10 μm). This study used an automated cell counter with a fluorescence detector and phytoplankton like microalgae as microbes. This study also evaluated the usefulness of this device on assessment of environmental samples. Results show that evaluations of microalgae using the automated cell counter was a higher-accuracy method than that using a hemocytometer. Moreover, it could detect not only cultured microalgae but also phytoplankton in environmental samples.

Experiments

Accuracy comparison of a automated cell counter with a hemocytometer

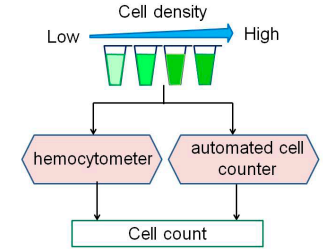

Evaluation of cell state using a automated cell counter

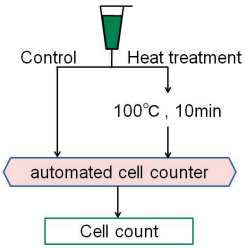

Measurement of environmental sample using a automated cell counter

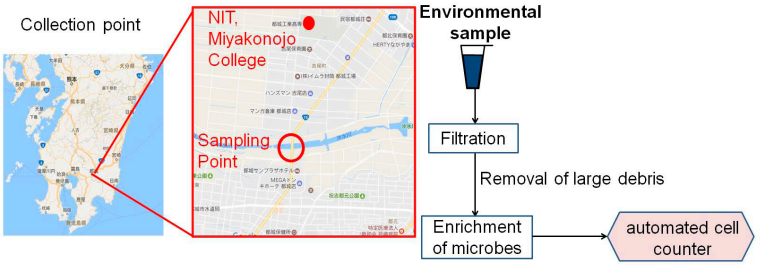

Results

Accuracy evaluation of a automated cell counter

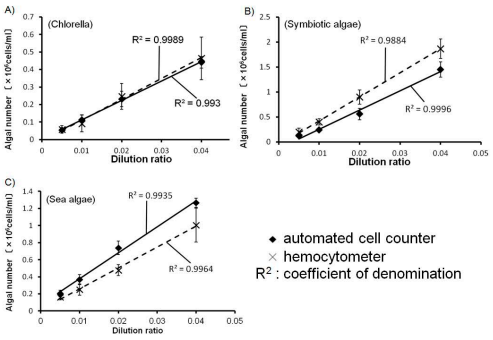

Fig. 1 Measurement of cell densities using a automated cell counter and a hemocytometer.

Measured values differed from each method slightly. R^2 values of each calibration curve from a automated cell counter were more than 0.9.

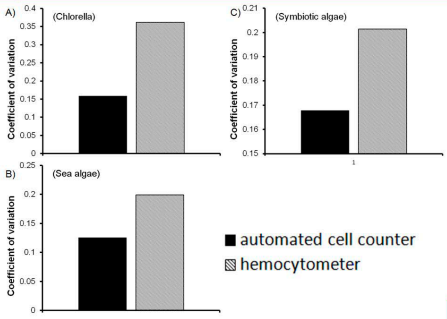

Fig. 2 Coefficients of variation from data using a automated cell counter and a hemocytometer.

In order to evaluate accuracy of each from data presented in Fig.1, method each coefficient of variation was determined based on the results obtained by each measurement method. Results show that the coefficient of variation from the automated cell counter was lower than that from the hemocytometer.

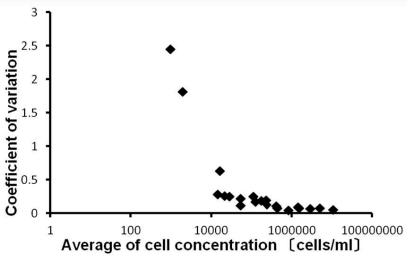

Fig. 3 Relation between cell densities and each value of variation coefficient.

A range that the automated cell counter could determine the exact value of cell densities was examined. Several concentrations of algal samples were prepared and measured using the automated cell counter. Each coefficient of variation was compared between samples with different cell densities. The result shows that values of variation coefficient drastically increased when cell densities less than 5.0×10^4 cell/ml were used. Thus, cell densities more than 5.0×10^4 cells/ml were needed for precise measurement using the cell counter.

Evaluation of cell status of microalgae using a automated cell counter

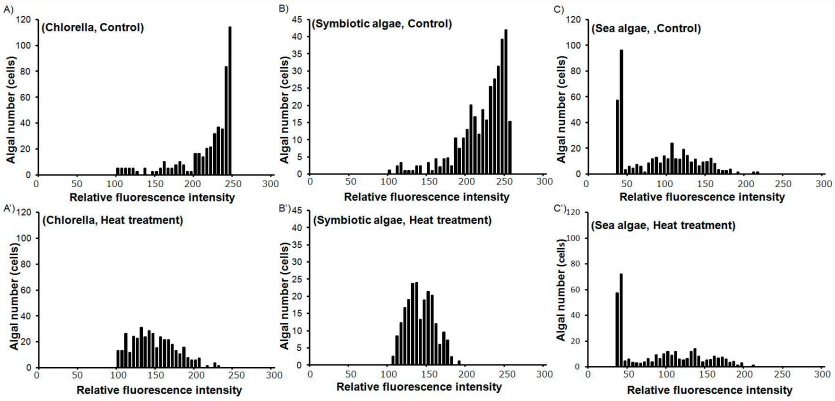

Fig. 5 Changes of microalgae in red fluorescence before and after heat treatment.

An influence of heat treatment on red fluorescence of algae was examined. Here, the red fluorescence of algae means the chlorophyll fluorescence. The result shows that the automated cell counter could detect changes of algal status after heat treatment of algae.

Evaluation of environmental samples using a automated cell counter

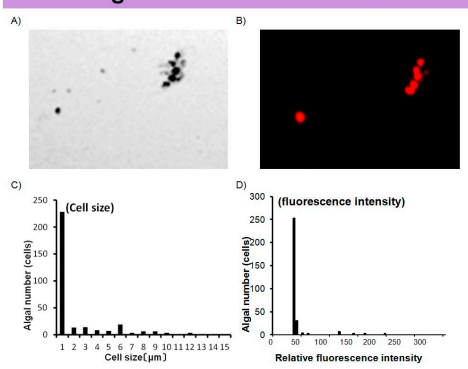

Fig.6 Detection of environmental phytoplankton using a automated cell counter.

Applicability of the cell counter to environmental evaluation was examined. Microorganisms in environmental samples were detected (A: bright field, B: fluorescence image) . The cell size and fluorescence intensity were determined (C & D).

Conclusion

- The automated cell counter method was able to measure cell densities of microalgae with high accuracy compared with hemocytometry.
- The automated cell counter was able to evaluate the cellular states of microalgae based on the fluorescence intensity.
- The automated cell counter was also able to detect microbes collected from aqueous environment.

Development of a new ammonia nitrogen removal system using microalgae secreting photosynthate

○Azusa Yamada[1], Momoko Higashiguchi[1], Toshiyuki Takahashi[2]
[1]Materials Engineering Advanced Course, National Institute of Technology, Miyakonojo College, Miyakonojo, Japan. [2]Department of Chemical and Engineering, National Institute of Technology, Miyakonojo College, Miyakonojo, Japan. (E-mail:mttaka@cc.miyakonojo-nct.ac.jp)

Introduction

Liquid waste water containing ammonia nitrogen has been discharged from several industries and sewage. The waste water causes water pollution such as eutrophication. This study paid attention to symbiotic algae in protozoa *Paramecium bursaria*. The algae have unique characteristics to release their photosynthetic products and to use ammonium ion as nutrient. Then, this study aimed to develop an ammonia removal method using these symbiotic algae. In this study, the algae encased in an alginate gel were treated with aqueous ammonia. After treatment of algae with ammonia, residual ammonia was determined using colorimetry based method. The relation between algal numbers and the removal capacity of ammonia was examined. Moreover, the ability of alginate gels containing algae to release photosynthate was also examined using thin layer chromatography and phenol-sulfuric acid method. Results show that the alginate gel containing algae could remove ammonia nitrogen. The removal efficiency of ammonia using algal gels was dependent on algal densities. The algae could release photosynthate even if algae in alginate gels.

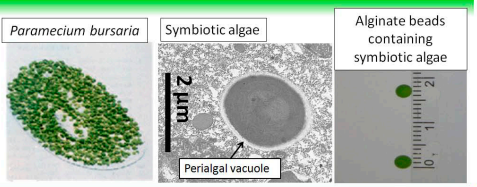

Experiments

Production of alginate beads containing algae

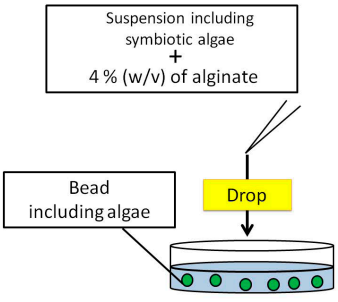

Evaluation of algal beads on absorbing ammonia

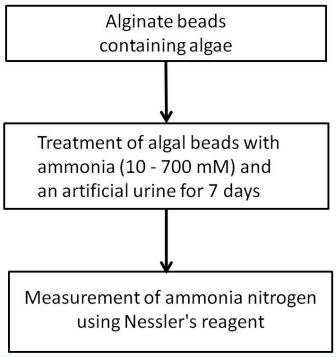

Evaluation of algal survival rate after treatment with ammonia

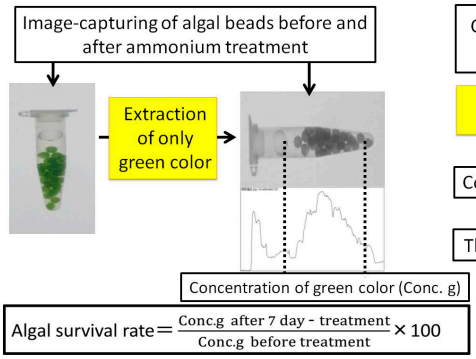

Evaluation of algal beads on photosynthate release

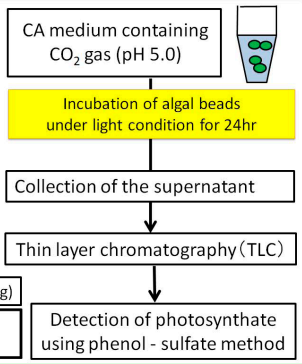

Experimental results

Quantification of algal numbers in each bead

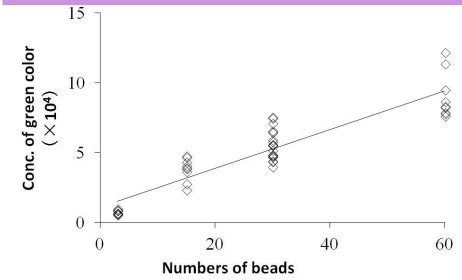

Fig. 1 Correlation between the number of beads and algal number as concentrations of green color.

The number of algal beads was clearly correlated with the concentration of green color (Conc. g). Thus, the Conc. g was used to quantify the number of algae in each bead.

Absorption capacity of ammonia nitrogen using the algal beads

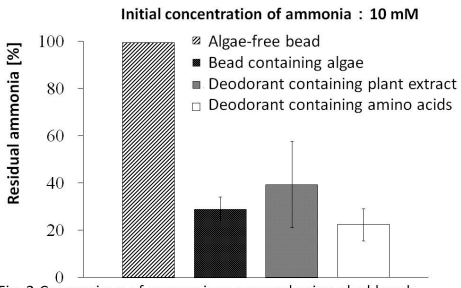

Fig. 2 Comparison of ammonium removal using algal beads with that using other deodorants.

The removal capacity of ammonia using algal beads was almost the same as that using commercially available deodorants.

Resistance of algae to ammonia

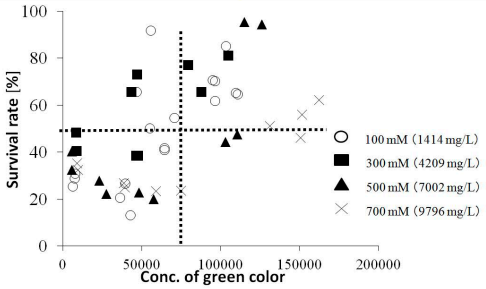

Fig. 3 Correlation between concentration of green color and survival rate of algae.

The more the conc. of green color was used, the more the survival rate of algae was after treatment with ammonia even if they are exposed to high concentration of ammonia.

Absorption capacity of ammonia nitrogen using the algal bead

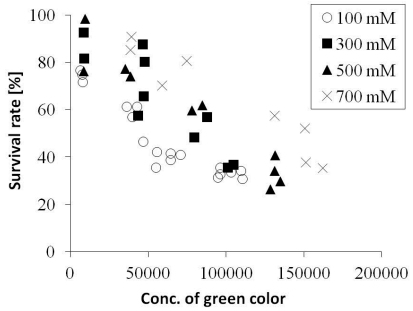

Fig. 4 Relationship between concentration of green color and the ammonia absorption capacity.

The more the concentration of color increased, the more the absorbed amounts of the ammonia increased.

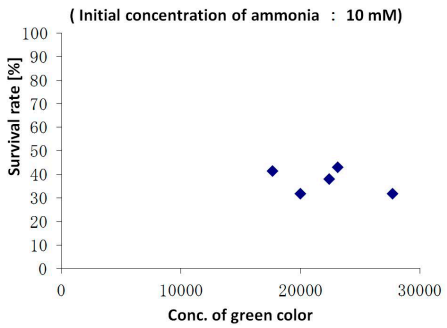

Fig. 5 An effect of algae absorbing ammonia nitrogen to human artificial urine.

The algal beads decreased ammonia less than half of the initial concentration of ammonia.

Release of photosynthate by algal beads

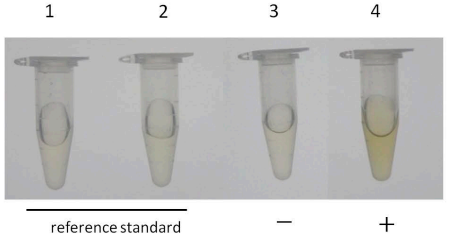

1 : ultrapure water
2 : CA medium
3 : only alginic acid after TLC
4 : culture supernatant of algal beads after TLC

Fig. 6 Detection of photosynthate using after TLC and phenol-sulfuric acid method.

Spots of mobility comparable to maltose on a TLC sheet was scraped off. These samples were subjected to phenol-sulfuric acid method to detect photosynthate from symbiotic algae encased in alginate beads. The Results show that the culture supernatant of algal beads contained photosynthate from algae.

Conclusion

Results obtained from this study can be summarized as the following.

A) The algal beads could absorb ammonia nitrogen.
B) The algal beads could handle high concentrations of ammonia by increase of their beads.
C) The algal beads could also absorb ammonia in urine.
D) The algae could release photosyntetic products even if algae in alginate beads.

Nagaoka University of Technology
Aqua & Soil Environmental Laboratory

Prof. Takashi YAMAGUCHI, Assoc. Prof. Masashi HATAMOTO, Asst. Prof. Takahiro WATARI

Bioreactor technology for wasetewater treatment

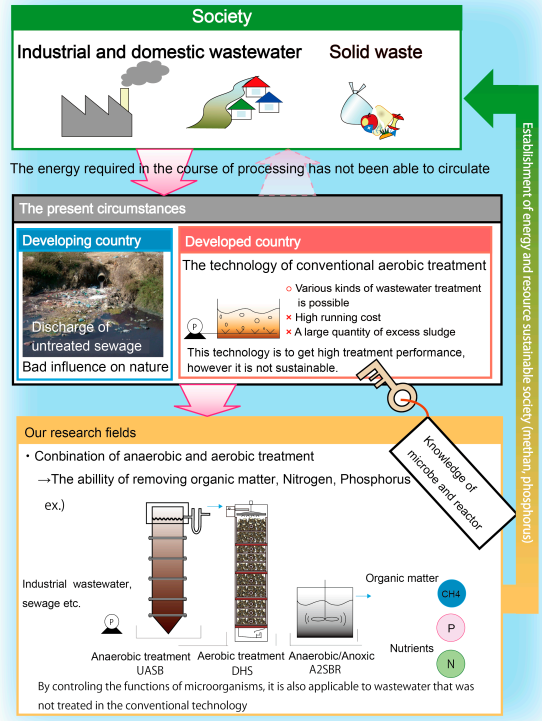

Analysis of microorganism in the bioreactor

- Knowledge of microorganism ecology is needed for the development of biotechnology.
- Developing new microorganism analysis and detection technology give us new knowledge.
- Isolation of novel microbes from bioreactors.
- Microbial community stracture analysis

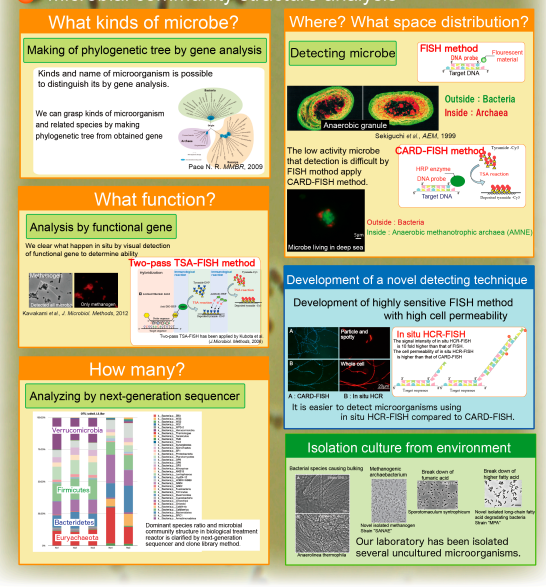

Biomass • Resource recovery

Using the unused biomass collect the sugar as a resource , methane gas as an energy

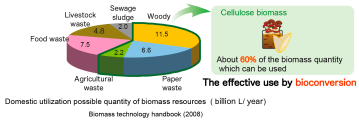

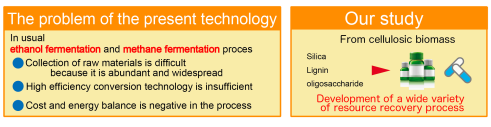

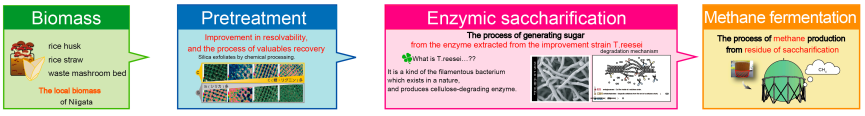

Research topics

Establishment of low cost sewage treatment system
- Removal of nutrients like nitrogen and phosphorus by anaerobic,anoxic sequencing batch reactors

Formulation of new sewage treatment system
- Development of organic and nutrients treatment system and analysis of sulfur dynamics of domestic sewage
- Development of less energy consuming technology for wastewater treatment in Thailand

Elemental technology development
- Application of DHS reactor for biological treatment of volatile organic compounds
- Development of nitrogen removal system of make-up water with breeding marine organism

Structural analysis of microbes in the environment and their isolation.
- Detection of archaea in deep-sea culture by Fluorescence In- Situ Hybridization method
- Investigation of enriched denitrifying anaerobic methane oxidizing microorganisms

Discovery of new method to detect the new microbial consortium.
- Development of new method for high sensitivity in situ HCR for osmosis on protists.

Biomass transformation for recovery of energy and resources
- Resource and energy recovery from cellulosic biomass by multiple-stage processes
- Development of resource recovery process of mushroom bed

Discovery of the Power of Microorganisms

- Bioresource engineering Laboratory, Nagaoka University of Technology -

Stuff

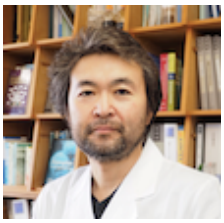

Prof. Wataru Ogasawara

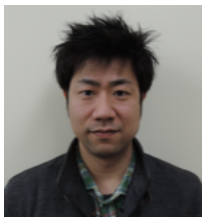

Assist. Prof Yosuke Shida

Member (foreign student)
PD: Yoshiyuki Suzuki
PM: 1 Assistant: 5
Ph.D. Student: 3 (2)
Graduate: 6 (1)
Undergraduate : 10

Microbial resources

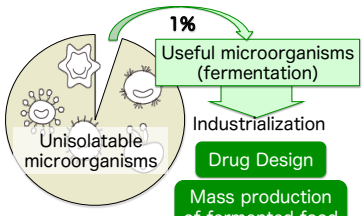

There are many organism that ability is unknown

Research Themes

- Analysis of the membrane protein involved in cellulase induction
- Comparative genomic analysis of *T. reesei* mutant
- Study on cellulase gene regulation system in *T. reesei*
- Morphological analysis of *T. reesei*
- Molecular breeding and analysis of oleaginous yeast
- Analysis of carotenoid production mechanism in R. toruloides
- Structure and function relationship of S46 peptidase
- Exploration of novel useful microorganism

Utilization by understanding the way of life

Utilization

Wood Degrader

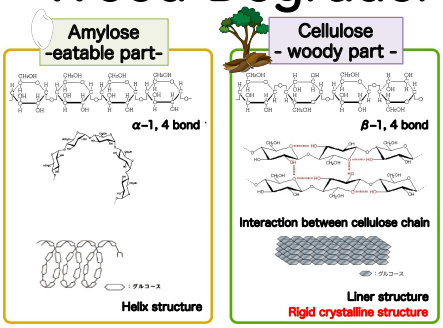

Sugar can be obtained from wood

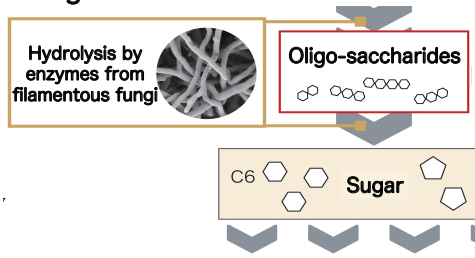

Fermentation

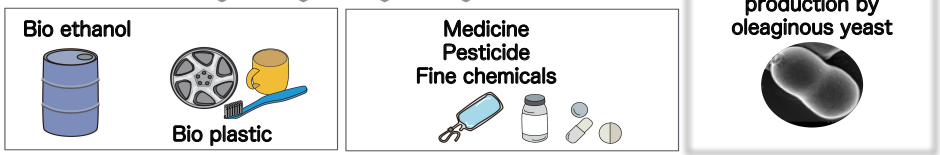

Oleaginous Yeast

Food supply
Food safety

Food and energy production from unutilized resource

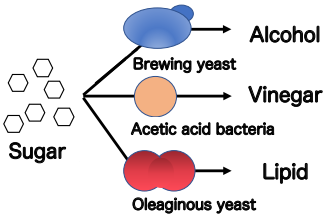

Production of valuable materials by fermenting sugar

The self-sufficiency of oil is only 3%

Medical terget

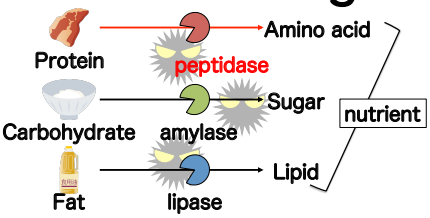

Pathogenic microorganisms also metabolize various substances

Periodontal disease
Food poisoning
There is no specific remedy

Target
Peptidase of disease causing bacteria

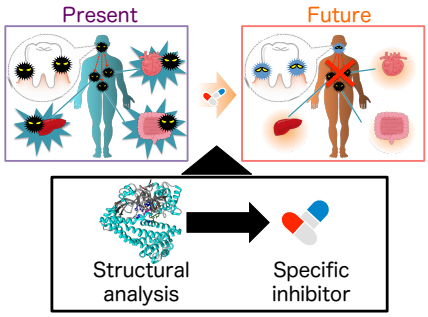

Valuable material production from Biomass (Unutilized resource)

Filamentous fungi *Trichoderma reesei*

- The best protein factory among microorganism
- 80% of secreted proteins are carbohydrate hydrolase

Oleaginous yeast *Rhodosporidium toruloides*

- Produced lipids occupy 70% of cell
- Carotenoid producer

Novel drug development

Bacteria specific enzyme S46 peptidase

- Important for the growth of pathogenic bacteria
- 3D structure was revealed in our laboratory for the first time in the world.

Strongest cellulase producer

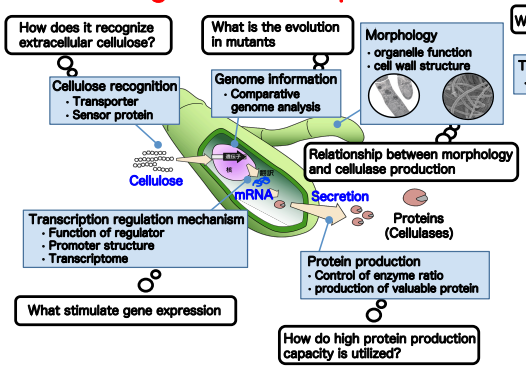

Producer of edible lipid and carotenoids

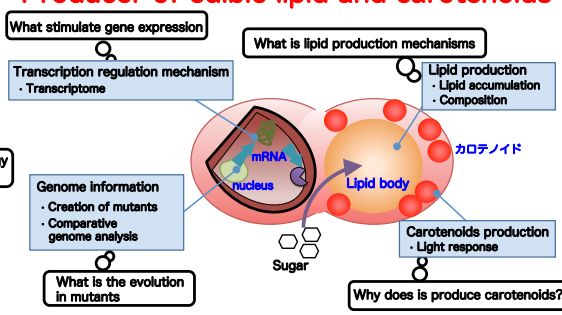

Target of drug design

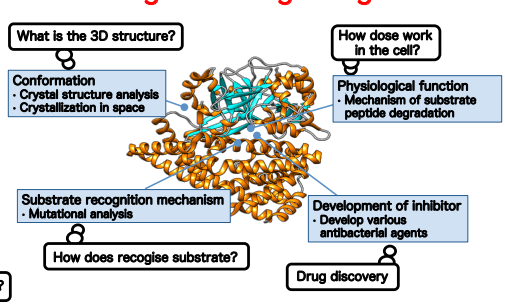

Contact
W. Ogasawara
E-mail: owataru@vos.nagaokaut.ac.jp
TEL: 0258-47-9455
Y. Shida
E-mail: yshida@vos.nagaokaut.ac.jp
TEL: 0258-47-9409

REGENERATIVE MEDICINE HYDROGELS PREPARED FROM WASTE BAGASSE SUGARCANE

Biosustainable Environmental Materials Engineering Laboratory

Nagaoka University of Technology, Department of Science of Technology Innovation

Takaomi Kobayashi

Kobayashi Lab has studied technological development of bio-interfacial and environmental materials which noticed that the biomass and their intelligent functionality. Herein, in their sustainable and environmental view, each material is related to control the material structure and nature from micro-scale to molecular scale and is to give novel intelligence and functionality of polymer, polymer-inorganic composite and inorganic materials mainly prepared from biomass and industrial-wastes. In particular, developing industry-academia cooperation aiming at the industrization as departed from our group at Nagaoka University of Technology aggressively. A study is being advanced by a global point of view and an international cooperation study is being performed through Mexico, Thailand, Malaysia, Vietnam, and Canada and there are a lot of students studying abroad in laboratory with abundant in the internationalism.

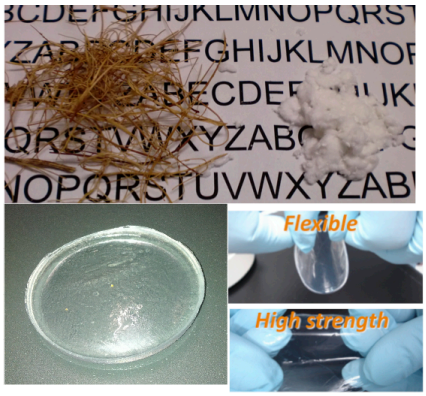

One of our reading research in the world is regenerative medicine prepared from waste bagasse[1] as seen in figure. We have reported that cellulose hydrogels have good mechanical strength and reproducibility, and their structures are readily controllable to provide ideal biocompatibility as implantable materials[2], tissue regeneration[3] and drug release[4].

1) T. Kobayashi, Studies in Natural Products Chemistry, Elsevier B.V. Amsterdam, Netherlands, Atta-ur Rahman Editior, Vol 45, Chapter 1, pp.1-15 (2015)
2) K. Nakasone, S. Ikematsu, T.Kobayashi, Industrial & Engineering Chemistry Research, *55* (1), 30–37(2016).
3) K. Tovar-Carrillo, S. Sugita, M. Tagaya,T. Kobayashi, Industrial & Engineering Chemistry Research, **52**(33), 11607-11613 (2013).
4) H. Jiang, K. Tovar-Carrillo, T. Kobayashi, Ultrasonics Sonochemistry 32,398–406(2016).